CHEMIA

S T U D I A

UNIVERSITATIS BABEŞ–BOLYAI

CHEMIA

3

CUPRINS – CONTENT – SOMMAIRE – INHALT

ISSUE EDITOR:

RADU SILAGHI-DUMITRESCU

MORPHO-STRUCTURAL CHARACTERIZATION OF TIO$_2$ NANOSIZED POWDERS WITH PHOTOCATALYTIC POTENTIAL

MONICA BAIA[a], MONICA SCARISOREANU[b], ION MORJAN[b], IULIANA P. MORJAN[b], LUCIAN BAIA[a], VERONICA COSOVEANU[c], RODICA ALEXANDRESCU[b], VIRGINIA DANCIU[c]

ABSTRACT. Anatase/rutile mixed nanopowders were obtained by laser pyrolysis technique and the influence of the flow rate of the oxidizing agent on their morpho-structural properties was explored by transmission electron microscopy (TEM), X-ray diffraction (XRD) and Raman spectroscopy. The revealed particularities were comparatively discussed with those of the commercial product Degussa P-25 from the perspective of the photocatalytic performances.

Keywords: *TiO$_2$ nanosized powders, morphological investigations, structural properties*

INTRODUCTION

The efficient treatment of industrial wastewaters and contaminated drinking water sources has became of great importance in a world that is facing ever increasing population and decreasing energy resources. An ideal waste treatment process will completely mineralize all the toxic species present in the waste stream without leaving behind any hazardous residues [1]. It should also be cost-effective. At the current phase of development, none of the treatment technologies approach this ideal situation.

Catalytic applications of TiO$_2$ have been studied for decades regarding the elimination of environmental pollutants because of its stability and non-toxicity. TiO$_2$ is the most investigated photocatalyst because it ensures efficient degradation of pollutants from air, water and soil. The band gap of this semiconductor is ca. 3.2 eV, corresponding to a radiation of wavelength around 380 nm [2]. Therefore, UV light is needed to excite the electrons

[a] *Babes-Bolyai University, Faculty of Physics, M. Kogalniceanu 1, 400084 Cluj-Napoca, Romania, monica.baia@phys.ubbcluj.ro*
[b] *National Institute for Lasers, Plasma and Radiation Physics, P.O.Box MG-36, Bucharest-Magurele, Romania*
[c] *Babes-Bolyai University, Faculty of Chemistry and Chemical Engineering, A. Janos 11, 400028 Cluj-Napoca, Romania*

from the valence band to the conduction band. The generated electron-hole pairs serve as the oxidizing and reducing agents. The photodegradation of pollutants in water takes place due to the $\cdot OH$ radicals, which are formed either through the interaction of water molecules with a hole or through the interaction of oxygen molecules with hot electrons, which are the key active species [3].

Since Gleiter's report [4] on nano-materials, more attention was directed towards the research of nanoparticles. It is known that the efficiency of TiO_2 is influenced by factors like crystalline structure [5], particle size [5, 6], and preparation methods [7]. There are many methods for preparing TiO_2 nanoparticles such as: sol-gel method, ball milling, chemical vapor deposition and microemulsion [7]. In a previous study [8] the synthesis of TiO_2 mixed nanopowders using the laser pyrolysis technique as a single-step reaction route was successfully reported. $TiCl_4$ and air were used as gas-phase precursors. Moreover, the influence of the laser power and the flow rate of the oxidizing agent of the samples structure was investigated, for certain synthesis parameters [9]. The photocatalytic performances of these materials were also assessed and the results showed that this preparation method is promising for producing highly active TiO_2 nanopowders [10].

In this work we propose to further explore the morpho-structural properties of this type of TiO_2 nanosized powders from the photocatalytic performance perspective. The influence of the air flows on the morphological and structural properties is analyzed, at a certain C_2H_4 flow through $TiCl_4$. As compared to previously analyzed samples [8-10], different values of the Ar confinement flow and Ar flow for windows cleaning were used in the synthesis of the powders under investigation. The morphology, crystalline structure and particle size were evaluated by transmission electron microscopy (TEM), X-ray diffraction (XRD) and Raman measurements and, the samples structural particularities were comparatively discussed with those of the commercial product Degussa P25.

RESULTS AND DISCUSSION

Prior to investigating the samples, which were coded SC 1-4 and SC 6, energy dispersive analysis by X-rays (EDAX) was performed and the elemental content is summarized in Table 1. One should note that the SC 6 sample was obtained with an increased air flow rate, as described in the Experimental section.

From Table 1 one can observe that a pronounced contamination with carbon occurs in both samples, in principal, due to the high amount of ethylene sensitizer decomposition. The presence of quasi-amorphous carbon in the environmental matrix was also observed in previous laser pyrolysis experiments [11, 12].

Table 1. Elemental content of the TiO$_2$ nanopowders.

Samples code	C At%	O At%	Cl At%	Ti At%
SC 1-4	60.29	23.71	4.47	11.54
SC 6	72.78	16.79	0.99	9.44

Ethylene sensitizer is not always chemically inert and could undergo various extents of dissociation. The favorable conditions for C$_2$H$_4$ dissociation mainly rely on the existence of a strong oxidizing atmosphere during titania gas-phase synthesis. This adventitious carbon is almost totally eliminated by heating the samples in air at rather low temperatures (about 250 ^{o}C). One can also notice the chlorine presence in both samples as a by-product of the synthesis reaction. However, with increasing the air flow rate (sample SC 6) the chlorine amount is more than four times smaller due to the accelerated TiCl$_4$ dissociation (see Table 1).

XRD measurements were further performed and the diffractogramms are illustrated in Figure 1. Both patterns exhibit a background located at small 2θ values due to the amorphous structure presence. The coexistence of anatase and rutile phases was identified.
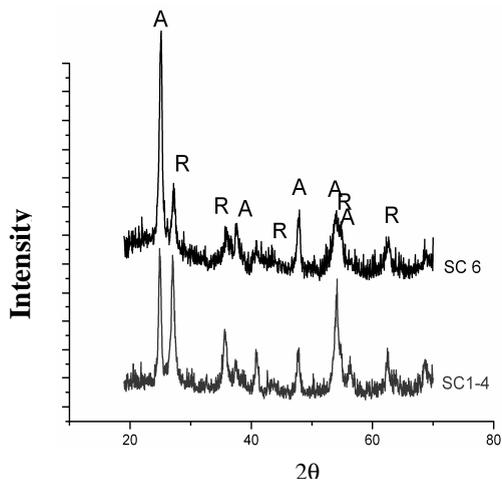
Figure 1. X-ray diffraction patterns of the TiO$_2$ nanopowders. **A** and **R** denote the anatase and rutile phases.

The estimations of the weight percentage of both phases, on the relative crystallized titania amount together with the crystallites mean size calculated according to the Scherrer's formula by considering the peaks

7

located around $2\theta=25^0$ are given in Table 2. For comparison purpose the commercial product Degussa P-25 was also investigated.

As can be observed from Table 2, different amounts of crystalline phases are developed inside the samples. Thus, in the case of the SC 1-4 sample the rutile phase is preponderantly formed, while in the SC 6 sample the anatase phase is the main developed crystalline phase. Previous studies reported [9, 13] about the effect of carbon coating in stabilization of the anatase phase. By taking into account the data summarized in Table 1 related to the carbon content, one can assume that the formation of the anatase phase in the sample SC 6 as the main phase could be associated with the existence of a higher amount of carbon.

Table 2. Structural parameters of the TiO_2 nano-powders as estimated from XRD analysis

Samples code	TiO_2 crystalline phase content (%)		Crystallites dimension (nm)		Specific surface area (m^2/g)
	A	R	A	R	
SC 1-4	42	58	20	16	81
SC 6	75.5	24.5	17	14	86
Degussa P-25	80	20	~ 20	~ 30	50
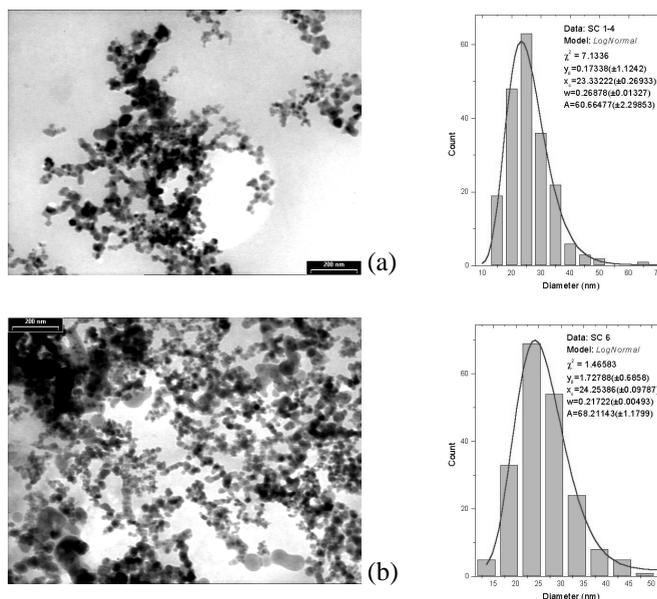
Figure 2. TEM micrographs of the TiO_2 nanopowders and the corresponding particle size distributions:(a) SC 1-4 and (b) SC 6.

By looking at the data from Table 2, related to the specific surface area of the pores, one can see small differences between these values. Therefore, one can infer that this morphological parameter cannot influence the photocatalytic potential of the prepared samples.

TEM micrographs of TiO$_2$ samples (Figure 2) show bunches of loosely-bound aggregated nanoparticles. The sharp particle distributions of the samples make easier the assessment of the mean diameter values that were found to be of ~ 25 and 23 nm and for the samples SC 1-4 (Figure 2a) and SC 6 (Figure 2b), respectively. Thus, with increasing the air flow the nanoparticles dimension decreases, in agreement with previously reported results [9]. However, the nanoparticles dimensions are higher than those of the before prepared samples [10], most probably due to the different synthesis conditions. As expected, an important difference related to the crystallites dimension between the data derived from TEM images and those obtained from XRD analysis exists. However, the mean sizes of the crystallites determined by TEM follow the same logic with those obtained by XRD, i.e. higher dimensions for SC 6 than for SC 1-4.

In order to get further insight into the nanoparticles' morphology TEM images in high resolution mode were also recorded and are presented in Figure 3. The polyhedral shapes and amorphous interfaces of nanoparticles are well noticeable. Thus, in the case of SC 1-4 sample (Figure 3a), an almost squared nanoparticle with lateral dimension of about 12 nm is displayed. The SC6 sample mainly contains elongated nanoparticles, with dimensions of about 30 nm in length and about 20 nm wide. Some ordered defects can be also observed at the nanoparticles interface (see the inset from Figure 3b).
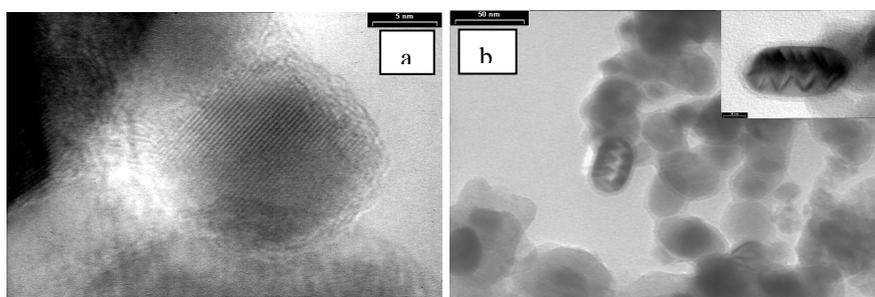
Figure 3. TEM micrographs in high resolution mode obtained from the TiO$_2$ nanopowders**:** SC 1-4 (a) and SC 6 (b).

The Raman spectra of the laser pyrolyzed TiO$_2$ nanopowders are illustrated in Figure 4 and show only two distinct peaks that can be associated with the carbon presence. The first one, located near 1350 cm^{-1} (D-band), is

attributed to the A_{1g} mode and is due to the in-plane disorder [14-16]. This band originates from the disorder-induced scattering generated by imperfections or loss of hexagonal symmetry in the carbon structures [16]. The second Raman characteristic is often present in all carbon and graphite materials spectra around 1595 cm^{-1} (G-band), and is associated with the $2E_{2g}$ mode. By looking at the above mentioned features one observes that the overall Raman signal given by carbon is more intense in the spectrum of sample SC 6 in comparison with that observed in the spectrum of sample SC 1-4. On the other hand, by analyzing the intensities ratio of the two bands it seems that the amorphous/crystalline ratio is not significantly modified as a result of the changes performed in the samples preparation. It should be mentioned that no signature of the anatase or rutile phase was evidenced in the recorded Raman spectra. Taking into consideration that these crystalline structures possess a high Raman sensitivity, i.e. their cross section is high, one can certainly infer that the carbon content is extremely high, as previously was found.
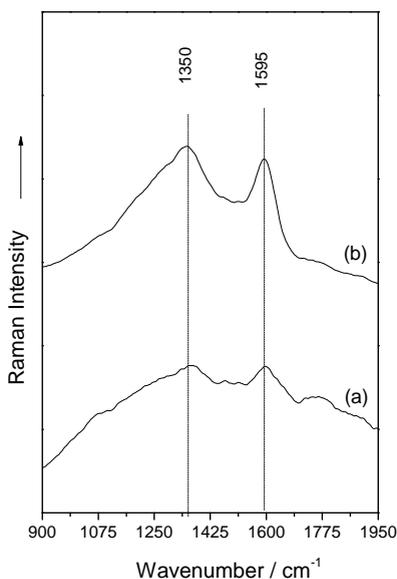
Figure 4. Raman spectra of the TiO$_2$ nanopowders:(a) SC 1-4 and (b) SC 6.

The revealed structural properties can be considered favorable from the perspective of the photocatalytic activity. Thus, from the viewpoint of the anatase phase formation, the best photocatalytic performance is expected from the sample with the highest anatase content, SC 6. On the contrary, the observed differences between the crystallites dimension achieved for the investigated samples and commercial product Degussa P-25 seem to indicate

a better photocatalytic potential for the SC 1-4 sample. However, although the specific surface area is a key parameter in the photocatalytic assessments, it does not completely influence the performance. Thus, another important parameter that certainly influences this evaluation of the photocatalytic properties is the carbon amount. Therefore, the higher carbon content found inside the sample SC 6 in comparison with SC 1-4 would certainly lead to a decrease of its photocatalytic performances. In order to further improve the samples photocatalytic performances a heat treatment that will eliminate the amorphous carbon should be applied.

CONCLUSIONS

Anatase/rutile mixed nanopowders have been obtained by laser pyrolysis and the influence of the flow rate of the oxidizing agent on their morpho-structural properties was evaluated from the perspective of photocatalytic applications. TEM, XRD and Raman spectroscopy were the complementary techniques used for this purpose and the results have been compared with those of the commercial product Degussa P-25, a well known photocatalyst. A substantial increase of the rutile to anatase phase ratio in comparison to Degussa P-25 powder was obtained when a reduced air flow was used, and the presence of a structure preponderantly of anatase was observed when the air flow was higher. One should also emphasize that the high carbon content present inside the prepared samples could be an important drawback in the improvement of the photocatalytic performances.

EXPERIMENTAL SECTION
Samples preparation

The samples were prepared by the laser synthesis technique with the help of a pyrolysis set-up elsewhere described [8], in which TiCl$_4$ and air are simultaneously allowed to emerge into the flow reactor. Ethylene served as a carrier for the TiCl$_4$ vapors and as an energy transfer agent. The used experimental parameters are displayed in Table 3.

Table 3. Experimental parameters for the TiO$_2$ nanopowders. Note the different values of the air flow used for the samples preparation.

Samples code	ϕ Ar$_f$ [sccm]	ϕ Ar$_{conf}$ [sccm]	ϕ Air [sccm]	ϕ C$_2$H$_4$ +TiCl$_4$ [sccm]	P [mbar]	P$_{Laser}$ [W]
SC 1-4	300	1100	50	100	450	200
SC 6	300	1100	75	100	450	200

slm – standard litre per minute, sccm – standard cubic centimetres per minute

Samples characterization

The elemental composition was evaluated from X-ray energy dispersive analysis (EDAX) performed with a SEM-EDX Philips apparatus, using 15 kV acceleration voltage, 1000x magnification and 200 s acquisition time. The surface area of the synthesized samples was determined by using a Sorptomatic 1990 equipment and N_2 adsorption. The specific surface area was obtained by the BET method. The XRD patterns were collected on a PANalytical X'Pert MPD theta–theta system in continuous scan mode (counting 20 s/0.02 2h) between $2\theta = 20–90^o$. A Ni filter, a curved graphite monochromator and a programmable divergence slit (enabling constant sampling area irradiation) were positioned in the diffracted beam ($\lambda = 0.15418$ nm). The powdery deposits were imaged in a transmission electron microscope (TEM) Philips CM120ST (Customized Microscope 120 Super Twin, 120 kV max acceleration voltage, about 2 A resolution, $C_s=\sim1.2$ mm). The samples were also analyzed by high resolution TEM (HRTEM). The Raman spectra of the samples were recorded by using a Witec confocal Raman system CRM 200 equipped with a 100x/0.8 microscope objective and a 300 lines/mm grating. In the recording of the spectra the 633 nm laser line with a power of 3 mW and a spectral resolution around 5 cm^{-1} were employed.

ACKNOWLEDGMENTS

REFERENCES

1. D. F. Ollis and H. Al-Ekabi (Eds.) "Photocatalytic Purification and Treatment of Water and Air", Elsevier, Amsterdam, **1993**.
2. M. Gratzel, "Photocatalysis: Fundamentals and Applications", N. Serpone, E. Pelizzetti (eds.) Wiley, New York, **1989,** 123.
3. H. Al-Ekabi, N. Sperpone, E. Pelizzetti, C. Minero, M. A. Fox, R. B. Draper, *Langmuir,* **1989,** *5,* 250.
4. H. Gleiter, *Prog. Materials Science,* **1989**, *33*, 223.
5. K. Tanaka, T. Hisanaga, A. P. Rivera, "Photocatalytic Purification and Treatment of Water and Air" D. F. Ollis, H. Al-Ekabi (eds.), Elsevier, Amsterdam, **1993,** 169.

6. Z. Zhang, C. C. Wang, R. Zakaria, J. Ying, *Journal of Physical Chemistry B,* **1998***, 102*, 10871.

7. N. Serpone, D. Lawless, R. Khairutdinov, *Journal of Physical Chemistry,* **1995***, 99***,** 16655.

8. R. Alexandrescu, F. Dumitrache, I. Morjan, I. Sandu, M. Savoiu, I. Voicu, C. Fleaca, R. Piticescu, *Nanotechnology* **2004**, *15***,** 537.

9. M. Scarisoreanu, Morjan, R.Alexandrescu, R. Birjega, I. Voicu, C. Fleaca, E. Popovici, I. Soare, L. Gavrila-Florescu, O. Cretu, V.Ciupina, E. Figgemeier, *Applied Surface Science* **2007**, *253*, 7908.

10. E. Figgemeier, W. Kylberg, E. Constable, M. Scarisoreanu, R. Alexandrescu, I. Morjan, I. Soare, R. Birjega, E. Popovici, C. Fleaca, L. Gavrila-Florescu, G. Prodan, *Applied Surface Sci*ence **2007**, *254*, 1037.

11. I. Morjan R. Alexandrescu, I. Soare, F. Dumitrache, I. Sandu, I. Voicu, A. Crunteanu, E. Vasile, V. Ciupina, S. Martelli, *Materials Science Engineering C* **2003**, *23,* 211.

12. I. Morjan, R. Alexandrescu, F. Dumitrache, R. Birjega, C. Fleaca, I. Soare, C. R. Luculescu, G. Filoti, V. Kuncer, L. Vekas, N. C. Popa, G. Prodan, *Journal of Nanoscience and Nanotechnology*, **2010**, *10*, 1223.

13. M. Inagaki, F. Kojin, B. Tryba, M. Toyoda, *Carbon* **2005**, *43*, 1652.

14. F. J. Maldonado-Hodar, C. Moreno-Castilla, J. Rivera-Utrilla, Y. Hanzawa, Y. Yamada, *Langmuir* **2000**, *16*, 4367.

15. G. A. M. Reynolds, A. W. P. Fung, Z. H. Wang, M. S. Dresselhaus, R. W. Pekala, *Journal of Non-Crystalline Solids* **1995**, *188,* 27.

16. L. C. Cotet, M. Baia, L. Baia, I. C. Popescu, V. Cosoveanu, E. Indrea, J. Popp, V. Danciu, *Journal of Alloys & Compounds* **2007**, *434–435*, 854

PREPARATION, CHARACTERIZATION AND SOLID STATE NMR INVESTIGATION OF A DYE-CONTAINING SMECTITE CLAY

SILVIA BORSACCHI[a,b] *, MARCO GEPPI[a,b], LUCIA RICCI[a], ANGELA CARDELLI[a], GIACOMO RUGGERI[a]

ABSTRACT. This paper presents the preparation and characterization of the smectite clay Laponite modified by intercalation of dimethyldioctadecylammonium chloride and the cationic dye methylene blue. The modified clay (Laponite Blue) has been characterized by FT-IR, X-Ray diffraction, thermogravimetric analysis, SEM and solid state NMR. The exploitation of several characterization techniques and of an extended multinuclear and multi-technique solid state NMR approach allowed us to obtain detailed information on the intercalation of the dye in the clay and the structural and dynamic properties of the organic-inorganic interface between the clay surface and the organic modifiers. Laponite Blue appears interesting for the future preparation of polymer nanocomposites with good mechanical and barrier performances as well as exploitable optical properties.

Keywords: Laponite, methylene blue, cation exchange, MAS NMR, CP dynamics

INTRODUCTION

Methylene blue (MB) is an interesting widely used cationic dye. Its optical properties change depending on polarity, composition or pH of the surroundings [1]. It has been successfully used in combination with clays; for example Sumitani et al. have studied an organic/inorganic hybrid compound consisting of methylene blue, a cationic surfactant and a reductant intercalated into saponite. Authors have found that methylene blue is a good oxygen indicator which changes colour in oxidative environment [2]; this system represents an ideal oxygen optical sensor for food packaging [3]. Furthermore, an analytical use of methylene blue deals with its absorption by clay minerals for determining both their cation exchange capacities and surface areas.

Here we present the preparation, characterization and solid state NMR investigation of Laponite, a synthetic layered silicate similar in structure and composition to the natural smectite hectorite (empirical formula $Na^+_{0.7}[Si_8Mg_{5.5}Li_{0.3}]O_{20}(OH)_4]^{0.7-}$ [4, 5]), modified by exchange reaction with dimethyldioctadecylammonium chloride ("$2C_{18}$"), and methylene blue ("MB") ("Laponite Blue"). Laponite platelets (diameter of 25 nm and height of 0.92 nm)

a *Dipartimento di Chimica e Chimica Industriale, Università di Pisa, v. Risorgimento 35, 56126 Pisa, Italy, silvi@ns.dcci.unipi.it*
b *I.N.S.T.M. Consorzio Interuniversitario Nazionale per la Scienza e Tecnologia dei Materiali, Firenze (Italy)*

are constituted by a sheet of magnesium ions in octahedral coordination with oxygen anions and hydroxyl groups and two outer tetrahedral silica sheets. The isomorphic substitution of some magnesium cations with lithium cations and the presence of some vacant positions, give rise to a partial negative charge, which is balanced by sodium cations absorbed on the platelets surface ("Laponite RD"), where a quite large amount of water is also physisorbed [6]. Sodium cations can be exchanged with organic cations, such as alkylammonium surfactants, so obtaining "organoclays" which are extensively used with apolar polymeric matrices (typically polyolefinic) for the preparation of nanocomposites exhibiting very good mechanical and barrier properties [7, 8, 9]. In this field, the intercalation of a dye in an organoclay can be helpful for obtaining a deeper interpretation of the complex mechanism of intercalation/exfoliation of the clay in a polymeric nanocomposite, and nanocomposites with interesting optical properties can also be prepared.

Laponite Blue has been here prepared and characterized by means of FT-IR, TGA, X-Ray powder diffraction, SEM and multinuclear solid state NMR. Spectroscopic techniques have been widely used to study the behaviour of the organic molecules adsorbed on clay surfaces [11, 12, 13, 14, 15, 16, 17]. In particular solid state NMR, thanks to the wide choice of observable nuclei and exploitable nuclear properties, is a very powerful technique for the characterization of organic-inorganic complex materials [18, 19] and it has been extensively applied to the study of modified clays [6, 17, 20, 21].

In this work the use of several characterization techniques and of different solid state NMR experiments, including ^1H, ^{13}C, ^{29}Si spectra and ^1H-^{29}Si Cross-Polarization dynamics experiments, and the comparison with unmodified Laponite (Laponite RD) and that exchanged with dimethyldioctadecylammonium chloride only ("Laponite-2C$_{18}$") allowed the obtainment of interesting and detailed information on the intercalation of the dye in Laponite Blue as well as on the structure and dynamic properties of the organic-inorganic interfaces.

RESULTS AND DISCUSSION

FT-IR analyses carried out on KBr pressed disk with the clay before and after the treatment confirm the occurred modification of Laponite with dimethyldioctadecylammonium chloride and methylene blue. Figure 1 shows the spectrum of Laponite Blue overlapped with that of Laponite RD. In the spectrum of Laponite Blue it can be observed the presence of typical absorption bands due to both 2C$_{18}$ and MB at 2924 cm^{-1} and 2852 cm^{-1} (asymmetric and symmetric stretching of -CH$_2$- in the alkyl chains of 2C$_{18}$) and the weak band at 1603 cm^{-1} (see inset), attributed to aromatic ring vibration of MB.

The amount of 2C$_{18}$ and MB in the clay could be quantified through thermogravimetric analysis. In the thermogram of Laponite Blue (Figure 2) a little weight loss is observable at about 75°C, attributed to water weakly bonded to the clay. A degradation step appears at about 345°C, which must be attributed to 2C$_{18}$ and MB. By deconvolution procedure of the

derivative of TGA curve (inset in Figure 2), we have estimated the amount of $2C_{18}$ and MB in the clay (respectively 23.7 and 8.3 wt.%).
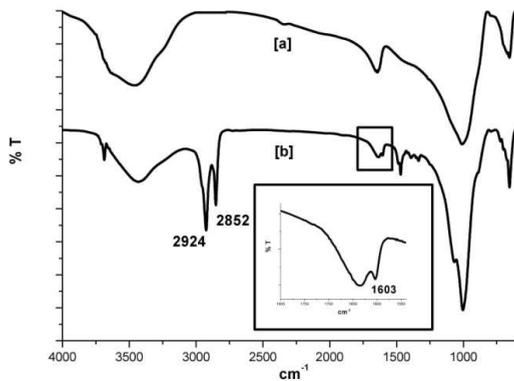
Figure 1. FTIR spectra of (a) Laponite RD and (b) Laponite Blue
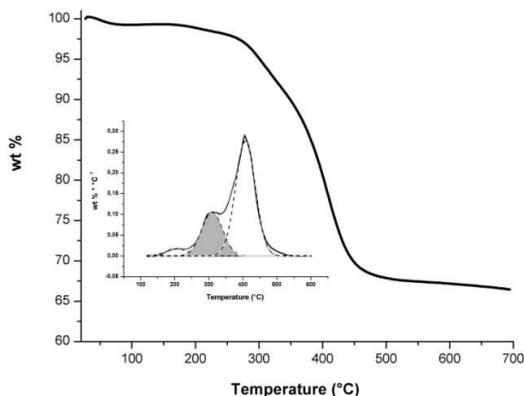
Figure 2. TGA thermogram of Laponite Blue with deconvolution of its derivative curve (inset)

Figure 3 shows the X-ray diffractograms of Laponite Blue, Laponite RD and Laponite-$2C_{18}$. It is evident an increase in the d-spacing (the spacing between two consecutive clay platelets) in passing from Laponite RD to both the modified clays. Furthermore, the d-spacing of Laponite Blue is larger than that of Laponite-$2C_{18}$, which can be attributed to the intercalation of both $2C_{18}$ and MB in the galleries between the clay platelets.
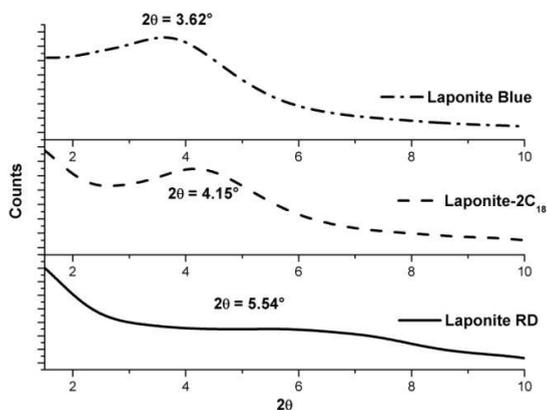
Figure 3. X-Ray diffractograms of Laponite RD, Laponite-2C$_{18}$ and Laponite Blue

SEM micrograph highlighted a non-homogeneous distribution of the particles size in both Laponite RD and Laponite Blue (Figure 4). The surface of Laponite Blue appears rougher than that of Laponite RD, probably because of the treatment with 2C$_{18}$ and MB.
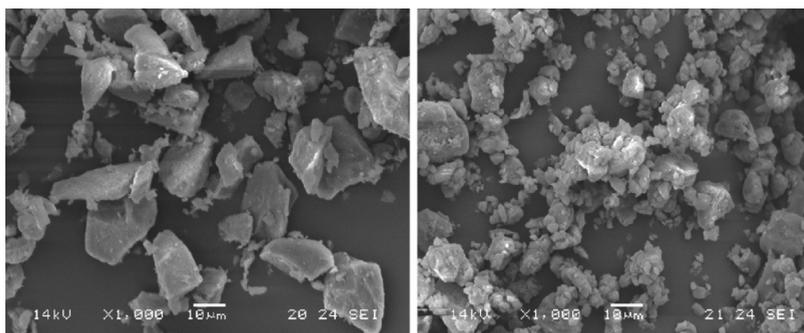
Figure 4. SEM micrograph of (left) Laponite RD and (right) Laponite Blue

Solid state NMR

In Figure 5 the [29]Si CP-MAS spectra of Laponite Blue, Laponite RD and Laponite-2C$_{18}$ are shown. The most intense peak in all spectra, observed at -94.7 ppm, arises from Q^3 $\underline{Si}$(OMg)(OSi)$_3$ silicon nuclei of the tetrahedral sheets, while the small and broad signal centered at about -85 ppm must be attributed to not fully condensed Q^2 silicon nuclei, mostly present as $\underline{Si}$(OMg)(OSi)$_2$(OH). In the two modified Laponite samples this signal clearly shows the presence of two components. In a previous work [6], we could assign the peak at -84.5 ppm to silanols present on the clay platelet edges,

while that at -86.5 ppm to those located onto the platelets surface. The scarce resolution of the Q^2 signal in the spectrum of Laponite RD can be attributed to the known presence of a large amount of physisorbed water, mostly removed in the organically modified samples, which gives rise to a noticeable heterogeneity of silanols environments, resulting in a distribution of isotropic chemical shift values. The ^{29}Si CP-MAS spectrum of Laponite Blue is substantially identical to that of Laponite-2C$_{18}$, indicating that, as expected, MB does not induce chemical modifications of the clay.
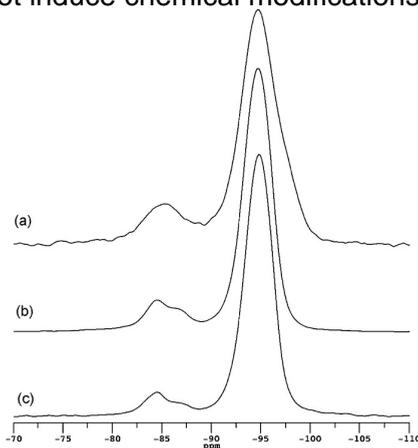
Figure 5. ^{29}Si CP-MAS spectra, recorded at a MAS frequency of 6 kHz, of (a) Laponite RD, (b) Laponite-2C$_{18}$, (c) Laponite Blue

Interesting information can be obtained from ^{1}H-MAS spectra, which are shown in Figure 6. As already reported [6], in passing from Laponite RD to Laponite-2C$_{18}$ the signal at 4.4 ppm, due to physisorbed water and hydrogen-bonded silanol protons, substantially disappears, as result of water removal; the signal due to Mg(OH) protons is still observed at 0.4 ppm and peaks at 1.6 and 1.8 ppm appear, arising from 2C$_{18}$ alkyl chains and silanols not involved in hydrogen-bonds, respectively. The spectrum of Laponite Blue shows the same signals observed for Laponite-2C$_{18}$, confirming that the treatment with both 2C$_{18}$ and MB still determines the removal of most of the physisorbed water and of silanol hydrogen-bonds. Signals of MB protons could not be observed probably due to the scarce amount of the dye and an intrinsic broadness of its signals, not efficiently removed by MAS. It is worth to notice that the spectrum of Laponite Blue shows a noticeable narrowing with respect to that of Laponite-2C$_{18}$. Even if the analysis of ^{1}H-MAS spectra is in general far from being straightforward, due to the complex effects of incomplete averaging of homonuclear dipolar couplings, the observed narrowing can be an indication of a larger mobility of the organic components in Laponite Blue with respect to Laponite-2C$_{18}$.
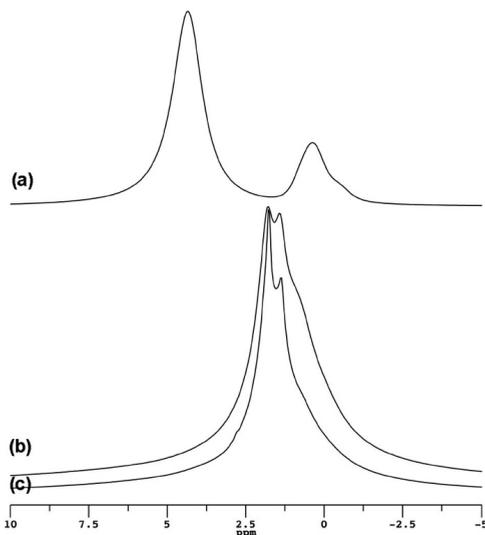
Figure 6. [1]H-MAS spectra, recorded at a MAS frequency of 6 kHz, of (a) Laponite RD, (b) Laponite-2C$_{18}$, (c) Laponite Blue

In order to obtain more detailed information on the organic-inorganic interface between Laponite and 2C$_{18}$ and MB, [1]H-[29]Si CP dynamics curves were experimentally built and analysed. This basic experiment, often used in the study of organic-inorganic multicomponent materials [17], consists in the registration of [29]Si CP-MAS spectra at different values of contact time (the time interval during which the ^{1}H magnetization is transferred to [29]Si nuclei); the peaks area is then plotted as a function of the contact time and the resulting trends fitted with suitable equations. For each peak, the values of the Cross-Polarization time, T$_{SiH}$, and of the ^{1}H spin-lattice relaxation time in the rotating frame, T$_{1\rho}$, both related to structural and dynamic properties of the interface, are obtained as best-fitting parameters. In Figure 7 the [29]Si CP-MAS spectra recorded at different values of contact time for Laponite Blue, Laponite-2C$_{18}$ and Laponite-RD are shown.

The experimental trends of the three samples appear clearly different, suggesting differences in the properties of the interface between the clay and the intercalated protonated species (water in the case of Laponite RD).

Q3 and Q2 signal areas vs contact time were fitted to equation 1 [21], or using its bi-exponential modification, when necessary.

$$I(ct) = M_0 \left(e^{-ct/T_{1\rho}(^1H)} - e^{-ct/T_{SiH}} \right) \qquad (eq.1)$$
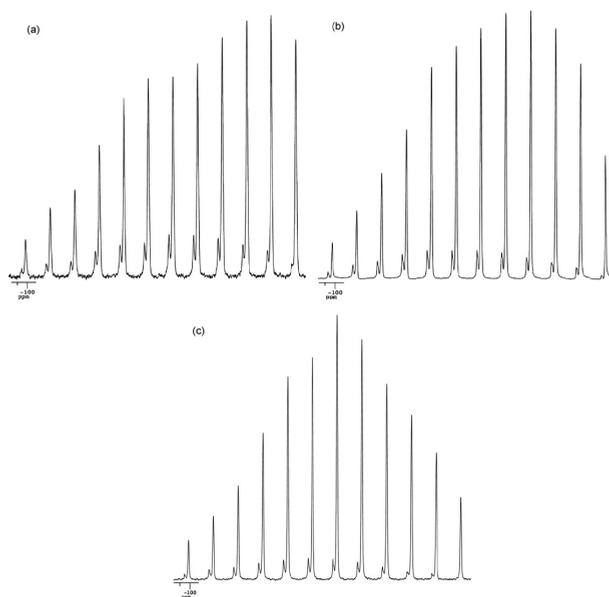
Figure 7. Selection of ^{29}Si CP-MAS spectra of (a) Laponite RD, (b) Laponite-2C$_{18}$, (c) Laponite Blue, recorded at a MAS frequency of 6 kHz and at the same contact time values, ranging between 0.1 and 20 ms

An example of fitted curve is reported in Figure 8, and the results of the analysis are summarized in Table 1.

T_{SiH} is a time constant related to the strength of the ^{1}H-^{29}Si dipolar couplings, being smaller for ^{29}Si nuclei more strongly coupled to protons. Stronger dipolar couplings arise either from a higher number of spatially close proton nuclei and a higher rigidity of the domain. In Laponite Blue the T_{SiH}'s of Q^{2} silicon nuclei are smaller than that of Q^{3}, in agreement with the presence and the lack of directly bonded OH groups, respectively. While directly bonded OH groups will be the main source of magnetization for Q^{2} silicons, fully condensed Q^{3} silicons will receive magnetization mainly from protons of the intercalated organic species 2C$_{18}$ and MB.

The interpretation of proton $T_{1\rho}$ values is more complex; in the solid state spin diffusion tends to average different intrinsic values of proton spin-lattice relaxation times in the rotating frame, related to differences in the molecular motions with characteristic frequencies of the order of kHz, to a single value. The measurement of a single $T_{1\rho}$ indicates that the sample is homogeneous approximately on a 10 Å spatial scale, while multiple partially averaged values are measured in samples heterogeneous on that scale. In Laponite Blue the detection of three different $T_{1\rho}$ indicates that the different
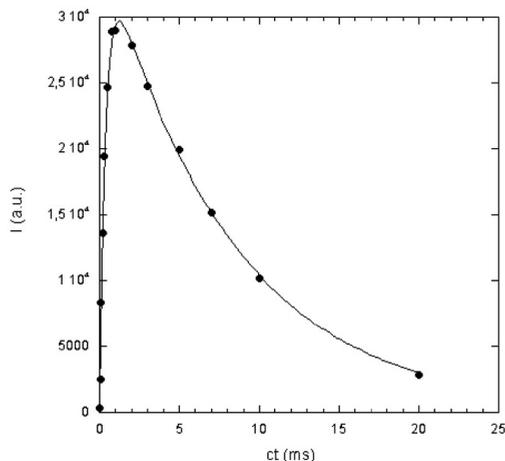
Figure 8. Fitting of the CP dynamics curve of the ^{29}Si signal at -86.5 ppm of Laponite-2C$_{18}$. On the *x* and *y* axes contact time values and signal areas are reported, respectively

protons (edge and surface silanol and organic ones) belong to domains with average dimensions larger than about 10 Å.

Table 1. T$_{SiH}$ and proton T$_1\rho$ as obtained from the analysis of the CP dynamics curves of the different silicon nuclei in Laponite RD, Laponite-2C$_{18}$ and Laponite Blue. In the cases in which multiple components were present their fractional weight is reported within parentheses.

	Q^2			Q^3	
	T$_{SiH}$ (ms)	T$_1\rho$ ms		T$_{SiH}$ (ms)	T$_1\rho$ms
Laponite RD	0.90 ± 0.01	1.0 ± 0.1 (w=0.75±0.03) 13.0 ± 2 (w=0.25±0.03)		0.46 ± 0.06 (w=0.31±0.02) 7.3 ± 0.9 (w=0.69±0.02)	3.0 ± 0.5 (w=0.22±0.03) 30 ± 2 (w=0.78±0.03)
	Q^2 (-84.5 ppm)		Q^2 (-86.5 ppm)		
	T$_{SiH}$ (ms)	T$_1\rho$ ms	T$_{SiH}$ (ms)	T$_1\rho$ms		
Laponite-2C$_{18}$	0.37 ± 0.02	8.0 ± 0.4	0.47 ± 0.03	12.6 ± 0.8	0.73 ± 0.06	23 ± 3
Laponite Blue	0.45 ± 0.03	5.2 ± 0.3	0.53± 0.08	6.4± 0.9	0.74± 0.04	10.0± 0.6

The comparison with the results obtained for Laponite-2C$_{18}$ allows us to gain some insights into the effect of the presence of MB. The T$_{SiH}$ of Q^3 silicons is not modified by the presence of the dye, suggesting that MB is not located in close proximity of the clay platelets surface, where 2C$_{18}$ cations would remain dominant, attracted by the surface negative charges of the clay. Moreover the T$_{1\rho}$ values measured in Laponite Blue are clearly smaller than those of Laponite-2C$_{18}$. This could be due either to a very small intrinsic T$_{1\rho}$ of MB, which, by spin diffusion, would strongly decrease all the other measured values, or, more likely, to an increase of mobility in the kHz regime of the most abundant alkyl chains, as already suggested by ^{1}H-MAS spectra.

At last it is interesting to observe the results obtained for Laponite-RD, which appears much different from those of the organoclays. The fitting of the curves required the use of two T$_{1\rho}$ components for both silicon signals and of two T$_{SiH}$ for Q^3 ones, indicating a strong heterogeneity of silicon environments, which is probably due to the presence of a large amount of water interacting in different ways with the clay platelets surface. The T$_{SiH}$ of Q^2 is larger than that detected in the organoclays, indicating that the physisorbed water makes the silanols environment on average quite mobile. The two values obtained for Q^3, the polarization of which mainly arises from water, again reflects the presence of water differently interacting with the clay and therefore showing different degrees of mobility. Moreover, the multiple values of T$_{1\rho}$ again indicate a noticeable distribution of different proton environments, as well as heterogeneity on a 10 Å scale.

Useful information on Laponite Blue could also be obtained from ^{13}C spectra. While the MB signals could not be easily observed, those of 2C$_{18}$ were evident and the comparison with the spectrum of Laponite-2C$_{18}$ was particularly useful. In Figure 9 the 20-45 ppm region of the ^{13}C CP-MAS spectra of the two organoclays is shown. The signals observed arise from 2C$_{18}$ alkyl chains and in particular those at 33 and 31 ppm are attributed to methylene groups in all-trans conformation and experiencing fast interconformational jumps between trans and gauche conformations, respectively. It is evident that in Laponite Blue the relative intensity of the peak at 31 ppm is significantly larger, suggesting that a higher fraction of surfactant alkyl chains experiences a noticeable mobility, in agreement with what already highlighted by proton MAS spectra and T$_{1\rho}$ results.

CONCLUSIONS

A smectite clay, Laponite, doubly organically modified by intercalation of an alkylammonium surfactant and a dye, methylene blue, has been successfully prepared. The intercalation of the dye could be verified with several characterization techniques and quite detailed information could be obtained through different solid state NMR experiments, also by exploiting the comparison with the same clay without dye. The organic modification of the clay causes the removal of most of the physisorbed water, present in a large amount in the untreated Laponite, with consequent strong modification of the environment of the nuclei present on the clay platelets surface. The d-
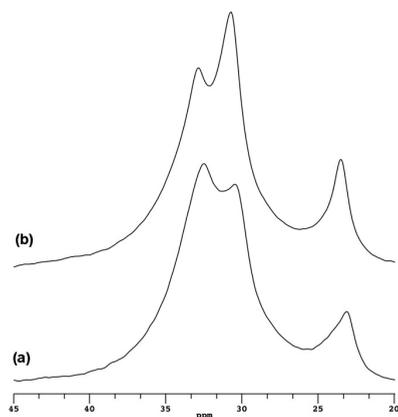
Figure 9. 20-45 ppm region of the ^{13}C CP-MAS spectra of (a) Laponite-2C$_{18}$ and (b) Laponite Blue, recorded at a MAS frequency of 6 kHz

spacing of the clay increases after the intercalation of the surfactant and a further increase is observed when the dye is added. Methylene blue seems to be dispersed among the surfactant chains, rather than directly adsorbed on the clay surface. The observed d-spacing increase is also associated with an increase of mobility of the 2C$_{18}$ alkyl chains clearly detected in several NMR experiments, which can also indicate a partial disorder in the clay platelets arrangement induced by the intercalation of both the organic modifiers. The dye-containing Laponite here obtained could be used for the preparation of polymer nanocomposites potentially exhibiting not only the good mechanical and barrier properties provided by the clay but also the interesting optical properties of methylene blue.

EXPERIMENTAL SECTION
Materials

Laponite RD (supplied by Rockwood Additives, UK), is a synthetic clay of the smectite group. Laponite has been modified with dimethyldioctadecylammonium chloride (Fluka) and methylene blue (Fluka), whose chemical structures are shown in Figure 10. Figure 11 shows an image of the powder before (Laponite RD) and after (Laponite Blue) the modification. Laponite-2C18 was available from a previous work [6].
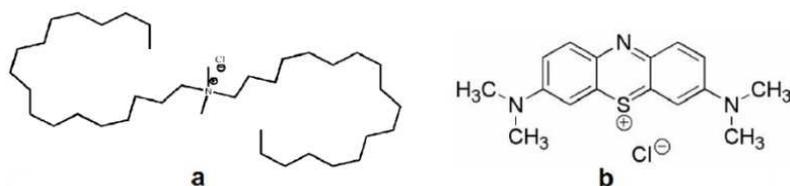
Figure 10. Structures of (a) dimethyldioctadecylammonium chloride and (b) methylene blue

Synthesis of Laponite Blue

In a three-neck flask equipped with magnetic stirrer, thermometer, dropping funnel and dropping cooling 2 l of H_2O was added. When temperature was at 60°C, 10.12 g of Laponite RD was constantly added under vigorous stirring.

The suspension was stirred for 2 hours. Afterwards, 500 cc of aqueous solution containing dimethyldioctadecylammonium chloride (4.59 g) and methylene blue (79.80 mg) was added.

The mixture was still stirred for 24 hours and then filtered under vacuum and washed with three portions of water (to remove all excess of both ammonium salts). The organoclay was freeze-dried, ground with ball mill and characterized (yield 79.7%).

Figure 11. Image of (left) Laponite RD and (right) Laponite Blue

Samples characterization

FT-IR spectra were recorded in a Perkin Elmer Spectrum One spectrometer on KBr pressed disk.

Thermogravimetric analysis (TGA) was carried out with a Mettler Toledo TGA/SDTA 851 calorimeter from 25 to 700 °C a t a scanning rate of 10 °C/min in nitrogen atmosphere.

X-ray diffractograms were achieved on a Diffractometer D 500/501 Siemens mod Kristalloflex 810 with CuKα radiation (λ = 0.15406 nm).

Scanning Electron Microscopy (SEM) were recorded with a microscope Jeol JSM mod. T-300.

Laponite Blue was ground with Retsch ball mill.

Solid state NMR spectra were recorded on a a double-channel Varian InfinityPlus 400 spectrometer, equipped with a 7.5 mm cross-polarization (CP) - Magic Angle Spinning (MAS) probehead, working at 399.88 MHz for ^1H, 79.44 MHz for ^{29}Si, and 100.56 MHz for ^{13}C. ^1H, ^{13}C, and ^{29}Si 90° pulse lengths were always between 4.0 and 5.0 µs. ^{13}C and ^{29}Si spectra were recorded under high-power proton decoupling conditions. ^{29}Si CP-MAS spectra were recorded with a MAS frequency of 6 kHz, a recycle delay of 2 s, contact times variable in the range 0.1-20 ms and accumulating 4000 transients. ^{13}C CP-MAS spectra were recorded with a MAS frequency of 6 kHz, a recycle delay of 2 s, a contact time of 5 ms and accumulating 2000 and 33000

transients for Laponite-2C$_{18}$ and Laponite Blue, respectively. [1]H-MAS spectra were acquired at a MAS frequency of 6 kHz, with a recycle delay of 2 s and accumulating 64 transients. TMS was used as a primary chemical shift reference for all nuclei, while hexamethylbenzene, 3-(trimethylsilyl)-1-propane-sulfonic acid sodium salt, and adamantane as secondary references for ^{13}C, [29]Si and ^{1}H, respectively. All of the experiments were performed at a temperature of 20 ℃, controlled to within ± 0.1 ℃.

ACKNOWLEDGMENTS

REFERENCES

1. J. Cenens, R. A. Schoonheydt, *Clays and Clay Minerals,* **1988**, *36*, 214.
2. M. Sumitani, S. Takagi, Y. Tanamura, H. Inoue, *Analytical Sciences,* **2004**, *20*, 1153.
3. A. Mills, *Chemical Society Reviews* **2005**, *34*, 1003.
4. N. J. Willenbacher, *Journal of Colloid and Interface Science,* **1996**, *182*, 501.
5. www.laponite.com (Rockwood Specialties).
6. S. Borsacchi, M. Geppi, L. Ricci, G. Ruggeri, C.A. Veracini, *Langmuir,* **2007**, *23*, 3953.
7. M. Alexandre, P. Dubois, *Materials Science and Engineering: R: Reports,* **2000**, *28*, 1.
8. S. Sinha Ray, M. Okamoto, *Progress in Polymer Science,* **2003**, *28*, 1539.
9. S.J. Ahmadi, Y.D. Huang, W. Li, *Journal of Materials Science,* **2004**, *39*, 1919.
10. P. T. Hang, G. W. Brindley, *Clays and Clay Minerals*, **1970**, *18*, 203.
11. A. Guerses, C. Dogar, M. Yalcin, M. Acikyildiz, R. Bayrak, S. Karaca, *Journal of Hazardous Materials,* **2006**, *131*, 217.
12. A. Al-Futaisi, A. Jamrah, R. Al-Hanai, *Desalination,* **2007**, *214*, 327.
13. C. A. P. Almeida, N. A. Debacher, A. J. Downs, L. Cottet, C. A. D. Mello, *Journal of Colloid and Interface Science,* **2009**, *332*, 46.
14. Q. Chen, W. T. Kerk, A. M. Soutar, X. T. Zeng, *Applied Clay Science,* **2009**, *44*, 156.
15. D. Ghosh, K. G. Bhattacharyya, *Applied Clay Science,* **2002**, *20*, 295.
16. M. Hajjaji, A. Alami, *Applied Clay Science,* **2009**, *44*, 127.
17. M. Geppi, S. Borsacchi, G. Mollica, C.A. Veracini, *Applied Spectroscopy Reviews,* **2009**, *44*, 1.
18. M. Geppi, S. Borsacchi, G. Mollica "Solid-state NMR of organic/inorganic multi-component materials" in Encyclopedia of Magnetic Resonance, Eds-in-chief R.K. Harris and R.E. Wasylishen, John Wiley, Chichester, DOI:10.1002/9780470034590. emrstm1014, published online **2008**.
19. J. Grandjean, *Clay Materials,* **2006**, *41*, 567.
20. D. Kubies, R. Jérôme, J. Grandjean, *Langmuir,* **2002,** *18*, 6159.
21. E.O. Stejskal, J. Schaefer, M.D. Sefcik, R.A. McKay, *Macromolecules,* **1981**, *14*, 275.

SPECTROSCOPIC EVIDENCE OF COLLAGEN ELECTRODEPOSITION ON ACRYLIC BONE CEMENT

SIMONA CAVALU[a], VIORICA SIMON[b], FLORIN BANICA[a], IOAN OSWALD[a], EMILIA VANEA[b], IPEK AKIN[c], GÜLTEKIN GÖLLER[c]

ABSTRACT. Complementary spectroscopic methods such as FTIR, FT Raman and XPS are applied in this work in order to investigate the surface of acrylic cements after electrolytic deposition of collagen. As an alternative of antibiotic, silver oxide was incorporated in the polymethyl metacrylate (PMMA) matrix and structural properties are discussed by comparing the information obtained using these methods.

Keywords: collagen, bone cement, ATR FTIR, FT Raman, XPS

INTRODUCTION

Poly(methyl methacrylate) (PMMA) bone cements are extensively used in certain types of total hip or total knee replacements and are of potential utility wherever mechanical attachments of metal to living bone is necessary [1, 2]. The main function of the cement is to serve as interfacial phase between the high modulus metallic implant and the bone, thereby assisting to transfer and distribute loads [3, 4]. From a chemical point of view, the curing process of the PMMA-based acrylic bone cement, also known as cold curing, is the result of the free radical polymerization of a mixture of PMMA and methyl methacrylate (MMA), initiated by the decomposition of benzoyl peroxide and activated by presence of tertiary amines. During the polymerization process the dough mixture becomes stiff in a short time (10-15 min), which allows the application in situ and the primary fixation of the joint prosthesis. Orthopedic acrylic bone cements have to fulfill several medical requirements, such as low values of maximum cure temperature (to avoid thermal necrosis of the bone tissue during the setting of the cement), moderate sitting time (so that cement does not cure too fast or too slowly), high values of compressive strength (allowing the cured cement mantle to withstand the compressive loads involved by normal daily activities) [5,6,9]. Silver based antimicrobials captured much

[a] *University of Oradea, Faculty of Medicine and Pharmacy, P-ta 1Decembrie 10, 410068 Oradea, Romania, scavalu@rdslink.ro*
[b] *Babes-Bolyai University, Faculty of Physics & Institute of Interdisciplinary Research in Bio-Nano-Sciences, Cluj-Napoca, Romania*
[c] *Istanbul Technical University, Metallurgical and Materials Engineering Dept, Istanbul, Turkey*

attention not only because of the non toxicity of the active Ag^+ to human cells [7] but also because of their novelty being a long lasting biocide with high temperature stability and low volatility. The antimicrobial efficacy of these composites depends on their ability to release the silver ions from these composites upon interaction with biological fluids [6]. Hence, silver doped materials are used as an alternative or complementary to antibiotic loaded cements. On the other hand, it has been previously demonstrated that collagen coating increases the proliferation of osteoblasts into the calcium phosphate ceramics [8], as it comprises 90% of the extracellular matrix of bone and occupies a key role in the interaction of osteoblasts and their environment. In the present study, in order to improve the biomineralisation and biocompatibity of the acrylic bone cement, electrolytic deposition of collagen was performed. The coating was confirmed by different spectroscopic methods: ATR-FTIR, FT-Raman and XPS.

RESULTS AND DISCUSSION

The ATR FTIR spectra recorded before and after collagen electrodeposition on $Ag_2O/PMMA$ bone cement are presented comparatively in Figure 1.
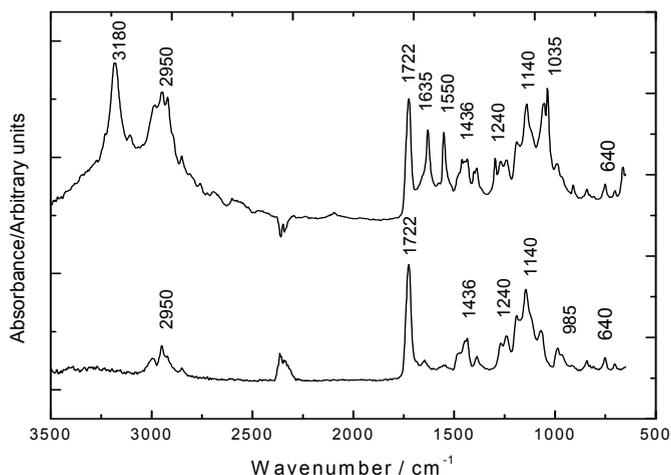
Figure 1. ATR FTIR spectra recorded on the surfaces of the $Ag_2O/PMMA$ before (upper) and after collagen electrodeposition (lower).

The marker bands of PMMA are a sharp and intense peak at 1722 cm^{-1} due to the presence of ester carbonyl group $v(C=O)$ stretching vibration, a broad band at 1436 cm^{-1} due to $\delta(CH_3)$ vibration mode, the peaks in the range 1260-1000 cm^{-1} assigned to O-C-O, $C-CH_3$ and C-COO stretching vibrations, and the region between 950-650 cm^{-1} due to the bending of C-H bond [5,10]. In the high wavelength range, the band at 2950 cm^{-1} is due to

28

CH_2 asymmetric and symmetric stretching, whereas in the low wavelength range, some characteristic bands of Ag_2O are present at 640 and 580 cm^{-1} as an asymmetric O-Ag-O bending mode [11]. The presence of the collagen on the samples surface is confirmed throughout the characteristics of the distinct peaks of collagen: amide I at 1635 cm^{-1} (C=O stretching), amide II at 1550 cm^{-1} (N-H deformation) and amide III around 1200 cm^{-1} (combined N-H bending and C-N stretching). Upon the electrodeposition procedure, the material absorbs a considerable amount of water, as indicated by the large and intense band at 3180 cm^{-1}. In order to obtain complementary information on the surface modifications upon collagen deposition, FT Raman analysis was applied before and after electrodeposition (Figure 2).
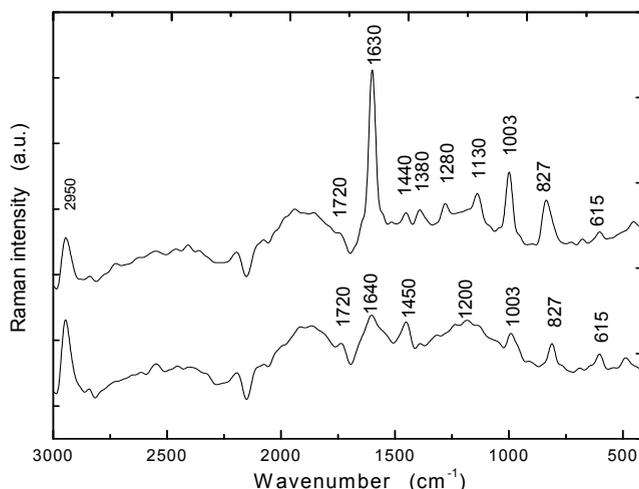
Figure 2. FT Raman spectra recorded on the samples surface before (lower spectrum) and after collagen electrodeposition (upper spectrum).

The main Raman scattering transitions have been observed in PMMA spectra located at 1720 and 1640 cm^{-1}. These transitions are assigned to a stretching mode of the C=O bond in the ester carbonyl group present in both monomer and polymer, and to a stretching mode of the C=C bond present in the monomer only, respectively. According to literature [12,13] the ratio of their intensities should therefore provide a measure of the mass percentage of the uncovered monomer inside the polymer. Other transitions are related to δ(CH_3) vibration mode at 1450 cm^{-1}, C-O-C stretch vibration at 1003 cm-1, CH_2 rocking vibration at 827 cm^{-1}, while in the low region the bands 615 and 490 cm^{-1} are the Raman vibrations of Ag_2O. Upon collagen deposition, the relative intensities of the Raman bands are strongly modified and shifted. According to the literature [14] the collagen matrix is related to

the Raman bands 1650 cm^{-1} (amide I), 1440 cm^{-1} (amide II), and around 1200 cm^{-1} (amide III). In our spectra, the band at 1720 cm^{-1}appears weaker and the band at 1640 cm^{-1} is enhanced and slightly shifted to lower wavenumbers after the electrodeposition procedure. This behavior indicates a reaction between the collagen layer and Ag$_2$O/PMMA substrate and can be attributed either to hydrogen bonding or to the formation of a new functional group, as the OH deformation band usually appears in the range 1600-1640 cm^{-1}, overlapping the amide I band. If hydrogen bonding occurs, it would involve a weak shift of the carbonyl bond (C=O), making the observation more difficult with Raman spectroscopy. In the IR spectra, frequencies associated with carbonyls (1720 cm^{-1}) are generally not noticeably shifted by hydrogen bonding. In fact, the carbonyl peak is assigned to both non-bonded and H-bonded carbonyls.

The XPS global spectra recorded on the acrylic cement with and without silver oxide, before and after collagen deposition are presented in Figure 3, whereas the core level spectra of nitrogen and silver are showed in Figure 4. The elemental composition on samples surface is presented in Table 1.
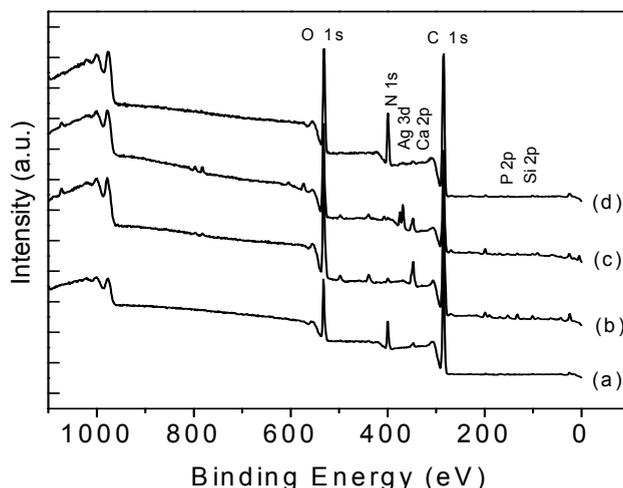
Figure 3. XPS survey spectra of (a) PMMA acrylic cement, (b) PMMA cement after collagen electrodeposition, (c) Ag$_2$O/PMMA acrylic cement and (d) Ag$_2$O/PMMA after collagen electrodeposition.

Table 1. Relative percentage of the main components before and after collagen deposition

Sample	% at						
	Si	Ca	P	Ag	O	C	N
PMMA	2	3.2	1.9	-	21	70.6	1.3
PMMA/Collagen	0.4	0.7	-	-	12.8	86.1	8.8
Ag$_2$O/PMMA	0.8	2.2	0.7	1.3	23.2	69.7	2.1
Ag$_2$O/PMMA/Collagen	0.6	0.3	-	0.1	16.2	70.3	12.5
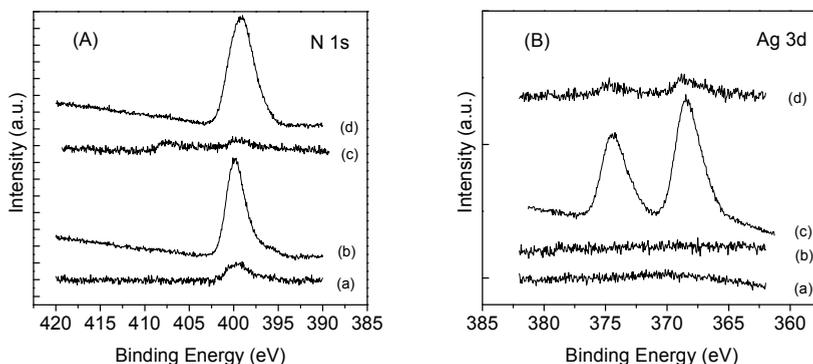
Figure 4. XPS N1s (A) and Ag 3d (B) high resolution spectra of (a) PMMA acrylic cement, (b) PMMA/collagen cement,
(c) Ag$_2$O/PMMA cement and (d) Ag$_2$O/PMMA/ collagen.

Generally both carbon and nitrogen can be used as markers of proteins attachment due to their presence in great amount in protein structure [15], but as the acrylic cements already contain a significant amount of carbon, in this study only the N 1s will be considered to evaluate collagen deposition. The adsorption of collagen is reflected thus by the evolution of the N 1s photoelectron peak. The nitrogen concentration was very small before protein adsorption and considerably increases especially for the silver containing acrylic cement. The N 1s core level spectra (Figure 4A) reveals a peak at 400 eV, characteristic to C-NH$_2$ groups [16]. On the other hand, due to the protein coverage, a significant reduction of Ag 3d photoelectron peaks (Figure 4B) is observed. The composition of the samples surface with respect to Si, Ca, P and Ag (Table 1) is also modified compared with that recorded before collagen deposition, being another proof of collagen surface coverage. At the same time, the amount of oxygen decreases for both collagen coated samples (with or without silver oxide) due to the fact that collagen is less rich in oxygen atoms comparing the substrate used. The results show that the silver oxide presence in PMMA matrix improves the protein attachment, and, according to the literature, Ag$^+$ reacts with thiol groups in proteins, due to a high affinity between sulphide and the soft metal [17, 18].

CONCLUSIONS

The surface of Ag$_2$O/PMMA acrylic bone cement was investigated by complementary FTIR, FT Raman and XPS spectroscopy before and after collagen electrodeposition. The results confirm the presence and stability of the collagen layer on the surface. Moreover, they indicate that silver oxide presence in PMMA matrix improves the protein attachment.

EXPERIMENTAL SECTION

The investigated materials were prepared using commercial PMMA based cements as starting material (Biomecanica Ind. Brasil), having the following composition: liquid- methylmethacrylate (monomer) 84.4%, butylmethacrylate 13.2%, N:N dimethyl p- toluidine 2.4%, hidroquinone 20 ppm; powder - methylmethacrylate (copolymer) 87.3%, polymethyl metacrylate 2.7 %, barium sulphate 10%. As antimicrobial agent, Ag_2O particles were incorporated with respect to the total powder amount in a concentration of 5 %(w/w). Electrolytic deposition of soluble collagen type I from calf skin (Fluka) was carried out in a three-electrode electrochemistry system working in chronoamperometric mode, as previously reported [9]. The sample surfaces were analyzed by complementary FTIR, FT Raman and XPS spectroscopy. The equipments used were Spectrum BX Perkin Elmer FTIR spectrometer, equipped with MIRacle ATR accessory (ZnSe crystal), spectra collected in the wavelength range 4000-400 cm^{-1} at a nominal resolution of 4 cm^{-1}, with a scanning speed of 32 cm^{-1}, total 100 scans being accumulated for each spectrum; FT Raman Bruker EQUINOX 55 equipment, spectra collected at 4 cm^{-1} resolution, with 600 scans and laser power between 100-370 mW; SPECS PHOIBOS 150 MCD system equipped with monochromatic Al-K_α source (250 W, hv=1486.6 eV), hemispherical analyser and multichannel detector;the typical vacuum in the analysis chamber during the measurements was in the range of 10^{-9}- 10^{-10} mBar and the binding energy scale was charge referenced to the C 1s at 284.6 eV. The samples surfaces were analysed before and after collagen electrodeposition.

ACKNOWLEDGMENTS

REFERENCES

1. J. Charnley, "Acrylic Cement in Orthopaedic Surgery" Williams and Wilkins Eds, Baltimore, USA, **1970,** chapter 1.
2. S. J. Breusch, K.-D. Kuhn, *Orthopade,* **2003**, *32*, 41.
3. F. R. DiMaio, *Orthopaedics*, **2002,** *25*, 1399.
4. W. R. Krause, "Encyclopedia of Medical Devices and Instrumentations", J. G. Webster (ed), Willey, New York, USA, **1988,** vol.1.
5. S. Cavalu, V. Simon, *Journal of Optoelectronics and Applied Materials,* **2006,** *8/4*, 1520.

6. S. Cavalu, V. Simon, G. Goller, I. Akin, *Digest Lournal of Nanomaterials and Biostructructures*, **2011** *6/2*, 779.
7. J. Hardes, A. Streitburger, H. Ahrens, T. Nusselt, C. Gebert, W. Winkelmann, A. Battmann, G. Gosheger, *Sarcoma*, **2007**, art. no. 26539.
8. Y. Fan, K. Duan, R. Wang, *Biomaterials* , **2005**, *26,* 1623.
9. S. Cavalu, V. Simon, F. Banica, *Digest Lournal of Nanomaterials and Biostructructures*, **2011***, 6/1,* 89.
10. A. Balamurugan, S. Kannan, V. Selvaraj, S. Rajeswari, *Trends in Biomaterials and Artificial Organs,* **2004**, *18*, 41.
11. G. I. N. Waterhouse, G. A. Bowmaker, J. B. Metson, *Physical Chemistry Physics*, **2001**, *3*, 3838.
12. F. Pallikari, G. Chondrokoukis, M. Rebelakis, Y. Kotsalas, *Materials Research and Innovations*, **2001**, *4,* 89.
13. C.P. Hagan, J.F. Orr, C.A. Mitchell, N.J. Dune, *Journal of Materials Science: Materials in Medicine*, **2009,** *20*, 2427.
14. J. Xu, I. Stangel, I.S. Butler, D.F.R. Gilson, *Journal of Dental Research*, **1997**, *76*, 596.
15. E. Vanea, V. Simon, *Applied Surface Science,* **2011**, *257*, 2346.
16. M. Advincula, X. Fan, L. Lemons, R. Advincula, *Colloid Surface B*, **2005**, *42*, 29.
17. A. Simchi, E. Tamjid, F. Pishbin, A.R. Boccaccini, *Nanomedicine : nanotechnology, biology, and medicine*, **2011,** *7,* 22.
18. Q.L. Feng, J. Wu, G.Q. Chen, F.Z. Cui, T.N. Kim, J.O. Kim, *Journal of Biomedical Materials Research,* **2000,** *52*, 662.

RAMAN IMAGING INVESTIGATION
ON PAA-CLOTRIMAZOLE SYSTEM

CORNEL-VIOREL POP[a], TRAIAN ŞTEFAN[a],
SIMION AŞTILEAN[a], MIHAI TODICA[a]

ABSTRACT. The dispersion of clotrimazole in the polyacrylic acid (PAA) matrix and the possible interaction between the drug and polymeric matrix were investigated by Raman imaging spectroscopy. The optical analysis shows an inhomogeneous distribution of the clotrimazole in the polymeric matrix. An area of 10x10 μm of the sample was scanned and a spectral image map of the most important bands was constructed. The imaging spectral map was constructed observing the intensity of the characteristic band 1045 cm^{-1} of clotrimazole respectively 1450 cm^{-1} of PAA, recorded for each point of the scanned area. The spectrum of the clotrimazole in the PAA matrix is essentially identical to the spectrum of pure clotrimazole. This indicates non interaction between polymeric matrix and clotrimazole.

Keywords: PAA, clotrimazole, Raman spectroscopy

INTRODUCTION

Systemic drug administration through the skin holds several advantages, such as the maintenance of constant drug levels in the blood, decrease of side effects and improvement of bioavailability by circumvention of hepatic first pass metabolism and increased patient compliance [1-4].

Hydrogels are usually macromolecular three dimensional networks of linear hydrophilic polymers capable of absorbing large amounts of water while remaining insoluble due to the presence of chemical or physical crosslinks [5–7]. Their relatively high water content is important in skin moisturization and elasticity, providing a better feel when applied to the skin, making them a good alternative to more conventional dosage forms such as creams, ointments and patches.

Chemical imaging is a methodology that allows automated measurements of samples through the combination of microscopes with vibrational (e.g. near-infrared and Raman) spectrometers to produce a 2D image of the components in a sample [12–16]. The final result of a chemical imaging experiment, be it mapping or true imaging, is a chemical image in which

---

[a] *Universitatea Babeş-Bolyai, Facultatea de Fizică, Str. Kogălniceanu, Nr. 1, RO-400084 Cluj-Napoca,Romania, cornel.pop@phys.ubbcluj.ro*

(ideally) all the components of the analyzed sample are identified based on their chemical composition and their spatial position in the sample [17]. This method allows the identification of chemical micro-structures that are not observed by bulk measurements of the sample. This can be particularly useful in pharmaceutical industry, where seemingly non-informative surfaces of tablets, powders, beads, and various other materials can be analyzed and a better understanding of the observed chemical images of the sample can be achieved [18-29].

Clotrimazole is a broad-spectrum antimycotic agent effective against pathogenic dermatophytes, yeasts and several species of Candida, Trichophyton, Microsporum, Epidermophyton and Malassezia [8]. The objective of the work presented here is to generate chemical images and characterize the pharmaceutical products which contain the clotrimazole integrated in PAA matrix. There are a number of reasons for studying this formulation by imaging approaches: first, it is useful to gain knowledge on whether the applied wet granulation process has been successful, or the granules are pure clotrimazole, and if any chemical interaction between the clotrimazole and the polymeric matrix (PAA) appears. Secondly, various physicochemical characteristics of the granules (such as dissolution) may be affected by their chemical structure (e.g. polymorphic or hydrate/solvate form) which will be determined by chemical imaging. Finally, the sizes of pure clotrimazole granules can be estimated; also this Raman technique can be a good method to verify the stability in time of the active substance integrated in polymeric matrix.

RESULTS AND DISCUSSION

For the beginning, each component of the PAA/Clotrimazole mixture was separately investigated by Raman spectroscopy. Figure 1 presents the two spectra of pure substance, which are included in the composition of the mixture.

The clotrimazole in powder state was introduced in the PAA gel, was stabilized and then was mixed to obtain a homogeneous distribution of active substance in the polymeric matrix. The optical microscopy analysis indicates a colloidal suspension of clotrimazole in the polymer matrix. The spectra obtained from different regions with different optical appearance are different. For example, curve A in figure 1 represents the spectrum of the PAA gel, and curve B represent the clotrimazole spectrum collected from an area with inhomogeneous optical appearance. These spectra were recorded in different regions of the same sample. On the other hand, if comparing the spectrum of the pure clotrimazole in powder state, with the spectrum recorded from the granules included in gel, they are identical. Therefore, the matrix of PAA did not affect the typical vibrational modes of the clotrimazole, figure 2. This result is very important for medical applications, showing that the active substance (clotrimazole) does not undergo any change in its properties when introduced into the polymeric matrix. Similar results were obtained for other concentrations of polymer.
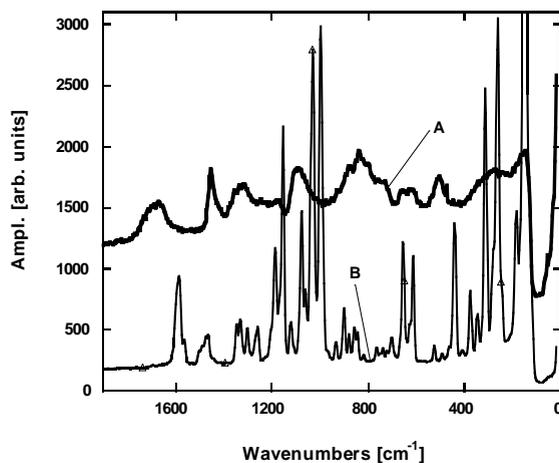
Figure 1. Raman spectra of pure PAA (A) and pure clotrimazole (B)
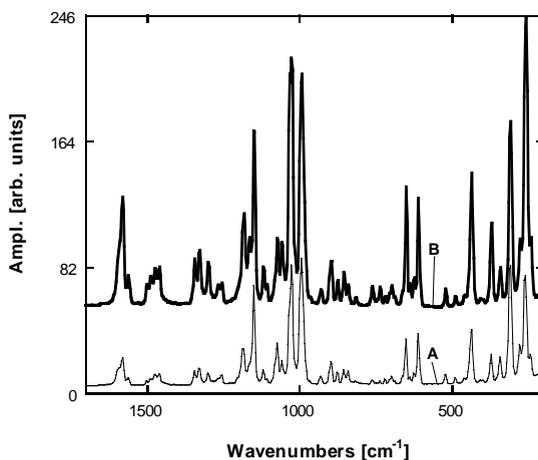
Figure 2. Raman spectra of pure Clotrimazol (B) and Clotrimazol granules embedded in PAA gel matrix (A).

Figure 3 shows the Raman spectrum of the stabilized gel with TEA at 1%concentration, the Raman spectrum of the same gel at the same concentration, after drying, and the Raman spectrum of the powder state of PAA. These show that the polymeric matrix hydration of the PAA is a reversible process, as water did not bring significant changes in the polymeric gel after drying. The bands in the Raman spectrum of powder state PAA are found exactly at the same positions as in the Raman spectrum for dry gel of PAA. The only significant change is the band at 846 cm^{-1}, band assigned by Bardet et *al*, as stretching vibration of carboxyl group of neighboring C-C bond [30].

37
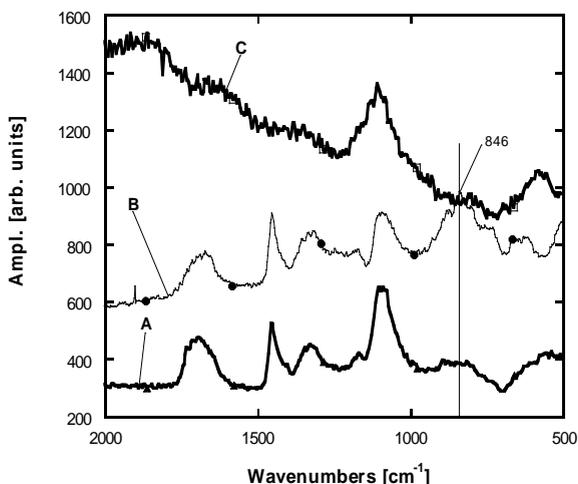
Figure 3. Raman spectra recorded on samples before and after drying PAA gels. After the first drying gel (A), pure PAA (B) and Raman spectrum recorded from same PAA gel stabilized with TEA (C)

This band does not disappear, but the Raman intensity of signal due the drying effect is greatly reduced because the carboxyl group was stabilized with TEA. The medium intensity band assigned to stretching vibration of C = O bond by Bardet et *al*, moves from 1683 cm^{-1} to 1688 cm^{-1} without change of intensity. This shift is due to the same effect, neutralizing the carboxyl group, which includes this C = O bond [22]. The spectrum of the stabilized gel with TEA of PAA has a Raman band intense presented only at 1105 cm^{-1}, assigned to the stretching vibration of C-CH_2 bond. This indicates that the level of dissolution did not influence the stability of the chain C - C bonds of acrylic acid monomer, figure 3. [30]. Following hydration and drying repeated processes, the PAA matrix remains stable, the hydration of these gels proved to be a reversible process.

Further investigations were carried out on dry PAA gels using AFM, analyzing the effects of the hydration-drying repeated process. The image AFM analysis shows that increasing of the polymer concentration, the roughness of the surface of PAA gel also increases. This takes the form of homogeneity in the gel polymer when the polymer concentration is higher. However, the increasing polymer concentration leads to increase of the sizes inhomogeneous zone. At 0.5% of PAA gel, in figure 4. b) more numerous homogeneous areas appear, while for the concentration of 1% an increase in surface roughness is observed, caused by the merger of inhomogeneous areas, figure 4 b).

Following the hydration and drying at 1% the roughness is increased due the emergence of distinct areas on a much smaller surface than the previous situation, figure 5. After the first and second drying such heterogeneous areas are not observed on the surface, but after the third cycle of hydration and drying, the surface has a pronounced roughness in the dry gel. A possible explanation

for this could be the presence of a specific division of conglomeration PAA gel, after several repeated processes of hydration and drying.

a   b
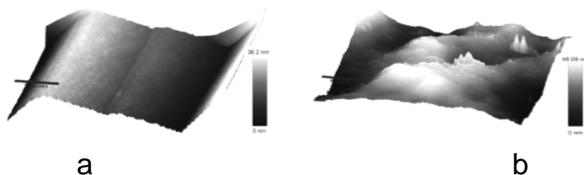
Figure 4. AFM images of 0.5% (a) and 1% (b) PAA gel after the first drying

a   b
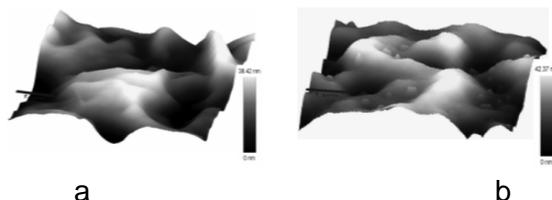
Figure 5. AFM of the 0.5% PAA gel after the second (a) and third (b) drying

Global Raman imaging

A (white) light microscopy composite image of a typical sample prior to mapping or imaging analysis is shown in Figure 7. This situation is repeated in a number of samples that were imaged, leading to conclusion that the large granules can very easily be prepared while the smaller granules of the analyzed formulation tend to stay closely agglomerated.

The method of investigation by Raman spectroscopy of clotrimazole granules can be optimized to identify the exact area they occupy in the polymeric matrix. This method involves scanning a predetermined area of the dry gel and step by step, recording the spectrum of this area. With the help of a map performed with the Witec 3.0 software the exact area that contains clotrimazole is obtained. A combination of Raman band at 1454 cm^{-1}, specific dry to PAA gel, and the band 1045 cm^{-1} specific to clotrimazole gel is presented in figure 7. These typical bands of the two phases were extracted from Raman spectra, figure 6. The bands employed for the Raman map of figure 7 are marked by gray arrows in figure 6. Zone B is the area denoted by the Raman spectra of clotrimazole and zone A is the map denoted by the Raman spectrum of specific dry PAA gel. Because there are no other distinct areas of interface between clotrimazole and the gel polymer, one can say that the two distinct components of this system do not interact chemically between each other.

CONCLUSIONS

The results presented here illustrate that chemical imaging is very useful for determining the chemical nature of the pharmaceutical granules. Raman applied mapping and imaging techniques clearly recognize the granules

consisting only of the major excipient (PAA) or the clotrimazole. The majority of the granules are found to be mixtures of clotrimazole and PAA gel. In addition,
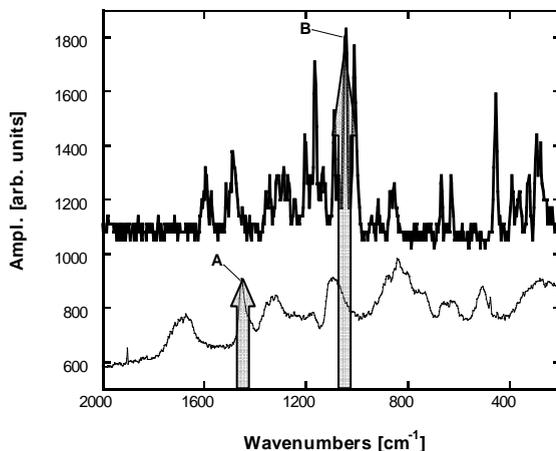
Figure 6. Raman spectra collected from two specific spots on the sample.
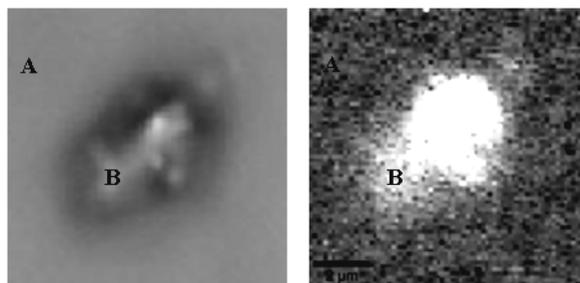
Figure 7. Optical image of the sample (left) and combined Raman map obtained by reconstructing the spatial distribution of the 1450 cm^{-1} (PAA - zone A) and 1045 cm^{-1} (Clotrimazole - zone B) bands.

it should be mentioned that smaller granules or particles (less than 10 µm) are also clearly visualized and can be chemically imaged. However, the information content is much higher in chemical mapping and imaging measurements. This makes them indispensable in preliminary experiments for determining the nature of the granules. An important observation concerns the stability of the topical mixture, insofar as clotrimazole immersed in the polymeric matrix does not have any chemical interaction.

EXPERIMENTAL SECTION

Materials: polyacrillic acid (PAA 940, B.F. Goodrich) and clotrimazole (Beijing Double Crane, Pharmaceutical Co. LTD, China).

Methods: Preparation of mucoadhesive gels was made by mixing the aqueous dispersion of the clotrimazole. The dispersions of PAA were neutralized with triethanolamine and the concentration of PAA was 1,5% in gel. Clotrimazole was incorporated by suspending it in a ratio of 1% in the gel.

Raman analyses: The dried granules were analyzed as obtained. No sample preparation of any sort was applied. Relatively large granules (dimensions of least 5-10 μm) were obtained. The samples also contained small granules which were not the focus of this study. For this reason no sampling methodology was developed to separate these particles. The complex product was deposed on thin films on microscope glass plates for the measurements [31]. The samples were investigated by Raman spectroscopy using a confocal Raman microscope (Witec CRM 200), at room temperature. Raman spectra were excited with 100mW of 633 nm light produced by a He-Ne laser and were recorded in backscattering geometry. No sample damage was detected in the experiments.

The AFM images were recorded with an Alpha 300 AFM module attached to the same Witec CRM 200 system. AFM scanning was performed by "tapping" mode, on an area of 5x5 μm. An average area of 10 μm × 10 μm was typically imaged. Since the granules were randomly distributed onto the microscope slide, the total imaging area was chosen to cover only one granule in a reasonable experimental time, typically less than 10 minutes. The imaged area was therefore slightly different from one experiment to another. All the Raman images were preceded by the acquisition of white light images of the sample across the area selected for imaging. Fortunately, the regions of strong and non-overlapping Raman bands for PAA and clotrimazole were found to be next to each other in the 400–1600 cm^{-1} region. This spectral region was employed for all the Raman measurements.

ACKNOWLEDGMENTS

REFERENCES

1. M. Brown, G.Martin, S. Jones, F. Akomeah, *Drug Delivery,* **2006**, *13,* 175.
2. N.A. Peppas, P. Bures,W. Leobandung,H. Ichikawa, *The European Journal of Pharmaceutics and Biopharmaceutics*, **2000**, *50,* 27.
3. E. Dinte, M. Todica, C. V. Pop, S. E. Leucuta; *Studia Universitatis Babes-Bolyai "Babes-Bolyai", Physica*, LIII, 1, **2008**, 55-64.
4. Siegfried Wartewig, Reinhard H.H. Neubert, *Advanced Drug Delivery Reviews*, **2005**, *57,* 1144–1170.

5. J. Berger, M. Reist, J.M. Mayer, O. Felt, R. Gurny, *The European Journal of Pharmaceutics and Biopharmaceutics,* **2004**, *57,* 35.
6. J. Berger, M. Reist, J.M. Mayer, O. Felt, N.A. Peppas, R. Gurny, *The European Journal of Pharmaceutics and Biopharmaceutics,* **2004***, 57,* 19.
7. Claudia L. Silvaa, Jorge C. Pereirab, Amılcar Ramalhoc, Alberto A.C.C. Pais, Joao J.S. Sousa, *Journal of Membrane Science*, **2008**, *320,* 268–279
8. E. Ghelardi, A. Tavati, A. Lupetti, F. Celandroni, E. Boldrini, M. Campa and S. Senesi, *Antimicrobial Agents and Chemotherapy*, **1998**, *42,* 2434–2436.
9. A. Valentin, C. Bernard, M. Mallic, M. Huerre and J. M. Bastide, *Mycoses*, **1993**, *36,* 379–384.
10. J. Van Cutsem, *American Journal of Obstetrics and Gynecology*, **1991**, *165,* 1200–1206.
11. Garima Sharma, S. Jain, A. K. Tiwary, Gurpreet Kaur, *Acta Pharmaceutica*, **2006**, *56,* 337–345
12. V. Canpean, M. Iosin and S. Astilean**,** *Chemical Physics Letters*, **2010**, *500(4-6)*, 277-282
13. Monica Potara, Endre Jakab, Annette Damert, Octavian Popescu, Valentin Canpean and Simion Astilean, *Nanotechnology*, **2011**, 22, 135101.
14. R.L. McCreery, "Raman Spectroscopy for Chemical Analysis", Wiley, New York, **2000**.
15. P.J. Treado, M. Nelson, in: J.M. Chalmers, "Handbook of Vibrational Spectroscopy", P.R. Griffiths (Eds.), vol. 2, Wiley, New York, **2001**.
16. D.E. Pivonka, J.M. Chalmers, "Applications of Vibrational Spectroscopy in Pharmaceutical Research and Development", P.R. Griffiths (Eds.), Wiley, Chichester, **2007**.
17. S. Sasic, *Analytica Chimica Acta*, **2008**, *611,* 73–79
18. S. Sasic, D.A. Clark, *Applied Spectroscopy*, **2006**, *60,* 494.
19. S. Sasic, D.A. Clark, J.C. Mitchell, M.J. Snowden, *Applied Spectroscopy*, **2005**, *59,* 630.
20. S. Sasic, *Pharmaceutical Research*, **2007**, *24,* 58.
21. S. Sasic, *Applied Spectroscopy*, 61, **2007**, 2237.
22. L. Zhang, M.J. Henson, S.S. Sekulic, *Analytica Chimica Acta*, **2005**, *545,* 262.
23. M. Henson, L. Zhang, *Applied Spectroscopy*, **2006,** *60*, 1247.
24. P.D.A. Pudney, T.M. Hancewicz, D.G. Cunningham, M.C. Brown, *Vibrational Spectroscopy*, **2004**, *34,*123.
25. A. de Juan, R. Tauler, R. Dyson, C. Marcolli, M. Rault, M. Maeder, TrAC, *Trends in Analytical Chemistry*, **2004**, *23,* 70.
26. J. Breitenbach, W. Schroff, J. Neumann*, Pharmaceutical Research*, **1999**, *16,* 1109.
27. W.H. Doub, W.P. Adams, J.A. Spencer, L.F. Buhse, M.P. Nelson, P.J. Treado*, Pharmaceutical Research*, **2007**, *24,* 934.
28. S. Ward, M. Perkins, J. Zhang, C.J. Roberts, C.E. Madden, S.Y. Luk, N. Patel, S.J. Ebbens, *Pharmaceutical Research*, **2005**, *22,* 1195.
29. F.C. Clarke, M.J. Jamieson, D.A. Clark, S.V. Hammond, R.D. Jee, A.C. Moffat, *Analytical Chemistry*, **2001**, *73,* 2213.
30. L. Bardet, G. Cassanas-Fabre, M. Alain, *Journal of Molecular Structure*, **1975**, *24,* 153-164.
31. D. Marconi, I. Matei, S. Manolache, C. Lung, A. V. Pop, *Journal of Optoelectronics and Advanced Materials*, **2008**, *10(4),* 926 - 928

SPECTROSCOPIC INVESTIGATION OF ANTI-BACTERIAL AGENTS ACTIVITY

VITALY ERUKHIMOVITCH[a], IGOR MUKMANOV[a], MAHMOUD HULEIHEL[b]

ABSTRACT. FTIR spectroscopy has been widely used in recent time as a efficient tool to biomedical investigations. In this study we examined the potential of FTIR microspectroscopy as analytical instrument for early evaluation of anti-bacterial therapy efficiency. For this purpose, the effect of propolis (PE) on the development of bacterial infection in cell culture was examined. PE is a natural honeybee product with a potent anti-bacterial activity. Our results show early (2h post treatment) unique and significant spectral indicators for successful treatment with PE. Some of these biomarkers demonstrate different trends in gram (-) compared to gram (+) bacteria. It seems that FTIR spectroscopy can be used as an effective analytical tool for an early evaluation of the efficiency of the anti-bacterial effect of PE and probably other used drugs.

Keywords: FTIR microscopy; Bacteria; Propolis

INTRODUCTION

Bacteria are considered as one of the major causes of human and animal serious and dangerous infections. Although antibiotics are known as the most effective antibacterial drugs, bacteria can develop resistant mutants to the used antibiotics and, in fact, several bacterial mutants are known today to be resistant to all available antibiotics. Therefore, both the search for new anti-bacterial drugs and early evaluation techniques for the used drug efficiency are highly essential and guarantee for future effective treatment [1,2]. Most commercially available identification systems based on physiological (morphology, growth temperature, etc.) and nutritional (media composition, sugar assimilation, enzymatic tests, etc.) characteristics [3] are time consuming and not always very specific.

The detection and identification of microorganisms by spectroscopic techniques promises to be of a great value because of their sensitivity, rapidity, low expenses and simplicity. This together with the large information already known about spectral peaks obtained from FTIR spectra of living

---

[a] *Analytical Equipment Unit, Ben-Gurion University of the Negev, Beer-Sheva, 84105, Israel*
[b] *Department of Virology and Developmental Genetics, Faculty of Health Sciences,Ben-Gurion University, Beer-Sheva, 84105, Israel*

cells, make FTIR spectroscopy as an attractive technique for detection and identification of pathogens. FTIR spectroscopy was used successfully for identification of different kinds microorganisms [1, 4, 5], cancer cells, cells infected with viruses [6 - 10]. It was also used lately for the evaluation of antiviral drugs efficiency [11].

Propolis (PE), a natural product produced by honeybee and based on resins collected by bees from certain trees and plants, has been used for thousands of years in folk medicine for several purposes. The most important group of compounds of PE(in terms of amount and biochemical activity) are the flavonoids, which are thought to play a significant role in its bioactivities [12-14]. Between its various bioactivities, this product showed impressive antimicrobial activity mainly against gram positive bacteria [15, 16].

In the present study we examined the potential of FTIR microscopy as rapid and efficient analytical method for early evaluation of PE anti-bacterial activity against gram positive [gram (+)] and gram negative [gram (-)] bacteria.

RESULTS AND DISCUSSION
Effect of PE on gram (+) and gram (-) bacteria growth.

Different gram (-) and gram (+) bacteria were grown in the presence and absence of various concentrations of *PE* in L. Broth (LB) medium at 37C for 24h. The obtained results show that *PE* at a concentration of 0.2% completely inhibited the growth of the examined gram (+) bacteria whereas it hadn't any inhibitory effect on all examined gram(-) bacteria. At higher concentrations it had only partial inhibitory effect on the gram (-) bacteria (Table 1). It can be seen also from Figure 1 that *PE* was able to inhibit completely the growth of gram (+) bacteria as early as 2h post-treatment.

Table 1. Effect of *PE* treatment on the growth of various gram (-) and (+) bacteria. Equal amounts (10^3 bacteria/ml) of gram (-) and (+) bacteria were grown in 2ml LB medium in the presence or absence of different concentrations of *PE* at 37°C for 24h. At the end of the incubation period, the amounts of bacteria were evaluated. Results are means ± SD (n=5); the SD for these means was negligible.

Bacterial strain	*PE* Concentration (%)					
	0		0.2		5	
	Bacteria Amount		Bacteria Amount		Bacteria Amount	
	(OD)	(No/	(OD)	(No\ml)	(OD)	(No/ml)
P. aeruginosa	1.31	5.8×10^7	0.95	4×10^7	0.74	6×10^6
S. enteridis	1.45	6.8×10^8	1.17	8×10^7	0.73	1×10^7
Micrococcus	1.01	6.2×10^7	0.20	1.3×10^2	0.01	0
B. subtilis	1.15	2.5×10^8	0.09	1.7×10^2	0.013	8
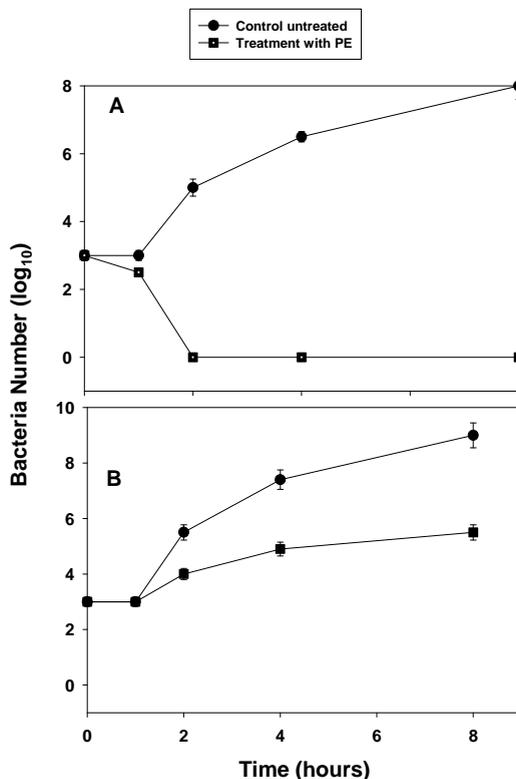
Figure 1. Effect of *PE* on the growth of Micrococcus [gram(+)](A) and P. aeruginosa [gram (-)] (B) bacteria. Micrococcus and P. aeruginosa bacteria were grown in LB medium containing 0.2% or 1% PE respectively and at various times post treatment. The number of living bacteria was evaluated by bacterial colonies counting as detailed in the "Experimental" section.

FTIR microscopy examination of gram (+) and gram (-) bacteria treated with PE

Similar aliquots (10^5 cells/ml) of the examined gram (+) or gram (-) bacterial strains were grown in LB medium in the presence or absence of 0.5 or 5% of *PE* respectively and examined by FTIR microscopy at 2h post-treatment. The obtained FTIR spectra of control untreated and *PE* treated Pseudomonas aeruginosa bacteria (as representative of gram (-) bacteria) and Micrococcus bacteria (as representative of gram (+) bacteria) share several bands as follow (Figure 2A, Figure 3A): the dominant bands at 1655 cm^{-1} and 1546 cm were attributed to protein amide I and II bands [17]. The shoulder at about^{-1} 1730 cm^{-1} was attributed to lipid C=O stretching vibrations [17]. The band at 1465 cm^{-1} was assigned to the CH$_2$ bending mode of the cell lipids. The bands at 1454 cm^{-1} and 1397 cm^{-1} were attributed to asymmetric and symmetric CH$_3$ bending modes of end ethyl groups and

branched methyl groups of proteins and lipids, respectively [18]. The peaks at 1237 cm^{-1} and 1082 cm^{-1} were attributed to asymmetric and symmetric stretching vibrations and phospholipids [19]. The peak at 1064 cm^{-1} resulted from the overlap of several bands, including absorption due to the vibrational modes of –CH$_2$OH and the C–O stretching vibration coupled to the C-O bending mode of cell carbohydrates [20].The peak at 857 cm^{-1} was attributed to N-type sugars[20].
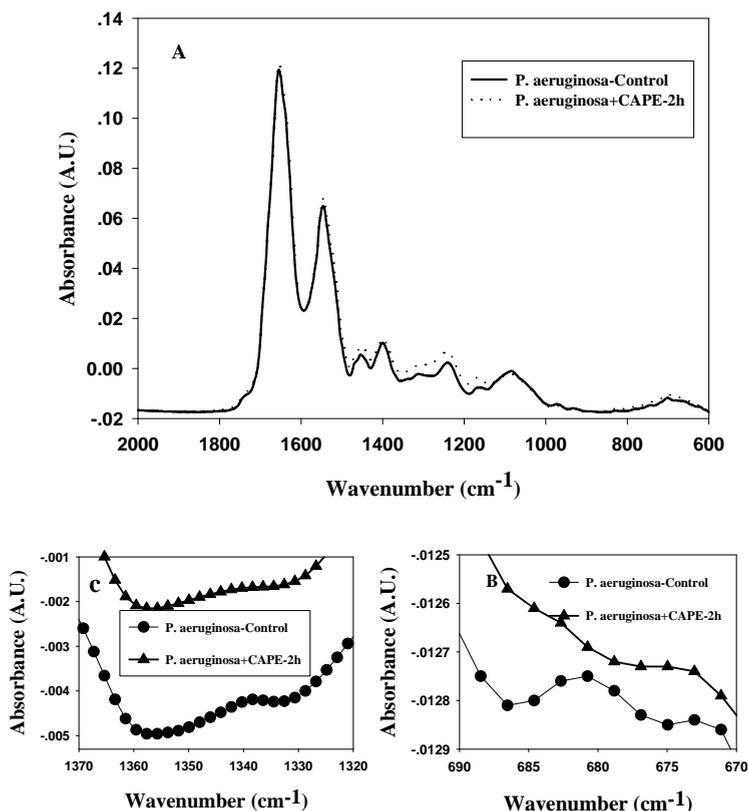
Figure 2. FTIR spectra of *P. aeruginosa* after 2h growth in medium with or without 5% *PE* at the regions (A) 600-2000 cm^{-1} (B) 674-686 cm^{-1} (C) 1330-1350 cm^{-1}.

The main consistent differences between the spectra of the control and the PE treated bacteria are at two specific spectral peaks:

1. Peak at 682 cm^{-1}: This peak represents NH bending of proteins [18]. A major decrease (about 25 folds) in the spectral absorption at this region was obtained at 2h post-treatment with *PE* in all examined gram (-) bacterial strains (Figure 2B). On the contrary, there was a considerable increase (about

8 folds) in all examined gram (+) bacterial strains in the spectral absorption at this region after treatment with *PE* (Figure 3B).

2. Peak at 1339 cm^{-1}: This peak which is assigned to adenosine (DNA) [21] highly (about 15 folds) decreases in gram (+) and almost don't change in gram (-) bacteria (Figs 2C, 3C).

Similar results were obtained with the other examined gram (+) and gram (-) bacteria (data not shown). The spectral discrepancies between normal and treated bacteria with *PE* at the various above peak areas of both gram (+) and gram (-) bacteria were statistically significant as assessed by t-Test (P< 0.001) and enough for identification of treated bacteria at very early stages of treatment.
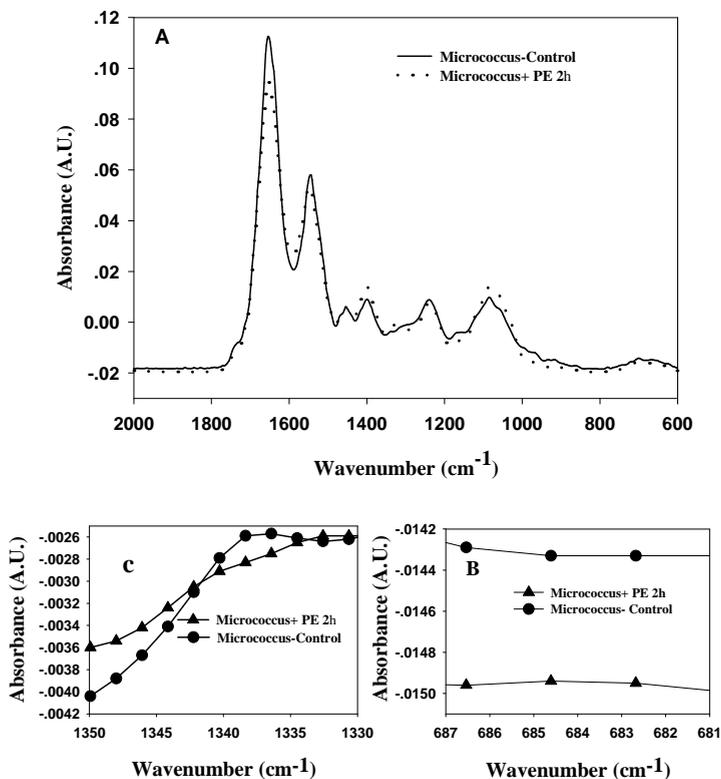
Figure 3. FTIR spectra of *Micrococcus* after 2h growth in medium with or without 5% PE at the regions (A) 600-2000 cm^{-1} (B) 680-686 cm^{-1} (C) 1330-1350 cm^{-1}.

As can be seen from these results, the behavior of the spectral peaks is clearly different in gram (+) compared to gram (-) bacteria as a result of treatment with *PE*. This difference seems to be a direct consequence of the different biological effect of *PE* on these bacteria. As our results (Table 1)

showed, *PE* significantly inhibits the growth of gram (+) bacteria at low doses (0.2%), whereas it has only a slight inhibitory effect on the growth of gram (-) bacteria even at high concentrations (5%). The mechanism of the anti-bacterial activity of *PE* is still unclear.

The obtained spectral changes of the treated bacteria with *PE* are an evidence of chemical composition variations of these cells. These changes could be a result of changes in the metabolic activity of these bacteria. The increase in protein level observed in treated gram (+) bacteria may be resulted by over expression of some of the bacterial genes as a consequence of treatment with *PE*. The major reduction in the peak area at 1339cm^{-1}, which seems to be assigned to nucleic acids, in gram (+) bacteria may be due to the termination of the bacterial DNA synthesis and/ or its degradation induced by the treatment with *PE*.

CONCLUSIONS

The results presented in this study proved the potential of FTIR microscopy for rapid and reliable determination of anti-bacterial efficiency of *PE*. It can be seen that different spectral peaks over the FTIR spectra of the examined samples may be used as excellent indicative biomarkers for the efficiency of the used drugs at very early stages of the treatment. It seems that these above biomarkers can be used successfully for follow up after efficacy of *PE* and might be useful for evaluation and determination of its required doses.

The present study together with our and others previous studies strongly support the possibility of developing the FTIR microscopy a**s a** rapid and efficient analytical tool for early evaluation of the efficiency of drug treatment.

EXPERIMENTAL SECTION

Bacteria

In the present study we used the following gram (-) and gram (+) bacteria:

gram *(-) bacteria are* Pseudomonas aeruginosa and Salmonella entenidis,

gram *(+) bacteria are* Micrococcus and Bacillus subtitis. All used bacteria were grown on Nutrient Agar (Difco) at 37 °C.

Propolis (PE)

An aqueous extract of propolis (20% of row propolis) was diluted with RPMI culture medium to give the required concentrations (0.1, 1, 5, 10 or 20%). The pH of the diluted extract was adjusted to 7.1-7.2 with sodium borate. As a control, we used phosphate buffered saline (PBS) (pH 7.2) containing the same amount of sodium borate, which was necessary to adjust the pH of propolis extract.

Amount of bacteria measurement

The amounts of bacteria were evaluated both by 2 methods:
(a) Examining their optical density (OD) by spectrophotometer () at wave length 620nm. This method gives an evaluation of the live and dead bacteria.
(b) Bacterial colonies counting. By plating raising dilutions of each bacteria on LB agar plates for 24h at 37°C and counting the number of the obtained colonies. This method gives the number of only live bacteria.

Sample preparation.

Since ordinary glass slides exhibit strong absorption in the wavelength range of interest to us, we used zinc-sellenide crystals, which are highly transparent to IR radiation. The amount of the examined bacteria was determined by measuring it's optical density with a spectrophotometer. Similar amounts of the examined bacteria were pelleted from a medium containing bacteria by centrifugation at 1000 rpm for 2 min. Each pellet was washed twice with H_2O and resuspended with 20μl of H_2O and a drop of 1μl of the obtained suspension was placed on a certain area on the zinc-sellenide crystal, air dried for 15min at room temperature (or for 5 min by air drying in a laminar flow) and examined by FTIR microscopy.

FTIR spectra measurement.

FTIR measurements were performed in the transmission mode with a liquid-nitrogen-cooled MCT detector of the FTIR microscope (Bruker IRScope II) coupled to an FTIR spectrometer (BRUKER EQUINOX model 55/S, OPUS software). The spectra were obtained in the mid-IR number range of 600-4000 cm^{-1}. Spectral resolution was set at 4 cm^{-1}. Baseline correction by the rubber band method and vector normalization were obtained for all the spectra by OPUS software. Peak positions were determined by means of a second derivation method by OPUS software. Since the samples to be analyzed were often heterogeneous, appropriate regions were chosen by FTIR microscopy so as to eliminate different impurities (salts, medium residuals, etc.). The aperture used in this study was 100μm, since this aperture gave the best signal/noise ratio. For each sample, the spectrum was taken as the average of five different measurements at various sites of the sample. Each experiment with each sample was repeated five times. It is important to mention that there were no significant differences in the spectra from various sites (SD did not exceed 0.005).

REFERENCES

1. K. Maquelin, C. Kirschner, L.P. Choo-Smith, et al., *Journal of Clinical Microbiology*, **2003**, *41*, 324.
2. M. Essendoubi, D. Toubas, M. Bouzaggou, J.M. Pinon M. Manfait, *Biochim*ica *Biophysica Acta,* **2005**, *1724*, 239.
3. J.M. Miller and C.M. O'Hara, *in Manual of Clinical Microbiology*, ed. P.R.Murray, E.J. Baron, M.A. Pfaller, F.C. Tenover, R.H. Yolken, ASM press, Washington, DC, **1999**, 193.
4. D. Naumann, D. Helm, H. Labischinski, *Nature*, **1991**, *351*, 81.
5. V. Erukhimovitch, V. Pavlov, M. Talyshinsky, Y. Souprun and M. Huleihel, *Journal of Pharmaceutical and Biomedical Analysis*, **2005**, *37*, 1105.
6. H.P. Wang, H.C. Wang, Y.J. Huang, *Science of the Total Environment*, **1997**, *204*, 283.
7. T. Gao, J. Feng, Y. Ci, *Analytical Cellular Pathology*, **1999**, *18*, 87.
8. B. Rigas, K. LaGuardia, L. Qiao, B.S. Bhandare, T. Caputo, M.A. Cohenford, *Journal of Laboratory and Clinical Medicine*, **2000**, *35*, 26.
9. V. Erukhimovitch, M. Talyshinsky, Y. Souprun, M. Huleihel, *Photochemistry and Photobiology*, **2002**, *76*, 446.
10. M. Huleihel, M. Talyshinsky, Y. Souprun, V. Erukhimovitch, *Applied Specoscopy.*, **2003**, *57*, 390.
11. V. Erukhimovitch, M. Talyshinsky, Y. Souprun, M. Huleihel, *Journal of Biomedical Optics*, **2006**, *11, 064009-1-6.*
12. A. Russo, N. Troncoso, F. Sanchez, J.A. Garbarino, A. Vanella, *Life Sciences,* **2006**, *78*, 1401.
13. Y.S. Song, C. Jin, K.J. Jung, E.H. Park, *Journal of Ethnopharmacology*, **2002**, *82*, 89.
14. A. Russo, R. Longo, A. Vanella, *Fitoterapia,* **2002**, *73*, S21.
15. Y. Onlen, C. Tamer, H. Oksuz, N. Duran, A.E. Altug, S. Yakan, *Microbiological Research*, **2007**, *162*, 62.
16. L.P. Broudiscou, H. Geissler, A. Broudiscou, *Anaerobe,* **1998**, *4*, 145.
17. R.K. Dukor, in *Handbook of Vibrational spectroscopy*, ed. J.M. Chalmers and P.R. Griffiths, John Wiley and Sons, New York, **2001**, 3335-3361.
18. D. Yang, D. Castro, I. El-Sayed, M. El-Sayed, R. Saxton, N.Y. Zhang, *Journal of Clinical Laser Medicine and Surgery,* **1995**, *13*, 55.
19. R.R. Dukor, M.N. Liebman, B.L. Johnson, *Cellular and Molecular Biology*, **1998**, *44*, 211.
20. K. Brandenburg, U. Seydel, in *Handbook of Vibrational Spectroscopy*, ed. J.M. Chalmers and P.R. Griffiths, John Wiley and Sons, New York, **2001**, 3481.
21. A.E. Taillandier, J. Liguier, in *Handbook of Vibrational Spectroscopy*, J.M. Chalmers and P.R. Griffiths, Eds., John Wiley and Sons, New York, **2001**, 3465.

PHOTOCATALYTIC ACTIVITY OF HIGHLY POROUS TiO$_2$-AG MATERIALS

DUMITRU GEORGESCU[a, b], ZSOLT PAP[c], MONICA BAIA[a], CARMEN I. FORT[c], VIRGINIA DANCIU[c], GEORGIAN MELINTE[a], LUCIAN BAIA[a], SIMION SIMON[a, b]

ABSTRACT. In the present work our interest is focused on evaluating the photocatalytic performances of TiO$_2$ aerogels containing silver and correlating these data with the structural and morphological particularities. The highly porous TiO$_2$ aerogels were obtained by TiO$_2$ gels' impregnation with various concentrations of AgNO$_3$ solutions, followed by supercritical drying. In order to determine the morpho-structural parameters several complementary techniques such as nitrogen sorption, transmission electron microscopy in high resolution mode (HRTEM) and diffuse reflectance UV-vis spectroscopy (DRS) were employed. The photocatalytic activity of the porous samples was also tested and correlated with the morpho-structural characteristics. The presence of silver led to the increase of the crystallization degree of TiO$_2$, with anatase and brookite phases being especially identified.

Keywords: *TiO$_2$ aerogel, silver, photocatalytic activity, morphology, structure*

INTRODUCTION

TiO$_2$ is a semiconductor with a band gap that permits UV light absorption and possesses a high oxidation power. In the last years it was widely employed in many photocatalytic processes. Destruction of chemical pollutants from water by this process is a rather complex issue because the improvement of the photocatalytic activity strongly depends on several factors such as: specific surface area, the type and concentration of dopant, crystalline structure, particle size, time of recombination of the electron-hole photogenerated pairs, etc. Titania based aerogels are nanoscopic pore-solid architectures with high surface area and a continuous mesoporous network formed from interconnected nano-quasicrystallite building blocks [1-3]. Their high surface area, non-toxic nature, stability and high homogeneity make them extremely attractive for applications [4-6].

[a] *Babes-Bolyai University, Faculty of Physics, M. Kogalniceanu 1, 400084 Cluj-Napoca, Romania,* dgeo.cnmv@gmail.com
[b] Interdisciplinary Research Institute on Bio-Nano-Sciences, Babes-Bolyai University, 400271 Cluj-Napoca, Romania
[c] *Babes-Bolyai University, Faculty of Chemistry and Chemical Engineering, A. Janos 11, 400028 Cluj-Napoca, Romania*

However, an important drawback of TiO_2 is that it absorbs only UV light, which represents less than 8% of the solar spectrum. Any shift in its optical response from the UV to visible spectral range could lead to a further increase of the photocatalytic performance. Therefore, obtaining novel porous TiO_2 based materials and understanding the morphological and structural particularities with the purpose of improving their photocatalytic activity still remain imperative challenges. In this respect, it has been reported that the addition of transition metals to TiO_2 can increase photocatalytic activity by decreasing the energy band gap or preventing electron – hole pair recombination [7, 8].

Having in mind the above mentioned aspects, in the present work, the interest was focused on evaluating the photocatalytic performances of silver doped porous TiO_2 materials and finding correlations between the morpho-structural parameters and apparent photodegradation rates. Besides the photocatalytic activity assessment, several complementary techniques like nitrogen sorption, transmission electron microscopy in high resolution mode (HRTEM) and diffuse reflectance UV-vis spectroscopy (DRS) were used in order to examine the influence of the silver amount on the TiO_2 porous structures from the perspective of improving the photocatalytic performances.

RESULTS AND DISCUSSION

Since a central point in the catalysts' investigations is their crystalline structure, XRD measurements were firstly performed and the obtained diffractograms are presented in Figure 1. The diffraction patterns of all investigated aerogels show weak and broad diffraction peaks. Identification of the titania crystal phase and confirmation of the silver presence cannot be done from these peaks due to the low signal/noise ratio. However, the location of the weak signals seems to indicate the existence of anatase and brookite crystallization centers that were later confirmed by HRTEM. The presence of these peaks suggests that the crystallization process has begun. The calculation of the particle size is nearly impossible by the *Scherrer* equation [9]. Due to the above mentioned facts, no obvious correlation between the crystallization degree and the silver concentration was found. In order to precisely identify these crystalline islands and to verify the presence of silver nanoparticles, TEM/HRTEM investigations were necessary.

Indeed, as Figure 2 shows, a few nanometer sized, crystallized titania zones (anatase (101), (004) and brookite (111), (120) crystal planes) were observed near the silver nanoparticles, meaning that the presence of silver favors the crystallization process. These crystallized zones in the aerogels could be responsible for the observed diffraction peaks (Figure 1). Obviously, the amorphous titania phase is dominating the samples.
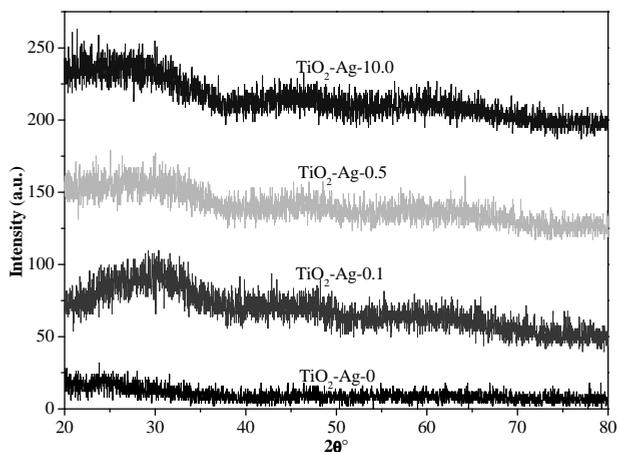
Figure 1. XRD patterns of TiO$_2$-Ag photocatalysts
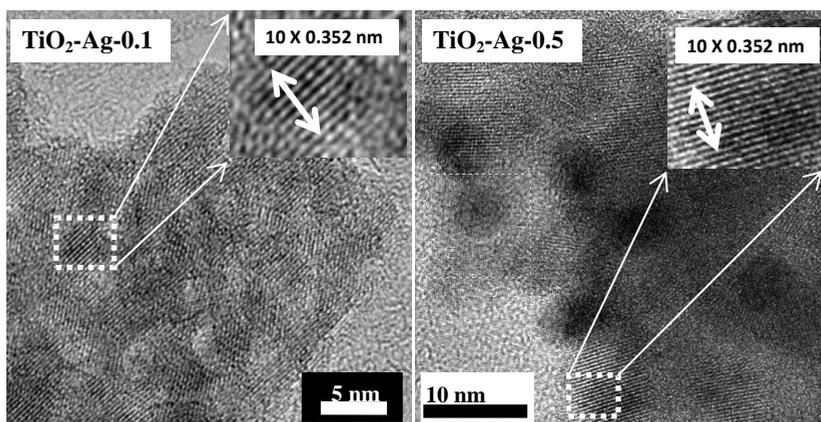
Figure 2. HRTEM micrographs of samples TiO$_2$-Ag-0.1 and TiO$_2$-Ag-0.5

The aerogels are highly porous materials and posses a high specific surface area [3, 5, 10], as Table 1 shows. Surprisingly, the area decreases as the added silver concentration grows. In the case of the blank sample, TiO$_2$-Ag-0, the measured surface area was 621 m^2/g and it decreased to 471 m^2/g for the sample TiO$_2$-Ag-10.0 (Table 1). This surface contraction phenomena could be due to the silver presence. We assume that, as more silver nanoparticles appear so the number of crystalline "islands" is higher and in these zones the highly porous structure collapses resulting a lower specific surface area.

Table 1. Structural parameters and photocatalytic performance (reaction rate and efficiency) of the investigated samples

Sample name	Crystal phase detected by HRTEM	Surface area S_{BET} (m²/g)	Calculated band-gap Eg (eV)	Degradation rate r (10^{-3} µM·s⁻¹)	Degradation efficiency (%degraded)
TiO$_2$-Ag-0	amorphous	621	3.19	28	42
TiO$_2$-Ag-0.1	anatase and/or brookite	491	3.27	37	52
TiO$_2$-Ag-0.5		489	3.24	102	56
TiO$_2$-Ag-10.0		471	3.17	158	74

To reinforce the fact that silver nanoparticles are omnipresent in the entire sample (and by this, indirectly, that TiO$_2$ crystallites are present in the whole material) and to demonstrate that these materials can harvest and utilize the visible light irradiation, the DRS spectra were recorded.
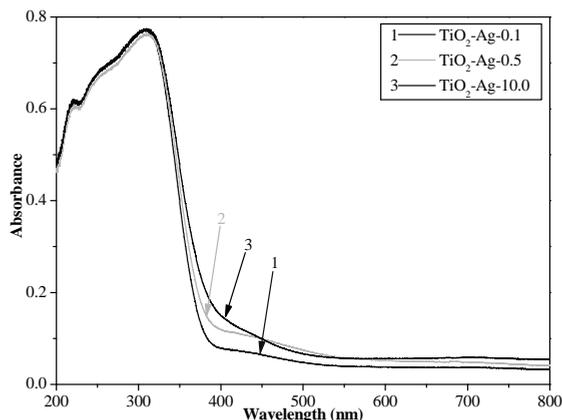
Figure 3. The DRS spectra of selected silver containing titania aerogels

All the investigated TiO$_2$-Ag samples exhibit a band centered at ~440nm (Figure 3), which is absent in the blank sample. These absorption signals can be associated with the existence of metallic silver nanoparticles, which give rise to a specific plasmon absorption band, usually centered between 395 and 445 nm [11] meaning that the silver nanoparticle deposition was successful. The band-gap energy values (Eg) were also estimated by using the Kubelka-Munk transformation and are presented in Table 1. It was found that the silver nanoparticles didn't have any influence at all on the Eg values.

The observed degradation curves for salicylic acid are shown in Figure 4. The least active photocatalyst was proved to be the reference sample, i.e. the blank sample TiO$_2$-Ag-0, with r = 28·10^{-3} µM·s^{-1} degradation rate. As the silver content increases, the measured rates are rising accordingly (Figure 5). Thus, in the case of the sample TiO$_2$-Ag-10.0 a 74% degradation efficacy can be obtained associated with r = 158·10^{-3} µM·s^{-1} degradation rate. These last activity/efficacy values mean that in our case even 564% (5.64 times higher) enhancement can be achieved by adding 10 mM of silver.

Even a very small amount of silver (0.1 mM, sample TiO$_2$-Ag-0.1) in the catalyst results in a material that is 1.3 (130%) times more active (r = 28·10^{-3} µM·s^{-1} – sample TiO$_2$-Ag-0; r = 37·10^{-3} µM·s^{-1} – sample TiO$_2$-Ag-0.1) and 1.2 times more effective (42% degradation sample TiO$_2$-Ag-0; 52% of degradation - sample TiO$_2$-Ag-0.1) than the reference material (sample TiO$_2$-Ag-0.0). All the reaction rates and degradation efficiencies can be found in Table 1.
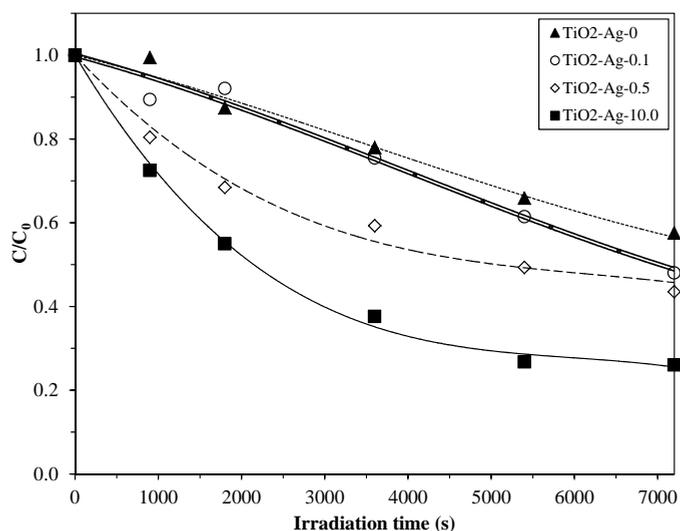
Figure 4. Photocatalytic decay curves of salicylic acid on TiO$_2$-Ag catalysts

One should note that similar improvements of the photocatalytic performances after addition of silver to the TiO$_2$ network by various chemical routes were previously reported [12, 13]. However, it should be emphasized that no thermal treatment was applied to the porous samples investigated in the present work in comparison with the above mentioned papers, where annealing at temperatures higher than 500 C was applied.
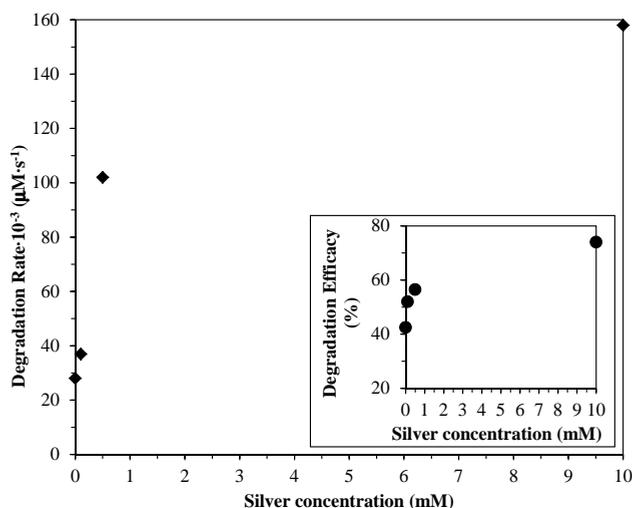
Figure 5. The dependence of the silver concentration (in the impregnation step) on the observed degradation rate and degradation efficiency (inserted figure)

It is now clear that the presence of silver nanoparticles is benefic for the overall photocatalytic performance. One of the possible reasons for the activity enhancement is that these materials absorb in the visible light region, due to the presence of the plasmonic absorption band of silver [14] at 400-440 nm (Figure 3). Thus, with the increase of the silver concentration, the samples absorb more visible light and by this much more electron-hole pairs are generated. Consequently, the observed photocatalytic degradation rates are dependent on the silver concentration. Furthermore, if a noble metal is present on the surface of an n-type semiconductor (where the major charge carriers are electrons) the charge separation is facilitated because of the electron uptake of the silver nanoparticles (phenomena also observed in core-shell Ag-TiO$_2$ catalysts [15]). By this, the life-time of the electron-hole pairs is prolonged, which means that more pollutant molecules can interact with these charged species, inducing higher photocatalytic activity.

The surface area of the studied samples is rather high (Table 1), and thus they are very efficient for well-adsorbing substrates' [16] (such as carboxylic acids) photodegradation. By having a high surface the silver nanoparticles are well distributed throughout the catalyst, generating partially crystallized zones (Figure 2) that can act as active centers in the degradation of salicylic acid. Thus, as the silver concentration grows so does the number of the mentioned active sites. At the same time a slight (25%) surface contraction is observed, as the silver content increases. However, the surface shrinkage is well compensated by the high abundance of the crystallized zones responsible for the already discussed activity enhancement.

CONCLUSIONS

We successfully synthesized highly active titania aerogels with different concentration of silver nanoparticles and tested them for salicylic acid degradation under UV-vis irradiation. The most efficient photocatalyst (TiO$_2$-Ag-10.0) obtained was 5.64 times more active and 1.74 times more efficient than the corresponding reference material (TiO$_2$-Ag-0). The observed activity enhancement can be explained by the presence of the silver induced crystallized zones, effective charge separation (the electron conducting role of silver) and high specific surface area.

EXPERIMENTAL SECTION

TiO$_2$ gels were prepared by the acid-catalyzed sol-gel method using titanium isopropoxide (TIP), HNO$_3$, EtOH and H$_2$O in 1/0.08/21/3.675 molar ratios. The gels were allowed to age for three weeks, then impregnated with various concentrations of AgNO$_3$ ethanol solution (0-10 mM) and subjected to supercritical drying with liquid CO$_2$ (T = 313 K and p = 95.23 atm) by using a home-made device.

The samples were coded TiO$_2$-Ag-x, where x is the concentration of silver ions in mM in the impregnation phase (e.g. TiO$_2$-Ag-5.0).

The specimens' morphology was examined by transmission electron microscopy (TEM) on a Jeol 2100F (FEG) microscope operating at 200 kV, equipped with a corrector for the spherical aberrations, with a point-to-point resolution of 2 Å. The samples were dispersed by ultrasounds in an ethanol solution during 5 minutes and a drop of solution was deposited on carbon-membrane copper-grid.

The surface area and the pore size distribution of the synthesized samples were determined by using a Sorptomatic 1990 equipment and N$_2$ adsorption. The specific surface area was calculated by the BET method.

The band gap energy of the composites was calculated from their diffuse reflectance spectra that were recorded by employing a Jasco spectrophotometer in the wavelength range of 800–200 nm. Reflectance data were converted to F(R) values according to the Kubelka-Munk theory. The band gap was obtained from the plot of $[F(R)\cdot E]^{1/2}$ versus energy of the exciting light (E) assuming that the investigated porous samples are indirect crystalline semiconductors.

The photocatalytic activity of the composites was established from the degradation rate of salicylic acid (used as standard pollutant molecule) as elsewhere reported [6]. The decrease in time of the salicylic acid concentration (the intensity of the band located at 295 nm) was monitored with a Jasco V-530 UV-vis spectrophotometer (C$_0$ = 10^{-3} M for all investigated samples). The composites immersed in salicylic acid solution were irradiated with a medium pressure Hg HBO OSRAM lamp (500 W). Before visible irradiation as well as before UV-vis measurements, the cell with the sample was kept in dark for 15 min in order to achieve the equilibrium of the adsorption-desorption process. The initial photocatalytic degradation rate, r_0, was used

to evaluate the efficiency of a given photocatalyst. To determine r_0, an empirical function was fitted to the experimentally observed $c = f(t)$ data points. The slope of this function at $t = 0$ yielded the initial rate of the photocatalytic reaction.

ACKNOWLEDGMENTS

REFERENCES

1. S. Kelly, F. H. Pollak, M. Tomkiewicz, *The Journal of Physical Chemistry B,* **1997,** *101*, 2730.
2. Z. Zhu, M. Lin, G. Dagan, M. Tomkiewicz, *The Journal of Physical Chemistry* **1995,** *99*, 15945.
3. G. Dagan, M. Tomkiewicz, *The Journal of Physical Chemistry* **1993**, *97*, 12651.
4. N. Hüsing, U. Schubert, *Angewandte Chemie International Edition* **1998**, *37*, 22.
5. L. Baia, A. Peter, V. Cosoveanu, E. Indrea, M. Baia, J. Popp, V. Danciu, *Thin Solid Films,* **2006,** *511-512*, 512.
6. L. Baia, L. Diamandescu, L. Barbu-Tudoran, A. Peter, G. Melinte, V. Danciu, M. Baia, *Journal of Alloys and Compounds* **2011**, *509*, 2672.
7. J. O.Carneiro, V. Teixeira, A. Portinha, A. Magalhaes, P. Coutinho, C. J.Tavares, R. Newton*, Materials Science and Engineering: B* **2007,** *138*, 144.
8. P. D. Cozzoli, E. Fanizza, R. Comparelli, M. L. Curri, A. Agostano, *The Journal of Physical Chemistry B* **2004**, *108,* 9623.
9. R. Jenkins, R. L. Snyder, Introduction to X-ray Powder Diffractometry. John Wiley & Sons: New York, **1996**.
10. G. Dagan, M. Tomkiewicz, *Journal of Non-Crystalline Solids,* **1994**, *175*, 294.
11. A. Slistan-Grijalva, R. Herrera-Urbina, J. Rivas-Silva, M. Avalos-Borja, F. Castillon-Barraza, A. Posada-Amarillas, *Physica E,* **2005,** *27,* 104.
12. L. Ren, Y. P. Zeng, D. Jiang, *Catalysis Commuications,* **2009**, *10*, 645.
13. C. C. Chang, J. Y. Chen, T. L. Hsu, C. K. Linb, C. C. Chan, *Thin Solid Films*, **2008**, *516*, 1743.
14. M. M. Mohamed, K. S. Khairou, *Microporous and Mesoporous Materials* **2011,** *142*, 130.
15. Hirakawa, P. V. Kamat, *Journal of the American Chemical Society* **2005**, *127*, 3928.
16. J. Ryu, W. Choi, *Environmental Science & Technology.* **2008**, *42*, 294.

GENERALIZED ZAGREB INDEX OF GRAPHS

MAHDIEH AZARI[a], ALI IRANMANESH[b]

ABSTRACT. In this paper, we introduce the generalized Zagreb index of a connected graph and express some of the properties of this index. Then we find the generalized Zagreb index of some nanotubes and nanotori.

Keywords: *The first and second Zagreb indices, Generalized Zagreb index, Nanotubes, Nanotori.*

INTRODUCTION

Throughout this paper, we consider only simple, undirected, connected and finite graphs. A simple graph is a graph without any loops or multiple edges. Let G be a graph with the set of vertices $V(G)$ and the set of edges $E(G)$. We denote by $\deg_G(u)$, the degree of a vertex u of G which is defined as the number of edges incident to u.

A topological index of G is a real number related to G and it is invariant under all graph isomorphism. In Chemistry, graph invariants are known as topological indices.

Wiener index, introduced by Harold Wiener in 1947, is the first topological index in Chemistry [1-2]. Wiener index of G is defined as the sum of distances between all pairs of vertices of G.

Zagreb indices were defined about forty years ago by Gutman and Trinajestic [3]. The first and second Zagreb indices of G are denoted by $M_1(G)$ and $M_2(G)$, respectively and defined as follows:

$$M_1(G) = \sum_{u \in V(G)} \deg_G(u)^2 \text{ and } M_2(G) = \sum_{uv \in E(G)} \deg_G(u)\deg_G(v).$$

We refer the reader to [4-9], for more information about these indices.

In this paper, we introduce the generalized Zagreb index of a connected graph and express some of the properties of this index. Then we find the generalized Zagreb index of some nano-structures.

---

[a] *Department of Mathematics, Kazerun Branch, Islamic Azad University, P. O. Box: 73135-168, Kazerun, Iran, azari@kau.ac.ir*
[b] *Department of Mathematics, Tarbiat Modares University, P. O. Box: 14115-137, Tehran, Iran, iranmanesh@modares.ac.ir*

DEFINITIONS AND PRELIMINARIES

Let G be a graph with the set of vertices $V(G)$ and the set of edges $E(G)$.

Definition 2.1 Generalized Zagreb index of G is defined as follows: If r and s are arbitrary nonnegative integers, then

$$M_{\{r,s\}}(G) = \sum_{uv \in E(G)} (\deg_G(u)^r \deg_G(v)^s + \deg_G(u)^s \deg_G(v)^r) \text{ and}$$

$$M_{\{0,-1\}}(G) = |V(G)|.$$

In the next Theorem, we express some of the properties of this index. Its proof follows immediately from the definition, so is omitted.

Theorem 2.2 The generalized Zagreb index of a graph G satisfies the following conditions.

(i) $M_{\{r,s\}}(G) = M_{\{s,r\}}(G)$;

(ii) $M_{\{0,0\}}(G) = 2|E(G)|$;

(iii) $M_{\{1,0\}}(G) = M_1(G)$;

(iv) $M_{\{1,1\}}(G) = 2M_2(G)$;

(v) $M_{\{r-1,0\}}(G) = \sum_{u \in V(G)} \deg_G(u)^r$;

(vi) $M_{\{r,r\}}(G) = 2 \sum_{uv \in E(G)} (\deg_G(u) \deg_G(v))^r$.

Let P_n, C_n, S_n, K_n and W_n denote the n-vertex path, cycle, star, complete graph and wheel respectively. Let $K_{a,b}$ be complete bipartite graph on $a+b$ vertices. Determining the generalized Zagreb index of these graphs is a matter of simple counting, so the proof of the next Theorem is also omitted.

Theorem 2.3

(i) $M_{\{r,s\}}(P_n) = 2^{r+1} + 2^{s+1} + (n-3)2^{r+s+1}$;

(ii) $M_{\{r,s\}}(C_n) = n2^{r+s+1}$;

(iii) $M_{\{r,s\}}(S_n) = (n-1)^{r+1} + (n-1)^{s+1}$;

(iv) $M_{\{r,s\}}(K_n) = n(n-1)^{r+s+1}$;

(v) $M_{\{r,s\}}(W_n) = (n-1)[2 \times 3^{r+s} + 3^r(n-1)^s + 3^s(n-1)^r]$;

(vi) $M_{\{r,s\}}(K_{a,b}) = a^{r+1}b^{s+1} + a^{s+1}b^{r+1}$.

Lemma 2.4 If H is a subgraph of G, then $M_{\{r,s\}}(H) \le M_{\{r,s\}}(G)$.
Proof. The proof is obvious.

Theorem 2.5 If T is a tree with exactly n vertices, then
$$M_{\{r,s\}}(P_n) \leq M_{\{r,s\}}(T) \leq M_{\{r,s\}}(S_n).$$
Proof. The proof is straightforward.

Theorem 2.6 If G is a graph with n vertices, then
$$M_{\{r,s\}}(P_n) \leq M_{\{r,s\}}(G) \leq M_{\{r,s\}}(K_n).$$

Proof. Since G is simple, then $|V(G)| = n$. So for every $u \in V(G)$,

$\deg_G(u) \leq n-1$. Consequently,

$$|E(G)| = \frac{1}{2} \sum_{u \in V(G)} \deg_G(u) \leq \frac{1}{2} \sum_{u \in V(G)} (n-1) = \frac{n(n-1)}{2}. \text{ Therefore}$$

$$M_{\{r,s\}}(G) = \sum_{[u,v] \in E(G)} (\deg_G(u)^r \deg_G(v)^s + \deg_G(u)^s \deg_G(v)^r) \leq 2 \sum_{[u,v] \in E(G)} (n-1)^{r+s} =$$

$$2(n-1)^{r+s} |E(G)| \leq 2(n-1)^{r+s} \frac{n(n-1)}{2} = n(n-1)^{r+s+1} = M_{\{r,s\}}(K_n).$$

It is a well-known fact that G has a subgraph T with n vertices, which is also a tree. Combining the previous Theorem and Lemma 2.4, we can obtain the desired results.

RESULTS AND DISCUSSION

Carbon nanotubes (CNTs) are allotropes of carbon with molecular structure and tubular shape, having diameters of the order of a few nanometers and lengths up to several millimeters. Nanotubes are categorized as single-walled (SWNTs) and multi-walled (MWNTs) nanotubes. In 1991, Iijima discovered carbon nanotubes as multi-walled structures [10]. When a nanotube is bent so that its ends meet a nanotorus is produced. In this section, we calculate the generalized Zagreb index of some nanotubes and their related nanotori.

3.1 Generalized Zagreb index in nanotubes and nanotori

A polyhex net is a trivalent covering made entirely by hexagons C_6. It can cover either a cylinder or a torus. Next, the polyhex covering can be modified, e.g., by the Stone-Wales isomerization [11], as shown by Diudea [12-15]. In the following, the generalized Zagreb index will be calculated in a series of nanotubes and their corresponding nanotori.

3.1.1. Polyhex nanotubes and nanotori

Let $G = TUZC_6(p,q)$ be an arbitrary zigzag polyhex nanotube, where p is the number of horizontal hexagons in each row and q is the number of zigzag lines in the molecular graph of G (see Figure 1). Then

$|V(G)| = 2pq$, $|E(G)| = 3pq - p$ and we have:

$$M_{\{r,s\}}(G) = 4p(2^r3^s + 2^s3^r) + (3pq - 5p)(3^r3^s + 3^s3^r) =$$
$$p(2^{r+2}3^s + 2^{s+2}3^r + 2(3q - 5)3^{r+s}).$$
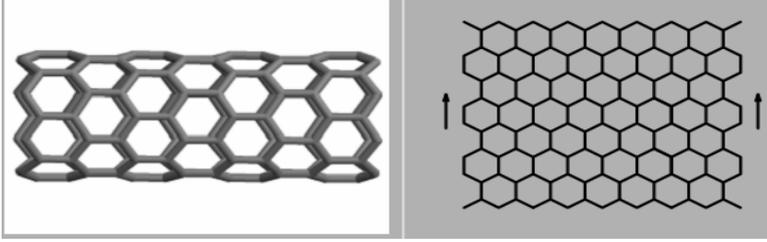
Figure 1. $TUZC_6(8,8)$

Let $T = TZC_6(p,q)$ be the nanotorus related to the nanotube TZC6(p,q). Then, $|V(T)| = 2pq$, $|E(T)| = 3pq$ and

$$M_{\{r,s\}}(T) = 3pq(3^r3^s + 3^s3^r) = 2pq3^{r+s+1}.$$

Let $G = TUAC_6(p,q)$ be an arbitrary armchair polyhex nanotube, where p is the number of horizontal hexagons in one row and q is the number of rows in the molecular graph of G (see Figure 2). Then $|V(G)| = 2pq$, $|E(G)| = 3pq - 2p$ and we have:

$$M_{\{r,s\}}(G) = 4p(2^r3^s + 2^s3^r) + 2p(2^r2^s + 2^s2^r) + (3pq - 8p)(3^r3^s + 3^s3^r) =$$
$$p(2^{r+2}3^s + 2^{s+2}3^r + 2^{r+s+2} + 2(3q - 8)3^{r+s}).$$
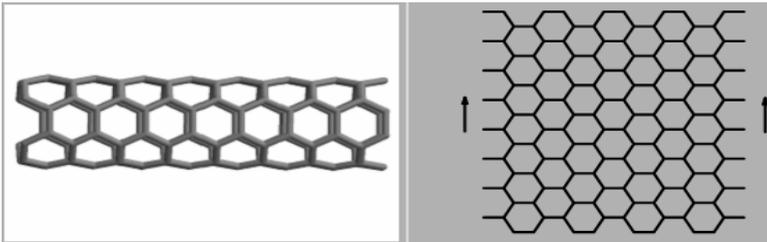
Figure 2. $TUAC_6(4,16)$

Let $T = TAC_6(p,q)$ be the nanotorus related to G. Then $|V(T)| = 2pq$, $|E(T)| = 3pq$ and $M_{\{r,s\}}(T) = 3pq(3^r3^s + 3^s3^r) = 2pq3^{r+s+1}$.

3.1.2 $C_4C_8(p,q)$ nanotubes and nanotori

A C_4C_8 net is a trivalent decoration made by alternating C_4 and C_8. It can cover either a cylinder or a torus.

Let $G = TURC_4C_8(p,q)$ (R means rhomb, see Figure 3). We denote the number of rhombs in each row by p and the number of rhombs in each column by q. Then $|V(G)| = 4pq$, $|E(G)| = p(6q-1)$ and we have:

$$M_{\{r,s\}}(G) = 4p(2^r3^s + 2^s3^r) + (6pq - 5p)(3^r3^s + 3^s3^r) =$$
$$p(2^{r+2}3^s + 2^{s+2}3^r + 2(6q-5)3^{r+s}).$$
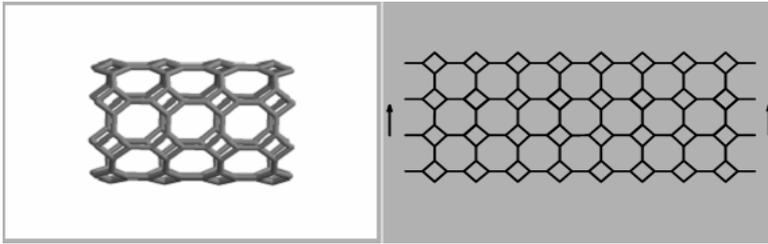
Figure 3. $TURC_4C_8(8,4)$

Now, let $T = TRC_4C_8(p,q)$ be the nanotorus related to G. Then $|V(T)| = 4pq$, $|E(T)| = 6pq$ and $M_{\{r,s\}}(T) = 6pq(3^r3^s + 3^s3^r) = 4pq3^{r+s+1}$.

Let $G = TUSC_4C_8(p,q)$ (S means square, see Fgure 4). We denote the number of squares in one row by p and the number of rows by q ($q \geq 2$). Then $|V(G)| = 4pq$, $|E(G)| = p(6q-2)$ and we have:

$$M_{\{r,s\}}(G) = 4p(2^r3^s + 2^s3^r + 2^{r+s} + (3q-4)3^{r+s}).$$
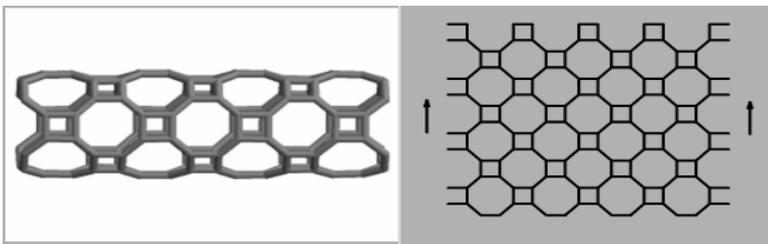
Figure 4. $TUSC_4C_8(4,8)$

Now, let $T = TSC_4C_8(p,q)$ be the nanotorus related to G. Then $|V(T)| = 4pq$, $|E(T)| = 6pq$ and $M_{\{r,s\}}(T) = 6pq(3^r3^s + 3^s3^r) = 4pq3^{r+s+1}$.

3.1.3 $C_5C_7(p,q)$ nanotubes and nanotori

A C_5C_7 net is a trivalent covering made by alternating C_5 and C_7. It can cover either a cylinder or a torus.

Let $G = TUHC_5C_7(2p,q)$ (see Figure 5), where 2p is the number of pentagons in each row. In this nanotube, the four first rows of vertices and edges are repeated, alternatively. We denote the number of this repetition by q. In each period of this nanotube, there are 16p vertices and we have q periods. So $|V(G)| = 16pq$. Also, the number of edges in each period is equal to 24p except from the last period which has 22p edges. So $|E(G)| = 24pq - 2p$ and we have:

$$M_{\{r,s\}}(G) = 8p(2^r3^s + 2^s3^r) + (24pq - 10p)(3^r3^s + 3^s3^r) =$$
$$4p(2^{r+1}3^s + 2^{s+1}3^r + 3^r + 3^s + (12q - 5)3^{r+s}).$$

Figure 5. $TUHC_5C_7(8,2)$

Let $T = THC_5C_7(2p,q)$ be the nanotorus related to G. Then $|V(T)| = 16pq$, $|E(T)| = 24pq$ and $M_{\{r,s\}}(T) = 24pq(3^r3^s + 3^s3^r) = 16pq3^{r+s+1}$.

Let $G = TUVC_5C_7(2p,q)$ (see Figure 6), where 2p is the number of heptagons in each row. In this nanotube, the four first rows of vertices and edges are repeated, alternatively. We denote the number of this repetition by q. In each period of this nanotube, there are 16p vertices and we have q periods. So $|V(G)| = 16pq$. Also, the number of edges in each period is equal to 24p expect from the last period which has 21p edges. So

$\left|E(G)\right| = 24p(q-1) + 21p = 24pq - 3p$ and we have:

$M_{\{r,s\}}(G) = 10p(2^r3^s + 2^s3^r) + p(2^r2^s + 2^s2^r) + (24pq - 14p)(3^r3^s + 3^s3^r) =$

$2p(5(2^r3^s + 2^s3^r) + 2^{r+s} + 2(12q - 7)3^{r+s})$.
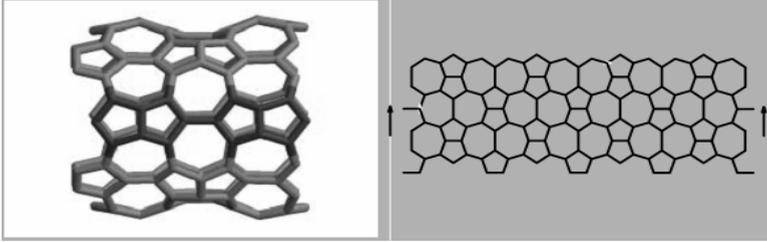
Figure 6. $TUVC_5C_7(8,2)$

Let $T = TVC_5C_7(2p, q)$ be the nanotorus related to G. Then $\left|V(T)\right| = 16pq$, $\left|E(T)\right| = 24pq$ and $M_{\{r,s\}}(T) = 24pq(3^r3^s + 3^s3^r) = 16pq3^{r+s+1}$.

Let $G = TUSC_5C_7(p, q)$ (S means spiral, see Figure 7). We denote the number of pentagones in the first row by p. In this nanotube, the two first rows of vertices and edges are repeated, alternatively. We denote the number of this repetition by q. In each period of this nanotube, there are 8p vertices except from the last period which has 6p vertices. Hence $\left|V(G)\right| = 8p(q-1) + 6p = 8pq - 2p$. Also, the number of edges in each period is equal to 12p except from the last period which has 7p edges. So $\left|E(G)\right| = 12p(q-1) + 7p = 12pq - 5p$ and we have:

$M_{\{r,s\}}(G) = 6p(2^r3^s + 2^s3^r) + p(2^r2^s + 2^s2^r) + (12pq - 12p)(3^r3^s + 3^s3^r) =$

$p(2^{r+1}3^{s+1} + 2^{s+1}3^{r+1} + 2^{r+s+1} + 8(q-1)3^{r+s+1})$.
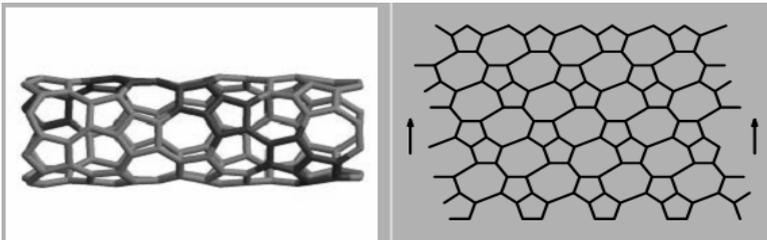
Figure 7. $TUSC_5C_7(4,4)$

Let $T = TSC_5C_7(p,q)$ be the nanotorus related to G. Then $|V(T)| = 8pq$, $|E(T)| = 12pq$ and $M_{\{r,s\}}(T) = 12pq(3^r3^s + 3^s3^r) = 8pq3^{r+s+1}$.

3.1.4. $XAC_5C_7(p,q)$ nanotubes and nanotori

Let $G = TUHAC_5C_7(p,q)$ (see Figure 8). We denote the number of heptagons in the first row by p. In this nanotube, the three first rows of vertices and edges are repeated, alternatively. The number of this repetition is denoted by q. In each period of this nanotube, there are 8p vertices and we have q periods. Hence $|V(G)| = 8pq$. Also, the number of edges in each period is equal to 12p except from the last period which has 11p edges. So $|E(G)| = 12p(q-1) + 11p = 12pq - p$ and we have:

$$M_{\{r,s\}}(G) = 4p(2^r3^s + 2^s3^r) + (12pq - 5p)(3^r3^s + 3^s3^r) =$$
$$2p(2^{r+1}3^s + 2^{s+1}3^r + (12q-5)3^{r+s}).$$
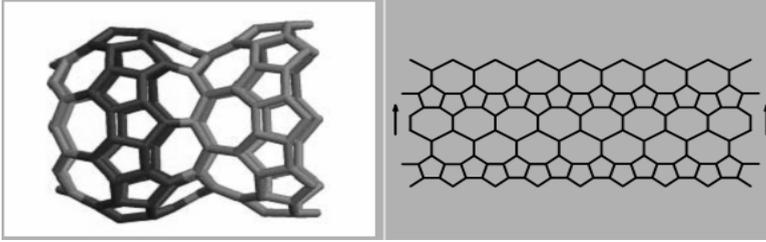
**Figure 8.** $TUHAC_5C_7(8,2)$

Let $T = THAC_5C_7(p,q)$ be the nanotorus related to G. Then $|V(T)| = 8pq$, $|E(T)| = 12pq$ and $M_{\{r,s\}}(T) = 12pq(3^r3^s + 3^s3^r) = 8pq3^{r+s+1}$.

Let $G = TUVAC_5C_7(p,q)$ (see Figure 9). In this nanotube, the three first columns of vertices and edges are repeated, alternatively. We denote the number of this repetition by q and the number of vertical lines in the first column of each period by p. In each period, there are 8p vertices and 12p-3 edges. So $|V(G)| = 8pq$ and $|E(G)| = (12p-3)q$ and we have:

$$M_{\{r,s\}}(G) = 8q(2^r3^s + 2^s3^r) + 2q(2^r2^s + 2^s2^r) + (12p-13)q(3^r3^s + 3^s3^r) =$$
$$2q(2^{r+2}3^s + 2^{s+2}3^r + 2^{r+s+1} + (12p-13)3^{r+s}).$$
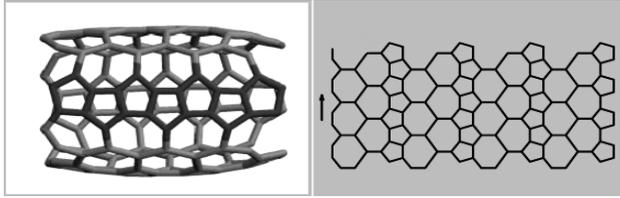
Figure 9. $TUVAC_5C_7(4,4)$

Now, let $T = TVAC_5C_7(p,q)$ be the nanotorus related to G. Then $|V(T)| = 8pq$, $|E(T)| = 12pq$ and $M_{\{r,s\}}(T) = 12pq(3^r3^s + 3^s3^r) = 8pq3^{r+s+1}$.

3.1.5 $C_5C_6C_7(p,q)$ nanotubes and nanotori

A $C_5C_6C_7$ net is a trivalent decoration made by alternating C_5, C_6 and C_7. It can cover either a cylinder or a torus.

Let $G = TUHAC_5C_6C_7(p,q)$ (see Figure 10). We denote the number of pentagons in the first row by p. In this nanotube, the three first rows of vertices and edges are repeated, alternatively. We denote the number of this repetition by q. In each period of this nanotube, there are 16p vertices and we have q periods. So $|V(G)| = 16pq$. Also, the number of edges in each period is equal to 24p expect from the last period which has 22p edges. So $|E(G)| = 24p(q-1) + 22p = 24pq - 2p$ and we have:

$$M_{\{r,s\}}(G) = 8p(2^r3^s + 2^s3^r) + (24pq - 10p)(3^r3^s + 3^s3^r) =$$
$$4p(2^{r+1}3^s + 2^{s+1}3^r + (12q-5)3^{r+s}).$$
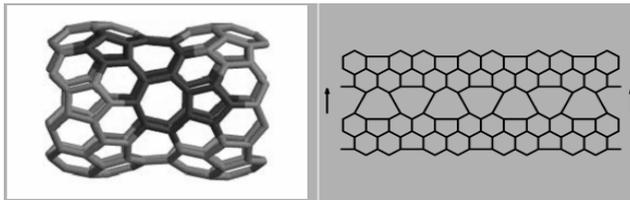
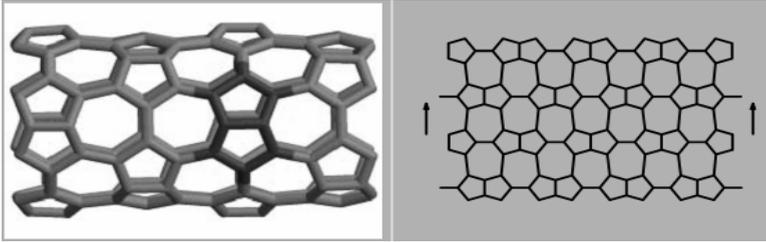**Figure 10.** $HAC_5C_6C_7(4,2)$

Now, let $T = THAC_5C_6C_7(p,q)$ be the nanotorus related to G. Then $|V(T)| = 16pq$, $|E(T)| = 24pq$ and

$$M_{\{r,s\}}(T) = 24pq(3^r3^s + 3^s3^r) = 16pq3^{r+s+1}.$$

Let $G = TUVAC_5C_6C_7(p,q)$ (see Figure 11). In this nanotube, the three first columns of vertices and edges are repeated, alternatively. We denote the number of this repetition by q and the number of pentagons in each period by p. In each period of this nanotube, there are 16p vertices and 24(p-1)+21 edges and we have q periods. So $|V(G)| = 16pq$ and $|E(G)| = 24pq - 3q$ and we have:

$$M_{\{r,s\}}(G) = 8q(2^r3^s + 2^s3^r) + 2q(2^r2^s + 2^s2^r) + (24pq - 14q)(3^r3^s + 3^s3^r) =$$
$$2q(2^{r+1}3^s + 2^{s+1}3^r + 2^{r+s+1} + (24p - 13)3^{r+s}).$$
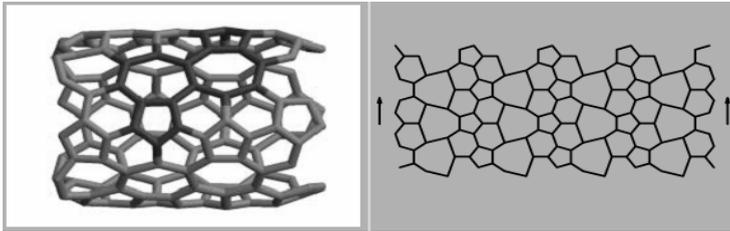
Figure 11. $VAC_5C_6C_7(2,4)$

Let $T = TVAC_5C_6C_7(p,q)$ be the nanotorus related to G. Then $|V(T)| = 16pq$, $|E(T)| = 24pq$ and

$$M_{\{r,s\}}(T) = 24pq(3^r3^s + 3^s3^r) = 16pq3^{r+s+1}.$$

The coverings and notations for nanotubes and nanotori are taken from Diudea's papers [11-14].

3. 2. CLASSICAL ZAGREB INDICES IN NANOTUBES AND NANOTORI

In this section, as the results of the previous section and Theorem 2.2, we derived the first and second Zagreb indices of the above-mentioned nanotubes and nanotori. They are been listed in the following tables.

Table 1. First and second Zagreb indices of some nanotubes

Nanotube G	$M_1(G) = M_{\{1,0\}}(G)$	$M_2(G) = \dfrac{1}{2}M_{\{1,1\}}(G)$
$TUZC_6(p,q)$	2p(9q-5)	3p(9q-7)
$TUAC_6(p,q)$	2p(9q-10)	p(27q-40)
$TURC_4C_8(p,q)$	2p(18q-5)	3p(18q-7)

Nanotube G	$M_1(G) = M_{\{1,0\}}(G)$	$M_2(G) = \dfrac{1}{2}M_{\{1,1\}}(G)$
$TUSC_4C_8(p,q)$	4p(9q-5)	2p(27q-20)
$TUHC_5C_7(2p,q)$	4p(36q-1)	6p(36q-5)
$TUVC_5C_7(2p,q)$	6p(24q-5)	2p(108q-31)
$TUSC_5C_7(p,q)$	2p(36q-19)	4p(27q-17)
$TUHAC_5C_7(p,q)$	2p(36q-5)	3p(36q-7)
$TUVAC_5C_7(p,q)$	6q(12p-5)	q(108p-61)
$TUHAC_5C_6C_7(p,q)$	4p(36q-5)	6p(36q-7)
$TUVAC_5C_6C_7(p,q)$	2q(72p-25)	q(216p-85)

Table 2. First and second Zagreb indices of some nanotori

Nanotorus T	$M_1(T) = M_{\{1,0\}}(G)$	$M_2(T) = \dfrac{1}{2}M_{\{1,1\}}(G)$
$TZC_6(p,q)$	18pq	27pq
$TAC_6(p,q)$		
$TRC_4C_8(p,q)$	36pq	54pq
$TSC_4C_8(p,q)$		
$THC_5C_7(2p,q)$	144pq	216pq
$TVC_5C_7(2p,q)$		
$TSC_5C_7(p,q)$	72pq	108pq
$THAC_5C_7(p,q)$		
$TVAC_5C_7(p,q)$		
$THAC_5C_6C_7(p,q)$	144pq	216pq
$TVAC_5C_6C_7(p,q)$		

CONCLUSIONS

The generalized Zagreb index was defined and next formulas for calculating this new topological index in some nanotubes and nanotori were derived. The classical Zagreb indices formulas for the considered nanotubes and nanotori were tabulated.

ACKNOWLEDGEMENT.

REFERENCES

1. H. Wiener, *Journal of the American Chemical Society*, **1947**, *69*, 2636.
2. H. Wiener, *Journal of the American Chemical Society*, **1947**, *69*, 17.
3. I. Gutman, N. Trinajstic, *Chemical Physics Letters*, **1972**, *17*, 535.
4. J. Braun, A. Kerber, C. Rucker, *MATCH - Communications in Mathematical and in Computer Chemistry*, **2005**, *54*, 163.
5. I. Gutman, K. C. Das, *MATCH - Communications in Mathematical and in Computer Chemistry*, **2004**, 50, 83.
6. S. Nikolic, G. Kovacevic, A. Milicevic, N. Trinajstic, *Croatica Chimica Acta*, **2003**, *76*, 113.
7. B. Zhou, *MATCH - Communications in Mathematical and in Computer Chemistry*, **2004**, *52*, 113.
8. B. Zhou, I. Gutman, *MATCH - Communications in Mathematical and in Computer Chemistry*, **2005**, *54*, 233.
9. B. Zhou, I. Gutman, *Chemical Physics Letters*, **2004**, *394*, 93.
10. S. Iijima, *Nature*, **1991**, *354*, 56.
11. A. J. Stone, D. J. Wales, *Chemical Physics Letters*, **1986**, *128*, 501.
12. M. V. Diudea, *Studia Universitatis "Babes- Bolyai", Seria Chemia*, **2003,** *48*(2), 17.
13. M. V. Diudea, In: M. V. Diudea, Ed., *Nanostructures-Novel Architecture*, NOVA, New York, **2005**, 203.
14. M. V. Diudea, *Forma* (Tokyo), **2004**, *19* (3), 131.
15. M. V. Diudea, Cs. L. Nagy*, Periodic nanostructures*, Springer, 2007.

ADSORPTION OF HORSE METHEMOGLOBIN ON BIOACTIVE GLASS AT HIGH SALT CONCENTRATION, STUDIED BY EPR AND FTIR SPECTROSCOPY

CRISTINA GRUIAN[a, b], HEINZ-JÜRGEN STEINHOFF[a], SIMION SIMON[b]

ABSTRACT. Although protein adsorption has been intensively studied in the last years, conformational changes which are likely to appear on the structure of the protein upon adsorption are difficult to evidence directly. Combined SDSL and EPR spectroscopy were applied to study adsorption of horse mehemoglobin methemoglobin on bioactive glass in solution with high salt concentration (500mM NaCl). Further studies using FTIR spectroscopy aimed at identifying changes in the secondary structure of the protein upon the adsorption process. EPR spectra of methemoglobin spin labeled at position β-93 in solution were compared to those obtained after adsorption to extract structural information. A consistent analysis of EPR spectra revealed that the adsorption of methemoglobin is influenced by the chemical treatment applied to the surface of bioactive glass. From the FTIR spectra details concerning the changes of secondary structure of the protein after 2 hours of sample immersion in protein solution were obtained.

Keywords: site-directed spin labeling, FTIR spectroscopy, protein adsorption, bioactive glasses

INTRODUCTION

Protein adsorption and subsequent changes in their conformation are known to be the first biomechanical events taking place at the surface of an implant after implantation and determinants for further physicochemical interactions [1]. Thus, the first step in evaluating the blood and tissue compatibility of any medical device is to study its behavior in terms of interactions with proteins. The total amount of adsorbed protein as well as the overall protein-implant surface area interactions are of primary importance for the biocompatibility of a bioengineered material. It was also shown that the ionic strength of the solution influences the adsorption rate and the stability of protein

---

[a] *Department of Physics, University of Osnabrueck, 49069 Osnabrueck, Germany*
[b] *Faculty of Physics, Babes-Bolyai University, 400084, Cluj-Napoca, Romania, simion.simon@phys.ubbcluj.ro*

binding [2-4]. Previous experiments conducted in our group have shown that low salt concentration positively influences the stability of methemoglobin adsorption on the type of bioactive glass (BG) used in this study (C. Gruian, H.J. Steinhoff, S.Simion - unpublished).

Other studies have shown that the use of protein coupling agents allows the control of protein release kinetics and maintains almost completely the native protein structure [5,6]. However, it is necessary to apply a certain chemical treatment to the surface for maintaining the protein-binding ability of the BG [7]. In this study the bioactive glass was silanized with 3-aminopropyl-triethoxysilane (APTS) [8] and subsequently modified with the protein coupling agent glutaraldehyde (GA).

Various techniques have been used to analyze secondary protein structures but they are not easily applicable to proteins that are adsorbed on solid surfaces so it is difficult to obtain structural information for adsorbed proteins. Many studies have used FTIR spectroscopy as a surface-sensitive technique to investigate protein structure because it has a high sensitivity to examine the structure of proteins in solution [9-11] and on surfaces [12-15]. Therefore, we investigated the conformational changes of horse methemoglobin during the adsorption on BG by using Fourier transform infrared (FTIR) spectroscopy and electron paramagnetic resonance (EPR) in combination with spin labeling. Changes in the secondary structure of the protein during the adsorption on the BG treated with GA were monitored by means of FTIR spectroscopy. In the amide I region, each type of secondary structure gives rise to a different C=O stretching frequency due to unique molecular geometry and hydrogen bonding pattern. Therefore, the observed amide bands are composed of several overlapping components representing helices, β-sheets, turns and random structures [16,17]. Moreover, from the amide I intensity we could monitor protein adsorption in time, until the surface was saturated.

Until now EPR was rarely used for studying the interaction between proteins and solid surfaces. Yet, the studies carried out to investigate the protein adsorption onto planar lipid bilayers [18, 19] or the partial unfolding of lysozyme on quartz [20] showed that this technique can successfully monitor the structural changes of a protein adsorbed to a solid surface. In this purpose, we introduced a spin label at position β-93 in methemoglobin [21]. It is important to mention that methemoglobin consists of four subunits: two α types and two β types. In each position β-93 the protein has a cysteine which was labeled with (4-(2-Iodoacetamido)-2,2,6,6-tetramethyl-1-piperidinyloxy) (JAA) (figure1).

a   b
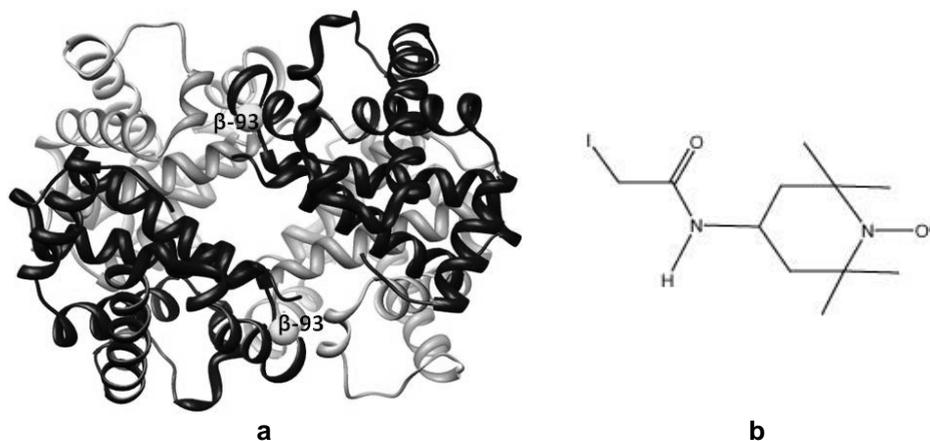
Figure 1 a) Structure of methemoglobin obtained by X-ray crystallography (2ZLU from Protein Data Bank). The α- and the β-chains are colored in different shades of grey. The native cysteins from position β-93which were mutated to Cys and spin labeled with JAA are indicated as spheres. **b)** Structure of 4-(2-Iodoacetamido)-2,2,6,6-tetramethyl-1-piperidinyloxy spin label.

From the corresponding continuous wave (cw) EPR spectrum information about the nitroxide side chain mobility was obtained [21,22]. The mobility analysis is based on the fact that the room temperature EPR spectral line shape is sensitive to the reorientational motion of the nitroxide side chain due to partial motional averaging of the anisotropic components of the g- and hyperfine tensors. Further on, the distance between spin labels in the frozen state was determined by using pulse EPR DEER (double electron electron resonance) [23], to test whether the structure in close vicinity to amino acid position β-93 unfolds or if the protein keeps its native conformation upon adsorption.

RESULTS AND DISCUSSION

Cw-EPR spectra of methemoglobin recorded before and after adsorption on BG substrate are shown in figure 2a. It is important to mention that for all EPR spectra the measurements were performed in buffer solution, in order to monitor the protein behavior in its native environment.

X-band cw-EPR spectrum of methemoglobin in solution consists in two components with different mobility: an immobile component (arrow 2 in figure 2) which was best interpreted by Moffat [31] as corresponding to spin labels trapped in a protein pocket, and a mobile component (arrow 1 in figure 2) which correspond to the surface exposed spin labels. After adsorption, the equilibrium between the two components is significantly shifted towards the immobile one, indicating an increase in spin label immobilization due to

protein adsorption on the BG substrate [32]. The fractions of immobilized spin labels depicted in figure 2 were determined from simulations of cw-EPR spectra, using the Freed method [33]. This immobilization was even more pronounced on the BG treated with GA, a situation which can be explained if we assume that GA induces polymerization of methemoglobin when the protein is attached on the BG.
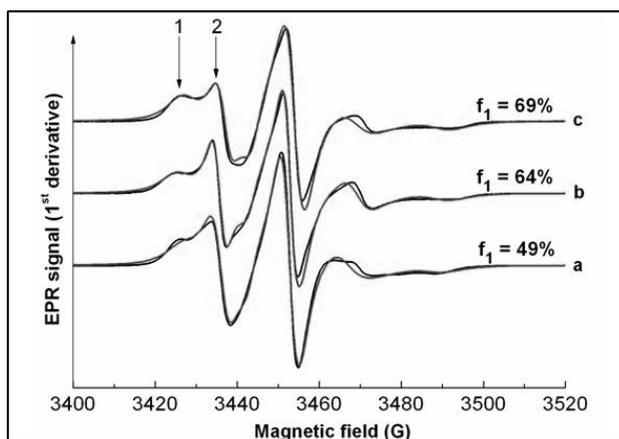
Figure 2. X-band cw-EPR spectra of horse methemoglobin spin-labeled in position β-93* recorded at room temperature; the black lines correspond to the spectra recorded in solution before (a) and after adsorption on the BG without GA (b) and with GA (c). The grey lines represent the best fit of the simulated spectra. The immobile and mobile components are indicated by arrows 1 and 2 respectively.

The information obtained from cw-EPR spectra is not sufficient to characterize protein adsorption in terms of structural changes; therefore, we performed pulse DEER EPR measurements. Figure 3 illustrates the experimental DEER time traces and the results after analysis with Tikhonov regularization (L-curve method) in DeerAnalyses2009 [30]. A first observation is that both DEER spectra recorded in adsorbed state have a very low modulation depth (<0.1 in case of BG without GA and 0 for BG treated with GA).

It is clear that when the protein is attached on BG a smaller number of spins have dipolar-dipolar interaction, compared with the protein in solution. We can explain this by assuming that a small part of methemoglobin dissociates upon adsorption. However, experiments conducted in our group have shown that this behavior is more pronounced when the solution has 50 times lower salt concentration (C. Gruian, H.J. Steinhoff, S.Simion, unpublished). Although electrostatic interactions have been proposed to dominate the protein–surface interaction [34], for the experimental conditions used here this balance is not in favor of the electrostatic interaction because of the high

salt concentration of the solution. Because protein dissociation was found to be less pronounced than in low salt conditions, one can conclude that electrostatic interactions play an important role in the dissociation of methemoglobin observed when the protein is adsorbed on the bioactive glass.

On the other hand, the total absence of modulation in the DEER signal on the BG treated with GA can be attributed also to a homogenous spatial distribution of the spin labels in the sample, as a consequence of polymerization induced by GA. We assume that in this case, both effects (dissociation and polymerization of the protein) are contributing to the overall DEER signal. Hence, after analysis with Tikhonov regularization a distance distribution could be obtained only for the protein in buffer solution and for protein adsorbed on BG without GA (figure 3). The Cβ-Cβ distances between the β-93 sites derived from the structures of the hemoglobin in solution and in the adsorbed state revealed a defined distance distribution, with a major distance at 24.8 Å in solution and 35 Å in adsorbed state. This increasing of major maximum in distance distribution suggests that the two β chains are slightly apart for the protein in adsorbed state. Projected on the protein, this means that in adsorbed state the tetrameric structure adopts a conformation which is slightly unfolded, as a consequence of interaction between protein and BG surface.
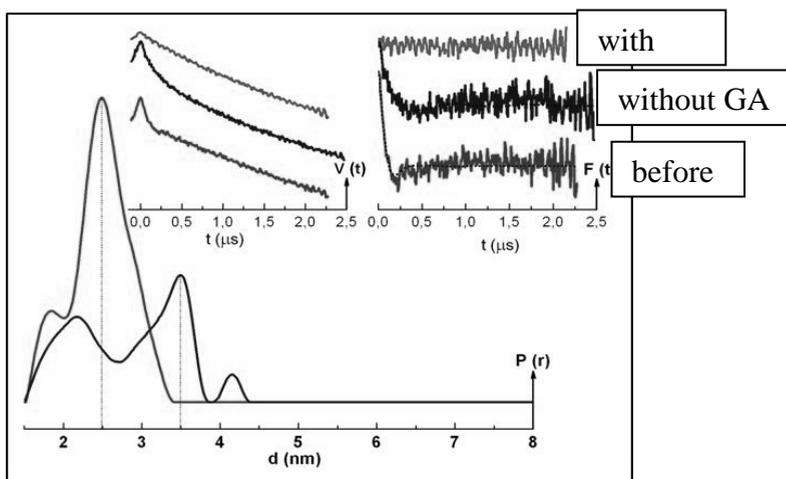
Figure 3 DEER analysis of methemoglobin in solution before and after adsorption on the bioactive glass without GA and with GA, with the resulting dipolar evolution function (V(t), upper left inset), the form factor (F(t), upper right inset) as well as the assumed Gaussian distance distribution P(r).

DEER measurements showed that the polymerization of the protein occurs when it is attached to the BG treated with GA. It remains questionable whether the secondary structure of the protein changes in this situation. In this purpose, FTIR measurements were performed on the BG treated with GA, in order to obtain information about the changes in secondary structure of methemoglobin after adsorption. FTIR spectra recorded before and after protein adsorption are shown in figure 4. In order to monitor the protein adsorption over time, we compared FTIR spectra recorded for BG immersed in protein solution for different periods of time: 10 min, 20 min, 30 min and 2 hours respectively. The amide I intensity increases with time immersion, and consequently with the amount of the protein attached on the BG, proving that the intensity of amide I band can be taken as a measure of the quantity of adsorbed protein (figure 4).
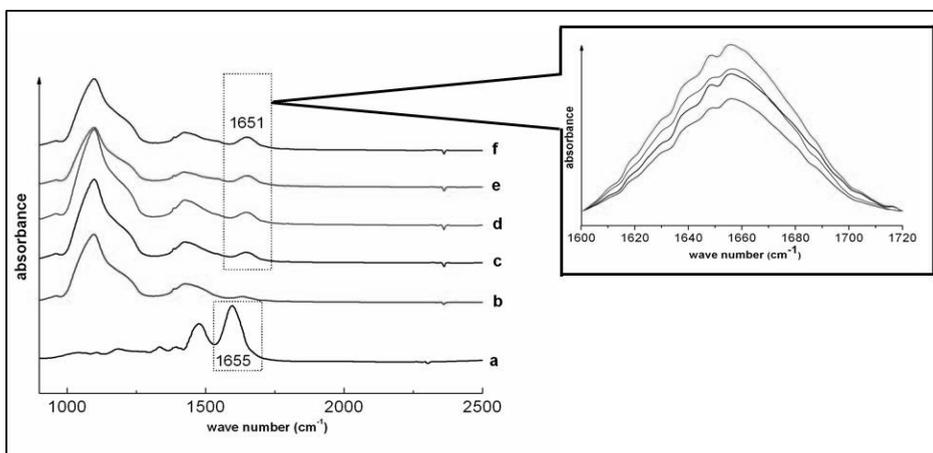
Figure 4. FTIR spectra (region 750-2000 cm^{-1}) of BG treated with GA (b), horse methemoglobin before (a) and after adsorption on BG with GA, after 10 min (c), 20 min (d), 30 min (e) and 2h (f) of immersion in protein solution. The amide I area is highlighted by the dashed line. The area enlarged in the upper right: separation of the amide I band of methemoglobin in adsorbed state, after the removal of corresponding band of the BG.

The FTIR signal characteristic to amide I functional group was located at 1655 cm^{-1} for lyophilized horse hemoglobin and 1651 cm^{-1} in case of the protein attached to the BG. The resulting component bands of amide I were assigned to different elements of the secondary structure, depending on their frequency. A Gaussian curve fitting procedure was applied to estimate quantitatively the area of each component representing a type of secondary structure. Peak locations were determined from the second derivative of the amide I band. In case of the protein in the adsorbed state, the BG signal was

prior subtracted, to eliminate the BG contribution in the amide I region. The results of the curve-fitting spectrum of amide I band are shown in figure 5 and the contribution of each element of the secondary structure is shown in figure 6. Hemoglobin is a α-helical protein and contains no β-structure [35]. The small peaks at ca. 1627 and 1638 cm^{-1} can therefore be assigned to β-turns (it can be associated with the short, extended chains connecting the helical cylinders) [36]. The pronounced peak between 1656-1658 cm^{-1} can be assigned to α-helices. The peak which appears around 1615 cm-1 is not related to the secondary structure and probably caused by other side-chain residues (it can be associated with tyrosine residues) [36]. The prediction of α-helix contribution determined from the amide I region is similar to other studies [37, 38]. The helix content of horse methemoglobin adsorbed on the BG treated with GA was found to be aprox. 4% lower than in the native protein, while the content of turns and random coil increased with 2% each.

a   b
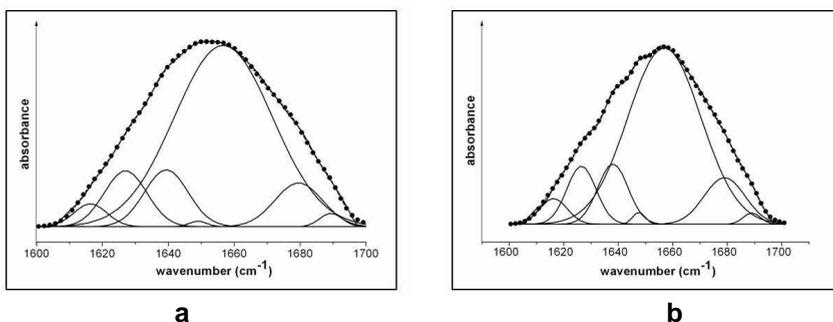
Figure 5. Separation of the amide I band into its components for the protein before **(a)** and after (**b**) adsorption on the BG treated with GA. The line with circle symbols represents the sum of the separated band components.
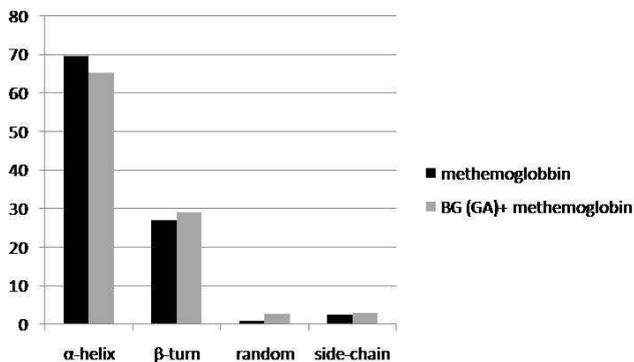
Figure 6. Relative percentage of secondary structure elements determined from amide I deconvolution for horse methemoglobin in native state (black) and after adsorption (gray) on BG with GA.

CONCLUSIONS

In this work EPR and FTIR measurements were carried out to study the adsorption of methemoglobin on bioactive glass system. Cw-EPR measurements confirmed that the protein immobilization is increasing in the adsorbed state while from DEER measurements we could conclude that a small fraction of protein dissociates after adsorption and GA induces polymerization of methemoglobin. FTIR experiments have shown that only small changes occur in the secondary structure of the protein in upon adsorption.

EXPERIMENTAL SECTION

Bioactive glass preparation

The bioactive glass was prepared via sol-gel method with the following composition (in weight %): 45% SiO_2, 24.5% Na_2O, 24.5% CaO and 6% P_2O_5. After preparation, the BG was milled and the obtained powder had particles with size between 500 nm and 1.5 µm. Further on, the BG powder was surface functionalized by following the protocol presented in other studies [7,8,24,25]. First, the powder was immersed for 4 hours into an aqueous APTS solution (0.45mol/L, pH adjusted to 8 by adding 1M HCl) at 80ºC. After 4h the sample was collected, washed in deionised water, then immersed for 1h in GA solution (1mol/L) at room temperature and finally washed again in deionised water.

Spin labeling

Oxyhemoglobin was extracted from fresh horse blood samples according to Benesch et al. [26], and then converted to methemoglobin by addition of a 2-fold amount of $K_3Fe(CN)_6$ [27]. Spin labeling of the methemoglobin with (4-(2-Iodoacetamido)-2,2,6,6-tetramethyl-1-piperidinyloxy) (JAA6) followed the procedure of McCalley et al. [28].

Protein adsorption

Powder samples were incubated at 37°C for 10 min, 2 0 min, 30 min and 2 hours respectively, in a solution of 150 mg/ml (2.32 mM) methemoglobin in phosphate buffer (0.01M, pH 8.0) with 500mM NaCl concentration. This protein concentration was chosen because it is in the range of the concentration of hemoglobin in horse blood (between 150-200 mg/ml). After the immersion the samples were washed three times with the buffer solution. For the FTIR measurements the samples were lyophilized for 48 hours in an Alpha 1-2 LD type freeze dryer at 217K and 0.05mbar.

FTIR spectroscopy

FTIR spectroscopic analyses were performed in reflection configuration by a Jasco IRT-5000 FT-IR microscope in the range 4000-650 cm^{-1} with a

resolution of 4 cm^{-1}. In order to subtract the background signal of the BG in the amide I region, the weight of the sample was the same for the spectra recorded on samples containing BG (0.73mg).

EPR SDSL spectroscopy

For the X-band continuous wave (cw) EPR measurements sample volumes of 15 µl (BG + protein) were filled into EPR glass capillaries with 0.9 mm inner diameter (the active volume of the sample tube is 10 µl). The cw-EPR experiments were performed using a home-made EPR spectrometer equipped with a Bruker dielectric resonator. The microwave power was set to 1.0 mW, the B-field modulation amplitude was 0.15 mT.

Pulse EPR measurements were accomplished at 50 K, in X-band frequencies (9.3-9.4 GHz) with a Bruker Elexsys 580 spectrometer equipped with a Bruker Flexline split-ring resonator ER 4118XMS3 and a continuous flow helium cryostat (ESR900, Oxford Instruments) controlled by an Oxford Intelligent temperature controller ITC 503S. Prior to freezing the protein in 3mm inner diameter EPR tubes, the samples had about 10% (by volume) glycerol. The measurements were performed using the four-pulse DEER sequence [29]:

$$\pi/2\,(\vartheta_{obs}) - \tau_1 - \pi(\vartheta_{obs}) - t' - \pi(\vartheta_{pump}) - (t_1 + t_2 - t') - \pi(\vartheta_{obs})$$
$$- \tau_2 - echo$$

All measurements were performed at a temperature of 50 K with observer pulse lengths of 16 ns for $\pi/2$ and 32 ns for π pulses and a pump pulse length of 12 ns. Data points were collected in 8-ns time steps. The total measurement time for each sample was 4–24 h. Analysis of the data was performed with DeerAnalysis2009 [30].

ACKNOWLEDGMENTS

REFERENCES

1. C.C. Berry, S. Adams, G. Curtis, *Journal of Physics D Applied Physics,* **2003**, *36*, 198.
2. C.T. Shibata, A.M. Lenhoff, *Journal of Colloid and Interface Science,* **1992**, *148*, 469.
3. C.T. Shibata, A.M. Lenhoff, *Journal of Colloid and Interface Science,* **1992**, *148*, 485.
4. J. Hermans, H. Scheraga, *Journal of the American Chernical Society*, **1961**, *83*, 3283.
5. M. Heule, K. Rezwan, L. Cavalli, L.J. Gauckler, *Advanced Materials*, **2003**, *15*, 1191.
6. H.H. Weetall, "Covalent Coupling Methods for Inorganic Support Materials Methods in Enzymology", Methods in Enzymology Vol. 44, *Academic Press,* New York, *1976*.
7. Q.Z. Chen, K. Rezwan, V. Françon, D. Armitage, S.N. Nazhat, F.H. Jones, A.R. Boccaccini, *Acta Biomaterialia,* **2007**, *3*, 551.
8. R.A. Williams, H.W. Blanch, *Biosensors and Bioelectronics*, **1994**, *9*, 159.
9. R.W. Sarver Jr., W.C. Krueger, *Analytical Biochemistry*, **1991**, *194*, 89.
10. A. Dong, P. Huang, W.S. Caughey, *Biochemistry*, **1990**, *29*, 3303.
11. A. Dong, W.S. Caughey, T.W. Du Clos, The *Journal of Biological Chemistry*, **1994**, *269*, 6424.
12. R.W. Sarver Jr., W.C. Krueger, *Analytical Biochemistry,* **1993**, *212,* 519.
13. J. Buijs, W. Norde, J.W.Th. Lichtenbelt, *Langmuir*, **1996**, *12,* 1603.
14. S.S. Cheng, K.K. Chittur, C.N. Sukenik, L..A Culp, K. Lewandowska, *Journal of Colloid and Interface Science*, **1994**, *162,* 135.
15. L.A. Buchanan, A. El-Ghannam, *Journal of Biomedical Materials Research Part A*, **2009**, *93A*, 537.
16. C.E. Giacomelli, M.G.E.G. Bremer, W. Norde, *Journal of Colloid and Interface Science*, **1999**, *220,* 13.
17. B. Stuart, "Biological Applications of Infrared Spectroscopy", John Wiley & Sons, Chichester, **1997**.
18. K. Jacobsen, S. Oga, W.L. Hubbell, T. Risse, *Biophysical Journal*, **2005**, *88,* 4351.
19. T. Risse, W.L. Hubbell, J.M. Isas, H.T. Haigler, *Physical Review Letters*, **2003**, *91,*188101.
20. K. Jacobsen, W.L. Hubbell, O.P. Ernst, T. Risse, *Angewandte Chemie International Edition*, **2006**, *45,* 3874.
21. E. Bordignon, H.J. Steinhoff, "Membrane protein structure and dynamics studied by side-directed spin labeling ESR", *ESR Spectroscopy in Membrane Biophysics, Springer Science and Business Media, New York,* **2007**.
22. J.P. Klare, H.J. Steinhoff, *Photosynthesis Research*, **2009**, *102,* 377.
23. J.P. Klare, H.J. Steinhoff, "Site-directed Spin Labeling and Pulsed Dipolar Electron Paramagnetic Resonance", Encyclopedia of Analytical Chemistry, Chichester, **2010**.

24. Q.Z. Chen, K. Rezwan, D. Armitage, S.N. Nazhat, A.R. Boccaccini, *Journal of Materials Science: Materials in Medicine*, **2006**, *17,* 979.
25. A. Nanci, J.D. Wuest, L. Peru, P. Brunet, V. Sharma, S. Zalzal, M.D. McKee, *Journal of Biomedical Materials Research*, **1998**, *40,* 324.
26. R.E. Benesch, R. Benesch, R.D. Renthal, N. Maeda, *Biochemistry*, **1972**, *11*, 3576.
27. H.J. Steinhoff, K. Lieutenant, A. Redhardt, *Biochimica et Biophysica Acta*, **1989**, *996,* 49.
28. R.C. McCalley, E.J. Shimshick, H.M.McConell, *Chemical Physics Letters*, **1972**, *13,* 115.
29. M. Pannier, S. Veit, A. Godt, G. Jeschke, H.W. Spiess, *Jornal of Magnetic Resonance*, **2000**, *142,* 331.
30. G. Jeschke, V. Chechik, P. Ionita, A. Godt, H. Zimmermann, J. Banham, C.R. Timmel, D. Hilger, H. Jung, *Applied Magnetic Resonance*, **2006**, *30,* 473.
31. Moffat JK, *Jornal of Molecular Biology*, **1971**, *55,* 135.
32. C. Gruian, H.J. Steinhoff, S. Simon, *Digest Journal of Nanomaterials and Biostructures,* **2011**, *6,* 373.
33. D.E. Budil, S. Lee, S. Saxena, J.H. Freed, *Journal of Magnetic Resonance Series A,* **1996**, *120,* 155.
34. J. McGuire, V. Krisdhasima, M.V. Wahlgren, T. Arnebrant, "Proteins at interfaces II, Vol. 602", American Chemical Society, Washington, **1995**.
35. **M. Levitt, J. Greer**, *Journal of Molecular Biology*, **1977**, *114,* 181.
36. H. Susi, D.M. Byler, *Biochemical and Biophysical Research Communications,* **1983**, *115,* 391.
37. S. Cai, B.R. Singh, *Biochemistry*, **2004**, *43,* 2541.
38. S. Luo, C-Y.F. Huang, J.F. McClelland, D.J. Graves, *Analytical Biochemistry*, **1994**, *216,* 67.

CYCLODEXTRINS AND SMALL UNILAMELLAR LIPOSOMES: A COMPARATIVE THEORETICAL APPROACH

CORINA COSTESCU[a], LAURA CORPAŞ[a], NICOLETA GABRIELA HĂDĂRUGĂ[a*], DANIEL IOAN HĂDĂRUGĂ[b], ZENO GÂRBAN[a]

ABSTRACT. Cyclodextrins and liposomes are generally used for protecting and controlled release of bioactive compounds. This is the first attempt to compare the cavity characteristics of cyclodextrins and small unilamellar liposomes by using molecular modeling techniques. The volume of the liposome cavity was 524 $Å^3$. In the case of β-cyclodextrin this cavity volume was only 87 $Å^3$, but with a slightly higher molecular volume (878 $Å^3$). As a conclusion, the smaller unilamellar liposome (theoretically modeled) could encapsulate bioactive compounds 5-6 fold bigger than β-cyclodextrin, while bioactive compound/cyclodextrin/liposome systems could be also obtained.

Keywords: liposome, β-cyclodextrin, molecular modeling

INTRODUCTION

Enhancing active compounds bioavailability is a permanent goal of the scientific community. Micro- and nanoencapsulation of biologically active compounds in various matrices is one of the most used techniques for this process [1,2]. Liposomes are widely used for micro- and nano-encapsulation of bioactive compounds, being empty micro- or nanospheres resulted by assembling of phospholipidic compounds in aqueous phases [3-6]; the liposome walls are formed by two or more double lipidic layers containing aqueous phase inside. Many liposome types are known such as multilamellar and unilamellar liposomes. Liposomes are obtained especially by inverse phase evaporation (large unilamellar liposomes) or ultrasonication (small unilamellar liposomes) [7]. The stability of liposomes can be enhanced by using various additives (polymers, cholesterol etc.) [3,8]. They are used especially in pharmaceutical, cosmetic, and food fields [3,4,9-13].

[a] *Banat's University of Agricultural Sciences and Veterinary Medicine, Faculty of Food Processing Technology, Department of Chemical Engineering, Calea Aradului 119, RO-300645 Timişoara, Romania, nico_hadaruga@yahoo.com*
[b] *"Politehnica" University of Timişoara, Faculty of Industrial Chemistry and Environmental Engineering, Department of Applied Chemistry and Organic-Natural Compounds Engineering, Victory Sq. 2, RO-300006 Timişoara, Romania, daniel.hadaruga@chim.upt.ro*

Other matrices used for encapsulation are cyclodextrins (the most used natural ones are α-, β-, and γ-cyclodextrin which are cyclic oligosaccharides with 6-8 glucopyranose moieties, having hydrophobic inner cavity and outer hydrosolubilizing hydroxyl groups)[14-17]. The encapsulation process is determined by the geometry and hydrophobicity of the bioactive molecule. As a result, cyclodextrins can encapsulate only small or thin molecules [15], while liposomes can encapsulate also bigger molecules by various processes such as by inserting in the lipidic bilayer, adsorption on the membrane surface or physical encapsulation in the (usually) aqueous inner cavity [3,18,19]. Generally, cyclodextrins encapsulate hydrophobic molecules, while liposomes can encapsulate even hydrophobic or less hydrophobic molecules. In both cases, the advantages of new formulations are obvious: enhancing the bioactive compound transportation in biological environments (by hydrosolubilization of hydrophobic compounds with cyclodextrins, or by physical transportation by liposome micelles), protection against degradation factors (oxygen/air, light, and other chemical or biochemical reagents from the environment), and controlled release.

Molecular modeling of biologically active compounds or even supramolecular assemblies could be very useful for evaluation of various expected properties such as bioactivity, reactivity, hydrophobicity, solubility, docking properties [20-24]. The molecular modeling of singular compounds is easier to perform, in comparison with molecular assemblies such as liposomes. The present study is the first attempt to compare the cavity characteristics of β-cyclodextrin (bCD) and small unilamellar liposomes by using molecular modeling techniques.

RESULTS AND DISCUSSION

Molecular modeling and conformational analysis of distearoyl-phosphatidylcholine (PC) structure revealed that the most stable conformation in vacuum has a helicoidal conformation for both hydrophobic moieties, but the best interaction between two opposite PCs appear in the case of pseudolinear conformations of these moieties (Figure 1a). In the last case, choline moieties are disposed outside and will forms the inner and outer hydrophilic micelle sides, while the fatty acid moieties will forms the hydrophobic micelle wall. The interaction energy for this unit is 27 kcal/mole (computed as difference between energies of unitary PCs and 2×PC unit).

Small energetically stable unilamellar liposome can be built and optimized by using these PC units. Micelle moieties consisting of 4, 2×2, 4×2, 4×4, 16×4, and 24×4 PCs were built in order to obtain an energetically stable unilamellar micelle (maximum of 96 PCs) (Figure 1b). The interaction energy increased with the number of PCs, the dependence being linear

(Figure 2). This demonstrates that the liposome stability is enhanced by increasing the PCs (in the studied range).

(a)   (b)
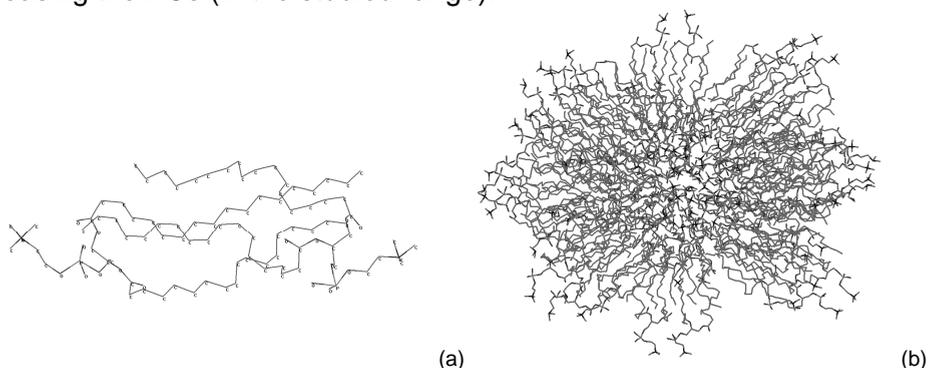
Figure 1. The most stable assemblies of the liposome PC unit, 2×PC (a) and the optimized smaller unilamellar liposome consists of 96 PC units (b)

$$E \text{ (kcal/mole)} = 59.88 * N \text{ (PC)} - 139.7$$
$$R^2 = 0.991$$
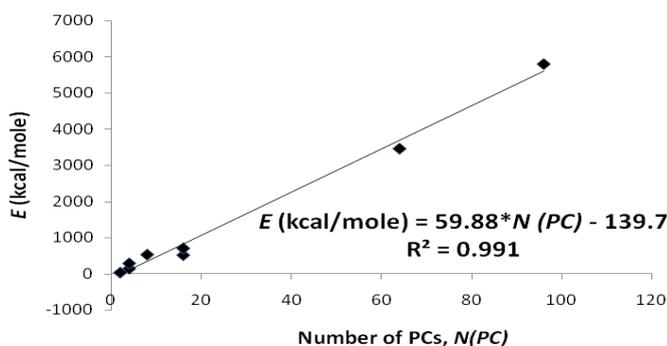
Figure 2. Variation of the interaction energy, E *(kcal/mole)*, in the micellar moieties with the number of PCs, N *(PC)*

The smaller unilamellar liposome which could be built has a pseudospherical cavity with an approximate volume of 524 Å^3; this volume was calculated considering the mean diameter of the closer opposite hydrogen envelopes of the choline moieties (see Experimental section).

In the case of β-cyclodextrin, the minimum energy conformation looks like a "pseudotruncated cone", with the primary (from C6 positions) and secondary (from C2 and C3 positions) hydroxyl groups oriented to the outside of the molecule, while the tetrahydropyrane moieties corresponding to the glucopyranose units were oriented to the interior. The external hydroxyl groups confer water solubility, while the cavity has hydrophobic properties. The geometric characteristics of the most stable conformation of bCD could be evaluated by knowing the Cartesian coordinates of all atoms (including hydrogen atoms). Thus, the mean external diameters of the primary

and secondary faces have approximate values of 12.9 Å and 17.5-18.3 Å, respectively. The mean interior diameters are relatively close for both faces (5.5 Å). The bCD stable conformation was evaluated in vacuum as well as in water periodic box and the main bCD characteristics could be determined (*i.e.* the torsion angles between the C_2-C_1-O_e-C_4' of alternative glucoside moieties of -140º and -122º in vacuum). The interior volume of bCD can be calculated by using the Cartesian coordinates of atoms for the most stable conformation (see Experimental section). The approximate volume of bCD cavity is only 87 $Å^3$, six times lower than the unilamellar liposome.

CONCLUSIONS

The following conclusion can be drawn from studies among molecular modeling of β-cyclodextrin structure and the smaller unilamellar liposome which can be builded by using distearoyl-phosphatidylcholine as unit: (1) the smaller unilamellar liposome has a volume of the cavity of 524 $Å^3$, little bit lower than the β-cyclodextrin molecular volume (878 $Å^3$); the interior volume of β-cyclodextrin is 5-6 fold lower than the liposome cavity (87 $Å^3$). As a result, a small unilamellar liposome can encapsulate bigger molecules than β-cyclodextrin; moreover, the flexibility of liposome is higher than in the case of β-cyclodextrin and facilitates the encapsulation process; (2) the liposome micelle has a hydrophilic cavity and can better interact with the β-cyclodextrin exterior; further, β-cyclodextrin can encapsulate hydrophobic small molecules and it is possible to obtain hydrophobic bioactive compounds / β-cyclodextrin / liposome systems with enhanced bioavailability.

EXPERIMENTAL SECTION

Molecular modeling and conformational analysis. Molecular modeling of biocompatible matrices (liposomes – phosphatidylcholine, PC, and β-cyclodextrin, bCD) was performed by using HyperChem 5.1 package (MM+ molecular mechanics program), with a RMS gradient of 0.005 kcal/mole and a Polak-Ribiere conjugate gradient algorithm. Phosphatidylcholine structure has a great number of flexible bonds which must be considered for identifying the most stable conformations, while bCD have only seven flexible bonds, corresponding to hydroxymethyl moieties. The following aspects must be considered in order to obtain the most stable conformations by using Conformational Search program from the HyperChem package: variation of the flexible torsion angles of ±60º ÷ ±180º, criterion of energy acceptance of 4 kcal/mole above best, all conformations which have distances between equivalent atoms lower than 0.5 Å and differences between torsion angles lower than 15º were neglected.

Structural descriptors. The capacity of encapsulation of the most stable small unilamellar liposome and bCD was evaluated by means of

cavity volume. This volume was calculated by knowing the Cartesian coordinates of all atoms from the most stable conformations; thus, the interior cavity of bCD was approximated with a cylinder having the diameter (d_{mean}) evaluated as the mean of interior distances between opposite hydrogen atoms, considering also the radius of these atoms (1.20 Å, according to Bondi [25]), and the cylinder length ($L_{cylinder}$) was that corresponding to the cyclodextrin height, including atoms radius (Figure 3a). The same algorithm was used in the case of small unilamellar liposome, but the cavity was approximated with a sphere (considering the mean diameter as the distance between the opposite hydrogen atoms envelope of the choline moieties, d_{mean}, Figure 3b).

(a)   (b)
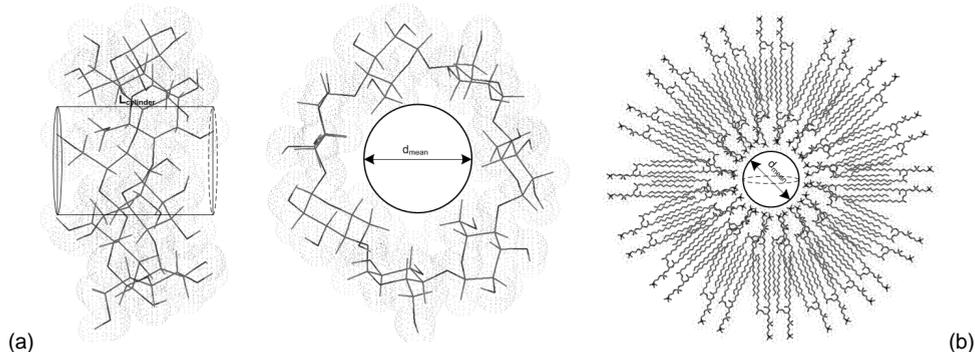
Figure 3. Calculation of the cavity volume for β-cyclodextrin (a)
and smaller unilamellar liposome (b)

ACKNOWLEDGMENTS

REFERENCES

1. Z. Fang, B. Bhandari, *Trends in Food Science & Technology*, **2010**, *21*, 510.
2. M. Gonnet, L. Lethuaut, F. Boury, *Journal of Controlled Release*, **2010**, *146*, 276.
3. A. S. L. Derycke, P. A. M. de Witte, *Advanced Drug Delivery Reviews*, **2004**, *56*, 17.
4. S. Ebrahim, G. A. Peyman, P. J. Lee, *Survey of Ophthalmology*, **2005**, *50*, 167.
5. K. A. Edwards, A. J. Baeumner, *Talanta*, **2006**, *68*, 1421.

6. J. Xi, R. Guo, *International Journal of Biological Macromolecules*, **2007**, *40*, 305.

7. F. Maestrelli, M. L. Gonzalez Rodriguez, A. M. Rabasco, P. Mura, *International Journal of Pharmaceutics*, **2006**, *312*, 53.

8. F. Bordi, C. Cametti, S. Sennato, *Colloids and Surfaces A: Physicochemical Engineering Aspects*, **2007**, *306*, 102.

9. H. J. Lim, E. C. Cho, J. Shim, D.-H. Kim, E. J. An, J. Kim, *Journal of Colloid and Interface Science*, **2008**, *320*, 460.

10. M. S. El Samaligy, N. N. Afifi, E. A. Mahmoud, *International Journal of Pharmaceutics*, **2006**, *319*, 121.

11. D. I. Hădărugă, N. G. Hădărugă, C. Lazău, C. Raţiu, C. Crăciun, I. Grozescu, *Digest Journal of Nanomaterials and Biostructures*, **2010**, *5*, 919.

12. D. I. Hădărugă, N. G. Hădărugă, C. Lazău, C. Crăciun, I. Grozescu, *Journal of Agroalimentary Processes and Technologies*, **2010**, *16*, 62.

13. N. G. Hădărugă, D. I. Hădărugă, P. Vlăzan, L. Barbu-Tudoran, *Journal of Agroalimentary Processes and Technologies* **2011**, *17*, 1.

14. R. Challa, A. Ahuja, J. Ali, R. K. Khar, *AAPS PharmSciTech*, **2005**, *6*, E329.

15. M. E. Brewster, T. Loftsson, *Advanced Drug Delivery Reviews*, **2007**, *59*, 645.

16. L. M. Hamilton, C. T. Kelly, W. M. Fogarty, *Enzyme and Microbial Technology*, **2000**, *26*, 561.

17. K. I. Popov, A. N. Filippov, S. A. Khurshudyan, *Russian Journal of General Chemistry*, **2010**, *80*, 630.

18. D. I. Hădărugă, N. G. Hădărugă, G. Merkh, H.-D. Isengard, *Journal of Agroalimentary Processes and Technologies*, **2010**, *16*, 230.

19. D. I. Hădărugă, N. G. Hădărugă, G. N. Bandur, H.-D. Isengard, *Food Chemistry*, **2011**, *in press*, doi: 10.1016/j.foodchem.2011.06.004.

20. S. Chaudhuri, S. Chakraborty, P. K. Sengupta, *Journal of Molecular Structure*, **2010**, *975*, 160.

21. E. Estrada, I. Perdomo López, J. J. Torres Labandeira, *Journal of Organic Chemistry*, **2000**, *65*, 8510.

22. D. I. Hădărugă, D. Balş, N. G. Hădărugă, *Chemical Bulletin of the "Politehnica" University (Timisoara)*, **2009**, *54*, 108.

23. A. A. Obaidat, R. A. Khanfar, M. N. Khawam, *Journal of Inclusion Phenomena and Macrocyclic Chemistry*, **2009**, *63*, 273.

24. Y. Zheng, A. H. L. Chow, I. S. Haworth, *Letters in Drug Design & Discovery*, **2008**, *5*, 512.

25. A. Bondi, *Journal of Physical Chemistry*, **1964**, *68*, 441.

PROTEIN ADHESION TO BIOACTIVE MICROSPHERES INVESTIGATED BY FLUORESCENCE SPECTROSCOPY

EMOKE LASZLOFFI[a], ADRIANA VULPOI[a], VIORICA SIMON[a]

ABSTRACT. This study is focussed on protein functionalization of spray dried samples of $CaO-SiO_2-P_2O_5$ bioactive glass system calcinated at different temperatures. The protein functionalization of the samples surface was achieved in simulated body fluid enriched with bovine serum albumin. Fluorescence quenching of bovine serum albumin is used for a first evaluation of protein adhesion to bioactive glass samples. Differential thermal analysis was used to determine the heat treatment temperatures. Structural changes induced in the silicate network by calcination were evidenced by X-ray diffraction. The results show that the scaled intensity of tryptophan fluorescence signal recorded from protein solution after glass samples incubation depends on samples heat treatment temperature.

Keywords: bioactive glass; surface functionalization; tryptophan fluorescence.

INTRODUCTION

Bioactive glasses and glass-ceramics of $SiO_2-CaO-P_2O_5$ system are intensely studied because of their surface chemical reactivity in contact with body fluids, and also for their osteogenetic potential and applications in tissue engineering [1–3]. In physiological fluids, an interface layer is self assembled as a result of the interface ion-exchange mechanism known as bioactivity [4]. For *in vitro* study of bioactive glasses and glass–ceramics, Kokubo et al. [5] proposed a simulated body fluid (SBF) with ionic concentration almost equal to that of human blood plasma. *In vitro* tests in SBF are widely used as preliminary tests on new materials showing bioactive properties.

When biomaterials surfaces are in contact with biological media, such as blood or serum, they are immediately coated by protein and their adsorption on to the surface has a fundamental roll in the field of biomaterials [6]. With regard to biomaterials considered for scaffolds in tissue engineering,

---

[a] *Babeş-Bolyai University, Faculty of Physics & Institute for Interdisciplinary Research on Bio-Nano-Sciences, Cluj-Napoca, Romania, Kogălniceanu Str. 1, RO-400084 Cluj-Napoca, Romania, viosimon@phys.ubbcluj.ro*

their most important role is to serve as support material for cells attachment and further grows and proliferation, but the cells do not attach directly to the culture substrate, they rather bind to proteins that are adsorbed to the surface of the scaffold [7, 8]. Bovine serum albumin is a protein commonly used for research purposes due to its stability, water solubility and versatile binding capacity [9].

The aim of this work was to synthesize a SiO_2-CaO-P_2O_5 system by spray drying method and to study the protein functionalization of the samples heat treated at different temperatures.

RESULTS AND DISCUSSION

The SEM images of the as prepared samples (Figure 1) show that the microspheres obtained by spray drying are still unseparated, they occur in aggregates, and there is a wide range of size distribution, from nanometers to micrometers. In this stage, the microspheres still contain traces of solvents. The thermal analysis (Figure 2) points out around 99°C an endothermic peak that is attributed to the loss of residual water and ethanol. The two endothermic peaks observed in the range 240-390 °C are associated with loss of alkoxy groups. The weight loss of 4.63 %, recorded around of 535°C, is associated with loss of hydroxyl groups [10]. According to these results, the as prepared samples were heat treated at 110^oC, 400^oC and 800^oC. It was considered the removal of water and ethanol after 110^oC treatment, the elimination of alkoxy groups after 400^oC treatment, and after 800^oC treatment the sample was expected to be completely free of other components than SiO_2, CaO and P_2O_5 oxides.
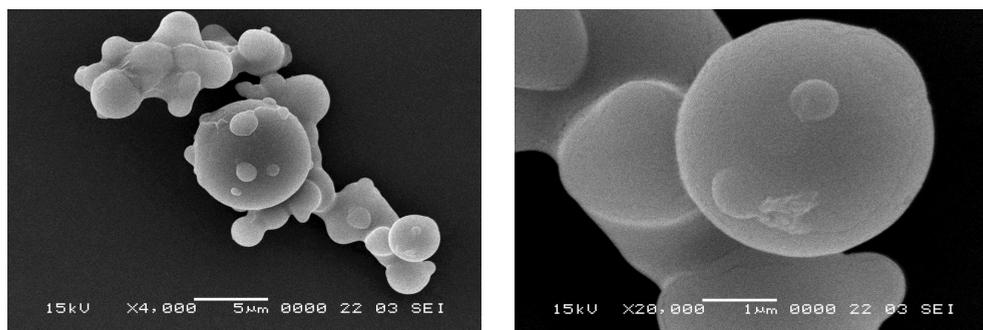
Figure 1. SEM images of the spray dried sample
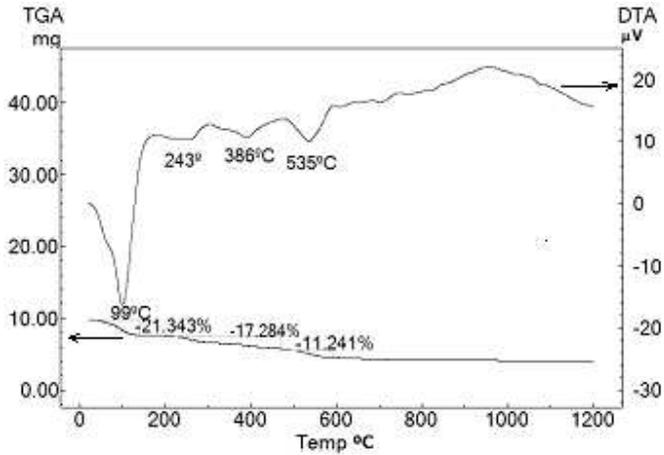
Figure 2. Differential thermal analysis (DTA) and thermal gravimetric analysis (TGA) runs of the spray dried sample.

X-ray diffraction patterns (Figure 3) of the thermal treated S_{110} sample show narrow lines of a crystalline phase identified as ammonium hydrogen phosphate, i.e. $(NH_4)_2HPO_4$ used as P_2O_5 precursor. With increasing the treatment temperature, the crystalline phase disappears, as observed in the diffraction pattern of samples S_{400} and S_{800}. No new crystalline phase is developed even after 800°C treatment. The X-ray diffraction pattern of S_{800} do not evidence any narrow line of crystalline phases, it consist of a broad line typical to amorphous systems.
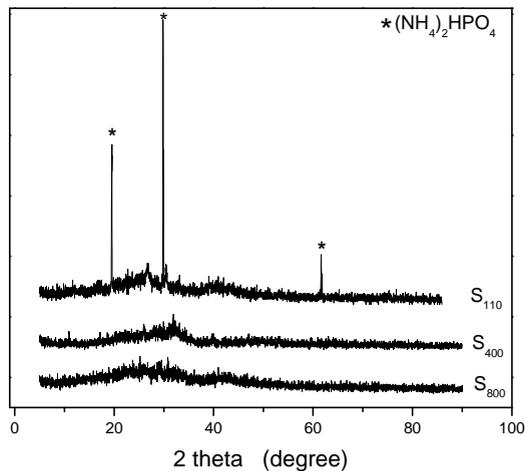
Figure 3. X-ray diffraction patterns of the thermal treated samples

Protein adsorption studies were made in the purpose to determine the interaction of the calcium-phospho-silicate system treated at different temperatures with the bovine serum albumin (BSA) protein. The protein concentration in BSA/SBF solution was 30 mg/ml. In the human blood the serum albumin concentrations are between 35 and 45 mg/ml [11-13], while in the interstitial fluid (tissue fluid) the concentration of albumin is much lower than in the blood [14, 15].

The fluorescence quenching of BSA in the incubated BSA/SBF solution was considered a measure of protein interaction with the glass microspheres [16]. The fluorescence is given by the tryptophan amino acid (which has much stronger fluorescence and higher quantum yield than the other two aromatic amino acids, tyrosine and phenylalanine), from the BSA [17]. This is an indirect method of determining the protein attachment to the sample surface, as the sample itself is not analyzed, but rather the liquid medium wherein the sample was incubated.

Quenching of fluorescence is a decrease in the fluorescence intensity and can occur due to non-molecular, intramolecular or intermolecular mechanisms. Non-molecular quenching can be due to attenuation of the incident light by the fluorophore itself or by other absorbing species; intramolecular quenching can occur if a quencher group interacts with the tryptophan aminoacid residue within a distance around 6-10Å; the intermolecular quenching processes can be either dynamic and/or static and require molecular contact between the fluorophore and quencher [18]. For this reason, quenching studies can be used to reveal accessibility of fluorophores to quenchers.

The samples were periodically measured in the first day, immediately after mixing (0 hour), after 2 hours respectively 4 hours immersion time. For the next six days the measurements were carried out once a day. The first 24 hours data (Figure 4) indicate a decrease in the fluorescence intensity given by the protein from the solution, which is supposed to happen because of protein adsorption on the samples surface. Protein adsorption onto the surface of the bioglass microspheres is further expected to mediate cell adhesion and tissue integration. Sample S_{110} takes up the highest quantity of protein compared to S_{400} and S_{800} samples. This fact is further remarked in the measurements carried out in steps of 24 hours for seven days.
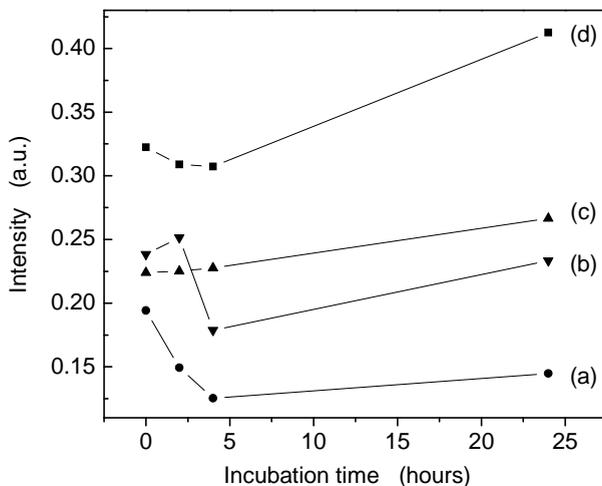
Figure 4. Time dependence of BSA fluorescence intensity during the first 24 hours in (a) SBF/BSA solution with S 110°C; (b) SBF/BSA solution with S 400°C; (c) SBF/BSA solution with S 800°C, and (d) SBF/BSA reference solution.

In the first four days, for the sample treated at 400 ^{o}C the fluorescence signal directly related to the protein is almost at the same intensity level, but after five days, the intensity of the signal increases, suggesting the detachment of the protein from the sample surface, followed in the next two days by protein reattachment (Figure 5). A similar behavior is observed for the sample treated at 800 ^{o}C up to the fifth day, when the intensity of the tryptophan signal from BSA and sinks to a lower value denoting a depletion of protein molecules in solution due to their adhesion to the sample surface. The protein surface usually exhibits one or a few charged spots and therefore the protein adsorption on a substrate may be energetically favourable due to the protein-substrate electrostatic interaction. In some cases [19] it was shown that with increasing protein coverage, the protein desorption increases and there is critical fraction of the area covered by protein, and adsorption above this fraction is hindered both kinetically and thermodynamically. Beside the substrate charge dependence, the protein adsorption/desorption depends on protein size and shape, concentration, hydratation, substrate microstructure, hydrophobic behavior, solution pH, ionic strength, temperature, competitive adsorption with other proteins and ions, as well as the solvent motion relative to the substrate [20]. It is interesting to note that the fluorescence intensity of SBF/BSA reference solution and SBF/BSA solution with S 800°C is increased after 24 hours. A similar effect was reported by Dai et al. [21], but the reason for this is unclear and requires further elucidation.
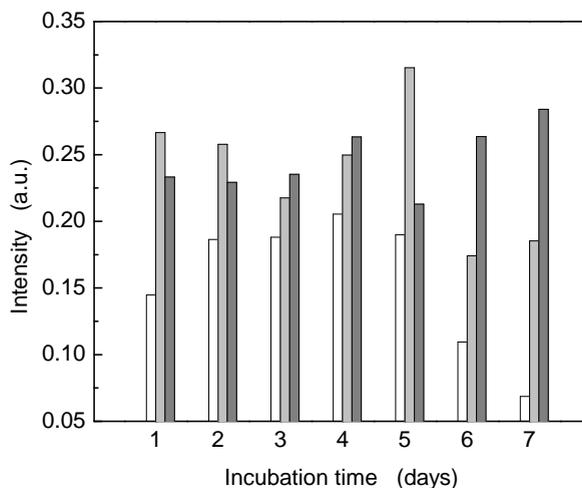
Figure 5. Time dependence of BSA fluorescence intensity during the first 24 hours in SBF/BSA solution with S 110°C (white columns), SBF/BSA solution with S 400°C (light gray columns), and SBF/BSA solution with S 800°C (dark gray columns).

The results may be correlated both with the presence of the residual crystalline phosphate phase on S_{110} microspheres and residual hydroxyl groups on S_{110} and S_{400} microspheres.

CONCLUSIONS

The fluorescence quenching of BSA in BSA/SBF solutions after incubation of spray dried SiO_2-CaO-P_2O_5 glass microspheres heat-treated at 110 °C, 400°C and 800 °C was used in order to investigate the protein attachment on these samples. The results obtained for several incubation times, up to seven days, show that the highest quantity of protein adheres on S_{110} sample. Different from S_{400} and S_{800}, the S_{110} sample contains a residual crystalline phosphate phase and a higher amount of residual hydroxyl groups. The heat treatment applied at 800 °C completely removed the hydroxyl groups from S_{800} sample which after the long term incubation attached less protein.

EXPERIMENTAL SECTION

The composition of the bioactive glass was $56SiO_2 \cdot 40CaO \cdot 4P_2O_5$ (mol %). The samples were prepared by spray drying method. The reason of using spray drying method instead of conventional sol-gel method was that the final product consists of microspheres with smooth surface, without edges or acicular shape. The reagents used were tetraethoxysilan $SiC_8H_{20}O_4$ (TEOS) - precursor for SiO_2, calcium nitrate tetrahydrate

$Ca(NO_3)_2 \cdot 4(H_2O)$ - precursor for CaO, and ammonium dibasic phosphate $(NH_4)_2HPO_4$ - precursor for P_2O_5 The mole ratio of the reactants $SiC_8H_{20}O_4$:$Ca(NO_3)_2 \cdot 4(H_2O)$:$(NH_4)_2HPO_4$ was 7:5:1. The calculated amount of tetraethoxysilan was mixed with the same amount of ethanol on a magnetic stirrer, and the other precursors were dissolved at room temperature in distillated water at saturation point. The compounds were mixed together at room temperature. The mixture was dried using Mini Spray Dryer B-290. Parts of the spray dried microspheres were separately treated at 110 ℃, 400 ℃ and 800 ℃ (noted S $_{110}$, S_{400} and S_{800}).

Protein adsorption on the surface of samples was analyzed in vitro. The SBF was prepared according to Kokubo protocol [5]. The ratio of S_{110}, S_{400} and S_{800} glass microspheres **:** BSA **:** SBF was 0.5 g **:** 0.9 g **:** 30 ml. The samples were incubated at constant temperature 36.5 ℃, up to 7 days, in polypropylene flasks. A reference solution consisting only of BSA and SBF was stored under the same conditions.

SEM imagines were recorded using a Jeol JSM 5510LV Scanning Electron Microscope. Differential thermal analysis (DTA) and gravimetric thermal analysis (GTA) were performed on Shimadzu analyzer DTG-60H, in air, using alumina crucibles, with heating rate of 10 ℃/min, from room temperature to 1000℃. The structure of the samples was analysed by X-ray diffraction with a Shimadzu XRD-6000 diffractometer, using Cu Ka radiation (λ=1.5418 Å), with Ni-filter. The fluorescence spectra were recorded from 250 to 450 nm on Jasco spectrofluorimeter FP-6300. The excitation wavelength was 295 nm.

ACKNOWLEDGMENTS

REFERENCES

1. L.L. Hench, *Journal of the American Ceramical Society* **1991**, *74,* 1487.
2. T. Kokubo, H. Kushitai, C. Ohtsuki, S. Sakka, T.Yamamuro, *Journal of Materials Science: Materials in Medicine* **1992**, *3*, 79.
3. L.L. Hench, *American Ceramic Society Bulletin* **1998**, *77*, 67.

4. P. Saravanapavan, L.L. Hench, *Journal of Biomedical Materials Research* **2001**,*54*, 608.
5. T. Kokubo, H. Kushitani, S. Sakka, *Journal of Biomedical Materials Research* **1990**, *24*, 721.
6. C.J. Wilson, R.E. Clegg, D.I. Leavesley, M.J. Pearcy, *Tissue Engineering* **2005**, *11*, 1.
7. Q.Z. Chen, K. Rezwan, D. Armitage*,* S.N. Nazhat, A.R. Boccaccini, Journal of Materials Science: Materials in Medicine **2006**, *17*, 979.
8. L.A. Buchanan, A. El-Ghannam, *Journal of Biomedical Materials Research A* **2010**, *93*, 537.
9. E.L.Gelamo, M. Tabak, *Spectrochimica Acta A* **2000**, *56*, 2255.
10. M. Veith, S. Mathur, N. Lecerf, V. Huch, T. Decker, H.P. Beck, W. Eiser, R. Haberkorn, "Sol-Gel Synthesis of Nano-Scaled $BaTiO_3$, $BaZrO_3$ and $BaTi_{0.5}Zr_{0.5}O_3$ Oxides via Single Source Alkoxide Precursors and Semi-Alkoxide Routes", in Sol-Gel Science and Technology, Ed. By S. Sakka, Kluver Academic Publ., 2003.
11. L.F. Steel, M.G. Trotter, P.B. Nakajima, T.S. Mattu,G. Gonye, T. Block, *Molecular & Cellular Proteomics* **2003**, *2*, 262.
12. M. Ellmerer, L. Schaupp, G.A. Brunner, G. Sendlhofer, A. Wutte, P. Wach, T.R. Pieber, *American Journal of Physiology - Endocrinology and Metabolism* **2000**, *41*, E352.
13. E. Laszloffi, K. Magyari, V. Simon, *Studia Universitatis Babes-Bolyai Seria Physica*, **2009**, *1*, 3.
14. S. Thijssen, G. Wystrychowski, L. Usvyat, P. Kotanko, N.W. Levin, *Journal of Renal Nutrition* **2007**,*17*, 70.
15. V. Simon, S. Cavalu, S. Simon, H. Mocuta, E. Vanea, M. Prinz, M. Neumann, *Solid State Ionics* **2009**, *180*, 764.
16. K. Magyari, O. Popescu, V. Simon, *Journal of Materials Science: Materials in Medicine* **2010**, *21*, 1913.
17. S. De, A. Girigoswami, S. Das, *Journal of Colloid and Interface Science* **2005**, *285*, 562.
18. D.M. Togashi,.A.G. Ryder, D. Mc Mahon, P. Dunne, J. McManus, *Proceedings Biomed. Opt. Imag. SPIE-OSA* **2007**, *6628*, 66281K.
19. V.P. Zhdanov, B. Kasemo B, *Biophysical Chemistry* **2010**, *146*, 60.
20. K.D. Lobel, L.L. Hench, *Journal of Sol-Gel Science and Technology* **1996**, *7*, 69.
21. X. Dai, Z. Yue, M.E. Eccleston, J. Swartling, N.K.H. Slater, C.F. Kaminski, *Nanomedicine: Nanotechnology, Biology and Medicine,* **2008**, *4*, 49.

LC/MS ANALYSIS OF STEROLIC COMPOUNDS FROM *GLYCYRRHIZA GLABRA*

IBRAHIM KHALAF[a], ANDREIA CORCIOVĂ[a], LAURIAN VLASE[b], BIANCA IVĂNESCU[c], DOINA LAZĂR[a]

ABSTRACT. In this study we have attempted to identify and quantify phytosterols from four samples of *Glycyrrhiza glabra* harvested from four different areas (Bilekh, Rakka, Alpo-Azaz, Rass-Aenn) of Syria. Beta-sitosterol and stigmasterol are predominant in all samples. The highest amount of beta-sitosterol and campesterol was found in Alpo-Azaz sample and the biggest quantity of stigmasterol and ergosterol was found in Bilekh sample. This investigation offers an approach to rapidly characterization of phytosterols in herbal products.

Keywords: HPLC-MS-MS, phytosterols, Glycyrrhiza glabra

INTRODUCTION

Phytosterols are naturally occurring substances found in greater quantity in higher plants, especially in oily seeds, legumes and cereals. The most common is sitosterol which is sometimes accompanied by a smaller percentage of stigmasterol. In nature, plant sterols are found in free or esterified form, as well as glycosides. They are used in the semisynthesis of steroid hormones and vitamin D. They seem to have an important role in the body by keeping cholesterol level low. The main biologically active components of *Glycyrrhiza glabra* licorice are triterpenoid saponins, flavonoids, chalcones and isoflavones. Numerous studies have been focused on researching these compounds. Beside those, a series of minor constituents, such as coumarins, stilbenoids, gamma-lactones and sterols, are also present. The literature mentions the presence of beta-sitosterol, stigmasterol and dihydrostigmasterol [1-4], but to the best of our knowledge, the sterol composition of licorice root has not been investigated yet.

[a] *"Gr. T. Popa" University of Medicine and Pharmacy Iasi, Faculty of Pharmacy, Department of Drugs Analysis, 16 Universitatii Street, RO-700115 Iasi, Romania, acorciova@yahoo.com*
[b] *„Iuliu Hatieganu" University of Medicine and Pharmacy Cluj –Napoca, Faculty of Pharmacy, Department of Pharmaceutical Technology and Biopharmaceutics, 13 Emil Isac Street, RO-400023 Cluj –Napoca, Romania*
[c] *"Gr. T. Popa" University of Medicine and Pharmacy Iasi, Faculty of Pharmacy, Department of Botany, 16 Universitatii Street, RO-700115 Iasi, Romania*

Analysis of sterols from four samples of *Glycyrrhiza glabra* harvested from Syria has been carried out by using a HPLC-APCI-MS method. The applied method of analysis is based on a published HPLC method from the literature [5], to which we've made some changes. The main modification was to change the chromatographic column and mobile phase. As a result, compared to the method published in literature, the analysis time decreased from 30 minutes to 5 minutes without affecting the separation and peak resolution of sterols [6-11].

For quantitative determination, four standards were used: beta-sitosterol, stigmasterol, campesterol and ergosterol, purchased from Sigma Company (Germany).

RESULTS AND DISCUSSION

According to chromatographic conditions, retention times of the four analyzed sterols are: 2.4 min for ergosterol, 3.7 min for both stigmasterol and campesterol (co elution) and 4.2 min for beta-sitosterol. Ions monitored by MS method are presented in Table 1. Since in the ionization conditions, all sterols lose a molecule of water, ions detected by the spectrometer are always of the form $[M-H_2O+H]^+$.

Table 1. Sterol-specific ions monitored in the screening method, in order of their retention times

Sterol	Retention time (min)	M	M-H$_2$O	M-H$_2$O+H$^+$
Ergosterol	2.4	396	378	379
Stigmasterol	3.7	412	394	395
Campesterol	3.7	400	382	383
Beta-Sitosterol	4.2	414	396	397

Total ion chromatogram of a mixture of four sterols is shown in Figure 1. The sum of all ions scanned by spectrometer was plotted, regardless of their mass.

Specific ions of the four sterol standards (379 for ergosterol, 395 for stigmasterol, 383 for campesterol and 397 for beta-sitosterol) were fragmented and based on fragments of the spectrum MS chromatograms of each compound extracted were drawn.

This method of analysis (also called MS/MS) is highly specific compared to the screening method, where is recorded only the intensity of the main ion and an isomer compound - with the same molecular weight - can give a false positive signal.

Based on analysis of fragments of the MS spectrum, which are specific to each structure separately and are not the same for different

isomers, the MS/MS method will detect only the compound of interest without interference from others.
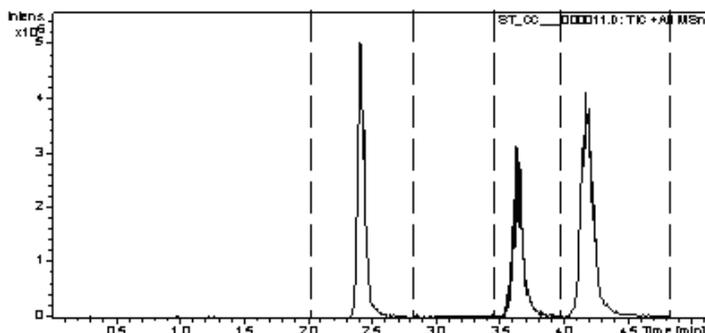
Figure. 1 Chromatogram of standard solution of sterols. Elution order: ergosterol (2.4 min), stigmasterol and campesterol (both at 3.7 min), beta-sitosterol (4.2 min)

Moreover, the intensity of ions in the mass spectrum is proportional to the concentration of the substance in the sample, so the method can also be applied for quantitative determination.

In order to quantify the four sterols from plant extracts, we have constructed the extracted chromatograms for each of them, taking into account the intensity of major ions in the mass spectrum. Ions used for quantification are listed in Table 2.

Table 2. Ions from MS spectra of the analyzed sterols, used in quantification

No.	Compound	Specific ions for identification
		$[M-H_2O+H^+]$ ion > ions from spectra
1	Ergosterol	379> 158.9; 184.9; 199; 213; 225; 239; 253; 295; 309; 323
2	Stigmasterol	395> 255; 297; 283; 311; 241; 201
3	Campesterol	383> 147; 149; 161; 175; 189; 203; 215; 229; 243; 257
4	Beta-Sitosterol	397> 160.9; 174.9; 188.9; 202.9; 214.9; 243; 257; 287.1; 315.2

In order to create calibration curves, the four sterol standards were dissolved in chloroform (concentration 1 mg/mL), after which successive dilutions were made in acetonitrile, at different concentration levels, selected as representative of the range of concentration in sample. Regression analyses of various concentrations of standard solutions (0.08-8 µg/ml) have good

correlation coefficients for the calibration curves of sterols in all cases. In Table 3 are presented the calibration curves for each standard.

Table 3. Parameters of calibration curve for each standard

STANDARD	CALIBRATION CURVE ECUATION	R^2
Ergosterol	y = 2006.6073 x + 14988.2649	0.9994
Stigmasterol	y = 656.1371 x + 6552.3729	0.9957
Campesterol	y = 2514.6804 x + 56452.9510	0.9987
Beta-Sitosterol	y = 2085.1047 x + 16268.9043	0.9937

The limit of quantification was set to 0.08 µg/ml for each analyte. The accuracy and precision were 97.2 % - 104.7 % and 8.1 % for ergosterol, 89.1 -110.5 % and 9.2 % for stigmasterol, 93.5 - 109.6 % and 11.7 % for campesterol and 92.9 - 112.7 % and 9.9 % for beta-sitosterol, respectively. For each analyte, the limit of detection was 0.02 µg/ml, based on a signal-to-noise ratio of 3.

Concentrations of sterols found in the four *Glycyrrhiza glabra* extracts are presented in Table 4. As expected, beta-sitosterol and stigmasterol are found in higher amounts than campesterol in all samples. The quantity of campesterol is very small in all extracts. The sample of Alpo-Azaz G3 has the largest amount of campesterol.

Of the four analyzed samples, the G1 sample of Bilek has a greater amount of stigmasterol than beta-sitosterol, which is less common in the plant world. Usually, in plants beta-sitosterol is predominant, as for samples G2-G4.

Table 4. Content of sterols in samples (concentration are registrated in HPLC sample injected)

Sample	G1	G2	G3	G4
Compound	Content (ng/ml)			
Ergosterol	3117.8	2053.1	2977.2	1894.3
Stigmasterol	7185.5	6346.0	5784.1	3241.9
Campesterol	1484.0	1411.5	2285.8	1074.2
Beta-Sitosterol	6624.8	7408.6	12448.7	5562.0

It's interesting to note that ergosterol quantity in all samples is appreciable, even higher than campesterol, although this compound is not specific to higher plants. Its presence in root extracts of *Glycyrrhiza glabra* is probably due to the mycorrhizal fungi. They can contribute to the biological activity of the vegetal product by the metabolites synthesized and also by increasing the glycyrrhizin concentration in roots [11].

Comparative sterols content in all four samples is presented in figure 2.
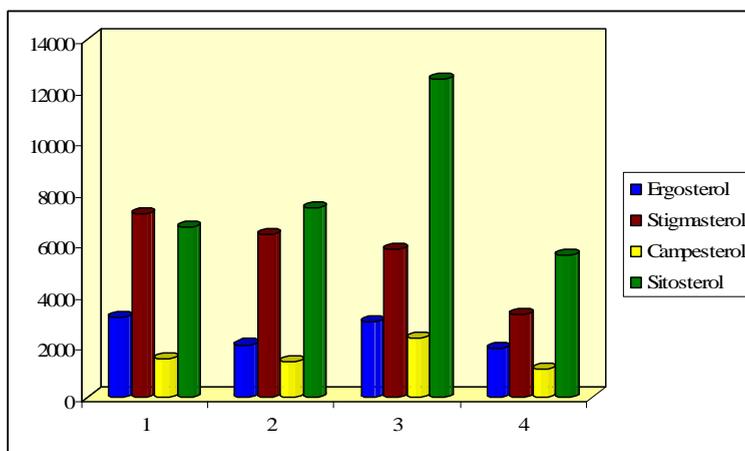
Figure. 2 Comparative sterols content in four extracts of *Glycyrrhiza glabra*

CONCLUSIONS

In the present study we have analyzed, for the first time, the phytosterols from roots of *Glycyrrhiza glabra* collected from four different areas of Syria. The presence of beta-sitosterol, stigmasterol, campesterol and ergosterol was assessed through a HPLC/APCI/MS method. This method permitted us the identification and quantification of plant sterols in the four extracts. In all samples beta-sitosterol and stigmasterol are predominant; the G3 sample of Alpo-Azaz has the highest amount of beta-sitosterol and campesterol and the G1 sample of Bilekh has the largest amount of stigmasterol and ergosterol.

EXPERIMENTAL SECTION

Plant material: The root parts of *Glycyrrhiza glabra* were collected from Syria in four different areas (Bilekh, Rakka, Alpo-Azaz, Rass-Aenn) and air-dried at room temperature. Plants were identified and a voucher specimen of each was deposited at the herbarium of Pharmaceutical Botany Department, Faculty of Pharmacy, University of Medicine and Pharmacy Iasi.

Sample preparation: Samples of 5 g pulverized roots material were extracted by refluxing with 25 mL methanol, in a Soxhlet extractor, for 1 hour. The resulting samples were appropriately diluted before injection in chromatograph. We marked the samples as follows: G1 (Bilekh), G2 (Rakka), G3 (Alpo-Azaz), G4 (Rass-Aenn).

Stock solutions: Stock solutions (1 mg/mL) were prepared from standards, kept at 4^0C and protected from day light. Before being used as working solutions, they were appropriately diluted with acetonitrile.

Chemicals: Methanol and acetonitrile of HPLC analytical-grade, and chloroform were purchased from Merck

Apparatus and chromatographic conditions. The analysis was carried out using an Agilent 1100 HPLC Series system equipped with G1322A degasser, G1311A binary pump and G1313A autosampler. For the separation we used a reversed-phased Zorbax SB-C18 analytical column (100 mm x 3.0 mm i.d., 5 µm particles) fitted with precolumn Zorbax SB-C18, both operated at 40^0C. The mobile phase was prepared from methanol and acetonitrile 30:70 (v/v), isocratic elution. The flow rate was 1 mL/min and the injection volume was 4 µL.

All solvents used were filtered through 0.5 ml Sartorius filters and degassed with ultrasounds. MS/MS detection using multiple reaction monitoring (MRM) of specific daughter ions was used for each sterol.

The HPLC was coupled with an Agilent Ion Trap 1100 VL mass detector, equipped with an atmospheric pressure chemical ionization (APCI) interface, working in positive ion mode. Operating conditions were: gas – nitrogen, flow rate 7 L/min, ion source temperature 250^0C, nebuliser - nitrogen at 50 psi pressure, capillary voltage -4000 V.

All chromatographic data were processed using ChemStation (vA09.03) software and Data Analysis (v 5.3) from Agilent,USA.

REFERENCES

1. M. N. Asl, H. Hosseinzadeh, *Phytotherapy Research*, **2008,** *22*, 709.
2. S. B. Denisova, V. T. Danilov, S. G. Yunusova, V. A. Davydova,Yu. I. Murinov, F. S. Zarudii., *Pharmaceutical Chemistry Journal.,* **2007**, *41(9)*, 35.
3. A. Suman, M. Ali, P. Alam, *Chemistry of Natural Compounds*, **2009**, *45(4)*, 487.
4. H. Hayashi, *Natural Medicines*, **2004**, *58(4)*, 132.
5. DI. Sanchez-Machado, J. Lopez-Hernandez, P. Paseiro-Losada, J. Lopez-Cervantes, Biomed. Chromatogr., **2004**, *18(3)*, 183.
6. C.M.López Ortíz, M.S.Prats Moya, V. Berenguer Navarro, *Journal of Food Composition and Analysis*, **2006,** *19,* 141.
7. M. Careri, L. Elviri, A. Mangia, *Journal of Chromatography A*, **2001,** *935,* 249.8. J. J. Palmgrén, A. Töyräs, T. Mauriala, J. Mönkkönen, S. Auriola, *Journal of Chromatography B*, **2005**, *821,* 144.
9. P. Breinhölder, L. Mosca, W. Lindner, *Journal of Chromatography B*, **2002**, *777(1-2)*, 67.
10. S. Leucuta, L.Vlase, L. Radu, C. Fodorea, S. Gocan, *Journal of Liquid Chromatography & Related Technologies*, **2005,** *28*, 3109.
11. D.I. Sanchez-Machado, J. Lopez-Hernandez, P. Paseiro-Losada, J. Lopez-Cervantes, *Biomedical Chromatography*, **2004**, *18*, 183.
12. J. Liu, L. Wu, S. Wei, S. Xiao, C. Su, P. Jiang, Z. Song, T. Wang, Z. Yu, *Plant Growth Regulation* , **2007**, *52,* 29.

INVESTIGATION OF THE EFFECTS OF DEGRADATION OF HIGH DENSITY POLYETHYLENE BY ^{13}C NMR SPECTROSCOPY AND ^{1}H RELAXOMETRY

DUMITRITA MOLDOVAN[a], MIHAELA POP[b], RADU FECHETE[a], ANNE BAUDOUINE[c], MIHAI TODICA[b]

ABSTRACT. The structural and dynamic changes occurring in high-density polyethylene exposed to gamma-, X-radiation and extreme temperature have been investigated by high-resolution solid state CP/MAS ^{13}C NMR and ^{1}H NMR relaxometry. The ^{13}C CP/MAS NMR spectra show that the gamma and X-radiation can induce the formation of Y-type branches in HDPE. The Laplace distribution of transverse T_2 and longitudinal T_1 relaxation times are used first to identify dynamics and morphological components of HDPE samples and then to characterize the degradation effects of these samples subjected to external aging factors. The small amplitude of the fourth component from T_2 Laplace spectra confirms the connection of free ends of polymer chains to form Y-branches HDPE subjected to X-radiation. The T_1 spectra Laplace show that the cooling at nitrogen temperature will affect mostly the crystallinity of HDPE.

Keywords: High Density Polyethylene (HDPE), gamma and X-ray irradiation, ^{13}C CP/MAS NMR, ^{1}H NMR, T_1, T_2, Laplace distributions.

INTRODUCTION

High density polyethylene consists of quasi-linear molecules with less than one branching point per 200 carbon atoms in the backbone. Therefore HDPE is characterized by high degrees of crystallinity, highest modulus and lowest permeability of all the classes of polyethylene. These properties make HDPE suitable for certain daily-use liquid holders and chemical storage tanks [1]. For such storage bottles, it is important to maintain unaltered their physicochemical properties therefore, the effects of degradation under the action of various ageing factors like high or low temperature or high energy

[a] *Technical University of Cluj-Napoca, Physics Department, Str. Memorandumului nr. 28, 400114, Cluj-Napoca, Romania, Dumitrita.Moldovan@phys.utcluj.ro*
[b] *Babeş-Bolyai University, Physical Faculty, Str. Kogălniceanu, No. 1, RO-400084 Cluj-Napoca, Romania*
[c] *CNRS-University Lyon-1, Service RMN du Solide, 43, Bd du 11 novembre 1918, 69616, Lyon, France*

irradiation, must be know. Such agents can produce modification at the level of chemical structure or polymer chain.
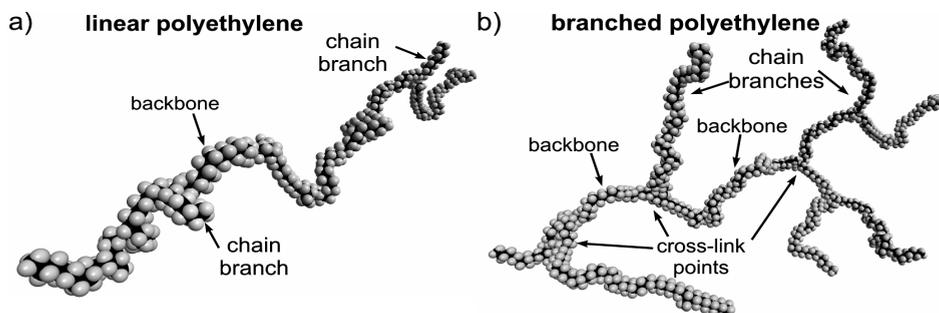
Figure 1. Schematic representation of a) liner b) branched polyethylene.

For example, the exposure of PE to high-energy radiation leads to backbone and branch scission, formation of new cross-links and formation of unsaturated and oxidized groups. Moreover, aging factors can produce changes in the melting behavior and crystallinity with direct effect on the elastic modulus [2]. The changes in the crystalline and amorphous phases, the formation and nature of the new cross-link points in gamma-irradiated HDPE were extensively studied [2, 3]. The branching analysis of polyethylene has been a subject of considerable interest in the past two decades due to the importance of branching type and distribution (see Figure 1) in such materials. The use of various solid-state NMR pulse sequences allows identifying the characteristic resonance peaks associated to crystalline and amorphous phases in semi-crystalline polymers (see Figure 2). The ^{13}C NMR technique is the primary method that is commonly used for such analysis [2-6]. In the last decade, ^{1}H relaxation times or Laplace distributions of transverse relaxation times were used for investigating the effects of aging under factors like temperature and UV-radiation [7, 8].

The aim of this paper is to investigate the effects on the structure and morphology of different aging agents like gamma and X-ray and extreme temperatures. The modifications at the level of functional groups are investigated by ^{13}C CP/MAS NMR spectroscopy, while the modifications in the HDPE polymer chain segmental dynamics are monitored via the changes in the Laplace distribution of transverse T_2 relaxation times. This is possible due to the fact that the peaks from T_2 distributions can be associated with rigid, mobile, loose loops and free ends polymer chain segments. The longitudinal T_1 relaxation time edits different characteristics than T_2 therefore the T_1 distributions are used to observe the effects of aging factors at the level of HDPE crystalline and amorphous phases.
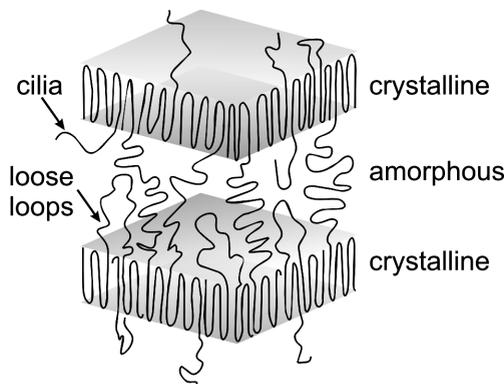
Figure 2. Schematic representation of high density polyethylene morphology.

RESULTS AND DISCUSSION

Figure 4 presents the CP/MAS ^{13}C NMR spectra of un-irradiated and gamma and X-ray irradiated high density polyethylene. In the spectra of the un-irradiated sample one can identify a high and narrow peak at 32 ppm and a broad peak at 31 ppm (Figure 4a). The narrow peak located at 32 ppm is associated to the methylene functional group from crystalline components and the peak from 31 ppm is associated to the amorphous phase [2]. In the spectrum of gamma irradiated sample an additional peak appears at 34 ppm (Figure 4b). This can be associated to the carbon-carbon bonds from cross-linking points in polyethylene [3, 5]. According to the interpretation of Horii et al. and Randall, these cross-link points are most likely the origin of Y-branches than H-branches [3, and references therein]. This means that the effect of gamma irradiation is connected with a higher probability a polymer chain-end to another backbone than to connect to backbones. Similar appearances of a peak located at 34 ppm and associated to the carbon-carbon bonds in crystalline phase of high density polyethylene are observed in the X-ray irradiated sample (Figure 4c). The relative intensity of the cross-link peak observed in the CP/MAS ^{13}C NMR spectra of HDPE irradiated with X-rays is higher than the relative intensity of the same peak observed in the case of HDPE irradiated with gamma rays. Taking into account also the fact that the irradiation dose was approximately 25 times smallest in the case of X-rays, one can conclude that this type of radiation produces significant higher degradation of HDPE than gamma radiation.
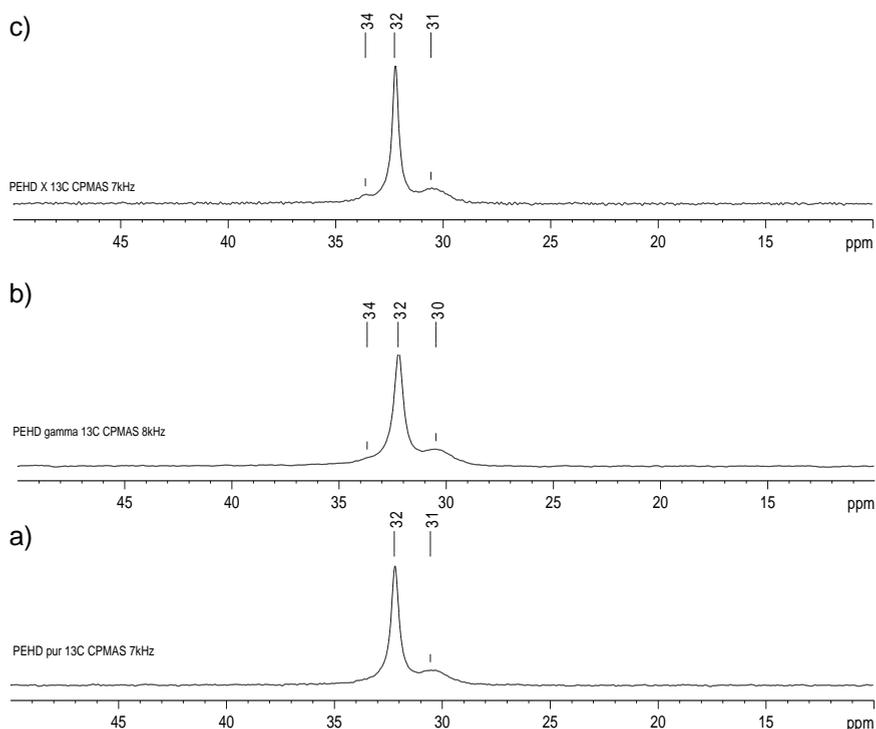
Figure 4. CP/MAS ^{13}C NMR spectra of a) pure; b) gamma irradiated and c) X-ray irradiated high-density polyethylene.

The degradation effects on high-density polyethylene morphology of X-ray irradiation are compared with those produced by extreme temperature. For that, a series of CPMG curves are recorded and presented in Figure 5a together with the curve corresponding to pure HDPE. Small differences can be observed among these decays. The CPMG curve (open gray stars) decay slowest than the pure HDPE (filled circles) while the curves corresponding to HDPE degraded (open squares) in liquid nitrogen and melted (open gray triangles) decay faster. A better analysis of these CPMG curves can be obtained from the corresponding T_2 distributions which are presented in Figure 5b. All distribution from the Laplace spectra presents four peaks. The main peak is located at the lowest T_2 values, around 200 µs, therefore characterized by a reduced mobility, and can be associated with the crystalline phase of HDPE (see Figure 2). The second peak located between 1–2 ms, is characterized by a mobility characteristic to linked polymer chains therefore can be associated to the amorphous phase of HDPE. With one order of magnitude higher one can find a peak associated to the more mobile chain segments like the loose loops from the amorphous phase, while with

106

two orders of magnitude one can find peaks which can be associated with the extremely mobile polymer chain segments like the end chains or cilia (see Figure 2).
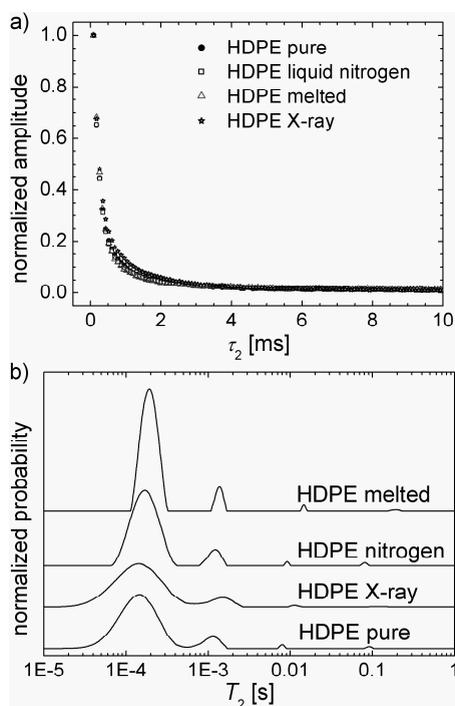
Figure 5. a) The CPMG echoes decays; b) the corresponding T_2 distributions for the pure and aged in liquid nitrogen, melted and X-ray irradiated HDPE.

The distributions of pure and X-ray irradiated sample are almost similar with two exceptions: i) the HDPE chain segments from amorphous phase become more mobile, observed from increased values of T_2, and ii) the peak corresponding to end segments almost disappear then can be associated with the formation of Y – branches observed also from ^{13}C CP/ MAS NMR spectra. The positions of peaks in the T_2 distributions for HDPE aged in liquid nitrogen correspond with the peaks of pure HDPE. Nevertheless, the effect of 5 min cure in liquid nitrogen leads to a more organized chain distribution into the crystalline and amorphous phases, as can be observed from the corresponding narrowed peaks. The highest homogeneity is produced by melting the HDPE sample. This treatment will increase also the mobility of loose loops and cilia from amorphous phase.

The melting cure lead to significant changes also into the saturation recovery build-up curve of the same pure and aged HDPE samples (see

Figure 6a). Only three components (see Figure 6b) can be identified in the T_1 distributions and these can be associated from right to left (decreasing T_1 values) with the crystalline, interface and amorphous phase of HDPE [1]. The discrepancy between T_2 and T_1 distributions arises from different NMR sensitivity of these two parameters for describing multiphase in polyethylene [2]. In contrast to the thermal treatment, irradiation with X-rays leads to a small ordering of HDPE network. The melting cure destroys a significant part of amorphous and crystalline phase and increase the interfacial high density polyethylene network.
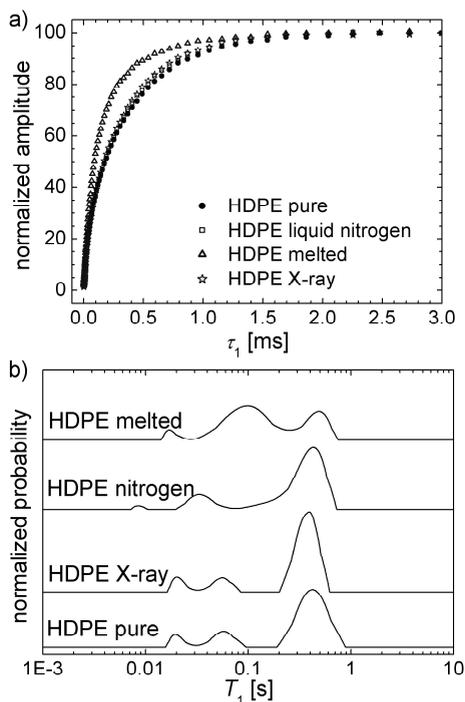
Figure 6. a) The saturation recovery and b) the corresponding T_1 distributions for the pure and aged in liquid nitrogen, melted and X-ray irradiated HDPE.

CONCLUSIONS

The resonance peaks due to direct cross-links and forming Y-branches have been detected in the ^{13}C of gamma- and X-irradiated HDPE. The T_2 Laplace spectra consisting in four well resolved peaks, associated to rigid, mobile, loose loops and free ends, after irradiation with X-rays or cured at extreme temperatures reveals changes in the HDPE polymer chain dynamics. The T_1 Laplace distributions edit a three-phase: crystalline,

amorphous and interface, morphology of HDPE. The major degradation effect was observed in the crystalline phase of melted HDPE sample. The ^{1}H NMR Laplace distributions was proved to be a valuable tool to investigate the high density polyethylene degradation.

EXPERIMENTAL SECTION

The ^{13}C CP/MAS NMR spectra were recorded with 500 MHz DSX Bruker spectrometer and a 4 mm probe-head. The rotor frequency was 7 kHz for the pure and X-ray irradiated HDPE and 8 kHz for the gamma-irradiated HDPE sample. The pulse program is presented in figure 3a. The recycle delay was 5 s and the scan numbers was set to 4. The spectra were recorded at a temperature of 28.5 ^{0}C.

The ^{1}H NMR data were recorded using the Bruker Minispec spectrometer with the 10 mm probe-head working at 19.688 MHz [1]H Larmor frequency. The tipping pulse was 8.4 µs and the refocusing pulse 16.8 µs. In order to ensure a good signal to noise ratio 256 scans were recorded for the 1000 CPMG echoes with an echo time of 70 µs (see Figure 3b) and a recycle delay of 3 s.
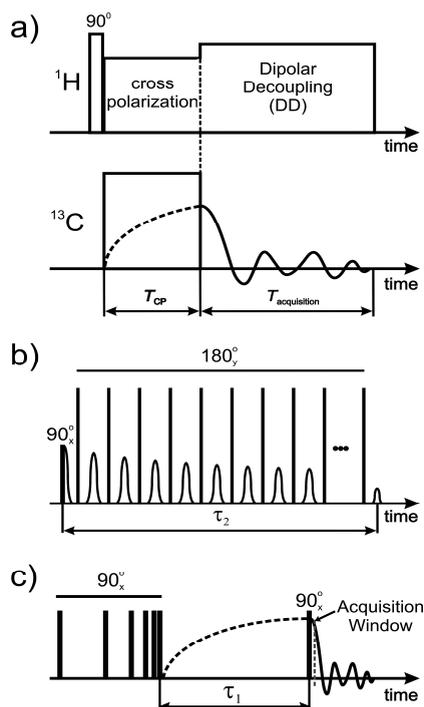
Figure 3. a) [1]H -^{13}C cross-polarization; b) CPMG and c) saturation recovery pulse sequences.

For the saturation recovery (see Figure 3c) the number of saturating pulses was 10 while the scans number was reduced at 64 [9]. The recovery time, τ_1 was increased from 1 ms with a ratio of 1.1 in unevenly 85 steps up to 3 s. In all measurements the temperature was set to 35 ^{o}C. Finally, in order to find the transverse T_2 and longitudinal T_1 relaxation times distributions, the CPMG decays and saturation- recovery build-up curves were analyzed using the well know UPIN algorithm, which perform a Laplace inversion of the measured data [10]. The HDPE samples were aged using various agents and different conditions: i) the dose of irradiation with gamma ray was 8989 Gy accumulated during 1696 h at a 5,3 Gy/h; ii) the accumulated dose of irradiation with X-ray was 358 Gy during 12 days; iii) HDPE was melted at a temperature of 256 ^{o}C during 24 h and then cooled at a room temperature; iv) HDPE was sinked into liquid nitrogen at -196 ^{o}C for 5 min and then heated at room temperature.

ACKNOWLEDGMENTS

REFERENCES

1. A. J. Peacock, *Handbook of Polyethylene: Structures, Properties, and Applications*, **2000**, Marcel Dekker, Inc., New-York, Bassel.
2. A. L. Cholli, W. M. Ritchey, J. L. KOENIG, *Applied Spectroscopy*, **1987**, *41,* 1418.
3. F. Horii, Q. Zhu, R. Kitamaru, H. Yamaoka, *Macromolecules*, **1990**, *23,* 977.
4. J. Schaefer and E. O. Stejskal, *Topics in Carbon-13 NMR Spectroscopy,* **1979**, *3*, 283.
5. A. N. Garroway, W. M. Ritchey, W. B. Moniz, *Macromolecules,* **2000**, *15*, 1501.
6. Schroeter and A. Posern, *Macromolecular Chemistry Rapid Communications*, **1982**, *2*, 123.
7. S. Anferova, V. Anferov, M. Adams, R. Fechete, G. Schröder and B. Blümich, *App. Magn. Reson.*, **2004**, *27 (3-4)*, 361-370**.**
8. M. Butnaru, R. Marcean, O. Cozar, I. Bratu and R. Fechete**,** *Studia Babes-Bolyai Seria Physica*, **2005**, *L 4b*, 641-645.
9. M. Todica, Metode aplicative de rezonanta magnetica nucleara, Presa Universitara Clujeana, 2001.
10. G. C. Borgia, R. J. S. Brown, and P. Fantazzini, *Journal of Magnetic Resonance*, **1998**, *132*, 65-77.

PM3 CONFORMATIONAL ANALYSIS OF THE (3S,5S,6S)-6 ACETYLAMIDOPENICILLANIC ACID. ELECTRONIC PROPERTIES.

DANIELA IVAN[a], MIRCEA MRACEC[b]

ABSTRACT. A conformational analysis with the semiempirical PM3 method was performed for (3S,5S,6S)-6-acetylamidopenicillanic acid. 105 distinct conformers were found within 25.53 kcal/mol. Dependence of some electronic properties of these conformers (HOMO and LUMO energies, dipole moment, v_{min} minimum vibration energy, maximum vibration energy $v_{MAX.}$, zero point vibration energy (ZPVE) and charge densities on atoms S1, N4, N14, O8, O12, O13 and O17) with respect to some geometric characteristics : pseudochirality of the N14 atom, the *syn-anti* arrangement of the O17 and H28 atoms of the amidic group and the three puckering classes of the thyazolidinic cycle noted with a, b, c, is demonstrated.

Keywords: conformational analysis, (3S,5S,6S)-6-acetylamidopenicilanic acid, PM3 method, electronic properties

INTRODUCTION

The (3S,5S,6S)-6-acetylamidopenicillanic acid is one of the simplest antibacterial compounds of the penicillin class. Its molecular structure contains two fused rings (a four-membered β-lactamic ring and a five-membered thiazolidinic ring) and three chiral centers, as shown in Figure 1 [1].
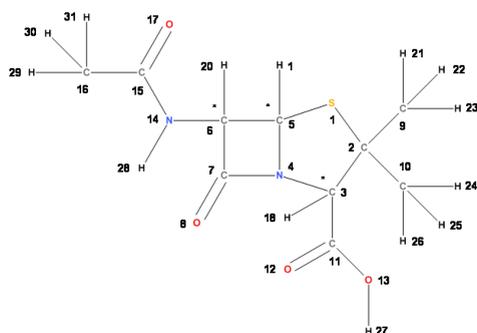
Figure 1. Atom numbering in (3S,5S,6S)-6-acetylamidopenicillanic acid (* denotes the chirality).

---

[a] *Institute of Chemistry of Romanian Academy, 24 Mihai Viteazul Bvd., RO-300223, Timisoara, Romania, dana_ivan@ acad-icht.tm.edu.ro*
[b] *Institute of Chemistry of Romanian Academy, 24 Mihai Viteazul Bvd., RO-300223, Timisoara, Romania, mracec@acad-icht.tm.edu.ro*

In this paper we present an analysis of the dependence of the electronic properties of the (3S,5S,6S)-6-acetylamido-penicillanic acid by the geometric characteristics of the conformers. The pyramidalization degree of the nitrogen N14 atom, as resulted from the PM3 method, is measured by the "conicity" of the improper angle C6-C15-H28-N14. The electronic properties are analysed with respect to the *anti* or *syn* orientation of atoms O17 and H28 of the exocyclic amidic group and the three puckering classes of the thyazolidinic cycle [1].

RESULTS

The semiempirical PM3 methods give 105 conformers [1,7]. Table 1 gives the list of ordered conformers, numbered in ascending order of formation enthalpies. Some related structural properties are also included in Table 1.

To be sure that the obtained conformers are minima on the potential energy surface (PES) and not saddle points, for each conformer a normal vibration calculation was performed. All vibrations were positive for all conformes. The wavelength number of the maximum vibration, v_{MAX} and zero point vibration energy, **ZPVE** are given in Table 1, too. A gap of 25.53 kcal/mol resulted between the lowest energy (01pm3) conformer and the highest energy (105pm3) one [1].

Table 1. Conformers of the (3S,5S,6S)-6-acetilamidopenicillanic acid in ascending order of the formation enthalpies, at PM3 level of theory and some of their energetic, structural and electronic characteristics.

Ascending Energy Order	HOMO (eV)	LUMO (eV)	Pseudo chir. N14	Position 17,28.	μ (Debye)	Vibrations (cm^{-1})		ZPVE (kcal/mol)
						$v_{min.}$	$v_{MAX.}$	
01	-9.802	-0.482	S	anti	4.116	25.32	3484.89	149.602
02	-9.795	-0.465	S	anti	4.114	27.79	3849.57	149.921
03	-9.776	-0.485	S	syn	3.546	26.06	3849.84	150.131
04	-9.753	-0.453	S	syn	3.248	27.97	3849.77	150.424
05	-9.827	-0.507	S	anti	3.980	28.32	3849.53	149.614
06	-9.773	-0.439	S	anti	3.331	37.04	3847.56	150.007
07	-9.800	-0.510	S	syn	1.605	27.34	3849.25	150.160
08	-9.826	-0.491	S	anti	3.939	31.86	3849.35	149.886
09	-9.780	-0.477	S	syn	1.590	29.66	3848.95	150.403
10	-9.667	-0.391	R	syn	3.425	13.27	3849.61	150.356
11	-9.693	-0.396	S	anti	4.315	20.51	3848.73	149.675
12	-9.681	-0.443	R	syn	3.789	26.88	3849.51	149.989
13	-9.780	-0.462	S	anti	3.229	28.24	3847.74	149.525
14	-9.760	-0.465	S	syn	3.445	27.89	3849.30	150.120
15	-9.730	-0.436	S	syn	3.479	31.84	3847.74	150.493
16	-9.658	-0.398	R	anti	3.946	25.43	3849.91	149.510
17	-9.817	-0.490	S	anti	4.337	36.38	3842.31	150.238
18	-9.753	-0.472	S	syn	3.697	29.12	3847.75	150.086
19	-9.707	-0.472	R	syn	3.819	26.51	3849.78	149.680

Ascending Energy Order	HOMO (eV)	LUMO (eV)	Pseudo chir. N14	Position 17,28.	μ (Debye)	Vibrations (cm^{-1})		ZPVE (kcal/mol)
						$v_{min.}$	$v_{MAX.}$	
20	-9.703	-0.465	R	syn	1.839	28.96	3849.19	150.007
21	-9.693	-0.416	R	syn	1.773	18.27	3849.10	150.333
22	-9.573	-0.313	R	anti	4.323	23.72	3847.99	149.646
23	-9.775	-0.485	S	syn	1.304	31.02	3842.38	150.744
24	-9.787	-0.488	S	syn	1.729	29.33	3848.84	150.098
25	-9.655	-0.386	R	syn	3.649	29.16	3847.32	150.383
26	-9.648	-0.356	R	anti	3.293	33.47	3847.59	149.890
27	-9.736	-0.447	S	syn	3.642	28.56	3847.67	150.129
28	-9.686	-0.426	R	anti	3.899	27.33	3849.45	149.499
29	-9.822	-0.511	S	anti	4.428	24.91	3842.04	149.732
30	-9.735	-0.500	R	syn	1.829	27.97	3849.01	149.703
31	-9.686	-0.398	R	anti	3.924	28.85	3849.04	149.795
32	-9.795	-0.518	S	syn	1.405	28.08	3842.23	150.362
33	-9.712	-0.436	R	syn	1.732	27.30	3848.61	150.057
34	-9.601	-0.371	R	syn	4.504	17.68	3848.11	150.122
35	-9.699	-0.436	R	syn	1.506	28.19	3842.35	150.641
36	-9.671	-0.437	R	syn	3.912	31.60	3847.35	149.863
37	-9.652	-0.389	R	anti	3.087	29.83	3847.46	149.406
38	-9.673	-0.405	R	syn	3.666	30.59	3847.28	150.102
39	-9.779	-0.494	S	syn	1.497	27.68	3842.09	150.381
40	-9.693	-0.410	R	anti	4.332	32.46	3842.26	150.114
41	-9.630	-0.406	R	syn	4.539	14.45	3848.28	149.808
42	-9.638	-0.368	R	anti	3.714	18.63	3846.82	149.576
43	-9.698	-0.467	R	syn	3.934	29.97	3847.61	149.605
44	-9.717	-0.455	R	syn	1.496	29.83	3841.94	150.369
45	-9.691	-0.435	R	anti	4.336	10.87	3842.18	149.561
46	-9.738	-0.511	R	syn	1.673	29.79	3841.60	149.868
47	-9.690	-0.498	R	syn	4.024	31.66	3848.19	150.231
48	-9.811	-0.569	R	anti	4.907	27.23	3848.79	150.179
49	-9.854	-0.600	R	anti	4.151	30.51	3848.64	150.170
50	-9.730	-0.533	R	syn	1.734	33.04	3848.21	150.194
51	-9.818	-0.557	R	anti	4.156	36.26	3847.04	150.203
52	-9.582	-0.344	S	syn	3.610	24.52	3849.30	150.181
53	-9.580	-0.408	S	syn	4.684	31.16	3848.24	149.888
54	-9.574	-0.393	S	syn	4.524	23.10	3848.69	149.775
55	-9.587	-0.281	R	anti	4.385	38.71	3851.67	149.961
56	-9.682	-0.341	R	anti	4.272	31.07	3851.14	149.662
57	-9.562	-0.255	R	anti	4.055	26.45	3852.10	149.921
58	-9.860	-0.608	R	anti	4.529	38.25	3841.93	150.402
59	-9.603	-0.318	R	anti	4.237	25.06	3851.52	149.582
60	-9.613	-0.381	S	syn	1.493	25.17	3848.50	150.135
61	-9.588	-0.286	R	anti	4.073	28.97	3849.97	149.826
62	-9.625	-0.452	S	syn	2.477	35.65	3848.09	149.874

Ascending Energy Order	HOMO (eV)	LUMO (eV)	Pseudo chir. N14	Position 17,28.	μ (Debye)	Vibrations (cm^{-1})		ZPVE (kcal/mol)
						$v_{min.}$	$v_{MAX.}$	
63	-9.616	-0.430	S	syn	2.237	22.78	3848.44	149.737
64	-9.635	-0.351	R	anti	4.088	22.67	3849.91	149.491
65	-9.693	-0.500	R	syn	3.669	27.05	3846.97	150.181
66	-9.544	-0.254	R	anti	3.887	37.21	3849.50	149.703
67	-9.642	-0.465	R	syn	4.160	22.64	3845.02	150.206
68	-9.708	-0.510	R	syn	1.730	42.18	3844.90	150.315
69	-9.569	-0.328	S	syn	3.075	30.66	3847.90	150.028
70	-9.556	-0.403	S	syn	5.002	53.11	3845.33	150.327
71	-9.300	-0.035	S	anti	3.289	28.98	3852.59	149.620
72	-9.329	-0.065	S	anti	4.490	38.41	3851.36	149.641
73	-9.617	-0.335	R	anti	3.862	31.32	3848.22	149.541
74	-9.333	-0.095	S	anti	4.239	31.16	3851.65	149.348
75	-9.737	-0.547	R	syn	1.725	35.72	3841.73	150.423
76	-9.300	-0.065	S	anti	3.332	27.16	3852.53	149.276
77	-9.585	-0.301	R	anti	4.348	34.66	3842.85	150.196
78	-9.326	-0.066	S	anti	4.185	28.60	3850.44	149.502
79	-9.541	-0.203	R	syn	2.200	24.14	3850.53	149.845
80	-9.612	-0.446	S	syn	2.822	55.13	3841.29	150.334
81	-9.613	-0.375	S	syn	1.829	33.70	3841.73	150.450
82	-9.700	-0.515	R	syn	2.283	39.59	3843.72	150.378
83	-9.342	-0.103	S	anti	4.103	23.65	3850.51	149.172
84	-9.664	-0.386	R	anti	4.314	29.70	3843.84	149.854
85	-9.575	-0.236	R	syn	2.891	34.42	3848.58	149.828
86	-9.617	-0.453	S	syn	4.445	29.36	3849.38	150.047
87	-9.327	-0.088	S	anti	4.189	35.07	3843.10	149.856
88	-9.311	-0.079	S	anti	3.809	33.59	3849.50	149.174
89	-9.352	-0.126	S	anti	4.129	30.53	3844.08	149.561
90	-9.571	-0.374	S	syn	2.946	9.40	3849.19	149.752
91	-9.556	-0.359	S	syn	2.945	20.21	3849.32	149.164
92	-9.550	-0.341	S	syn	3.325	16.07	3850.22	149.809
93	-9.561	-0.326	S	syn	2.817	26.89	3849.93	149.755
94	-9.611	-0.487	S	syn	3.216	11.09	3848.28	149.871
95	-9.549	-0.382	S	anti	2.892	32.05	3843.13	149.658
96	-9.527	-0.242	R	anti	3.424	33.76	3852.73	149.991
97	-8.565	-0.132	S	anti	0.567	30.72	3850.40	150.083
98	-8.560	0.005	R	anti	2.328	30.73	3851.68	150.023
99	-8.650	-0.194	S	anti	2.909	31.22	3848.41	150.035
100	-8.640	-0.064	R	anti	4.431	30.73	3849.80	150.032
101	-8.507	-0.246	S	anti	2.057	15.41	3849.52	149.681
102	-8.450	-0.045	R	anti	3.064	26.99	3849.67	149.636

Ascending Energy Order	HOMO (eV)	LUMO (eV)	Pseudo chir. N14	Position 17,28.	μ (Debye)	Vibrations (cm^{-1})		ZPVE (kcal/mol)
						$v_{min.}$	$v_{MAX.}$	
103	-8.505	-0.255	S	anti	2.861	33.32	3843.62	149.986
104	-8.483	-0.092	R	anti	3.806	35.55	3843.70	149.994
105	-8.516	-0.236	S	anti	2.084	25.86	3842.61	149.892

The charge densities for some atoms important for biological activity – S(1), N(4), N(14), O(8), O(12), O(13), O(17)) – of the conformers resulted from PM3 calculations, are listed in Table 2.

Table 2. Charge densities on some atoms of the conformers of (3S,5S,6S)-6-acetilamidopenicillanic acid, arranged in ascending variation of the formation enthalpies, computed at PM3 level of theory.

Ascending Energy Order	Net Charge on atom (e)						
	S(1)	N(4)	N(14)	O(8)	O(12)	O(13)	O(17)
1	-0.022	-0.124	-0.030	-0.229	-0.363	-0.298	-0.353
2	-0.012	-0.122	-0.037	-0.226	-0.366	-0.297	-0.352
3	-0.004	-0.122	-0.039	-0.228	-0.360	-0.300	-0.348
4	0.001	-0.120	-0.039	-0.224	-0.362	-0.298	-0.349
5	-0.021	-0.122	-0.031	-0.237	-0.376	-0.290	-0.351
6	-0.019	-0.114	-0.039	-0.242	-0.377	-0.282	-0.352
7	-0.003	-0.120	-0.040	-0.238	-0.376	-0.289	-0.348
8	-0.010	-0.120	-0.038	-0.234	-0.374	-0.294	-0.350
9	0.003	-0.117	-0.041	-0.233	-0.374	-0.292	-0.349
10	0.009	-0.117	-0.035	-0.229	-0.363	-0.298	-0.354
11	-0.014	-0.137	-0.023	-0.240	-0.377	-0.294	-0.358
12	0.001	-0.118	-0.031	-0.234	-0.361	-0.299	-0.354
13	-0.029	-0.114	-0.033	-0.246	-0.378	-0.282	-0.352
14	0.000	-0.119	-0.037	-0.223	-0.362	-0.298	-0.347
15	-0.005	-0.112	-0.042	-0.240	-0.373	-0.285	-0.347
16	-0.008	-0.122	-0.024	-0.234	-0.366	-0.297	-0.352
17	-0.017	-0.116	-0.039	-0.242	-0.362	-0.296	-0.351
18	-0.011	-0.112	-0.041	-0.246	-0.375	-0.284	-0.346
19	0.002	-0.118	-0.041	-0.234	-0.360	-0.299	-0.351
20	0.002	-0.116	-0.030	-0.243	-0.375	-0.291	-0.355
21	0.011	-0.114	-0.035	-0.239	-0.374	-0.294	-0.355
22	0.002	-0.136	-0.025	-0.244	-0.386	-0.292	-0.356
23	-0.003	-0.114	-0.043	-0.240	-0.364	-0.293	-0.347
24	0.002	-0116	-0.039	-0.232	-0.374	-0.292	-0.347
25	0.002	-0.109	-0.037	-0.247	-0.373	-0.285	-0.353
26	-0.005	-0.113	-0.034	-0.248	-0.379	-0.282	-0.352

Ascending Energy Order	Net Charge on atom (e)						
	S(1)	N(4)	N(14)	O(8)	O(12)	O(13)	O(17)
27	-0.006	-0.111	-0.040	-0.239	-0.373	-0.284	-0.345
28	-0.008	-0.120	-0.024	-0.242	-0.375	-0.293	-0.352
29	-0.026	-0.118	-0.033	-0.244	-0.364	-0.293	-0.351
30	0.003	-0.116	-0.041	-0.244	-0.375	-0.290	-0.352
31	0.003	-0.118	-0.032	-0.240	-0.373	-0.296	-0.351
32	-0.008	-0.116	-0.041	-0.244	-0.365	-0.291	-0.347
33	0.012	-0.114	-0.040	-0.240	-0.373	-0.296	-0.351
34	0.009	-0.131	-0.029	-0.245	-0.372	-0.295	-0.351
35	0.004	-0.110	-0.037	-0.247	-0.363	-0.294	-0.354
36	-0.006	-0.109	-0.033	-0.252	-0.374	-0.284	-0.353
37	-0.016	-0.113	-0.027	-0.252	-0.379	-0.283	-0.353
38	0.003	-0.109	-0.043	-0.247	-0.373	-0.285	-0.349
39	-0.004	-0.113	-0.040	-0.240	-0.363	-0.293	-0.346
40	-0.004	-0.114	-0.033	-0.248	-0.362	-0.297	-0.351
41	0.009	-0.131	-0.038	-0.245	-0.371	-0.295	-0.348
42	-0.005	-0.131	-0.026	-0.251	-0.368	-0.307	-0.353
43	-0.005	-0.109	-0.043	-0.252	-0.374	-0.285	-0.350
44	0.005	-0.111	-0.043	-0.247	-0.363	-0.294	-0.350
45	-0.013	-0.115	-0.027	-0.250	-0.364	-0.295	-0.352
46	-0.003	-0.112	-0.042	-0.251	-0.364	-0.291	-0.351
47	0.000	-0.124	-0.032	-0.238	-0.371	-0.296	-0.352
48	-0.001	-0.125	-0.080	-0.219	-0.368	-0.295	-0.305
49	0.000	-0.123	-0.078	-0.225	-0.370	-0.298	-0.306
50	-0.002	-0.120	-0.030	-0.248	-0.371	-0.299	-0.350
51	-0.010	-0.115	-0.080	-0.234	-0.378	-0.281	-0.307
52	0.010	-0.117	-0.051	-0.243	-0.370	-0.297	-0.348
53	0.006	-0.126	-0.025	-0.245	-0.373	-0.296	-0.361
54	0.007	-0.124	-0.025	-0.245	-0.373	-0.296	-0.362
55	-0.033	-0.118	-0.013	-0.230	-0.389	-0.272	-0.354
56	-0.032	-0.125	-0.022	-0.227	-0.386	-0.274	-0.348
57	-0.034	-0.122	-0.014	-0.218	-0.346	-0.310	-0.350
58	-0.009	-0.118	-0.078	-0.233	-0.360	-0.297	-0.307
59	-0.033	-0.128	-0.023	-0.216	-0.347	-0.307	-0.342
60	0.009	-0.113	-0.045	-0.253	-0.373	-0.297	-0.349
61	-0.042	-0.108	-0.015	-0.232	-0.386	-0.283	-0.357
62	0.003	-0.121	-0.022	-0.255	-0.370	-0.301	-0.359
63	0.005	-0.119	-0.023	-0.255	-0.371	-0.300	-0.361
64	-0.041	-0.114	-0.024	-0.228	-0.382	-0.285	-0.350
65	-0.008	-0.110	-0.035	-0.256	-0.376	-0.284	-0.349
66	-0.041	-0.111	-0.016	-0.236	-0.375	-0.286	-0.352
67	0.011	-0.131	-0.041	-0.239	-0.382	-0.287	-0.353

Ascending Energy Order	Net Charge on atom (e)						
	S(1)	N(4)	N(14)	O(8)	O(12)	O(13)	O(17)
68	0.006	-0.123	-0.031	-0.247	-0.361	-0.309	-0.350
69	0.002	-0.107	-0.059	-0.261	-0.377	-0.285	-0.340
70	0.011	-0.132	-0.031	-0.242	-0.380	-0.289	-0.358
71	-0.014	-0.117	-0.005	-0.231	-0.349	-0.310	-0.352
72	-0.013	-0.114	-0.004	-0.244	-0.391	-0.273	-0.356
73	-0.039	-0.117	-0.026	-0.228	-0.376	-0.284	-0.347
74	-0.012	-0.120	-0.011	-0.243	-0.389	-0.274	-0.350
75	-0.006	-0.113	-0.033	-0.254	-0.362	-0.296	-0.349
76	-0.012	-0.123	-0.012	-0.232	-0.348	-0.309	-0.344
77	-0.039	-0.116	-0.014	-0.235	-0.374	-0.281	-0.352
78	-0.024	-0.104	-0.005	-0.245	-0.385	-0.286	-0.359
79	0.001	-0.116	-0.098	-0.242	-0.367	-0.299	-0.327
80	0.007	-0.125	-0.025	-0.253	-0.363	-0.307	-0.356
81	0.004	-0.108	-0.059	-0.260	-0.363	-0.295	-0.340
82	0.000	-0.128	-0.023	-0.247	-0.363	-0.307	-0.361
83	-0.021	-0.110	-0.012	-0.242	-0.382	-0.287	-0.353
84	-0.036	-0.123	-0.025	-0.226	-0.371	-0.282	-0.345
85	0.001	-0.114	-0.101	-0.249	-0.379	-0.292	-0.325
86	-0.006	-0.121	-0.023	-0.236	-0.360	-0.302	-0.358
87	-0.020	-0.112	-0.005	-0.248	-0.376	-0.279	-0.354
88	-0.020	-0.113	-0.013	-0.242	-0.375	-0.287	-0.351
89	-0.018	-0.119	-0.013	-0.241	-0.375	-0.279	-0.350
90	-0.017	-0.113	-0.076	-0.241	-0.380	-0.286	-0.308
91	-0.026	-0.114	-0.081	-0.240	-0.380	-0.286	-0.314
92	-0.013	-0.126	-0.077	-0.224	-0.359	-0.300	-0.305
93	-0.011	-0.124	-0.077	-0.229	-0.381	-0.284	-0.311
94	-0.020	-0.111	-0.052	-0.252	-0.383	-0.283	-0.329
95	-0.019	-0.123	-0.081	-0.239	-0.368	-0.287	-0.312
96	-0.019	-0.134	-0.038	-0.233	-0.322	-0.300	-0.299
97	0.135	-0.121	-0.009	-0.257	-0.388	-0.297	-0.292
98	0.136	-0.122	0.010	-0.257	-0.377	-0.302	-0.302
99	0.130	-0.116	-0.008	-0.266	-0.378	-0.304	-0.289
100	0.132	-0.118	0.005	-0.264	-0.384	-0.296	-0.298
101	0.105	-0.099	-0.013	-0.265	-0.387	-0.289	-0.282
102	0.108	-0.108	-0.005	-0.262	-0.397	-0.291	-0.290
103	0.109	-0.109	-0.014	-0.262	-0.375	-0.289	-0.282
104	0.110	-0.113	-0.004	-0.260	-0.378	-0.287	-0.290
105	0.107	-0.100	-0.012	-0.259	-0.367	-0.299	-0.283

Analysis of some energetic properties

Analysis of the HOMO and LUMO energies (Table 1) did not alow a clustering of the conformers with respect to the following geometric properties: pseudochirality of the N14 atom, *syn-anti* arrangement of the O17 and H28 atoms of the amidic group or the puckering class of the thiazolidinic ring (a, b, c) [1]. Average values of the above properties were calculated.

The HOMO and LUMO energy average values with respect to the (R, S) pseudochirality of the N14 atom are:

HOMO(R) = -9.585±0.312eV   LUMO(R) = -0.384±0.136eV
HOMO(S) = -9.519±0.360 eV   LUMO(S) = -0.355 ±0.152eV

They are not statistically distinct. However, comparing the average values for the R conformers with the average values of the S conformers it seems that the HOMO energies are lower for the (S) conformers, while the LUMO energies are higher for the (S) conformers, and the data dispersion (SD) is narrower. Overall, one can conclude that through the pyramidalization of the N(14) atom the HOMO and LUMO energies are not significantly described by the PM3 method.

The HOMO and LUMO energy average values calculated with respect to the *syn-anti* criterion are:

HOMO(*syn*) = -9.686±0.068eV   LUMO(*syn*) = -0.451 ±0.050eV
HOMO(*anti*) = -9.434±0.419eV   LUMO(*anti*) = -0.306 ±0.160eV

Compared to *anti*, the *syn* conformers have the HOMO energy average values lower and the LUMO energy values higher. Even if they are influenced by the *syn-anti* arrangement, the differences of the HOMO and LUMO energies, respectively, are not significant. In conclusion, the *syn-anti* arrangement of the O17 and H28 atoms has a weak influence on the HOMO and LUMO energy in the PM3 merthod.

The HOMO and LUMO energy average values calculated with respect to the puckering criteria of the thiazolidinic cycle (a, b, c) are:

HOMO(a) = -9.343±0.464 eV   LUMO(a) = -0.314 ±0.154eV
HOMO(b) = -9.510 ±0.350 eV   LUMO(b) = -0.345 ±0.157eV
HOMO(c) = -9.720 ±0.081 eV   LUMO(c) = -0.441 ±0.074 eV

There is a small difference between the average values of the three puckering classes. Due to the large dispersion for the HOMO in (b) puckering class, we cannot conclude that these average values are statistically distinct. However, we can make some remarks: the (b) puckering class has the lowest HOMO energy average values and the highest LUMO energy values.

To see the extent in which the HOMO and LUMO average values of the (a,b,c) puckering classes are influenced by the pyramidalization at

N(14) or by the *syn-anti* arrangement, the average values function of these criteria were calculated.

The HOMO and LUMO average values for the (a,b,c) puckering classes calculated function of the R-S pseudochirality are:

HOMO(R,a) = -9.106 ±0.540 eV   LUMO(R,a) = - 0. 213±0.144eV
HOMO(S,a) = -9.326 ±0.493 eV   LUMO(S,a) = - 0.347 ±0.129 eV
HOMO(R,b) = -9.580±0.321eV   LUMO(R,b) = -0.389±0.130eV
HOMO(S,b) = -9.443±0.369eV   LUMO(S,b) = -0.303±0.170eV
HOMO(R,c) = -9.700±0.076eV   LUMO(R,c) = -0.431 ±0.091 eV
HOMO(S,c) = -9.741 ±0.082eV   LUMO(S,c) = -0.452 ±0.052 eV

The statistical analysis of the data suggests that both for the average values of the HOMO and LUMO energies with respect to the (a), (b) and (c) puckering classes and the R-S N14 pyramidalization, there are no statistically distinct values.

The HOMO and LUMO average values for the (a,b,c) puckering classes calculated with respect to the *syn-anti* criterion are:

HOMO(*syn*,a) = -9.615±0.046eV   LUMO(*syn*,a) = -0.429 ±0.047eV
HOMO(*anti*,a) = -9.359 ±0.471 eV   LUMO(*anti*,a) = -0.284 ±0.176eV
HOMO(*syn*,b) = -9.667±0.073eV   LUMO(*syn*,b) = -0.451 ±0.063eV
HOMO(*anti*,b) = -9.396 ±0.423 eV   LUMO(*anti*,b) = -0.269 ±0.160eV
HOMO(*syn*,c) = -9.698±0.077eV   LUMO(*syn*,c) = -0.425 ±0.068eV
HOMO(*anti*,c) = -9.765 ±0.072 eV   LUMO(*anti*,c) = -0.474 ±0.078 eV

Even admitting a superimposition of the confidence intervals, we can appreciate that the average values are distinct only for the (c) puckering class. For (a) puckering class, the average values for the HOMO *syn* and *anti* energies are not distinct, while the LUMO energies are distinct and respect the rule of statistical differentiation: the LUMO(*syn*,a) energy is lower than the LUMO(*anti*,a) energy. For the (b) puckering class, the average values of HOMO as well as for LUMO energies are not statistically distinct: the (*anti*,b) average values are lower than the (*syn*,b) average values. For (c) puckering class, the average values of both HOMO and LUMO energies are statistically distinct, and the (*syn*,c) average values are lower than the (*anti*,c) average values. In conclusion, only in the (c) puckering class the *syn-anti* orientation influences significantly both the values of the HOMO and the LUMO energies.

These results prove that for all *syn-anti* conformers the HOMO and LUMO energies are influenced more by the spatial arrangement of the exocyclic amidic group, while the N14 atom pseudochirality does not influence significantly these values.

HOMO   LUMO

01pm3

HOMO   LUMO
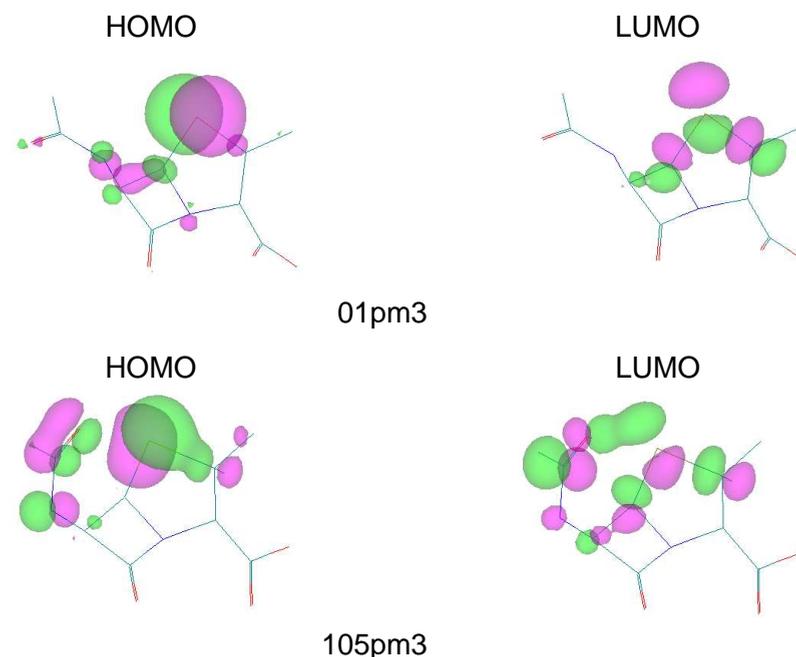
105pm3

Figure 2. The weight of the Sulphur (S1) atom in HOMO and LUMO of conformers 01pm3 (with the lowest energy) and 105 pm3 (with the worst concordance with experimental geometry) computed with PM3

Orbital distribution at HOMO and LUMO levels for the conformers: 01pm3 (with the lowest energy) and 105 pm3 (with the worst concordance with experimental geometry) are given in Figure 2 [1].

For all the conformers the contribution of the sulfur atom, S1 to the HOMO or LUMO level is the most important. For the HOMO level, the contributions of the σ bonds between C2-C9, C2-C10, C5-C6 and C5-H19 are important while of lower importance are the local contributions of the N4, O8, N14 and O17 atoms. For the LUMO level, the contributions of the C2 and C5 atoms are important and in a lower measure those of the N3, C6, C7 and O8 atoms.

Analyzing the data in Table 1 one can observe that there is no influence of the pyramidalization of the N14 atom on the dipole moment, as it results from the average values calculated with the R-S criterion: $\mu(R) = 3.447 \pm 1.010$ Debye, $\mu(S) = 3.203 \pm 1.055$. Even if these average values seem different, due to their high standard deviation they are not statistically distinct.

The influence of the *syn-anti* arrangement on the dipole moment is more obvious. The *syn* structures have lower values of the dipole moment in the interval 1.304 - 5.002 Debye for conformers 23pm3 and 70pm3,

120

respectively. Comparatively, the *anti* structures have higher values in the interval 0.567 - 4.907 Debye for conformers 97pm3 and 48pm3, respectively (Table 1).

The average values are μ(*syn*) = 2.889 ±1.076 Debye, and μ(*anti*) = 3.771 ±0.777 Debye. Statistically these average values are distinct.

The influence of the puckering on the dipole moment is proven by the average values for the three puckering classes (a,b,c):

$$\mu(a) = 3.488 \pm 1.234 \text{ Debye}$$
$$\mu(b) = 3.483 \pm 0.886 \text{Debye}$$
$$\mu(c) = 2.982 \pm 1.124 \text{ Debye}$$

Even if these average values are different, due to the high dispersion, they are not statistically distinct.

The influence of the *syn-anti* arrangement on the average values of the dipole moment, calculated with respect to the (a,b,c) puckering classes, are:

$$\mu(syn,a) = 3.759 \pm 1.174 \text{Debye}$$
$$\mu(anti,a) = 3.693 \pm 0.944 \text{ Debye}$$
$$\mu(syn,b) = 3.068 \pm 1.018 \text{ Debye}$$
$$\mu(anti,b) = 3.784 \pm 0.636 \text{ Debye}$$
$$\mu(syn,c) = 2.418 \pm 0.905 \text{ Debye}$$
$$\mu(anti,c) = 4.109 \pm 0.480 \text{ Debye}$$

From these data, for each puckering class there is an evident differentiation of the dipole moments function of the *syn-anti* arrangement.

As expected, these average values prove that for all conformers the dipole moment is strongly influenced by the *syn-anti* spatial arrangement of the O17 and H28 atoms of the exocyclic amidic group.

The minimum vibration energy, v_{min}, is a backbone vibration and all atoms are implicated in it through their out-of-the-plane vibration (Fig. 3). The v_{min} average value is of 27.733 ±10.605 cm^{-1}, with a large dispersion, which proves the dependence of this vibration on the conformation. The maximum vibration energy, v_{MAX}, is an elongation vibration implicated only in the bond between the O13 and H27 atoms and it takes place in the bond plane. Its average value is of 3844.159 ±35.529 cm^{-1} while disperion is large, which proves the non-dependence on the conformation. If the dependence of these vibrations on the N14 pyramidalization (R-S pseudochirality), on the *syn-anti* arrangement and on the puckering classes are taken into account, the following average values are obtained:

$v_{min.}(R) = 28.82 \pm 6.47$ cm^{-1} $v_{MAX.}(R) = 3847.58 \pm 3.04$ cm^{-1}

$v_{min.}(S) = 26.63 \pm 13.57$ cm^{-1} $v_{MAX.}(S) = 3840.67 \pm 50.40$ cm^{-1}

$v_{min.}(syn) = 26.03 \pm 13.69$ cm^{-1} $v_{MAX.}(syn) = 3847.25 \pm 2.76$ cm^{-1}

$v_{min.}(anti) = 29.47 \pm 5.66$ cm^{-1} $v_{MAX.}(anti) = 3841.01 \pm 50.46$ cm^{-1}

$v_{min.}(a) = 31.12\pm11.78$ cm^{-1} $v_{MAX.}(a) = 3847.98\pm2.90$ cm^{-1}
$v_{min.}(b) = 26.39\pm11.94$ cm^{-1} $v_{MAX.}(b) = 3841.84\pm48.21$ cm^{-1}
$v_{min.}(c) = 28.52\pm6.78$cm^{-1} $v_{MAX.}(c) = 3846.43\pm3.22$ cm^{-1}

Comparing these average values one observes that the $v_{min.}$ backbone vibration depends on the puckering classes, but is not influenced by pseudochirality and the *syn-anti* arrangement. At the same time the $v_{MAX.}$ vibration is not influenced neither by thepseudochirality, the *syn-anti* arrangement, nor by the puckering classes. We can generalize that, independent of the conformer, the vibrations of the functional groups are not influenced by the three factors: pseudochirality, *syn-anti* arrangement and puckering classes, while the vibrations involving the backbone depend on the puckering classes and do not depend on pseudochirality and *syn-anti* arrangement.

The average values of the puckering classes calculated for the backbone vibration energies v_{min}, and $v_{MAX.}$ with respect to the R-S pseudochirality or the *syn-anti* arrangement are:

v_{min} v_{max}

01pm3

v_{min} v_{max}

105pm3

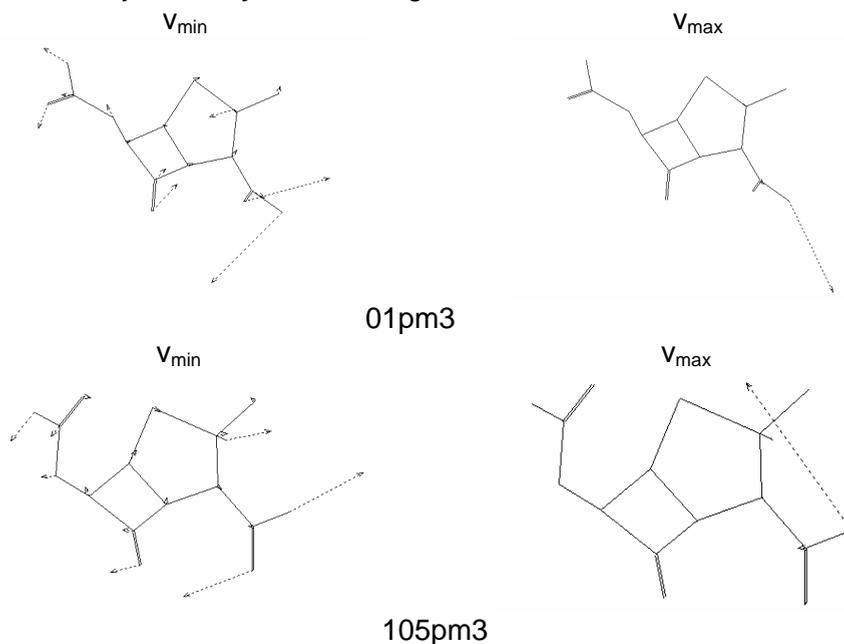**Figure 3.** Movement vectors proportional with force constants for vibration v_{min} and v_{MAX} of conformers 01pm3, 105pm3, computed b PM3.

$v_{min.}(a,R) = 27.50\pm5.68$cm^{-1} $v_{MAX.}(a,R) = 3849.57\pm1.97$ cm^{-1}
$v_{min.}(a,S) = 36.77\pm12.71$cm^{-1} $v_{MAX.}(a,S) = 3847.21\pm3.01$cm^{-1}
$v_{min.}(b,R) = 30.20\pm4.70$cm^{-1} $v_{MAX.}(b,R) = 3848.11\pm2.73$ cm^{-1}

$v_{min.}(b,S) = 22.70 \pm 15.34 \, cm^{-1}$ $v_{MAX.}(b,S) = 3835.78 \pm 67.55 \, cm^{-1}$

$v_{min.}(c,R) = 27.79 \pm 7.50 \, cm^{-1}$ $v_{MAX.}(c,R) = 3846.22 \pm 3.30 \, cm^{-1}$

$v_{min.}(c,S) = 29.30 \pm 6.08 \, cm^{-1}$ $v_{MAX.}(c,S) = 3846.66 \pm 3.22 \, cm^{-1}$

$v_{min.}(a,syn) = 35.25 \pm 15.77 \, cm^{-1}$ $v_{MAX.}(a,syn) = 3846.15 \pm 2.79 \, cm^{-1}$

$v_{min.}(a,anti) = 26.16 \pm 8.87 \, cm^{-1}$ $v_{MAX.}(a,anti) = 3848.64 \pm 2.82 \, cm^{-1}$

$v_{min.}(b,syn) = 22.17 \pm 16.79 \, cm^{-1}$ $v_{MAX.}(b,syn) = 3848.18 \pm 1.94 \, cm^{-1}$

$v_{min.}(b,anti) = 29.46 \pm 4.89 \, cm^{-1}$ $v_{MAX.}(b,anti) = 3837.22 \pm 63.34 \, cm^{-1}$

$v_{min.}(c,syn) = 27.31 \pm 6.12 \, cm^{-1}$ $v_{MAX.}(c,syn) = 3846.58 \pm 3.67 \, cm^{-1}$

$v_{min.}(c,anti) = 30.95 \pm 7.67 \, cm^{-1}$ $v_{MAX.}(c,anti) = 3846.15 \pm 3.25 \, cm^{-1}$

Comparing these data it seems that both pseudochirality and syn – anti arrangement do not influence the v_{min} and v_{MAX} vibration energies.

Based on the above results we can conclude that both the backbone vibrations as well as the vibrations of the functional groups do not depend on the *syn*-anti arrangement or the pseudochirality of the N14 atom. However, they depend significantly on the puckering class. For all the 105 conformers optimized with the PM3 method, the nature of these two types of vibrations do not change.

The equilibrium energy (ZPVE) is relatively constant around the average value of 149.935 ±0.331 kcal/mol. It is contained in the interval 149.164 kcal/mol and 150.744 kcal/mol. The average calculated values for ZPVE using the *syn-anti* arrangement, R-S pseudochirality and puckering classes criteria lead to the conclusion that this energy does not change. ZPVE is a measure which does not depend significantly on the conformer's nature.

The net charge on the S1 atom varies in relatively small limits, between 0.136 and -0.042. The average value for all conformers is $q_{S1} = -0.002 \pm 0.038$. The standard deviation is higher than the average value. To evidence some influences on the S1 charge a statistical analysis was performed applying the three criteria: the influence of the R-S pseudochirality, the influence of the *syn-anti* arrangement and the influence of the three puckering classes. The obtained average values are all almost zero and do not allow evidencing any dependence of the S1 atom charge on the three criteria:

$q_{S1}(S) = 0.0024 \pm 0.038$ $q_{S1}(R) = 0.0015 \pm 0.038$

$q_{S1}(anti) = 0.005 \pm 0.054$ $q_{S1}(syn) = -0.0001 \pm 0.008$

$q_{S1}(a) = 0.036 \pm 0.061$ $q_{S1}(b) = -0.003 \pm 0.038$ $q_{S1}(c) = -0.002 \pm 0.008$

The net charges on the atoms: q_{N4}, q_{N14}, q_{O8}, q_{O12}, q_{O13}, q_{O17} are all negative for all conformers (*Table 2*). Even if the two nitrogen atoms (N4, N14) are of the same type (amidic nitrogen), the N4 atom is strongly pyramidalized due to its steric vicinity in the two cycles. The N4 atom has a real pyramidalization, while N14 has a pyramidalization generated by the quanto-chemical computation method. The N4 atom has a negative net charge significantly higher than the exocyclic N14 notrogen atom. The average value of the charge is $q_{N4} = -0.118 \pm 0.007$, while $q_{N14} = -0.034 \pm 0.021$. The

net charge on N4 varies in quite small limits, between -0.137 and -0.099; it can be considered almost constant and independent of the conformation, while the net charge on N14 varies in large limits between -0.101 and 0.01 and depends on the conformation. For these two atoms (N4, N14) the average charges for the conformers with R and S pseudochirality are:

$$q_{N4}(R) = -0.118 \pm 0.007 \qquad q_{N14}(R) = -0.034 \pm 0.022$$
$$q_{N4}(S) = -0.117 \pm 0.007 \qquad q_{N14}(S) = -0.033 \pm 0.020$$

For the conformers with *syn-anti* arrangement they are:

$$q_{N4}(syn) = -0.117 \pm 0.006 \qquad q_{N14}(syn) = -0.042 \pm 0.017$$
$$q_{N4}(anti) = -0.118 \pm 0.007 \qquad q_{N14}(anti) = -0.025 \pm 0.021$$

and for the three puckering classes the average charges for N4 and N14 are:

$$q_{N4}(a) = -0.127 \pm 0.006 \qquad q_{N14}(a) = -0.020 \pm 0.014$$
$$q_{N4}(b) = -0.116 \pm 0.006 \qquad q_{N14}(b) = -0.029 \pm 0.019$$
$$q_{N4}(c) = -0.114 \pm 0.004 \qquad q_{N14}(c) = -0.048 \pm 0.019$$

These average charges show that the net charges for the two amidic nitrogen atoms do not differ significantly from the average values of all conformers. Even if for the N14 atom the values are different between R and S and *syn* and *anti*, because of the high standard deviations their charges are not statistically distinct. For N14 there is a certain dependence on the puckering classes. On N14 the lowest charge is for class c, followed by class a, and the most negative charge is obtained for the puckering class b. Taking the puckering classes into account together with *syn-anti* or R-S criterion one does not observe any supplementary regularity. From these data one can draw the conclusion that the net charges on the N4 atom are relatively constant and independent of the conformation. For the N14 atom the net charge depends obviously on the conformation. This fact is demonstrated by the high dispersion of the values. There is a certain regularity, but only function of the puckering class.

The average value of the net charge on the O8 β-lactamic atom: $q_{O8} = -0.242 \pm 0.011$ is lower than the average values of the net charges for the other oxygen atoms: $q_{O12} = -0.371 \pm 0.011$, $q_{O13} = -0.292 \pm 0.008$, $q_{O17} = -0.341 \pm 0.021$. The q_{O8} net charge is relatively constant, independent of the conformation and varies between -0.266 and -0.216. On the atoms O12, O13 and O17 the net charge varies between -0.397 and -0.322, -0.31 and -0.272 and respectively -0.362 and -0.282. For these oxygen atoms the average values of the net charge taking the R and S pseudochirality into account, are:

$$q_{O8}(R) = -0.241 \pm 0.011 \qquad q_{O8}(S) = -0.242 \pm 0.011$$
$$q_{O12}(R) = -0.371 \pm 0.011 \qquad q_{O12}(S) = -0.372 \pm 0.009$$
$$q_{O13}(R) = -0.292 \pm 0.008 \qquad q_{O13}(S) = -0.291 \pm 0.008$$
$$q_{O17}(R) = -0.341 \pm 0.021 \qquad q_{O17}(S) = -0.340 \pm 0.022$$

Taking into account the *syn-anti* arrangement, the average charges are:

$q_{O8}(syn) = -0.243\pm0.008$ $\qquad$ $q_{O8}(anti) = -0.241\pm0.012$
$q_{O12}(syn) = -0.370\pm0.006$ $\qquad$ $q_{O12}(anti) = -0.372\pm0.013$
$q_{O13}(syn) = -0.293\pm0.006$ $\qquad$ $q_{O13}(anti) = -0.291\pm0.010$
$q_{O17}(syn) = -0.346\pm0.013$ $\qquad$ $q_{O17}(anti) = -0.335\pm0.026$

and taking the three puckering classes into account the following average values are obtained:

$q_{O8}(a) = -0.249\pm0.009;$ $\quad$ $q_{O8}(b) = -0.240\pm0.011$ $\quad$ $q_{O8}(c) = -0.240\pm0.009$
$q_{O12}(a) = -0.371\pm0.015$ $\quad$ $q_{O12}(b) = -0.372\pm0.011$ $\quad$ $q_{O12}(c) = -0.369\pm0.006$
$q_{O13}(a) = -0.298\pm0.005$ $\quad$ $q_{O13}(b) = -0.290\pm0.011$ $\quad$ $q_{O13}(c) = -0.291\pm0.005$
$q_{O17}(a) = -0.336\pm0.029$ $\quad$ $q_{O17}(b) = -0.341\pm0.021$ $\quad$ $q_{O17}(c) = -0.342\pm0.015$

Statistically, it results that the oxygen net charges do not differ significantly from the average values for all conformers. If the puckering classes and the *syn-anti* or R-S criteria are taken into account, there is also no regular pattern.

Based on these results we can affirm that the net charges do not fluctuate following certain regular patterns. The only exception is the N14 atom whose net charge depends on the conformation. This means that the conformational changes generated by the rotation of the free groups and by the different puckering classes do not influence significantly the charges, except for the N14 atom.

The effect of this relatively constant distribution on the net charges determines an isosurface of the electrostatic potential relatively similar for all conformers. This is illustrated by the isosurface of the electrostatic potential presented in Fig. 4 for the conformers of the minimum energy (01pm3) and maximum energy (105pm3), respectively. The iso-surfaces of the electrostatic potential depend in a small degree on the spatial arrangement mode of the exocyclic groups attached to the N14 amidic atom.
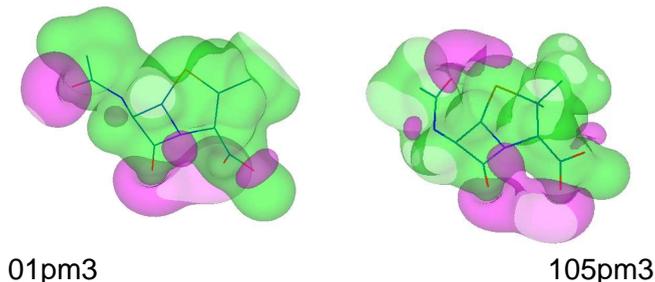
01pm3 $\qquad\qquad\qquad\qquad$ 105pm3

Figure 4. Iso-surface of the electrostatic potential computed with PM3 for the contour value of 0.04, for conformers 01pm3,and 105pm3.

In case the atoms O8 and O17 are closer, an extended negative potential occurs (the case of conformer 105pm3). Function of distance between the O12 or O13 atoms and the N4 atom, the isosurface of the negative electrostatic potential changes its shape (the case of conformer 01pm3).

CONCLUSIONS

A conformational analysis performed by the PM3 method on the 105 conformational isomers of (3S,5S,6S)-6-acetylamidopenicillanic acid led to the conclusions:

- for all the conformers, the pseudochirality of the atom N14 does not influence significantly the HOMO and LUMO energies. On the contrarily, the energy of these levels is influenced by the *syn-anti* arrangement of the exocyclic amidic group as well as by the puckering of the thiazolidinic ring.

- the analysis of orbital contribution to the HOMO and LUMO levels, suggested the S1 atom has the dominant contribution, while the geometry factors - pseudochirality of the N14 atom, the *syn-anti* arrangement and the puckering of the thiazolidinic cycle do not influence significantly this contribution.

- the dipole moment is influenced strongly by the *syn-anti* arrangement. The puckering slightly influences the dipole moment, while the pseudochirality does not influence it at all.

- from the vibration analysis one can draw the conclusion that both the backbone vibrations as well as the vibrations of the functional groups do not depend by the *syn-anti* arrangement or by the pseudochirality at the N14 atom, but depend significantly on the puckering. ZPVE does not depend significantly on the geometry of the conformer.

Analysing the average values of the net atomic charges one can conclude that the charge densities on the N4 atom are not dependent on conformation, they being almost constant. For the N14 atom the net density is dependent on the conformation and this was proved by the high dispersion of the values. There is a certain pattern with respect of the puckering, but such pattern was not observed for pseudochirality or the *syn-anti* arrangement. The constant charge distribution leads to an isosurface of the electrostatic potential relatively similar for all conformers.

METHODS

Gas phase equilibrium geometry of conformers was obtained by semiempirical PM3 calculations with an SCF convergence of 10^{-5}, and an RMS gradient of 10^{-2} kcal/Å·mol [2,3]. Conformational search was performed by varying the C2-C3-C11-C12, C5-C6-N14-C15 and C6-N14-C15-C16 dihedrals in the range 0 ±180° with steps of 15°. Energy crit erion was set to 30 kcal/mol

above the minimum energy conformer. Calculations have been performed with Conformational Search module [4], from HyperChem7.52 package [5].

ACKNOWLEDGMENTS

REFERENCES

1. D. Ivan, M. Mracec, *Annals of West Univerity of Timisoara,* **2010**,*19(4)*,83.
2. C. D. Nenițescu, "Chimie organică" Vol. 2, Editura Didactică and Pedagogică, Bucureşti, **1968**, Ed. 6-a, 629.
3. I. N. Levine, "Quantum Chemistry", 5th Edition, Prentice Hall, Inc., Upper Saddle River, New Jersey 07458, **2000,** Chap. 15, Chap. 17.
4. M. J. S. Dewar, E. G. Zoebisch, E. F. Healy, and J. J. P. Stewart, *Journal of The American Chemical Society*, **1985**, *107*, 3902.
5. *** ChemPlus 1.6[TM], "Extension for HyperChem[®], Molecular Modeling for Windows[TM]", Hypercube, Inc., Gainesville, Florida, US, 1994, Chap. 8.
6. *** HyperChem[TM], Release 7.52 for Windows, Copyright 2003, Hypercube, Inc, 1115 NW 4th Street, Gainesville, FL 32601, US.
7. M. Mracec, M. Schulz, E. Şişu, N. Dincă, and M. Mracec, *Science and Technology Bulletin of University "A. Vlaicu" Arad,* **2007,** *12,* 1.
8. I. Csoregh, and T.-B. Palm*, Acta Crystallogr., Sect.B: Struct. Crystallogr. Cryst.Chem.,***1977**,*33*,2169.
    http://www.middlebury.edu/~ch0337/atteridge/penicillin/fig1.gif

^{13}C NMR STUDY OF GAMMA IRRADIATED POLYSTYRENE

MIHAELA POP[a], STEFAN TRAIAN[a], LIVIU DARABAN[a], RADU FECHETE[b]

ABSTRACT. The ^{13}C CP/MAS NMR spectra of *polystyrene* were recorded for un-irradiated samples and for samples exposed to a 8989 Gy dose of gamma radiation. The most intense peaks of unirradiated sample appear at 145 and 127 ppm and are assigned to non-protonated and protonated aromatic carbons, respectively. The gamma irradiation leads to an important decay of $T_{1\rho}$ relaxation time corresponding to aromatic and methylene-methine functional groups.

Keywords: Polystyrene, ^{13}C CP/MAS NMR, $T_{1\rho}$

INTRODUCTION

Polymeric materials are strongly affected by ionizing radiation. Based on different values of the absorbed dose, radiation effects on polymers may be classified as follows: i) scission and/or cross-linking of the polymer chains with a consequent molecular weight decrease and/or increase; ii) occurrence of chemical reactions leading to small volatile products and, eventually, organic radicals and iii) occurrence of structural modifications of polymer chains, such as changes in the number of unsaturations, presence of charged units. Such modification can be observed by the use of methods and techniques sensitive to the physical phenomena occurring an atomic and molecular scale, as NMR. This method provides information concening the chemical shift, relaxation process of the magnetization of molecular spins, interaction between neighboring atoms [1]. Using cross-polarization magic angle spinning experiments improved signals can be obtained for nuclei with low gyromagnetic ratio or poor natural abundance sach as ^{13}C nuclei [2]. Other information, such the existence of crystalline and amorphous phase, can be used in NMR experiment special pulse sequence excitation.

Such methods were used to investigate posible modifications induced by gamma irradiation on the structure of polystyrene.

[a] *"Babes-Bolyai" University, Faculty of Physics, M. Kogalniceanu No 1, 400084 Cluj-Napoca, Romania, profmihaelapop@yahoo.com*
[b] *"Technical University" of Cluj-Napoca, Physics Department, Str. Memorandumului nr. 28, 400114, Cluj-Napoca, Romania*

RESULTS AND DISCUSSION

In chemical terms, polystyrene is a long chain hydrocarbon wherein alternating carbon centers are attached to phenyl groups (Figure 1).

Some properties of such materials are determined by short range van der Waals attractions between polymers chains. Since the molecules are long hydrocarbon chains, that consist of thousands of atoms, the total attractive force between the molecules is large. Polystyrene results when styrene monomers interconnect. In the polymerization one carbon-carbon double bond (in the vinyl group) is replaced by a much stronger carbon-carbon single bond, hence it is very difficult to depolymerize polystyrene. Typically about a few thousand monomers comprise a chain of polystyrene, giving a molecular weight of 100,000-400,000.

A 3-D model would show that each of the chiral backbone carbons lies at the center of a tetrahedron, with its 4 bonds pointing toward the vertices. Say the -C-C- bonds are rotated so that the backbone chain lies entirely in the plane of the diagram. From this flat schematic, it is not evident which of the phenyl groups are angled toward us from the plane of the diagram, and which ones are angled away. Following the alternation of styrene groups, the polystyrene can adopt sindiotactic or atactic conformations. The isomer where all of them are on the same side is called *isotactic* polystyrene, which is not produced commercially. Sindiotactic arrangement of atoms corresponds to more local order and is characteristic for crystaline phase of the samples. Atactic conformation means less local order and it characteristic for amorphous phase.
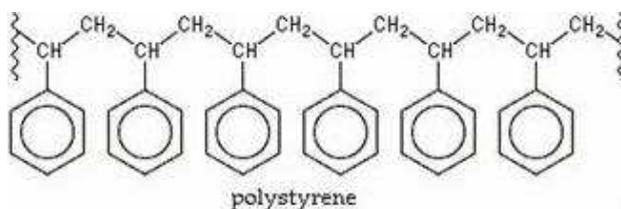
Figure. 1 Chemical structure of polystyrene

Such bonds can be affected by external physical excitations like gamma radiation, resulting in breaking of the chains with corresponding reducing of molecular mass, or modification of local conformation. On the molecular scale the modification of the conformation can affect the vecinity of the nuclear spins attached to the polymeric chain. Two mechanisms can be taken into account: the chemical shift and the relaxation of the magnetization of the nuclear spins. Our interest was to observe such modifications on polystyrene samples irradiated at different doses with gamma photons. For this aim, the high resolution spectra of non-irradiated sample were compared with the spectrum of the irradiated one.
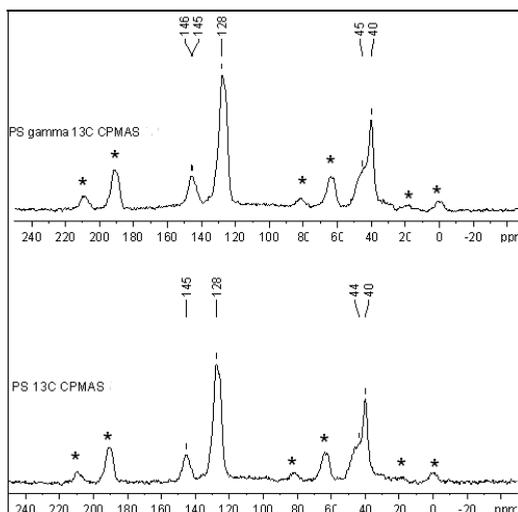
Figure. 2 The CP/MAS ¹³C NMR spectra of un-irradiated and gamma irradiated polystyrene

Figure 2 shows the CP/MAS ¹³C NMR spectra of commercial PS recorded at room temperature. A control measurement was performed on un-irradiated polystyrene samples. To correctly assign the signals of PS we used the data described in the literature [2, 3]. Resonances at 145 and 128 ppm were assigned to non-protonated and protonated aromatic carbons, respectively. Methylene and methyne carbon resonances were ascribed signals at 46 and 40 ppm, respectively [4]. All observed resonance lines were very broad, as the material is an amorphous polymer. The remaining of CP MAS ¹³C NMR spectra signals are sppining side bands.[2]

Next, we studied the polystyrene gamma irradiated sample. Gamma radiation can excite the electrons from theirs initial state higher energy level and can even break chemical bonds. We expect that the radiation may produce some structural changes, with corresponding chemical shift of the resonance lines. Gamma irradiated sample shows the same peaks but with smaller amplitude. In the table I we can see the chemical shifts peaks of CP/MAS ¹³C NMR spectra of polystyrene before and after gamma irradiated.

Table 1. NMR parameters for PS

un-irradiated PS (ppm)	gamma irradiated PS (ppm)
40	40
44	45
128	128
145	145

Note that basedon the NMR spectra there was no change in the chemical bonds induced by such doses.

In order to quantify the effects of irradiation on the polystyrene chain dynamics the longitudinal relaxation times in rotating frame, $T_{1\rho}$ for different functional groups (aromatic, aliphatic), were measured. The evolution of the spin system magnetization function of spin-lock time τ, for different functional groups in un-irradiated and gamma irradiated polystyrene, shows multi- or mono-exponential dependences (see Figure 3). Therefore, the values of $T_{1\rho}$ can be determined by fitting the decays corresponding to the aromatic component (filled symbols in Figure 3) with a bi-exponential decay given by,

$$M(\tau) = M_0^{(f)} \exp\left\{-\frac{\tau}{T_{1\rho}^{(f)}}\right\} + M_0^{(s)} \exp\left\{-\frac{\tau}{T_{1\rho}^{(s)}}\right\}, \tag{1}$$
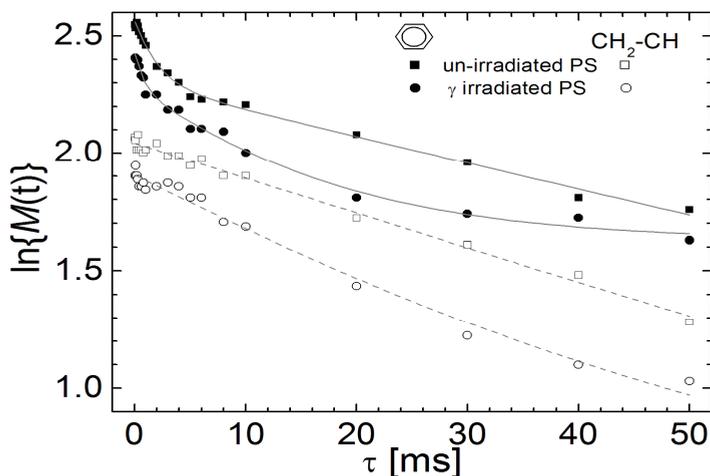
Figure. 3 Logarithmic plots of ^{13}C resonance intensities corresponding to aromatic (filled symbols) and methylene-methine (open symbols) functional groups function of spin-lock time τ for un-irradiated (squares) and gamma irradiated polystyrene (circles).

where $M_0^{(f)}$ is the equilibrium magnetization and $T_{1\rho}^{(f)}$ the relaxation time in rotating reference frame of the fast decaying component and $M_0^{(s)}$ is the equilibrium magnetization and $T_{1\rho}^{(s)}$ the relaxation time in rotating reference frame of the slow decaying component. The values of $T_{1\rho}$ corresponding to

the methylene-methine component can be found by fitting the decays (open symbols in Figure 3) with a mono-exponential decay given by [5].

Table 2. Relaxation times for PS

Sample	C protonated aromatic		C methylene-methine
	$T_{1\rho}^{(f)}$ (ms)	$T_{1\rho}^{(s)}$ (ms)	$T_{1\rho}$ (ms)
PS un-irradiated	1.9	81.3	63.8
PS gamma irradiated	0.7	14.3	32.7

$$M(\tau) = M_0 \exp\left\{-\frac{\tau}{T_{1\rho}}\right\}, \qquad (2)$$

The experimental data were fitted with equation (1), continuous lines in figure 3, or eq. (2), dashed line in figure 3, and the corresponding $T_{1\rho}$ values are summarized in Table II. One can observe a general decrease of $T_{1\rho}$ after irradiation. The $T_{1\rho}^{(f)}$ corresponding to aromatic groups is reduced at half for the gamma irradiated polystyrene sample, while a dramatically effect off irradiation can be observed for the slow decaying components since the $T_{1\rho}^{(s)}$ decays with approximately 5.7 time after irradiation. The $T_{1\rho}$ relaxation time in rotating reference frame corresponding to methylene-methine functional group decays also approximately two times. All these results can be associated with a low effect of crystallization induced by irradiation.

Analyzing the $T_{1\rho}$ values we observed that the carbons showed different values depending on the gamma doses. They can be attributed to the fact that the microstructure has different molecular mobility and consequently belongs to different domains [6].

CONCLUSIONS

The effect of gamma radiation on the properties of polystyrene was investigated by CP/MAS ^{13}C NMR spectroscopy. The $T_{1\rho}$ of the protonated carbon located in different functional groups were measured by combining the solid state CP/MAS with the spin-lock experiments. The $T_{1\rho}$ values obtained for PS gamma irradiated samples were several times smaller than those for un-irradiated PS. These results make it possible to obtain information on the polymer microstructure, showing that the radiation gamma led to a decrease of PS molecular mobility. Changes in the microstructure of polystyrene

are due to rupture of molecular bonds. After irradiation the shrinkages and collapse of PS chains take place.

EXPERIMENTAL SECTION

Polystyrene was received as a gift sample from SC Napochim SA (Cluj Napoca). The samples were exposed to gamma radiations using a source of ^{60}Co, which offers a high and compact density of radiation, [4]. The doze of radiation was D = 5,3Gy/h and samples were exposed until 8989 Gy Solid state ^{13}C NMR spectra were recorded at 500 MHz ^{13}C Larmor frequency with a Bruker Avance 500-spectrometer. All NMR experiments were performed at room temperature and the sample was centred- packed in zirconium rotors. In the modified CP/MAS experiment, the proton field was turned off after cross-polarization. After a delay ranging from 10 µs to 100 ms, the acquisition was performed under high-power decoupling.

For proton relaxation time in the rotating frame ($T_{1\rho}$) measurements, we used the normal cross-polarization pulse sequence. The magnetization initially builds up to a maximum due to de carbon-proton dipolar interactions, and the signal decays exponentially to equilibrium with time constant $T_{1\rho}$ [7]. Thus $T_{1\rho}$ can be obtained from a semi-log plot of the intensity as a function of spin-locking time (t) after the signals have reached their maximum intensity [8].

ACKNOWLEDGMENTS

REFERENCES

1. M.Todica, " Metode Aplicative de Rezonanță Magnetică Nucleară ", Presa Universitara Clujeana, **2001,** 5.
2. C. R. Martins,F. Hallwass**,** Annals of Magnetic Resonance **2007**, 6,46.
3. R.R. Wu, H.M. Kao, J.C. Chiang, E.M. Woo, Polymer **2002,** 43, 171.
4. M. Li, C. Li, B. Zhang, W. Huang, A. Men, B. He, European Polymer Journal **1998,** 34, 515.
5. T. Nakaoki, M. Kobayashi, Journal of Molecular Structure **2003,** 343.
6. S.G.Bond,J.R.Ebdon,M.N.Hussin, Polymer **1998**, 39, 6875.
7. E.O. Stejskal, J.D. Memory, High Resolution NMR in the Solid State,**1994,** 35, 48.
8. N.Carretta,V.Tricoli, F.Picchioni, Journal of Membrane Science , **2000,** 166, 189

COMPUTATION INFORMED SELECTION OF PARAMETERS FOR PROTEIN RADICAL EPR SPECTRA SIMULATION

DIMITRI A. SVISTUNENKO[a], MARY ADELUSI[a], MARCUS DAWSON[a], PAUL ROBINSON [a], CATERINA BERNINI[b], ADALGISA SINICROPI[b], RICCARDO BASOSI[b]

ABSTRACT. Many important enzymatic reactions are characterised by free radical intermediates that can be detected experimentally. EPR spectroscopy can be used for monitoring formation of free radical states in enzymes. This provides vital information about the kinetic mechanism of the reactions. To uncover the molecular mechanism of the enzyme, it is necessary to know which part of the enzyme is involved in the electron transfer - where on the enzyme the radical is formed. This question is often addressed by site directed mutagenesis methods. However, the conclusions drawn from such studies are often ambiguous. A complementary method will be presented that allows radical site assignment on the basis of the EPR spectrum lineshape. Computer simulation of the lineshape requires a large number of parameters to be explicitly specified. These parameters are intimately linked to the radical conformation and its immediate microenvironment. Thus, provided the 3D structure of the enzyme is known, an experimental spectrum can be related to a specific amino acid residue in the enzyme. Unfortunately, the credibility of such approaches is weakened by the large number of input parameters in the EPR spectral simulation procedure. This difficulty can be overcome by finding relationships between these parameters. These relationships can be used for diminishing the dimension of the input parameters space. We have performed Density Functional Theory (DFT) calculations of EPR parameters of model tyrosine and tryptophan (neutral) radicals for an array of the residues' conformations, each of which is involved in a hydrogen bond of variable strength. Calculated EPR parameters are thus presented as dependences on two variables. This opens the possibility to formulate continuous functions that allow one to significantly diminish the input parameters space dimension. Successful derivation of such functions might lead to a method when an experimental EPR spectrum of a protein radical can be confidently used to pinpoint the radical location in a protein, if the protein structure is known.

Keywords: *Tyrosine radical; Tryptophan radical; Enzymes; EPR, DFT*

[a] *Department of Biological Sciences, University of Essex, Wivenhoe Park, Colchester, Essex CO4 3SQ, United Kingdom, svist@essex.ac.uk*
[b] *Department of Chemistry, University of Siena, Via A. De Gasperi 53100 Siena - Italy*

INTRODUCTION

Many biological enzymes operate by employing a free radical in their mechanisms. In absolute majority of reported cases, the free radical is found either on a tyrosine (Tyr) or on a tryptophan (Trp) of polypeptide part of the enzyme. Examples of the first include: ribonucleotide reductase [1-3], prostaglandin H synthase [4,5], catalase-peroxidase [6,7], cytochrome *c* oxidase [8], galactose oxidase [9], glyoxal oxidase [10], dehaloperoxidase [11]. Trp radicals have been reported in cytochrome *c* peroxidase [12], DNA photolyase [13,14], ribonucleotide reductase [15,16], lignin peroxidase [17], ascorbate peroxidase [18], cytochrome *c* oxidase [19,20], versatile peroxidase [21-24].

Free radicals may also form on the proteins that are not enzymes and thus do not catalyse structural modification of molecules but rather have functions of electron transfer or small molecule (e.g. O_2, NO) binding for further storage and/or transfer. Haem containing globins represent a class of such molecules, and both Tyr and Trp radicals have been shown to form on the globins when they are treated with peroxides [25-30].

The method of Electron Paramagnetic Resonance (EPR) spectroscopy allows detection of these protein bound radicals with a great degree of detail, sufficient not only to tell one radical type from another, but also to resolve differences between radicals of *the same type* if they are located at *different sites* of the protein. Thus, an EPR spectrum of a protein bound radical can be used, in principal, to figure out where on protein the radical is located.

The knowledge of radical's location is always required for understanding of the molecular mechanism of enzymes. When this knowledge is complemented with kinetic studies of the radical formation and decay, the mechanisms can be elucidated [11]. The question of radical location in proteins and enzyme is often addressed by the site directed mutagenesis method. This, however, might lead to erroneous conclusions because replacement of a residue that is not the radical's site but a site involved in the radical transfer towards the final location where the radical is observed, would affect the EPR spectrum as if the removed residue is actually the radical's host [31].

EPR spectra of radicals can be simulated on computer. Input parameters for an EPR spectra simulation program are those bits of information that are very specific to the radical type and its immediate molecular environment. The values of these parameters have to be translated into structural information, if one wants to determine a radical's location from its EPR spectrum. This is not a straightforward task since it is dozens of numerical parameters that have to be specified as an input for an EPR spectrum simulation. The Tyrosyl Radical Spectra Simulation Algorithm (TRSSA) [32] is a tool that allows diminishing the dimension of this input

136

space into just two truly independent input variables. These two variables are the spin density on a tyrosine's atom C1 and the rotation angle of the phenoxyl ring. To formulate a similar algorithm for Trp radicals would mean to find relationship between parameters of a Trp radical spectrum simulation and to link these relationships with as few input parameters as possible. This has not been done yet.

In order to advance in creating such an algorithm, we undertook a computational study of how EPR simulation parameters for Trp and Tyr radicals depend on two major structural factors, on the angle of rotation of the phenoxyl (in Tyr) or indole (in Trp) ring and on the strength of hydrogen bond the radicals might be engaged with. Computational works previously performed on protein radicals have demonstrated that the ring rotation angle should have a significant effect on the hyperfine interaction constants of the methylene protons, whereas a hydrogen bond should affect the g-factors, particularly the biggest, the g_x component [33-37]. In this work, we studied these effects systematically on a full range of the rings rotation (at a 30° interval) and on a range of hydrogen bond stren gths corresponding to the range of its length of 1.55-4.2 Å

RESULTS AND DISCUSSION

Model structures of tyrosyl and tryptophanyl radicals (Figure 1) were used to generate an array of input files for the calculation of the EPR parameters. Different rotational orientations of the rings (a full 360° turn at a 30° interval, Figure 2) were considered. For each of the ring rotation angles, a set of 6 values of distance d was considered. In total, 144 structures were used in the calculations, this is 2 radical types x 12 ring rotation orientations x 6 distances to water

Figure 3 shows dependences of the calculated principal g-factor values on the length of the hydrogen bond for tyrosyl and tryptophanyl radicals, when the ring rotation angle ϕ (ϕ_6 for Tyr and ϕ_4 for Trp) was 60°. The y and z components of the g-factors of both Tyr and Trp radicals are practically invariant when the strength of the hydrogen bond is varied. In contrast, the g_x component of both radicals exhibits a noticeable decrease in value when the length of the H-bond becomes shorter, i.e. the bond becomes stronger. This is in agreement with previous reports [35,37-39]. Although the g-values of both radicals show similar qualitative behavior as functions on distance d, (Figures 3, A and B), the absolute spreads of the values are quite different quantitatively: if plotted on the same scale, the three curves shown in pane B will be accommodated inside the grey area in pane A.
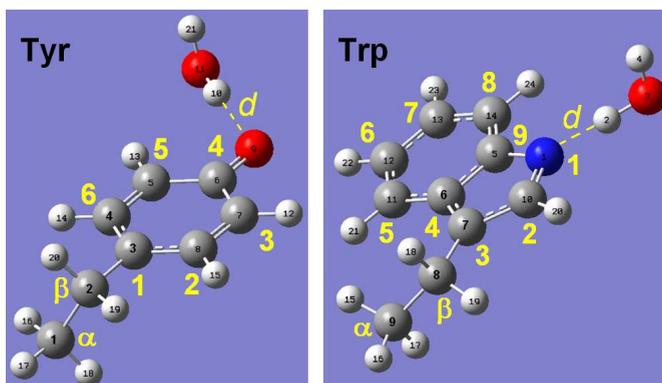
Figure 1. Basic Tyr and Trp model structures used in the computations. Numbers in a bigger font size and Greek letters α and β represent conventional atom nomenclature in the two structures, whereas the smaller font size labels on the atoms stand for the internal numbering used in the computation. A water molecule is bound to the phenoxyl oxygen in the tyrosyl radical (left) and to the indole nitrogen in the tryptophanyl radical (right). The hydrogen bonds are shown as dashed lines, their lengths d were varied in the calculations. Also varied were the rotational orientations of the phenoxyl ring (around the Cβ-C1 bond) and indole ring (around Cβ-C3 bond) – dihedral angles ϕ_6 = Cα-Cβ-C1-C6 (Tyr) and ϕ_4 = Cα-Cβ-C3-C4 (Trp), respectively.

Dependences plotted for other rotational orientations of the phenoxyl (Tyr) and indole (Trp) rings were very similar to those shown in Figure 3. In fact, the g-factor values plotted as dependences on rotation angle, for a fixed H-bond distance, were practically horizontal lines (Figure 4). Apparently greater variations of the g-values in Trp radical are illusive: when plotted on the same scale with Tyr radicals, the three curves shown in pane B will be accommodated within the narrow grey strip in pane A (Figure 4)

Very small variations on ring rotation angle in the g-values have a 120° period for Trp radical, with maxima at ϕ_4 = 60°, 180° and 300° (Figure 4, B) whereas the Tyr dependences have a period of 180° with extreme values of the three g-factors at ϕ_6 = 0° and 180° (not shown).

Principal g-values of Tyr radicals are much wider spread as compared to principal g-values in Trp radicals (Figures 3 and 4). The width of the spread behaves similar in two radicals when the strength of the hydrogen bond changes: the shorter the bond, the smaller the g_x value and therefore smaller the spread. Hydrogen bond strength has been linked before to the spin density on the Cγ atom of tyrosyl radical, on C1 [32]. It has been demonstrated that the stronger the hydrogen bond, the higher the spin density on C1 [32,38,39]. This finding was new and very useful in TRSSA

since it allowed using one parameter, P_{C1}, in finding apparently independent entities required for an EPR spectrum simulation – the hyperfine interaction constants for the Cβ protons in accordance with empirical McConnell relationship [40], but also the g-factor. Now it appears that the situation with Trp radicals is quite different. Instead of a positive, it is a negative dependence between the strength of the hydrogen bond and the spin density on the Cγ atom: the shorter the distance of the H-bond (the stronger the bond), the smaller the g_x value is and the smaller the P_{C3} is (Figure 5). This is a clear effect of the nature of the ring (indole ring instead of phenoxyl) with a different distribution of the spin density over the atoms.
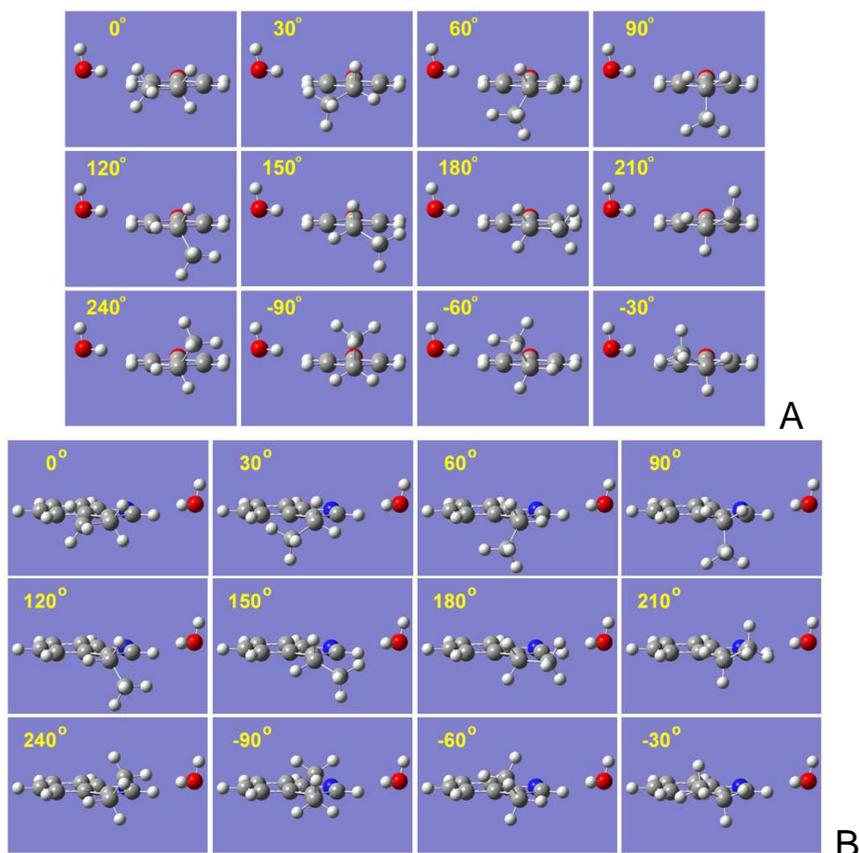
Figure 2. Twelve rotational conformations of the phenoxyl ring (plus water, $d = 4.20$ Å) in tyrosyl radical (A) and twelve rotational conformations of the indole ring (plus water, $d = 4.20$ Å) in tryptophanyl radical (B). The values of the dihedral angle $\phi_6 = $ Cα-Cβ-C1-C6 (in Tyr, A) and $\phi_4 = $ Cα-Cβ-C3-C4 (Trp, B) are shown on each pane.
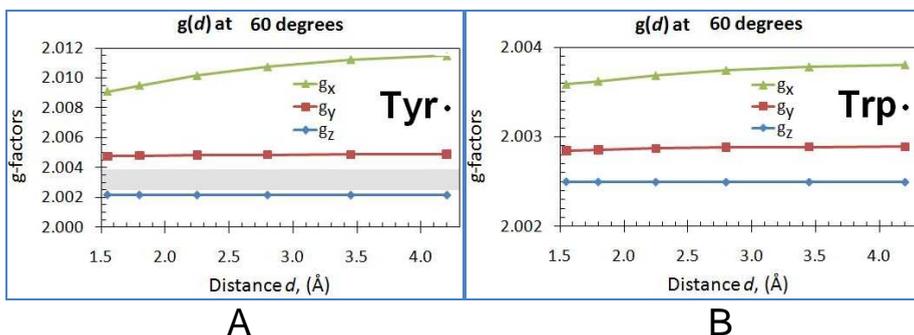
Figure 3. Three principal g-values of Tyr (A) and Trp radicals (B) as functions of the hydrogen bond length d. The calculations were performed for the phenoxyl ring rotation angle $\phi_6=60^o$ and the indole ring rotation angle $\phi_4=60^o$. The range of g-values coloured grey in pane A corresponds to the range of the g-factor values calculated for a Trp radical presented in pane B.
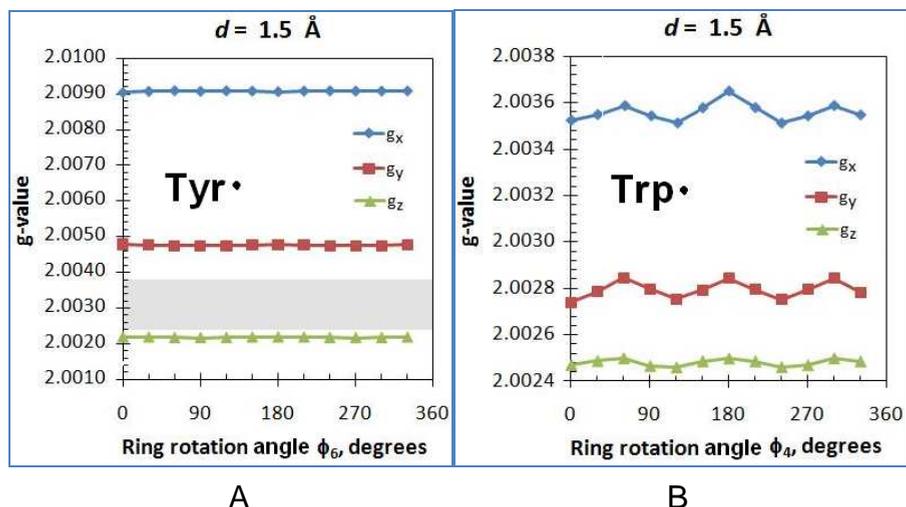
Figure 4. Three principal g-values of Tyr (A) and Trp radicals (B) as functions of phenoxyl or indole ring rotation angle. The data are presented for the case of the hydrogen bond length of 1.5 Å, in both radicals.

Knowing the hyperfine interaction constants for protons and nitrogens is vital for EPR spectra simulation. Generally it is accepted that a variation of the spin density distribution on a radical caused by interaction with the environment, particularly with the groups able to create H-bonds, does not affect the hyperfine interaction constants A very strongly. Thus the length of the H-bond is not expected to have a significant effect on these parameters. In contrast, rotation of the ring, either in Tyr or in Trp,

while having a minimal effect on the hyperfine interaction constant of the ring protons (and of the indole nitrogen in the Trp case) should have a dramatic effect on the constants of the two methylene proton of the β carbon (β-protons). Figure 6 illustrates these dependences for the β protons in Tyr and Trp radicals for the case of H-bond length of 1.8 Å. A periodical pattern of change of the constants is in agreement with the McConnell relationship.
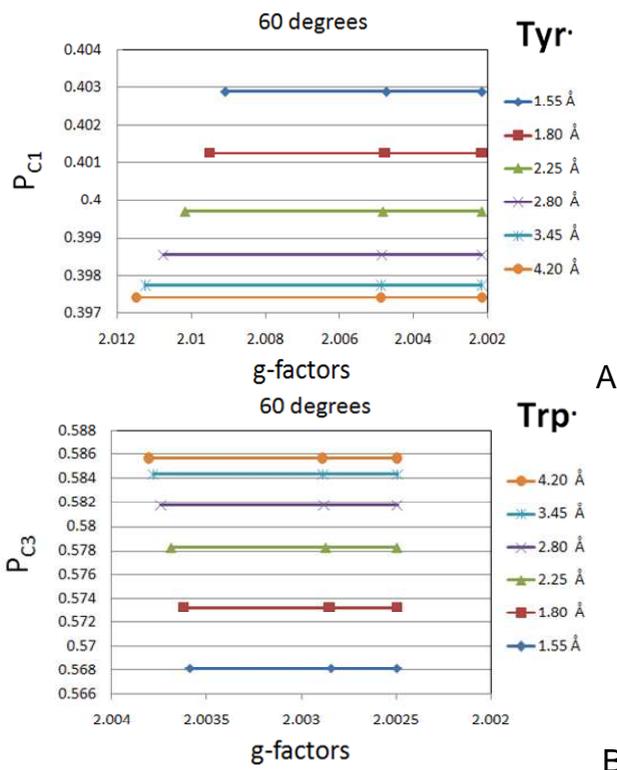
Figure 5. Principal g-factors of Tyr (A) and Trp (B) radicals plotted as the $P(g)$ charts [38], i.e. when the triads of the g-factors are arranged at different heights along the vertical axis of the spin density on the γ carbon atoms (P_{C1} in Tyr and P_{C3} in Trp). The data points calculated for different length (strength) of the hydrogen bond illustrate strong dependences of g_x and no dependence of g_y and g_z on the spin density on the γ carbon atoms. The g_x value of Trp radicals increases as the spin density increases while the g_x in Tyr decreases.

For each proton, two of the three components of the **A**-tensor are close to each other whereas the third component (cc) is greater than either of the two. That makes the symmetry of the **A**-tensor of the methylene β protons axial and of a slightly *prolate* shape (cigar like, in contrast to the *oblate,* which is a disk like shape).

141

Figure 6. Hyperfine interaction constants for the β (methylene) protons in Tyr (A) and Trp (B) radicals. Dependences on the rings rotation angles ϕ_6 (Tyr) and ϕ_4 (Trp) are presented for the case of the H-bond length of 1.8 Å. Three principal components of the hyperfine interaction tensor **A** are presented for each proton, corresponding to the directions aa, bb and cc. The β1 and β2 protons are atoms H19 and H20, respectively, in Tyr and atoms H18 and H19, respectively, in Trp (see Figures 1 and 2)

As expected for the range of the H-bond lengths studied, the methylene protons' hyperfine interaction constants depend weakly on the H-bond strength (Figure 7). It has been shown, however, at least for tryptophan radicals, that as the H-bond length becomes very short and a proton transfer becomes possible (which would turn a neutral tryptophanyl radical into a cation radical) the spin density on C3 and, correspondingly, the **A**-values for methylene protons decrease significantly [37]. When comparing these dependences calculated for the two types of radical (with $d \geq 1.55$ Å), when one of the protons is in the ring plane and thus having principal **A**-values close to zero, we would notice that the constants for the other proton in Tyr are slightly increasing as the H-bond strength becomes stronger. An immediate explanation that comes to mind is that this is because the spin density on C1 is increasing (Figure 5, A) and this causes an increase in the **A**-values in accordance with the McConnell relationship. We, however have to admit that the mechanism is likely to be more complex than that, since the increase of the P_{C1} in the range of H-bond

142

distances studied is ~1.7% (Figure 5, A) whereas the increase of the average $\mathbf{A}$-value for β2 proton is about 8% (Figure 7, A). This fact highlights once again the conclusion [38] that McConnell relationship is approximate and that the coefficients B' and B'' in it are not particularly constant when the relationship is applied to different cases.

The $\mathbf{A}$-value dependences on shortening of the H-bond in Trp radical are not as clear monotonous curves as in the Tyr case, likely because the P_{C3} is decreasing in Trp radical, in contrast to P_{C1} in Tyr radical (Figure 5).

CONCLUSIONS

A full analysis of the EPR parameters of the 144 structures of Tyr and Trp radicals is under way and will be published elsewhere. The principal g-factor values and hyperfine interaction constants for H and N atoms will be reported for an array of ring orientations and hydrogen bond strengths (12 rotation angles x 6 H-bond distances), for each radical. This two dimensional array of data points for each EPR parameter will create a basis of analytical formulation of a continuous surface that could be used to find the parameter for any combination of rotation angle and H-bond strength. Derivation of such functions should lead to a new method of assigning of an experimental EPR spectrum of a Tyr or Trp radical to a specific Tyr or Trp site on the protein, with a high degree of confidence.

EXPERIMENTAL SECTION

A technical background describing relationship between empirical (simulation derived) radical parameters and those calculated by the computational chemistry methods from the crystal structure of the radicals is given elsewhere [38]. The structures as shown in Figure 1 but with variable angle of the rings rotation and with variable distance towards the water molecules were analysed. The *Gaussian03* software package [41] was used for both the optimisations of the structures and the calculation of the EPR parameters, both at the B3LYP/6-31G* level of theory. During the optimization, the atom coordinates that define the rings rotation angles and the distances to the water molecule were kept frozen. Single point calculations were then performed for finding g-factor values, spin densities and hyperfine interaction constants.
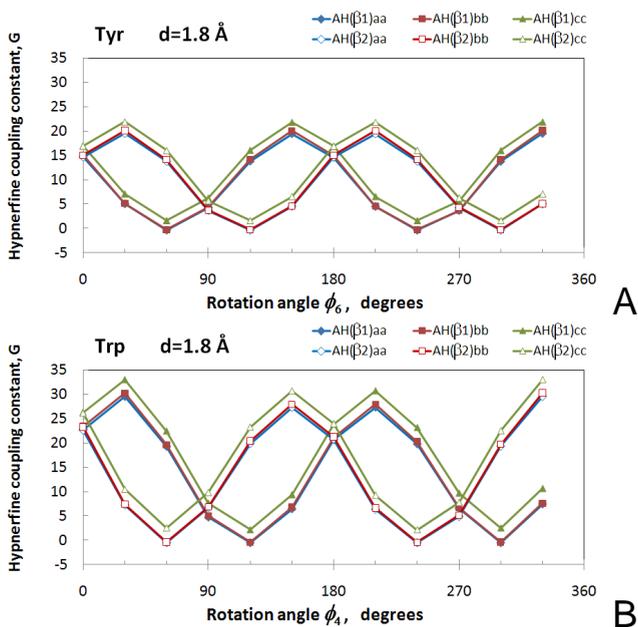
ACKNOWLEDGMENTS
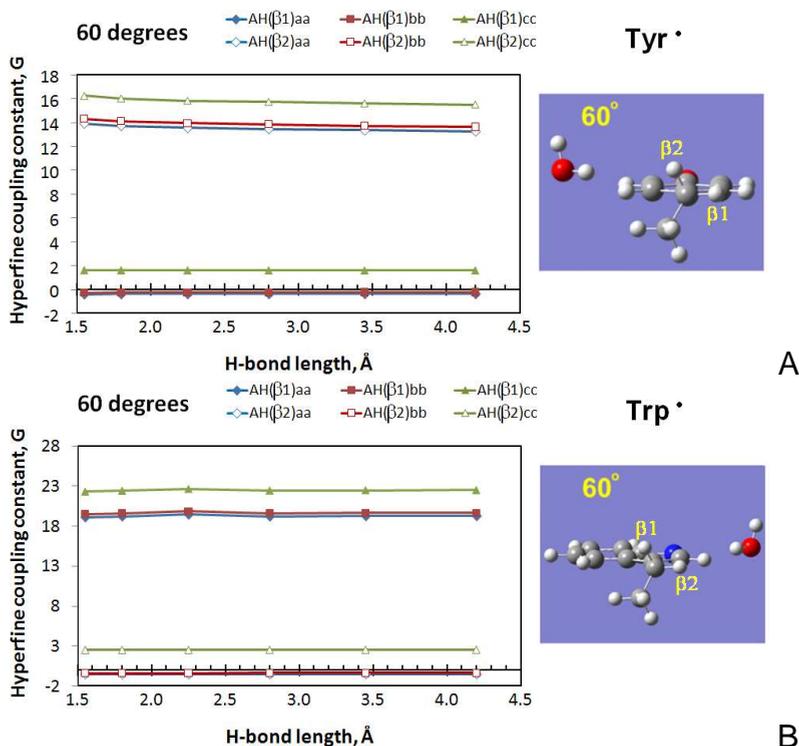
Figure 7. Hyperfine interaction constants for the β (methylene) protons in Tyr (A) and Trp (B) radicals. Dependences on the hydrogen bond length are presented for the case of the phenoxyl (in Tyr) and indole (in Trp) rings rotation angle of 60°. As in Figure 6, three principal components of the hyperfine interaction tensors are presented; the nomenclature of the β1 and β2 protons in each case is as given in Figure 6 caption.

REFERENCES

1. M. Sahlin; A. Gräslund; A. Ehrenberg, B.-M. Sjöberg, *Journal of Biological Chemistry,* **1982,** *257,* 366-369.
2. P. Reichard, A. Ehrenberg, *Science,* **1983,** *221,* 514-519.
3. P. Allard; A. L. Barra; K. K. Andersson; P. P. Schmidt; M. Atta, A. Gräslund, *Journal of The American Chemical Society,* **1996,** *118,* 895-896.
4. L. C. Hsi; C. W. Hoganson; G. T. Babcock, W. L. Smith, *Biochemical and Biophysical Research Communications,* **1994,** *202,* 1592-1598.
5. P. Dorlet; S. A. Seibold; G. T. Babcock; G. J. Gerfen; W. L. Smith; A. L. Tsai, S. Un, *Biochemistry,* **2002,** *41,* 6107-6114.

6. S. Chouchane; S. Girotto; S. Yu, R. S. Magliozzo, *Journal of Biological Chemistry,* **2002,** *277,* 42633-42638.
7. X. Zhao; S. Girotto; S. Yu, R. S. Magliozzo, *Journal of Biological Chemistry,* **2004,** *279,* 7606-7612.
8. D. A. Svistunenko; M. T. Wilson, C. E. Cooper, *Biochimica et Biophysica Acta,* **2004,** *1655,* 372-380.
9. G. T. Babcock; M. K. El-Deeb; P. O. Sandusky; M. M. Whittaker, J. W. Whittaker, *Journal of The American Chemical Society,* **1992,** *114,* 3727-3734.
10. M. M. Whittaker; P. J. Kersten; N. Nakamura; J. Sandersloehr; E. S. Schweizer, J. W. Whittaker, *Journal of Biological Chemistry,* **1996,** *271,* 681-687.
11. M. K. Thompson; S. Franzen; R. A. Ghiladi; B. J. Reeder, D. A. Svistunenko, *Journal of The American Chemical Society,* **2010,** *132,* 17501-17510.
12. M. Sivaraja; D. B. Goodin; M. Smith, B. M. Hoffman, *Science,* **1989,** *245,* 738-740.
13. S. T. Kim; A. Sancar; C. Essenmacher, G. T. Babcock,Proceedings of the National Academy of Sciences*U.S.A.,* **1993,** *90,* 8023-8027.
14. C. Aubert; M. H. Vos; P. Mathis; A. P. Eker, K. Brettel, *Nature,* **2000,** *405,* 586-590.
15. M. Sahlin; G. Lassmann; S. Pötsch; A. Slaby; B. M. Sjöberg, A. Gräslund, *Journal of Biological Chemistry,* **1994,** *269,* 11699-11702.
16. F. Lendzian; M. Sahlin; F. MacMillan; R. Bittl; R. Fiege; S. Pötsch; B.-M. Sjöberg; A. Gräslund; W. Lubitz, G. Lassmann, *Journal of The American Chemical Society,* **1996,** *118,* 8111-8120.
17. W. Blodig; A. T. Smith; K. Winterhalter, K. Piontek, *Archives of Biochemistry and Biophysics,* **1999,** *370,* 86-92.
18. A. N. Hiner; J. I. Martinez; M. B. Arnao; M. Acosta; D. D. Turner; E. Lloyd Raven, J. N. Rodriguez-Lopez, *European Journal of Biochemistry,* **2001,** *268,* 3091-8.
19. F. G. Wiertz; O. M. Richter; A. V. Cherepanov; F. MacMillan; B. Ludwig, S. de Vries, *FEBS Letters,* **2004,** *575,* 127-30.
20. F. G. Wiertz; O. M. Richter; B. Ludwig, S. de Vries, *Journal of Biological Chemistry,* **2007,** *282,* 31580-91.
21. R. Pogni; M. C. Baratto; S. Giansanti; C. Teutloff; J. Verdin; B. Valderrama; F. Lendzian; W. Lubitz; R. Vazquez-Duhalt, R. Basosi, *Biochemistry,* **2005,** *44,* 4267-4274.
22. R. Pogni; M. C. Baratto; C. Teutloff; S. Giansanti; F. J. Ruiz-Duenas; T. Choinowski; K. Piontek; A. T. Martinez; F. Lendzian, R. Basosi, *Journal of Biological Chemistry,* **2006,** *281,* 9517-9526.
23. R. Pogni; C. Teutloff; F. Lendzian, R. Basosi, *Applied Magnetic Resonance,* **2007,** *31,* 509-526.
24. F. J. Ruiz-Duenas; R. Pogni; M. Morales; S. Giansanti; M. J. Mate; A. Romero; M. J. Martinez; R. Basosi, A. T. Martinez, *Journal of Biological Chemistry,* **2009,** *284,* 7986-7994.
25. D. Tew, P. R. Ortiz de Montellano, *Journal of Biological Chemistry,* **1988,** *263,* 17880-17886.
26. M. J. Davies, A. Puppo, *Biochemical Journal,* **1992,** *281,* 197-201.
27. J. A. DeGray; M. R. Gunther; R. Tschirret-Guth; P. R. Ortiz de Montellano, R. P. Mason, *Journal of Biological Chemistry,* **1997,** *272,* 2359-2362.

28. D. A. Svistunenko, *Biochimica et Biophysica Acta,* **2005,** *1707,* 127-155.
29. D. A. Svistunenko; B. J. Reeder; M. M. Wankasi; R.-L. Silaghi-Dumitrescu; C. E. Cooper; S. Rinaldo; F. Cutruzzolà, M. T. Wilson, *Dalton Transactions,* **2007,** 840-850.
31. D. A. Svistunenko; J. 30.   B. J. Reeder; M. Grey; R. L. Silaghi-Dumitrescu; D. A. Svistunenko; L. Bulow; C. E. Cooper, M. T. Wilson, *Journal of Biological Chemistry,* **2008,** *283,* 30780-30787.
Dunne; M. Fryer; P. Nicholls; B. J. Reeder; M. T. Wilson; M. G. Bigotti; F. Cutruzzolà, C. E. Cooper, *Biophysical Journal,* **2002,** *83,* 2845-2855.
32. D. A. Svistunenko, C. E. Cooper, *Biophysical Journal,* **2004,** *87,* 582-595.
33. S. Un; M. Atta; M. Fontecave, A. W. Rutherford, *Journal of The American Chemical Society,* **1995,** *117,* 10713-10719.
34. F. Himo; A. Gräslund, L. A. Eriksson, *Biophysical Journal,* **1997,** *72,* 1556-1567.
35. S. Un, *Magnetic Resonace Chemistry,* **2005,** *43,* S229-S236.
36. M. Brynda, R. D. Britt, *Research In Chemical Intermediates,* **2007,** *33,* 863-883.
37. C. Bernini; R. Pogni; F. J. Ruiz-Duenas; A. T. Martinez; R. Basosi, A. Sinicropi, *Physical Chemistry Chemical Physics,* **2011,** *13,* 5078-5098.
38. D. A. Svistunenko, G. A. Jones, *Physical Chemistry Chemical Physics,* **2009,** *11,* 6600-6613.
39. C. Bernini; A. Sinicropi; R. Basosi, R. Pogni, *Applied Magnetic Resonance,* **2010,** *37,* 279-288.
40. H. M. McConnell, D. B. Cheshunt, *Journal of Chemical Physics,* **1958,** *28,* 107-117.
41. M. J. Frisch, G. W. Trucks, H. B. Schlegel, G. E. Scuseria, M. A. Robb, J. R. Cheeseman, J. Montgomery, J. A., T. Vreven, K. N. Kudin, J. C. Burant, J. M. Millam, S. S. Iyengar, J. Tomasi, V. Barone, B. Mennucci, M. Cossi, G. Scalmani, N. Rega, G. A. Petersson, H. Nakatsuji, M. Hada, M. Ehara, K. Toyota, R. Fukuda, J. Hasegawa, M. Ishida, T. Nakajima, Y. Honda, O. Kitao, H. Nakai, M. Klene, X. Li, J. E. Knox, H. P. Hratchian, J. B. Cross, V. Bakken, C. Adamo, J. Jaramillo, R. Gomperts, R. E. Stratmann, O. Yazyev, A. J. Austin, R. Cammi, C. Pomelli, J. W. Ochterski, P. Y. Ayala, K. Morokuma, G. A. Voth, P. Salvador, J. J. Dannenberg, V. G. Zakrzewski, S. Dapprich, A. D. Daniels, M. C. Strain, O. Farkas, D. K. Malick, A. D. Rabuck, K. Raghavachari, J. B. Foresman, J. V. Ortiz, Q. Cui, A. G. Baboul, S. Clifford, J. Cioslowski, B. B. Stefanov, G. Liu, A. Liashenko, P. Piskorz, I. Komaromi, R. L. Martin, D. J. Fox, T. Keith, M. A. Al-Laham, C. Y. Peng, A. Nanayakkara, M. Challacombe, P. M. W. Gill, B. Johnson, W. Chen, M. W. Wong, C. Gonzalez, J. A. Pople 2004 *Gaussian 03.* 2004, Gaussian, Inc.: Wallingford CT.

THE INFLUENCE OF SOME SYNTHESIS CONDITIONS ON THE STRUCTURE OF CALCIUM PHOSPHATE POWDERS

MILICA TODEA[*a], TEODORA MARCU[b], MONICA TAMASAN[a], SIMION SIMON[a], CATALIN POPA[b]

ABSTRACT. Calcium phosphate powders were synthesized based on a wet chemical precipitation method at room temperature. A critical aging time of the precipitate is required in order to form a desired intermediate complex that permits a further transformation to apatite phase under appropriate thermal treatment. The processing parameters effect on apatite formation was systematically studied in terms of aging time and different condition of synthesis using Thermal Analysis, X-ray diffraction and Fourier transform infrared spectroscopy. The transformation of calcium phosphate deficient apatite (monetite and $Ca_2P_2O_7$) obtained after one and two weeks of aging time into hydroxyapatite is completed when a heat treatment is applied at 600 ^{o}C under air. The HA nanocrystal sizes decrease with the increase of the aging periods, from 90 to 50 nm. The results show that by suitable tailoring of the processing parameters one can obtain calcium phosphate powders of desired dimensions.

Keywords: hydroxyapatite, nanocrystalls, DRX, FTIR, DTA.

INTRODUCTION

Calcium phosphate is recognized to be one of the most attractive candidate materials for bone replacement since the human skeleton consists of a composite of calcium phosphate crystals with a matrix phase of collagen. Inorganic bioceramic hydroxyapatite ($Ca_{10}(PO_4)_6(OH)_2$) as the main constituent of natural bone and teeth has excellent biocompatibility and tissue bioactivity. The morphological characteristics of HA particles, such as shape, size, and size distribution play an important role in the mechanical, chemical, and biological properties of HA-based materials. The precipitation mechanism of HA follows a nucleation-aggregation-growth sequence of events [1]. In this approach, HA particles with sizes ranging from nanometric to micrometric can be obtained; from the morphological point of view they may be irregular or ordered aggregates [2]. Bone substitute materials must be actively resorbed in vivo by the osteoclasts [3] (cells that

a   *Faculty of Physics & Institute of Interdisciplinary Research on Bio-Nano-Sciences, Babes Bolyai University, Cluj-Napoca, 400084, Romania*
b   *Technical University of Cluj-Napoca, Faculty of Materials and Environmental Engineering, Department of Materials Science and Technology, Muncii Avenue 103-105, 400641 Cluj-Napoca, Romania*

are able to resorb the fully mineralized bone) as they are equipped with a variety of enzymes, which lower the local pH to a range of 3.9 to 4.2. This occurs via a process called cell-mediated acidification in which the host bone can deposit new bone on the resorption sites by the means of osteoblasts (cells that build the extracellular matrix and regulate its mineralization).

Several compositions containing calcium and phosphorous, like hydroxyapatite (HA, $Ca_{10}(PO_4)_6(OH)_2$), beta tricalcium phosphate (β-TCP, $Ca_3(PO_4)_2$), or their composites (biphasic calcium phosphates, BCP) have received particular attention. HA is considered to be a bioactive and non-biodegradable bone replacement material, while TCP is resorbable and significantly more soluble than HA [4, 5]. BCP ceramics were developed in order to combine the high bioactivity of Ha and the solubility characteristics of TCP in a composite material. [6].

Brushite ($CaHPO_4·2H_2O$) is a layered structure in which the layers are held together by water molecules via hydrogen bonds. Upon heating, brushite loses its water molecules and will transform into $CaHPO_4$ (monetite) [7]. Being a relatively high solubility calcium phosphate compound, brushite is known to convert into apatite-like calcium phosphate when soaked in SBF solutions at the human body temperature for about one week [8–22].

Both brushite [23, 24] and monetite [25] phases are successfully used as starting materials in the preparation of the powder components of self-hardening apatitic calcium phosphate cements [26]. Aging of the precursor solution has been found to be critical in developing an apatitic phase. A critical aging time is required to complete reaction between Ca and P molecular precursor to form a desired intermediate complex that allows a further transformation to apatite phase under appropriate thermal treatment [27].

The main purpose of this study was to analyze systematically the influence of aging time, heat treatment and different synthesis condition (eg washing samples) on the structure of calcium phosphate samples obtained by the precipitation method at room temperature.

RESULTS AND DISCUSSION

Calcium phosphate powders were synthesized based on a wet chemical precipitation method at room temperature, with calcium nitrate and diammonium hydrogen phosphate, as detaile din the Methods section.

In order to establish the calcination temperatures, differential thermal analysis (DTA) and thermogravimetric (TG) results were used. The DTA and TGA (STA: simultaneous thermal analysis) curves for the as prepared calcium phosphate powder are displayed in Figure 1. These show, in the 35-150ºC range, an endothermic event with mass decrease of 3 % due to the loss of surface adsorbed water. A second mass decrease of about 20 % is recorded in 200-300ºC temperature range, and this is accompanied by an endothermic peak in DTA curve, with the maximum at 270ºC. Based upon the formula $CaHPO_4·2H_2O$ the theoretical mass loss for the dehydration

of brushite is 20.93%. In our study, the experimentally determined mass loss attributed to the dehydration of brushite is around 20% in very good accord with the literature [7, 26, 29, 38]. These authors observed that brushite transformed to monetite at around 200ºC with a weight loss of 20.3% and the monetite to calcium pyrophosphate ($Ca_2P_2O_7$) transition was complete above 440ºC, with 6% weigh loss. The following reactions take place during the thermal decomposition:

$$2CaHPO_4 \cdot 2H_2O \rightarrow 2CaHPO_4 + 4H_2O$$
$$2CaHPO_4 \rightarrow Ca_2P_2O_7 + H_2O$$
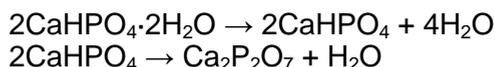
In this approach, the further mass loss (around 12 %) recorded in the 400-500 temperature range with a maximum at around 440ºC, can be related to the monetite to $Ca_2P_2O_7$ transition (with a weigh loss of 6%) and pyrolysis of the organic component and/or residual nitrate groups occurring in the samples during the synthesis of the samples (with a weigh loss of 6%) [26, 30, 31, 38].
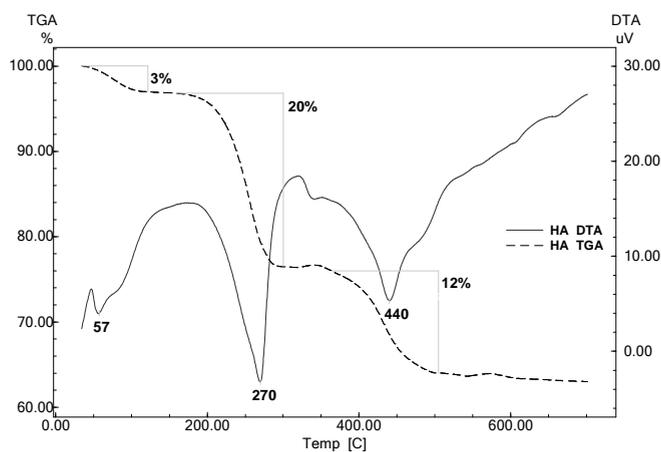
Figure 1. DTA and TG curves of as-prepared sample

The X-ray diffraction patterns for the calcium phosphate samples aged, washed and then heat treated are different in the crystalline aspect (Figs. 2 and 3). The crystalline phase identified in the as-prepared sample (0 week) is brushite. The intensity of the diffraction peaks indicated that the particles were fairly well-crystallized. As we mentioned before, by losing water during the aging periods, brushite transforms into monetite (Figure 2a). This transformation is reversible, as it can be seen in Figure 3a for the samples that were aged one or two weeks (monetite) after washing in pure water the main crystalline phase became brushite.

Figure 2. *XRD patterns of the samples after different aging time periods a) not heat treated b) heat treated at 600°C*

The XRD reflection peak at $2\theta = 12^0$ is attributed to brushite powder. The average crystallites size, determined by Scherrer's formula for the peak with $2\theta = 12.1^0$ for the as-prepared sample is of about 55 nm (Table 1). It is important to notice that in the washed samples the crystallites size value increases at 132 nm due to the hydration of the samples. Brushite as main crystalline phase transform into two phase mixture of calcium phosphate containing $Ca_2P_2O_7$ and a small amount of β-TCP after the heat treatment (Figure 2b).
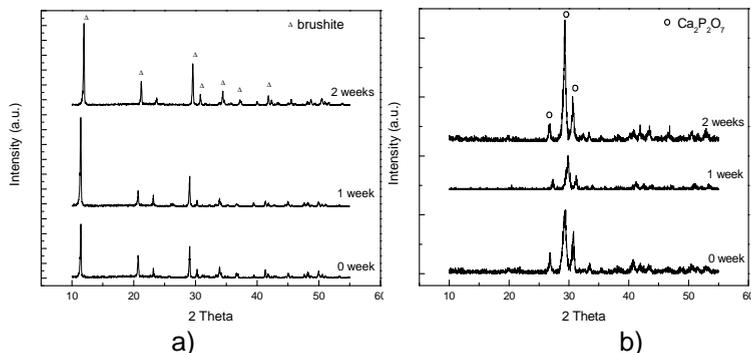
Figure 3. *XRD patterns of the samples washed after different aging time periods a) not heat treated b) heat treated at 600°C*

This applies to not aged as-prepared samples and all samples that were washed in pure water. The crystallites size has values ranging between 35-44 nm (Table 1). Both $Ca_2P_2O_7$ and β-TCP phases are not necessarily detrimental components of bioceramics, since they provide faster than apatite dissolution rate in physiological environments [26, 27].In fact, this would be an advantage from the bioresorbtion point of view.

The transformation of calcium phosphate deficient apatite (monetite and $Ca_2P_2O_7$) obtained after one and two weeks (Figure 2a) of aging into hydroxyapatite (Figure 2b) is completed at 600 ^{o}C [6]. The XRD results confirm those obtained from DTA. The HA crystallites size decreases with the increase of the aging periods, from 90 to 50 nm (Table 1). The crystallite size of HA is of main importance for the biomedical application. A smaller size is expected to result in a higher bioactivity.

Table 1. Crystalline phases and corresponding crystallites size of calcium phosphate samples

Sample		Crystalline phase	2 theta[^{o}]	Crystallites size [nm]
	0 week	brushite	12.1	55
		monetite	29.9	69
	1 week	$Ca_2P_2O_7$	26.2	73
		monetite	30.5	83
	2 weeks	$Ca_2P_2O_7$	27.0	21
heat treated	0 week	$Ca_2P_2O_7$	26.8	52
		β-TCP	30.7	44
	1 week	HA	32.3	90
	2 weeks	HA	31.8	50
washed	0 week	brushite	12.1	132
	1 week	brushite	11.4	132
	2 weeks	brushite	11.9	132
washed and heat treated	0 week	$Ca_2P_2O_7$	26.8	41
		β-TCP	30.6	35
	1 week	$Ca_2P_2O_7$	26.8	36
	2weeks	$Ca_2P_2O_7$	26.3	36

FTIR measurements were performed to evaluate possible differences in the chemical composition of the calcium phosphate powders with different Ca/P ratios. The FTIR spectra of calcium phosphate powders for different aging periods before and after the heat treatment at 600°C are presented in Figures 4 and 5. The crystalline phases identified by XRD were also confirmed by FTIR spectral analysis. The spectra of calcium phosphate samples before the heat treatment (Figure 4a) show the characteristic peaks of absorbed water, hydroxyl, phosphates and carbonate species.

The bands between 3250-3500 cm^{-1} corresponding to the O-H stretching of adsorbed water [7, 32] are broad for all the samples aged and unwashed (Figure 4a). The spectra clearly indicate a band at around 1640 cm^{-1} (bending mode), which is attributed to the presence of the adsorbed water [7]. The bands around 1135, 1060 cm^{-1} and in the range of 660- 528 cm^{-1} are characteristic for vibrational mode of phosphate group in several distinctive sites [6].
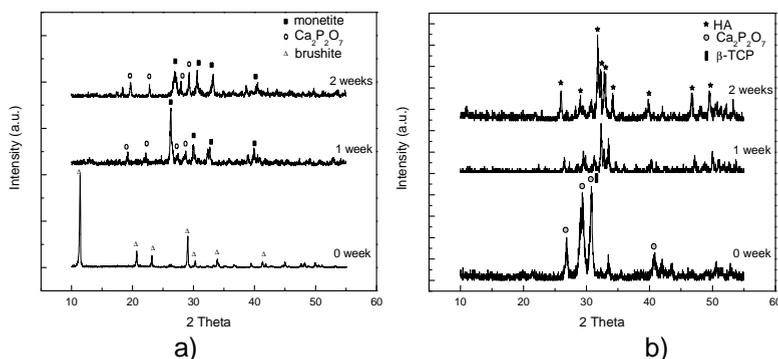
a)   b)
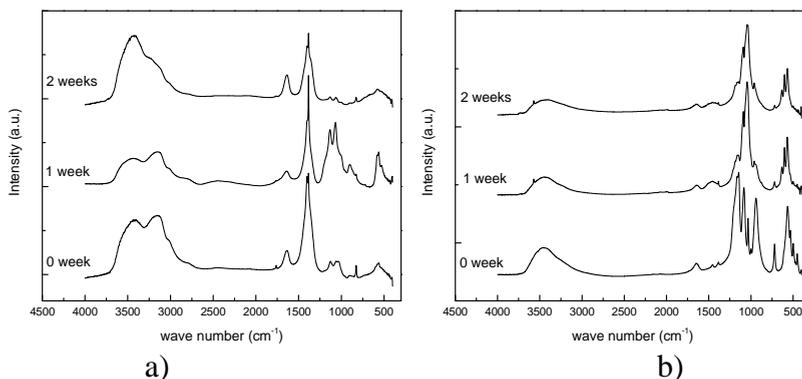
Figure 4. *FT-IR spectra of the samples after different aging time periods a) not heat treated b) heat treated at 600°C*

The XRD results show that the crystalline phases identified in these samples are monetite and $Ca_2P_2O_7$. The P-OH stretching modes in HPO_4 groups have been identified around 880 cm^{-1} [7]. The bands at 825 and 1385 cm^{-1} were attributed to residual NO_3^- groups resulting from synthesis precursors [39]. The absorption bands around 1470 cm^{-1} and 890 cm^{-1} represent an indicative of carbonate species, which is presumed to have come from the atmosphere during the aging period [32]. The total intensity of these bands decreases for the samples washed after all aging periods.
The spectra of the heat treated samples aged for one and two weeks (Figure 4b) are characteristic for calcium hydroxyapatite [2, 34]. All bands originating from PO_4 and OH groups are clearly visible. The OH vibrations at 3400-3200 cm^{-1} (stretching) are well-defined but they diminished upon heating the samples. The bands assigned to the stretching modes 3570 cm^{-1} and librational modes at 631 cm^{-1} of OH group in the hydroxyapatite, are clearly observed in the spectra [34].

The bands in the region 1650–1600 cm^{-1} are a result of H–O–H vibrational modes of adsorbed water [35, 36]. The presence of broad distinct bands in the range 1500–1400 cm^{-1} means that the HA samples contain small quantities of carbonate ions. These bands are missing from the FTIR spectra of the washed samples and then heat treated (Figure 5b). These facts confirm the elimination of the carbonate from the samples when they are washed and then heat treated. The main vibrational bands of the hydroxyapatite PO_4 groups are observed at around 1157, 1095, 1040, 960, 601 and 571 cm^{-1} for one and two weeks aged samples, after the heat treatment [32-36]. This result sustains the X-ray diffraction conclusions.

After washing, the FT-IR spectra for all the samples present bands in the same regions but they became sharper and narrower (Figure 5a). The bands at 3543, 3494, 3281, 3163 cm^{-1} and also the shoulder at around
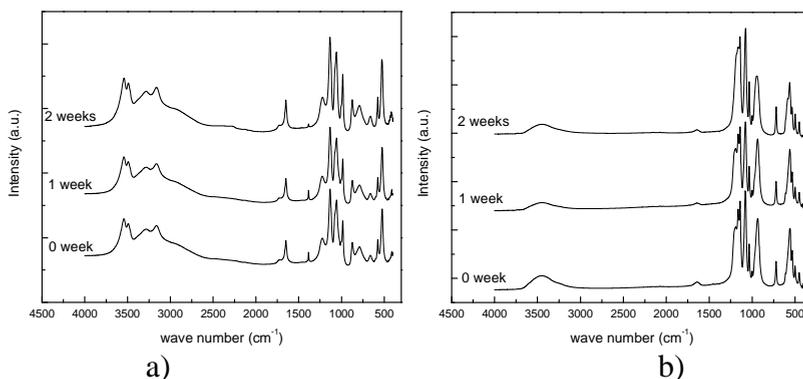
Figure 5. *FT-IR spectra of the samples washed after different aging time periods a) not heat treated b) heat treated at 600 °C*

2955 cm^{-1} were due to the O-H stretching of water. The band at 1648 can be assigned to the bending vibration of water. Bands at 874 cm^{-1} and 1220 cm^{-1} assigned to the HPO_2^{-4} group of brushite [7,40] were observed in all the washed samples. The band at 985 cm^{-1} originated from the P-OH symmetric stretching vibration of PO_3^{4-}. In addition, the band at around 1060 cm^{-1} was attributed to the v_3 vibration of the PO_3^{4-}. Stretching vibrations of PO groups at 1136 cm^{-1} was assigned vibration of HPO_2^{-4} ions in brushite [40]. Water libration was observed for all the samples at 791 cm^{-1}. The bending vibrations of the P-O-P mode were recorded at 660, 576, 528 cm^{-1}, attributed to phosphate groups associated with brushite, the only crystalline phase present in this samples [7, 26, 33, 34, 35].

Figure 5b, referring to washed and heat treated samples, shows, as well as all of the above-mentioned bands, a unique sharp peak at around 720 cm^{-1} which is characteristic of the P–O–P vibrational mode indicating the presence of pyrophosphates ($Ca_2P_2O_7$) [37, 40]. FTIR spectra of as-prepared samples heat treated (Figure 4b) show the same feature. The results confirm the ones from XRD patterns, indicating the predominant presence of $Ca_2P_2O_7$ as a decomposition product, after heat treatment, in these samples.

CONCLUSIONS

Calcium phosphate powders were found to display different physical and chemical characteristics according to the preparing aging periods. The transformation of calcium phosphate deficient apatite (monetite and $Ca_2P_2O_7$) obtained after one or two weeks of aging into hydroxyapatite is completed only when a heat treatment is applied at 600 °C in air. Hydroxyapatite crystallite sizes decrease with the increase of the aging period. The two weeks aging time gave the best result in terms of HA crystallites size, as the bioactivity increase with the decrease of the grains size.

EXPERIMENTAL SECTION

Calcium phosphate powders were synthesized based on a wet chemical precipitation method at room temperature using calcium nitrate tetrahydrate $(Ca(NO_3)_2 \cdot 4H_2O$) and diammonium hydrogen phosphate $(NH_4)_2HPO_4$). All chemicals were reagent grade (Sigma Aldrich) and used without further purification. The white sol was stable and no gelation occurred over an aging period as long as several weeks. During the aging process, the pH of the sol increases from 4.5 at the beginning to 4.8 after the final aging period. Diammonium hydrogen phosphate hydrolyzed sol was added dropwise to the constantly stirred aqueous calcium nitrate solution at the molar ratio of Ca to P equal to 1.67. The mixed sol solution was then continuously stirred for about 50 min to obtain a white consistent sol with pH 4.5. The precipitate was taken at an aging time period of one and two weeks at room temperature and parts of them were washed with distilled water followed by filtration and dried at 80℃. Aft er drying, the powders were calcinated at 600ºC, for 30minutes in air atmosphere.

Phase identification of the samples before and after calcination was performed by X-ray diffraction (XRD) with a Shimadzu XRD-6000 diffractometer, using Cu-K_α radiation (λ = 1.5418 Å), with Ni–filter. The XRD patterns were recorded in the 2θ scan range 10-80º, with a scan speed of 2%min, using as calibrating material quartz powder . All powder samples were characterized after being lightly grinded by an agate mortar and pestle.

The crystallite size was estimated from the X-ray diffractograms using the Scherrer formula [28].

$$D = k\lambda/\beta_{1/2} \cos \theta,$$

Where D is the crystallite size (Å), k is a shape factor equal to 0.9, λ is the X-ray wavelength (1.5405 Å), θ is the diffraction angle expressed in radians, and $\beta_{1/2}$ is defined as

$$\beta_{1/2} = (B^2 - b^2)^{1/2}$$

B being the diffraction peak width at half height and b the natural width of the instrument.

Thermal analysis was conducted on a Shimadzu type derivatograph DTG-60H at a heating rate of 10ºC/min, up to 700ºC. Alumina open crucibles and α-alumina powder as reference material were used and the measurement was made in a dynamic nitrogen and air atmosphere at a flow rate of 70 ml/min.

The infrared measurements were carried out using a Bruker Equinox 55 spectrometer. The FTIR spectra were recorded on powdered samples pressed in KBr pellets, with a spectral resolution of 2 cm^{-1}, over the range of 4000 to 400 cm^{-1}.

ACKNOWLEDGMENTS

REFERENCES

1. R. R. Clemente, A. L. Macipe, J. G. Morales, J. T. Burgues, and V. M. Castanho, *Journal of the European Ceramics Society*, **1998**, *18*, 1351–1356
2. M.A. Martins, C. Santos, M.M. Almeida, M.E.V. Costa, *Journal of Colloid Interface Science* **2008**, *318*, 210-216
3. F Monchau; A Lefèvre; M Descamps; A Belquin-myrdycz; P Laffargue; H FHildebrand, *Biomolecular Engineering*, **2002**,*19(2-6)*,143-152
4. C. P. A. T. Klein, A. A. Driessen, K. Groot, and A. Hoof, *Journal of Biomedical Materials Research*, **1983**, *17*, 769-784
5. P. Ducheyne, S. Radin, L. King, *Journal of Biomedical Materials Research,* **1993**, *27*, 25-34
6. J. Marchi, P. Greil, J.C.Bressiani, A. Bressiani, F. Muller, *International Journal of Applied Ceramic Technology*, **2009**, *6*, 60-71
7. S. Mandel, A.C. Tas, *Materials Science and Engineering C* **2010**, *30*, 245–254
8. D. Walsh, J. Tanaka, *Journal of Materials Science: Materials in Medicine*, **2001**, *12*, 339-343
9. S.J. Lin, R.Z. LeGeros, J.P. LeGeros, *Journal of Biomedical Materials Research* **2003**, *66A*, 819-828
10. H.S. Azevedo, I.B. Leonor, C.M. Alves, R.L. Reis, *Materials Science and Engineering: C* **2005**, *25*, 169-179
11. Lu X and Leng Y, *Biomaterials*, **2005**, *26*, 1097-1108
12. Zainuddin, Hill DJT, Traian CV, Whittaker AK, Kemp A. *Biomacromolecules*, **2006**, *7(6)*, 1758-1765
13. M. Kumar, H. Dasarathy, C. Riley, *Journal of Biomedical Materials Research* **1999**, *45*, 302-310
14. C.Y. Kim, H.B. Lim, *Key Engineering Materials*, **2004**, *254-256*, 305-310
15. J.A. Juhasz, S.M. Best, A.D. Auffret, W. Bonfield, *Journal Of Materials Science: Materials in Medicine* **2008**, *19*, 1823-1829

16. J. Pena, I. Barba-Izquierdo, A. Martinez, M. Vallet-Regi, *Solid State Sci.* **2006**, *8*, 513-519
17. Y. Honda, S. Kamakura, K. Sasaki, T. Anada, T. Masuda, O. Suzuki, *Key Engineering Materials*, **2007**, *330–332*, 479-482
18. R. Gildenhaar, G. Berger, E. Lehmann, C. Knabe, *Key Engineering Materials*, **2008**, *361–363*, 331-334
19. L. Grondahl, F. Cardona, K. Chiem, E. Wentrup-Byrne, T. Bostrom, *Journal of Materials Science: Materials in Medicine* **2003**, *14*, 503-510
20. A. Rakngarm, Y. Mutoh, *Materials Science and Engineering: C,* **2009**, *29(1)*, 275 - 283
21. F. Yang, J.G.C. Wolke, J.A. Jansen, *Chemical Engineering Journal*, **2008**, *137*, 154-161
22. L.P. Xu, E.L. Zhang, K. Yang*, Journal of Materials Science: Materials in Medicine,* **2009**, *20*, 859-867
23. K. Kurashina, H. Kurita, M. Kotani, C.P.A.T. Klein, K. de Groot, *Biomaterials*, **1997**, *18*, 539-543
24. D. Knaack, M. E. P. Goad, M. Aiolova, C. Rey, A. Tofighi, P. Chakravarthy and D. D. Lee, *The Journal of Biomedical Materials Research*, **1998**, *43(4)*, 399-409
25. E.M. Ooms, J.G.C. Wolke, M.T. van de Heuvel, B. Jeschke and J.A. Jansen, *Biomaterials* **2003**, *24*, 989–1000
26. A. C. Tas and S. B. Bhaduri, Bioceramics: Materials and Applications V, Ceramic Transactions, Vol. **164**, pp. 119-128, (Eds.) V. Sundar, R. P. Rusin, and C. A. Rutiser, The American Ceramic Society, 2004, USA, ISBN 1-57498-185-4.
27. D-M. Liu, T. Troczynski, W. J. Tseng, *Biomaterials* **2002**, *23*, 1227-1236
28. T.J. Burgues, R.R. Clemente, *Crystal Research and Technology,* **2001**, *36*, 1075-1082
29. A. Dosen and R.F. Giese, *American Mineralogist*, **2011**, *96*, 368-373
30. M. Mozafari, F. Moztarzadeh, M. Tahriri, *Journal of Non-Crystalline Solids*, **2010**, *356*, 1470–1478
31. I. Bogdanoviciene, A. Beganskiene, K. Tonsuaadu, J.Glaser, H.Juergen. Meyer, A. Kareiva, *Materials Research Bulletin* , **2006**, *41*, 1754–1762
32. T.V. Thamaraiselvi, K. Prabakaran and S. Rajeswari, *Biomaterials and Artificial Organs*, **2006**, *19*, 81-83
33. N. Temizel, G. Girisken, and A. C. TAS, *Materials Science and Engineering C: Materials for Biological Applications*, **2011**, *31(5)*, 1136-1143
34. Soon-Ho Kwon, Youn-Ki Jun, Seong-Hyeon Hong, Hyoun-Ee Kim, *Journal of the European Ceramic Society,* **2003**, *23,* 1039–1045
35. X. Bai, K. More, C.M. Rouleau, A. Rabiei, *Acta Biomaterialia*, **2010**, *6*, 2264-2273
36. A. C. Tas, *Biomaterials*, **2000**, *21 (14)*, 1429-1438
37. A. C. Tas, *Journal of The American Ceramic Society*, **2001**, *84 (2)*, 295-300
38. R. L. Frost and S. J. Palmer*, Thermochimica Acta*, **2011**, *521*, 14-17
39. D.K. Pattanayak, R. Dash, R.C. Prasad, B.T. Rao, T.R. Rama Mohan, *Materials Science and Engineering: C*, **2007**, *27*, 684-690
40. J. P. Maity, Tz-J. Lin, H. P-H Cheng, C-Y. Chen, A. S. Reddy, S.B. Atla, Y-F. Chang, H-R. Chen and C-C Chen, *International Journal of Molecular Sciences*, **2011**, *12*, 3821-3830

DETECTION OF SOME ROMANIAN HONEY TYPES ADULTERATION USING STABLE ISOTOPE METHODOLOGY

EDINA DORDAI[a], DANA ALINA MĂGDAŞ[a], STELA MARIA CUNA[a], GABRIELA CRISTEA[a], ISTVÁN FUTÓ[b], GERGELY VODILA[b], VALENTIN MIREL[a]

ABSTRACT. 12 Romanian samples of honeys from different floral sources were analyzed for the determination of high fructose corn syrup (HFCS) adulteration of honey, by coupling an isotope ratio mass spectrometer to an elemental analyzer. Using the difference in stable carbon isotope ratio ($\delta^{13}C$) between honey and its protein fraction it is possible to evaluate the adulteration with small extent (minimum 7%). An obvious adulteration was observed for the multifloral honey, while for other 5 samples the negative difference indicated that these samples are not adulterated. For the other 6 samples, the positive difference indicates the absence of adulteration.

Keywords: honey; adulteration; carbon isotope ratio; δ13C.

INTRODUCTION

Among the numerous sectors affected by fraud, foods are not exempt and for the same reason: considerable financial gains. Beyond the harmful economic consequences for honest producers who comply with regulations, fraud in the food sector can have serious effects on public health, since certain added components may be toxic.

Honey is not produced in large quantities and is not a high added value product. Nevertheless, the product is not immune to fraud that involves the addition of syrups from a variety of sources (sugar cane, corn or beets). Fraud by spiking with syrups increased considerably in the 1970s as a result of massive production of these syrups. The market was flooded with low cost-price products of higher quality and whose oligosaccharide composition was close to those of native honey (case of totally invert sugars). The difficulty in detecting adulteration arises from the precise separation of these sugars with practically identical compositions [1]. For the detection of

[a] *National Institute for Research and Development of Isotopic and Molecular Technologies, 65-103 Donath Str., P.O.Box 700, RO-400293 Cluj-Napoca 5, ROMANIA, Edina.Dordai@itim-cj.ro*
[b] *Institute of Nuclear Research of the Hungarian Academy of Sciences Laboratory of Environmental Studies Bem ter 18/c P.O.Box 51, 4001 Debrecen, HUNGARY*

these adulterations a very precise method was developed by Doner and White in 1977 [2] based on the analysis of the stable carbon isotopic ratio analysis by mass spectrometry (SCIRA-MS).

Depending on their origin, sugars added are divided into two types: C3 and C4. Sucrose and the natural sugars of honey belong to the C3 type while cane sugar and sugars produced from the hydrolysis of maize starch are of the C4 type [3]. Maize and sugarcane metabolize by the Hatch-Slack or C4 metabolic pathway. The isotopic technique for the detection of adulterated honey is based on the natural differences in isotopic ratios between plants using C3 and C4 photosynthetic pathways. Generally, C4 plants, for example, corn, have $^{13}C/^{12}C$ isotopic ratios, referred to as $\delta^{13}C$ values, ranging between -8 and -13‰, whereas C3 plants, generally nectar-bearing plants, have values between -22 and -30‰ [4]. For the detection of adulterated honey (addition of C4 plant sugars such as cane sugar and corn syrup), an internal standard $^{13}C/^{12}C$ isotope ratio method was developed [5]. This procedure utilizes the $\delta^{13}C$ value of the protein extracted from the honey as an internal standard, the purity of the honey is then judged in comparison to the $\delta^{13}C$ of the corresponding whole honey [6-9]. The method currently used, allows the detection of 7-10% adulteration with cane sugar or maize syrups. Since bees produce all proteins in honey by reaction between enzymes and nectar, the isotope ratio of honey and its protein will have very close values if honey is pure [10]. Addition of C4 sugars will affect just the isotopic ratio of the honey, but not its protein composition.

In this work, as different sources of honey can have different $\delta^{13}C$ values, it was considered as appropriate to include four types of Romanian honey in this initial study to establish a baseline range of $\delta^{13}C$ values for Romanian honeys. For this purpose 12 honey samples from four different floral types were analyzed.

RESULTS AND DISCUSSION

From the 12 samples analyzed, 6 samples have had the difference between $\delta^{13}C$ protein and $\delta^{13}C$ honey positive, indicating the absence of adulteration. At five samples the negative values obtained, range -0.06 to -0.98, gives us the reason to calculate apparent adulteration, the values obtained being between 0.38 and 6.39%. Since these differences are below the internationally accepted threshold of - 1 ‰ (7 % adulteration), the samples are considered not adulterate. For sample number 5 the adulteration is higher than the bench-mark, the calculated value being 10.81%, this indicating the presence of added C4 sugars.

Regarding the honey authenticity related to the botanical origin, the variations of parameters are presented in Table 2. The lowest values were obtained for honeydew and the highest for tilia.

158

Carbon isotopic ratios of honey protein are also influenced by the climate, and can be used as a discriminating factor to determine the geographical origin of honey [11] in addition with the values of other isotopes [12,13]. Depending on the climate area, relatively large differences (1, 8‰) have been shown in samples from different European regions even for the same floral type of honey [13].

Table 1. Experimental data obtained for the analysis of honey and its protein

No.	Botanical origin	$\delta^{13}C_{protein}$	Average $\delta^{13}C_{protein}$	$\delta^{13}C_{honey}$	Average $\delta^{13}C_{honey}$	Difference $\delta^{13}C_{protein}$ - $\delta^{13}C_{honey}$	Adulteration (%)
1	Honeydew	-24.97 / -25.17	-25.07	-25.21 / -25.23	-25.22	0.15	-
2	Acacia	-24.77 / -24.75	-24.76	-24.35 / -24.16	-24.26	-0.5	-
3	Honeydew	-25.42 / -25.47	-25.45	-25.16 / -25.09	-25.12	-0.33	-
4	Tilia	-24.54 / -24.51	-24.53	-25.87 / -25.83	-25.85	1.32	-
5	Multifloral	-25.83 / -25.95	-25.89	-24.17 / -24.10	-24.14	-1.75	10.8
6	Honeydew	-25.06 / -25.05	-25.06	-26.50 / -26.47	-26.48	1.42	-
7	Acacia	-24.86 / -24.82	-24.84	-25.98 / -25.97	-25.98	1.14	-
8	Tilia	-25.59 / -25.74	-25.67	-25.60 / -25.62	-25.61	-0.06	-
9	Honeydew	-25.16 / -25.16	-25.16	-25.85 / -25.89	-25.87	0.71	-
10	Honeydew	-25.77 / -26.06	-25.91	-25.84 / -25.74	-25.79	-0.12	-
11	Honeydew	-25.52 / -25.32	-25.42	-25.80 / -25.80	-25.80	0.38	-
12	Tilia	-24.93 / -25.15	-25.04	-24.11 / -24.01	-24.06	-0.98	-

We found $\delta^{13}C$ values for the acacia honey protein in the range of that from literature. The $\delta^{13}C$ values for acacia honey protein from France [1]

varies between -23.55 ‰ and -25.78 ‰, similar values being found for acacia honey protein from different regions of Europe [13]. In the case of honeydew protein the mean value of $\delta^{13}C$ obtained by us was -25.35 ‰, close to that from Spain, (-24.7‰)[14]. Also comparable values to that obtain by us were also found in two regions from Slovenia, -25.6‰ and -24.7‰ [12].

Table 2. Range of $\delta^{13}C$ for different botanical origin of honey

No.	Botanical origin	$\delta^{13}C$ protein		$\delta^{13}C$ honey	
		max.	min.	max.	min.
1	acacia	-24.76	-24.84	-24.26	-25.98
2	tilia	-24.53	-25.67	-24.06	-25.85
3	honeydew	-25.06	-25.91	-25.12	-26.48
4	multifloral	-25.83	-25.95	-24.10	-24.17

The negative differences in $\delta^{13}C$ values can be due to isotope effects that occur in the synthesis of protein material from different dietary constituents, differences in pollen content from various sources or from feeding C4 plant sugars syrups to bees at the start of the season to build up colony strength. It is known that $\delta^{13}C$ values of animals and their products are dependent [9,15,16] on their diet. Some differences are due to isotopic effects in the synthesis of the protein from dietary constituents, but these effects are reduced because usually the honey is collected from more than one colony, from different locations on a period of several weeks. At the beginning of spring, when bees are fed with sugar syrups, the protein produced by the bees may reflect the isotopic composition of the food, but the bee population being constantly renewed at 3-4 weeks and fed with honey collected previously, the influence of corn sugars to the $\delta^{13}C$ values of the proteins is diluted quickly [5].

The results, obtained for investigated honey samples, pointed out that the mean value of honey protein for our samples (-25,35‰) is very close to that found for samples from temperate climate areas (-25.4‰ in Limousin, France and -26.1‰ in Allgau, Germany [13]).

It is internationally accepted that adulteration with C4 sugars is not confirmed unless the negative difference between the honey and protein $\delta^{13}C$ values is equal to or more negative than -1 ‰. When the differences between $\delta^{13}C$ values are positive, they indicate the absence of adulteration with C4 sugars, being considered as zero.

CONCLUSIONS

In this work 12 Romanian honeys from different floral sources and their corresponding protein extracts were analyzed in order to determine the presence of adulteration. The detection of honey adulteration with HFCS was realized by coupling an isotope ratio mass spectrometer to an elemental analyzer. Using the difference in stable carbon isotope ratio between honey and its protein fraction it is possible to evaluate the adulteration of honey with small amounts (minimum 7%).

The results of the 12 analyzed samples with different geographical origin (acacia, tilia, honeydew, multifloral) showed an obvious adulteration for the multifloral honey, while for other 5 samples a negative difference was observed between $\delta^{13}C$ protein si $\delta^{13}C$ honey, but lower than the internationally accepted value of -1‰ , indicating that for this samples no C4 sugars were added. For the other 6 samples the differences between the $\delta^{13}C$ values of the honeys and their corresponding protein extracts were positive, indicating the absence of adulteration. Also, the obtained results denoted (indicated) that the mean value of honey protein of our samples correspond to that obtained for samples from temperate climate areas.

EXPERIMENTAL SECTION

The detection of sugar adulteration of honey can be realized by measuring the difference between the isotope ratio value of the whole honey sample and that of its separately prepared protein fraction. The procedure consists in diluting a known amount of honey in distilled water adding sodium tungstate solution and sulphuric acid to precipitate proteins. This solution is immersed in an 80ºC water bath until visible flocculates form. After the proteins are separated and dried. To measure the whole honey, the honey samples are placed in an oven for drying [17-18].

The analyzed CO_2 was obtained by a microcombustion technique. The samples, whole honey and its protein fractions, were loaded into Sn capsules and moved into the quartz tube of an elemental analyzer (NA1500 NCS, Carlo Erba Instruments) where the samples were combusted in a stream of oxygen at 1020ºC. The quartz tube was filled with tungstic oxide on alumina and elemental Cu where the oxygen excess was reduced. On the PORAPAQ column the resulting mixture of combustion gases were separated (due to the different times of retention of the gases on the column). The CO_2 obtained was trapped in an ampoule at liquid nitrogen temperature. The water resulting from the combustion reaction was absorbed by a $MgClO_4$ trap. CO_2 was purified and before connecting the ampoule containing the sample to the mass spectrometer a gas pressure adjustment was made [19].

In this work we used the on-line technique, which is called EA-IRMS, i.e. Elemental Analyzer coupled with Isotope Ratio Mass Spectrometry.

This method makes it possible to eliminate the nuisance of off-line purifying procedures and gives an easy, fast, comfortable and more precise way to measure our samples. This solution allows the measurement the $\delta^{13}C$ value of original honey samples as low as 10 gram. However we needed only 2 mg of prepared (flocculated and/or dried) samples to measure in.

^{13}C to ^{12}C ratio was measured in a Delta Plus type mass spectrometer developed by Thermo Finnigan, coupled with Carlo Erba Elemental Analyzer. The spectrometer has a dual inlet system and triple ion collector (the ion signals are measured simultaneously). The carbon stable isotope ratio analysis values are reported with respect to the VPDB international standard. However the laboratory utilizes our own working standard gas in daily operations.

The apparent sugar content might be calculated as follows:

$$Adulteration[\%] = \left[\frac{\delta^{13}C_{protein} - \delta^{13}C_{honey}}{\delta^{13}C_{protein} - (-9.7)} \right] \times 100$$

where the $\delta^{13}C$ value of -9.7 ‰ is derived from the mean value for the high fructose corn syrup.

To establish the reproducibility of the technique 2 replicates of each honey samples were analyzed.

ACKNOWLEDGMENTS

REFERENCES

1. J. F. Cotte, H. Casabianca, J. Lheritier, C. Perrucchietti, C. Sanglar, H. Waton, M.F.Grenier-Loustalot, *Analytica Chimica Acta*, **2007**, *582*, 125.
2. L. W. Doner, J. W. White, *Science*, **1977**, 891.
3. R. Singhal, P. Kulkarni, D. Rege, "Honey, quality criteria. Handbook of indices of food quality and authenticity" Woodhead publishing ltd., Cambridge, England, **1997**.
4. W. Korth, J. Ralston, *RIRDC Publication No 02/047*, **2002**.
5. J. W. White, K. Winters, *Journal of the Association of Official Analytical Chemists*, **1989**, *72 (6),* 907.
6. A. Rossmann, C. Lullmann, H. L. Schmidt, *Zeitschrift für Lebensmittel-Untersuchung und –Forschung*, **1992**, *195*, 307.
7. J.W. White, *Journal - Association of Official Analytical Chemists,* **1992**, *75,* 543.

8. J. W. White, K. Winters, P. Martin, A. Rossmann, *Journal - Association of Official Analytical Chemists*, **1998** , *81*, 610.

9. M. J. De Niro, S. Epstein, *Geochimica et Cosmochimica Acta*, **1978**, *42*, 495.

10. G. J. Padovan, L. P. Rodrigues, I. A. Leme, D. De Jong, J. l. S Marchini, *Eurasian Journal of Analytical Chemistry*, **2007**, *2*, 134.

11. G. D. Farquhar, J. R. Ehleringer, K. T. Hubick, *Annual Review of Plant Physiology and Plant Molecular Biology*,**1989**, *40*, 503.

12. U. Kropf, J. Bertoncelj, M. Korošec, M. Nečemer, P. Kump, N. Ogrinc, T. Golob, *APIACTA*, **2009**, *44*, 33.

13. A. Schellenberg, S. Chmielus, C. Schlicht, F.Camin, M. Perini, L.Bontempo, K. Heinrich, S. D. Kelly, A. Rossmann, F. Thomas, E. Jamin, M. Horacek *Food Chemistry,* **2010**, *121*, 770.

14. J. S. Bonhevi, F. V. Call, *Food Science and Technoogy International*, **1995**, *1*, 25.

15. D. J. Minson, M. N. Ludlow, J. H. Troughton, *Nature*, **1975**, *256*, 602.

16. F. J. Winkler, H. L. Schmidt, *Zeitschrift für Lebensmittel-Untersuchung und – Forschung*, **1980**, *171*, 85.

17. AOAC Official method 978.17 – Corn and Cane sugar products in honey.

18. AOAC Official method 991.41 – C4 Plant sugars in honey.

19. Zs. Szanto, E. Svingor, I. Futo, L. Palcsu, M. Molnar, *Studia Universitatis Babes – Bolyai Seria Physica*, **2001**,*Special Issue*, 124.

UV ABSORPTION PROPERTIES
OF DOPED PVA TiO$_2$ MEMBRANES

MIHAI TODICA[a], LUCIANA UDRESCU[a], CORNEL VIOREL POP[a], MIHAELA POP[a], STEFAN TRAIAN[a], SIMION SIMON[a]

ABSTRACT. The effect of UV exposure on PVA membranes doped with TiO$_2$ was observed by UV-vis and Raman spectroscopy. After several hours of moderate UV exposure, the absorption coefficient of non doped membranes is modified. The absorption property of PVA was enhanced by addition of TiO$_2$.

Keywords: *PVA, UV-vis Raman spectroscopy, TiO$_2$*

INTRODUCTION

Poly vinyl alcohol (PVA) is one of the most popular polymers with applications in different domains of activity, beginning with the industry, and finishing with the medicine [1, 2, 3]. In medicine it is used as matrix for drug controlled release, in making artificial blood vessels, or contact lenses [4, 5]. During these applications, especially in the skin care, the polymeric matrix may be deliberately or accidentally exposed to UV radiation. Such high energy radiation can have destructive effects on the microscopic structure of the polymer. The interest is to maintain unaffected, as long as possible, the properties of the polymeric matrix against the aggressive actions. PVA provides only a weak protection against UV radiation at 291 nm. Usually the protection against this radiation is enhanced by adding TiO$_2$, which is well tolerated by the biological tissues at small concentration [6, 7]. The aim of our work was to observe the behaviour of this polymeric matrix submitted to UV exposure, and the possibility to enhance the UV absorption property by addition of TiO$_2$. The investigations were done by methods sensitive on molecular scale, Raman and UV-vis spectroscopy.

RESULTS AND DISCUSSION

We observed the absorption property as a function of UV time exposure. In Figure 1 are presented the absorption spectra for the membrane with polymeric concentration 20% in initial state and after 4 hours of UV irradiation.

[a] *"Babes-Bolyai" University, Faculty of Physics, M. Kogalniceanu No 1, 400084 Cluj-Napoca, Romania, mihai.todica@phys.ubbcluj.ro*

The spectrum of the non irradiated sample is broad, showing an important absorption in the domain 250-350 nm, (Figure 1 curve B). The maximum absorption peak appears at 281 nm and its amplitude is $A_{0\ 20}=0.156$ a.u. The width of the spectrum suggests a large distribution of the energetic states of absorbent molecules, determined by rotation and vibration of molecules.
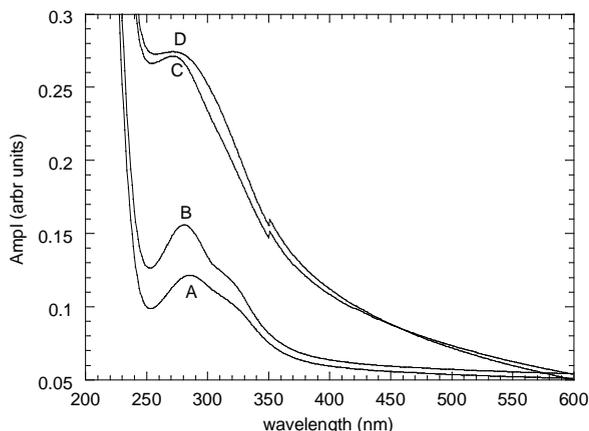
Figure 1 The UV-vis absorption spectra of doped and non doped membranes: Curve A the non doped membrane after 4 hours UV irradiation; Curve B the non doped membrane before irradiation; Curve C membrane with 10% TiO_2 before irradiation; Curve D membrane with 10% TiO_2 after 4 hours UV irradiation.
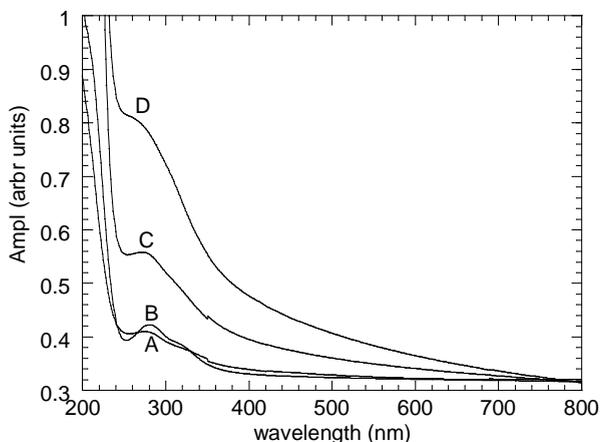
Figure 2 The UV-vis absorption spectra for the non doped membrane and membranes with different content of TiO_2, before irradiation. Curve A, the non doped membrane; Curve B, with 1% TiO_2; Curve C, with 10% TiO_2; Curve D, with 20% TiO_2

When the time of exposure increases, the amplitude of the peak decreases continuously. After 4 hours of irradiation its amplitude is $A_{4\ 20}=0.12$

a.u., (Figure 1 curve A). The intense UV irradiation facilitates the apparition of local order, even formation of crystalline domains in polymeric materials, and the polymeric network became more rigid [8].These modification of the molecular order are responsible for the modification of the absorption spectrum after irradiation.

Enhancement of the UV absorption property can be obtained by addition of different inert compounds to the polymeric matrix. We selected TiO$_2$ because it is known as one of the substances characterized by very good absorbance in the UV domain and also for its compatibility with biological tissues [9]. We observed the absorption properties of polymeric membranes doped with different concentrations of TiO$_2$ in initial state and after different time intervals of UV irradiation. At 1% concentration the absorption spectrum is very little modified. As the concentration of TiO$_2$ increases, the absorption peak is observed at the same wavelength but its amplitude increases continuously, being few times greater than that of the non doped membrane, (Figure 2). This behaviour shows clearly the enhancement of absorption properties after addition of TiO$_2$ [10].

The doped membranes were subsequently irradiated for different time intervals with UV radiation and, the absorption spectra were recorded again. For all the concentrations of TiO$_2$ the amplitude and the shape of absorption spectra are very little modified after irradiation, (Figure 1 curves C and D). This behaviour is contrary to those of non doped membranes, where the absorption is reduced after irradiation. The doped membranes appear to be more stable under UV irradiation compared with the non doped ones.

In the next stage of our work we were interested to observe the existence of possible interaction between the polymeric matrix and the TiO$_2$, and possible modifications on the molecular structure of doped and non doped membranes after UV exposure. For this aim we compared the Raman spectra of non doped and doped membranes before and after UV irradiation, (Figure 3). The spectrum of non doped membrane before irradiation contains well defined vibration bands in the domain 1200-1600 cm^{-1}, (Figure 3 curve D). The most intense bands are assigned as follows: 1290 cm^{-1} – CH wagging, 1365 cm^{-1} – CH- bending and OH – bending; 1414 cm^{-1}– CH$_2$ bending. These bands appear also in the spectrum of the doped membrane, before irradiation, at the same wave number. Supplementary bands appear at 400 cm^{-1}, 514 cm^{-1} and 638 cm^{-1} for the samples containing TiO$_2$. As reported in literature, in the domain 200-800 cm^{-1} TiO$_2$ exhibits three vibration bands at 400, 514 and 638 cm^{-1} [11]. The apparition of vibrational bands of PVA and TiO$_2$ at the same wave number before and after doping suggests no interaction between the polymeric matrix and the TiO$_2$, and that the chemical structure of both components remains unchanged after doping.
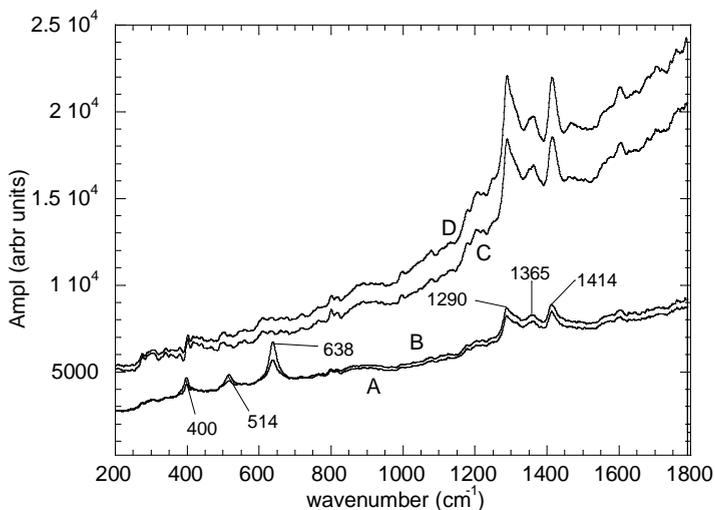
Figure 3 The Raman spectra of doped and non doped membranes. Curve A, membrane with 20% TiO_2 before irradiation; Curve B, membrane with 20% TiO_2 after 4 hours irradiation UV; Curve C, non doped membrane after 4 hours irradiation UV; Curve D, non doped membrane before irradiation

The same analysis was done after UV irradiation. The spectra of doped membranes are very similar before and after irradiation without modifications, (Figure 3 curves A and B). The spectra of non doped membranes show some differences in the domain 1200-1600 cm^{-1} before and after irradiation. The vibrational bands appear at the same wavelength in both spectra, but the amplitude of irradiated one is reduced, (Figure 3 curve C). This behaviour indicates no modifications on the chemical structure of components after UV irradiation.

CONCLUSIONS

The effect of UV radiation on the properties of PVA was observed by UV-vis and Raman spectroscopy. The amplitude of the absorption peak of PVA diminishes continuously with the time of UV exposure. This effect suggests an effect of crystallization induced by iradiation. The absorption property of PVA is enhanced by addition of TiO_2. The absorption coefficient increases with the concentration of dopant. The absorption properties of doped membranes are very little affected by UV irradiation. This fact demonstrates the stabilization effect of TiO_2 on the absorption property. Raman analysis of doped and non doped membranes indicates no modification of chemical structure after UV exposure.

EXPERIMENTAL SECTION

A PVA membrane with polymeric concentrations of 20% was employed, in initial state and after addition of TiO$_2$. The membrane was obtained by mixing the polymer with distilled water, at constant temperature 25^0 C, during several hours, until a homogeneous dispersion of polymer was obtained. Then the gel was displayed on a glass plate and kept 24 hours in dark, at room temperature, until the water evaporates. To obtain doped samples, the TiO$_2$ was introduced in the polymeric gel in concentration 1%, 10% and 20%, mixed many hours, and then dried on open air [12]. These samples were analyzed in their original state and after UV irradiation at different intervals of time. The UV irradiation was performed with an VL 215 G lamp, at 254 nm and 76 mW/cm^2 intensity. For all the samples the UV-vis spectra were measured with a Jasco V-670 system with scan speed 200 nm/min, UV-vis bandwidth 2 nm, and NIR bandwidth 8 nm. The Raman investigations were performed with R 3000 CN systems, with excitation power 150 mW at wavelength λ= 785 nm.

ACKNOWLEDGMENTS

REFERENCES

1. D. Lopez, I. F. Cendoya, J. Torres, C. Tejada, J. Mijanagos, *Appl. Polym.,* **2001***, 82,* 3215.
2. M. Krumova, D. Lopez, R. Benavente, C. Mijanagos, J. M. Perea, *Polymer,* **2002***, 42*, 591.
3. Y. Badr, K. M. Abd El-Kader, R. M. Khafagy, *Journal of Applied Polymers,* **2004***, 92,* 1984.
4. S. Horike, S. Matsuzawa, K. Yamaura, *Journal of Applied Polymers,* **2002***, 84,* 117.
5. I. Kaetsu, "Drug Delivery system", CMC, Tokyo, **1986.**
6. H. Ruixia, W. Leigang, W. Jin, H. Nan*, Applied Surface Science*, **2010**, *256*, 5000.
7. G. Thilo, S.T. Nordwig, M. Georg, H. Julia, D. Heinrich, A. Peter, K. Alexander, *Journal of the American of Dermatology,* **2006***, 55*, 882.
8. B. Stuart, "Polymer analysis", John Wiley and Sons, Chicester, **2002.**
9. R. Yanagisawa, H. Takano, K. Inoue, E. Koike, T. Kamachi, K. Sadakane, T. Ichinose, *Experimental Biology and Medicine*, **2009**, *234*, 314.
10. J. Zhang, M. Li, Z. Feng, J. Chen, C. Li, *J. Phys. Chem. B*, **2006**, *110*, 927.
11. H. C. Choi, Y. M. Jung, S. B. Kim, *Vibrational Spectroscopy*, **2005**, *37*, 33.
12. A. Maurya, P. Chauhan, *Polymer Bulletin* **2011**, DOI 10.1007/s00289-011-0589-6

EFFECT OF DIFFRENT SUBSTRATE TEMPERATURE ON GROWTH OF NANO CRYSTALLINE DIAMOND BY HFCVD TECHNINQUE

HASTI ATEFI[a], MAHMOOD GHORANNEVISS[a, *], ZAHRA KHALAJ[a], MIRCEA V. DIUDEA[b]

ABSTRACT. In this paper, we investigated the effects of different substrate temperature and nitrogen etching gas on synthesis of Nano Crystalline Diamonds (NCDs). We prepared all samples by Hot Filament Chemical Vapor Deposition (HFCVD) system. Silicon wafers (100) were used as substrates for all experiments. All samples were coated by Au at 50 nm thickness, as catalyst layers, by sputtering system. To remove the native oxide on silicon, all the samples were cleaned in ultrasonic bath by acetone, ethanol and de-ionized water, respectively. Substrate temperature was controlled by thermocouple in contact with substrate holder, between 550°C and 650°C. The samples were examined by X-Ray diffraction spectroscopy at room temperature. The changes of surface morphology of the diamond Nano crystals were clearly viewed by the Scanning Electron Microscopy SEM. The results show nanocrystalline diamond films and diamond nano crystals grown on substrate under various temperatures with different crystalline structures.

Keywords: Etching, Hot filament CVD, Nanocrystalline diamond films, SEM.

INTRODUCTION

Due to the unique properties such as high thermal conductivity, chemical stability, and high field failure diamond nano crystals are used in various fields including mechanical, electrical, semiconductor parts, optical application, etc [1-11]. Since 1950, many researcher groups have investigated the growth of diamond by various Chemical Vapor Deposition CVD techniques in view of finding particular ways to obtain diamond for different applications by low pressure, low temperature methods instead of those methods using high pressure, high temperature [12 -25,38]. Compared to the other CVD technique, the Hot Filament Chemical Vapor Deposition HFCVD process presents several advantages, such as the possibility of deposition of thick layers on

---

[*] *Author for correspondence: Prof. Mahmood Ghoranneviss, Tel: +98 21 44869624, Fax: +98 21 44869626 Email:Ghoranneviss@gmail.com*

[a] *Plasma Physics Research Center, Science and Research Branch, Islamic Azad University, Tehran, Iran, P.O.BOX:14665-678*

[b] *Faculty of Chemistry and Chemical Engineering, Babes-Bolyai University, Cluj, Romania*

large areas (over 1000cm^2), the possibility of coating various types of substrate surface, high film uniformity, easy to operate, relatively cheap, etc [29,7].

Since 1990, studies were shifted from poly-crystal to nano-crystal diamond [34]. In these studies, different parameters have been varied: type of gas, gas pressure, gas concentration, substrate preparation, surface roughness, filament's temperature, on seed size and crystal growth rate, etc [7, 28-33]. Some studies reported measurements of the experimental parameters in the growth of Nano Crystalline Diamonds NCD [11, 25-26]. According to D.C. Barbosa's group [11], one of the most important parameters in growing NCD films is the substrate temperature (in the range 550°C to 850°C). In 2008, C. J. Tang et al. added N_2 and O_2 in the mixture of CH_4 and H_2 at MPCVD method; they could grow large-grained polycrystalline and nanocrystalline diamond [34]. They used N_2 as the main gas in the reaction chamber to promote the secondary nucleation rate. Similarly, Sobia Allah et al. have grown NCDs films by HFCVD in $Ar/N_2/CH_4$ gas mixtures; they found that N_2 concentration in the flow added to plasma has a great influence on the grain size of the nano diamonds, as measured by X-Ray Diffraction XRD. In this case the diamond peaks became narrower [32].

In this work, we investigate the growth of diamond nano-crystals on silicon substrate using HFCVD method and the effect of different temperatures on surface morphology and the formation of diamond crystals. The nitrogen was used in the pretreatment of the substrates for the first nucleation. Scanning electron microscopy SEM, X-ray diffraction XRD and Dektak profilometer were used for analyzing the samples.

RESULTS AND DISCUSSION
A. Methods for Substrate pre-treatment

Several methods for coating, including sputtering, evaporation, ion implantation and plasma-assisted chemical vapor deposition (CVD) can be used. Substrate coating adhesion can be enhanced by carrying out several pre-treatments of the substrate. Owing to growing diamond for better quality, we used some pretreatments before the main growing process.

In this study all samples were prepared by a sputtering system, previously described in ref [35]. Figure 2 shows the thickness of the gold catalyst layer, deposited on the substrates for 8 minutes (Dektak profilometer 3, version 2.13). The substrate temperature reached 550°C when the nitrogen was introduced into the system. This made gold islands on the surface; clearly, the nitrogen etching-treatment changed the morphology of the surface by creating nucleation sites thus increasing the diamond deposition.

B. Morphology Study

The surface morphology of the nanocrystalline diamond films was observed by SEM analysis (model XL30, Philips Company, Holland) as shown in Figure 3. In a first sample (Figure 3, a), the cauliflower nano crystalline diamond,

grown at 550 ℃ substrate temperature, is evidenced . When the substrate temperature increased to 600 ℃, the particle size decreased and a higher distribution of NCD could be observed (Figure 3, b). At 650℃, the grain size the particles became low and one can see a low density of NCD, which dispersed over the substrate surface (Figure 3,c). Thus, by increasing the temperature from 550℃ to 650℃ the crystal quality lowers. This indicates that nano crystalline diamond is suitably formed in a lower-temperature process.

C. X-Ray Diffraction XRD analysis

In XRD, the main peak is observed at $2\theta=41.68°$, $2\theta=41.81°$ and $2\theta=41.67°$, which indicates the diffraction of (101) d iamond for samples (a), (b) and (c), respectively. The results indicate a decrease in the quality of NCD by increasing the temperature up to 650℃ and s uggested that the film has a strong (101) preferential texture. The full-width-half-maximum (B) of these peaks was used to calculate the grain size from the well-known Sherrer's formula [7].

$$L(hkl) = \frac{K\lambda}{B\,Cos\theta\,hkl}$$

Here K=0.9, λ=1.54A° and θ is the Bragg angel.

The grain size decreases from 43.1nm to the 35.9nm with the substrate temperature increasing. Similar results have been reported by Barbosa's group. They suggested that the increase in defect density is induced by temperature raising [11]. Next, the patterns show the peaks with $2\theta=42.72°$ and $42.90°$ which indicate the diffraction of (102) diam ond structure. Figure 4 shows the XRD patterns for NCD grown on substrates at different temperatures.
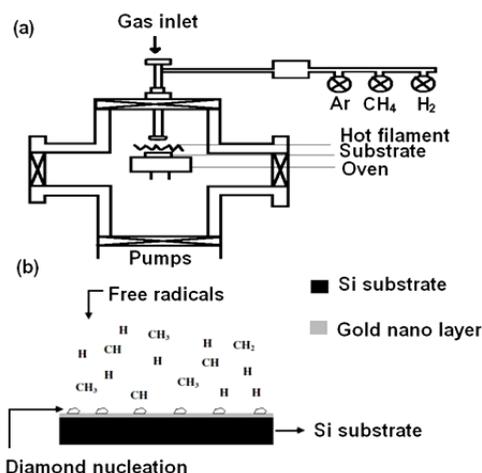

Figure 1. Generalized schematic HFCVD system (a) and the growth process in a diamond CVD reactor (b).
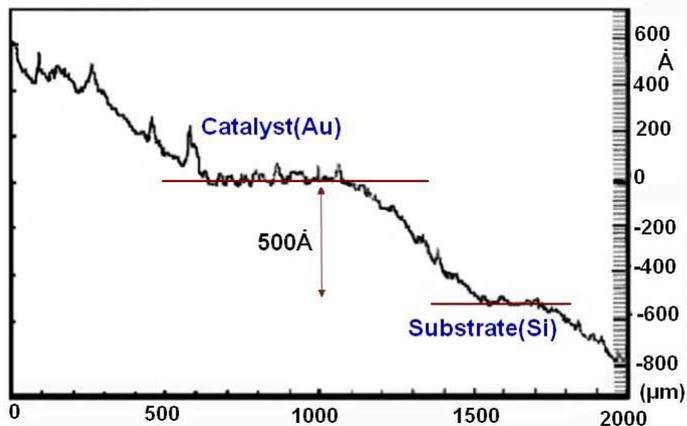
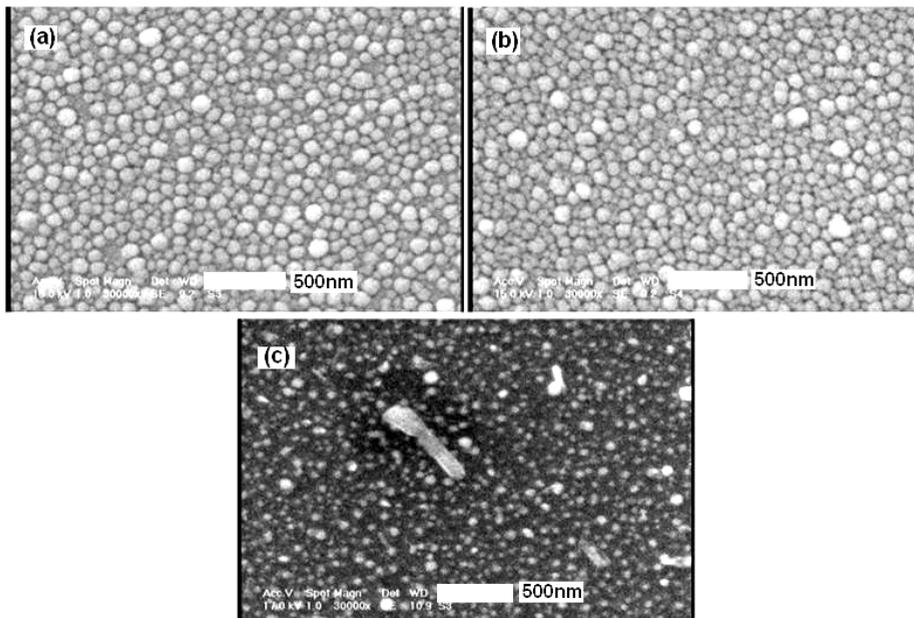**Figure 2.** The gold layer thickness, on silicon substrates, equals 50nm.

Fig. 3. SEM images of nanocrystalline diamond NCD grown at different substrate temperature (a): 550℃, (b):600℃, (c):650℃.
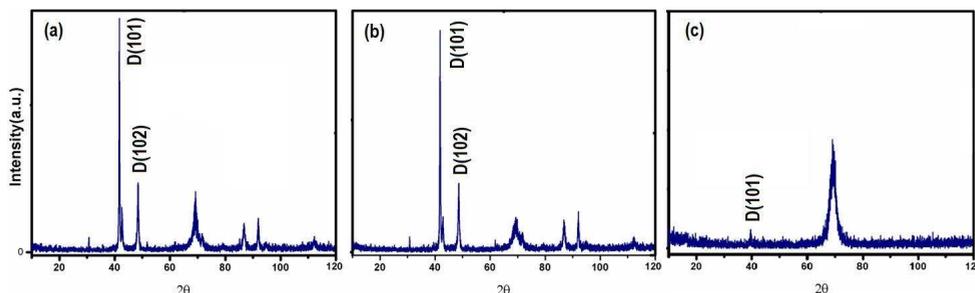
Fig. 4. X-Ray diffraction of nano crystalline diamond grown at different substrate temperature (a):550℃; (b):600℃; (c):650℃.

CONCLUSION

In this paper, we investigated the effects of variation of the substrate temperature on the synthesis of nano crystalline diamond NCD. For enhancing the diamond nucleation, we used gold as a catalyst nano layer and nitrogen as an etching gas. We prepared all samples by a hot filament chemical vapor deposition system. The results show that the optimum conditions are placed at the minimum temperature (550 ℃) in this experiment . The XRD, SEM and DEKTAK profilometer were the equipments used for analyzing the results in this experiment.

EXPERIMENTAL SECTION
A.HFCVD System

We prepared all samples in a Hot Filament Chemical Vapor Deposition HFCVD system. It consists of a reaction chamber, two rotary and diffusion pumps, an oven, water cooled vessel, a gas mixture, and a movable filament holder. The filament consists of a flat tungsten wire of 0.5mm in diameter for activating the source gas. The scheme of this system and therein reaction is shown in Figure 1.

B. Growth Process

Silicon wafers [p-typed Si (100)] was used as the substrates for all experiments. For pre-treating the samples and reducing the surface containments, we cleaned them, in an ultrasonic bath, by acetone, ethanol and de-ionized DI water for 15 min, respectively. The substrates were loaded to the CVD reaction chamber after pre-treatment. The distance between the substrate and filament was kept around 2cm. Before deposition process, to enhance diamond nucleation density and to improve the crystalline quality, argon Ar gas, was introduced into the system at a pressure of 8 Torr, and a flow ratio of 80 Sccm, for 45 minutes. Then N_2 gas was added to the reaction chamber. By using N_2 as etching gas, a suitable surface roughness was made [35]. In this step, the pressure, flow ratio,

substrate temperature and etching time were: 15 Torr, 80 Sccm, 550 °C, and 45min respectively. For the deposition process, the chamber was evacuated down to 8.5×10^{-5} Torr. All the parameters were fixed during the deposition process except the substrate temperature, of which variation was controlled by a thermocouple in contact with the substrate holder, between 550°C and 650°C. The total flow rate of CH_4 /H_2 was fixed at 220 Sccm (concentrations Vol. 5.5% CH_4/ H_2). The overall pressure was 25 Torr while the deposition time was 80 min for each experiment.

Recall that the mechanism of deposition process was reported in many articles. In the growth process on silicon based materials by HFCVD, SiH_4 undergoes a catalytic decomposition into SiH_x or Si_2H_x (x = 1, 2, 3) radical species by the hot filament [36]. The radicals thus resulted can either deposit on substrates or further react with other gas phase species to produce precursor radicals for film deposition. These radicals were found to play an important role in producing high quality amorphous hydrogenated and polycrystalline silicon thin films [36]. Therefore, the nature of the precursor radicals has a great influence on the structure of the as-deposited films [36]. Recent studies performed by Matsumura et al. [37] on the radicals desorbed from a tungsten hotwire, by using threshold ionization mass spectrometry, evidenced various precursor radicals and their effect on the growth process. They shown that the H radical is one of the key radicals and it is used to determine the structure and characteristics of the as-grown diamond films. It was found that the crystalline fraction increased with the increasing dilution ratio (H_2/SiH_4), and amorphous and crystalline silicon were etched rapidly by the H radical [36, 37].

In this paper, the quality of diamond crystals was examined by X-Ray diffraction spectroscopy at room temperature. The surface morphology of the samples was investigated by the scanning electron microscopy SEM. The thickness of the catalyst layer was examined by Dektak profilometer.

ACKNOWLEDGMENTS

REFERENCES

1. C. Popov, G. Favaro, W.Kulisch, J.P.Reithmaier, *Diamond and Related Materials*, **2009,** *18*, 151.
2. C.Popov. W.Kulisch, S.Bliznakou, G.Ceccone, D. Gilliland, L.Sirghi, F.Rossi*, Diamond and Related Materials*, **2008,** *17*, 1229.
3. ShanShan Wang, Guohuo Chen, Fenglin Yang, *Thin Solid Films*, **2009,** *317*, 3559**.**
4. C.K.Lee, *Applied Surface Science*, **2008,** *254*, 4111.

5.   C.S. Abreu, M. Amaral, F.J. Oliveira, J.R. Gomes, R.F. Silva, *Diamond and Related Materials*, **2009,** *18*, 271.
6.   Waqar Ahmed, Htet Sein, Mark Jackson, Riccardo Polini, *Tribology International*, **2004,** *37*, 957.
7.   A. Amorim, P.A. P.Nascente, V.J.Trava.Airoldi, E.J.Corat, A.R.Alves, J.R.Moro, *Vacuum*, **2009,** *83*, 1054.
8.   Z.L.Wang, C.Lu, J.J.Li, C.Z.Gu, *Diamond and Related Materials*, **2009,** *18*, 132.
9.   N.Kohmura, K.Sudoh, K.Sato, K.K.Hiraku, K.Miake, G.Friedbacher, *Diamond and Related Materials*, **2005,** *14*, 283.
10. C.Pietzka, A.Denisenko, A.Romanyuk, P.J.Schafer, L.A.Kibler, J.Scharpf, E.Kohn, *Diamond and Related Materials*, **2010,** *19*, 213.
11. D.C.Barbosa, F.A.Almeida, R.F.Silva, N.G.Ferreia, V.J.Trava-Airoldi, E.J.Corat, *Diamond and Related Materials*, **2009,** *18*, 1283.
12. Qiu-ping Wei, Z.M. Yu, Michael N.R. Ashfold, J. Ye, L. Ma , *Applied Surface Science*, **2010,** *256*, 4357.
13. B.J.Jones, S.Wright, R.C.Barklie, J.Tyas, J.Franks, A.J.Reynolds, *Diamond and Related Materials*, **2008,** *17*, 1629.
14. K.Subramanian, W. P. Kang, J.L.Davidson, W.H.Hofmeister, *Diamond and Related Materials*, **2005,** *14*, 404.
15. M. Akbarzadeh Pasha, A.Shafiekhani, M.A.Vesaghi, *Applied Surface Science*, **2009,** *256*, 1365.
16. Lianh Guo, Guohua Chen, *Diamond and Related Materials*, **2007**, *16*, 1530.
17. A.H.Mahan, P.A.Parilla, K.M.Jones, A.C.Dillon, *Chemical Physics Letters***, 2003,** *413*, 88.
18. Min-Sheng You, Franklin Chau-Nan Hong, Yeau-Ren Jeng, Shih-Ming Huang, *Diamond and Related Materials*, **2009,** *18*, 155.
19. W.L.Wang, R.Q.Zhang, K.L.Liao, Y.W.Sun, B.B.Wang *Diamond and Related Materials*, **2000,** *9*, 1660.
20. M.Kadlečikova, M.Vojs, J.Breza, M.Veselŷ, Z.Fragla, M.Michalka, J.Matějková, A.Vojačková, T.Daniš, M.Marton, *Microelectronics Journal*, **2007,** *38*, 20.
21. Yu.A.Mankelevich, P.W, May, *Diamond and Related Materials*, **2008,** *17*, 1021.
22. Yong k, Cho, Woo S.Jang, Sehoon Yoo, Sang G.Kim, Sung W.Kim, *Surface Coating Technol.*, **2008,** *202*, 5390.
23. A.K. Dua, M. Roy, J. Nuwad, V.C. George, S.N. Sawant, *Applied Surface Science*, **2004,** *229*, 254.
24. S. Gastélum, E. Cruz-Zaragoza, A. Favalli, R. Meléndrez, V. Chernov, M. Barboza-Flores, *Diamond and Related Materials*, **2008,** *17*, 1283.
25. Shumin Yang, Zhoutong He, Qintao Li, Dezhang Zhu, Jinlong Gong, *Diamond and Related Materials*, **2008,** *17*, 2075.
26. Qiu-ping Weia, Z.M. Yua, Michael N.R. Ashfoldb, J. Yea, L. Mac, *Applied Surface Science*, **2010,** *256*, 4357.
27. D. Franta, L. Zaíčková, M. Karásková, O. Jašek, D. Nečes, P. Klapetek, M. Valtr, *Diamond and Related Materials*, **2008,** *17*, 1278.
28. S. Porro, G. De Temmerman, S. Lisgo, Ph. John, I. Villapando, J. W. Zimmer, B. Johnson, J. I.B. Wilson, *Diamond and Related Materials*, **2009,** *18*, 740.

29. Sobia Allah Rakha, Zhou Xintai, Dezhang Zhu, Yu Guojun, *Current Applied Physics*, **2010,** *10*, 171.
30. M.Amaral, A.J.S.Fernandes, M.Vila, F.J.Oliveria, R.F.Silva, *Diamond and Related Materials*, **2006,** *15*, 1822.
31. Z.L.Wang, C.Lu, J.J.Li, C.Z.Gu, *Applied Surface Science*, **2009,** *255*, 9522.
32. Yongqing Fu, Bibo Yan, Nee Lam Loh, *Surface Coating Technology* ,**2000,** *130*, 173.
33. H.Li,Hak-Joo Lee, Jong-Keuk Park,Young-Joon Baik, Gyu Weon Hwang, Jeung-hyun Jeong, Wook-Seong, *Diamond and Related Materials*, **2009,** *18*, 1369.
34. C.J.Tang,A.J.Neves, S.Pereira, A.J.S.Fernandes, J.Grácio, M.C.Carmo, *Diamond and Related Materials*, **2008,** 17, 72.
35. Z. Khalaj, M. Ghoranneviss, S. Nasirilaheghi, Z. Ghorannevis, R. Hatakeyama*, Chinese Journal of Chemical Physics*, **2010,** *23*, 689.
36. GUO Xiao-Song, BAO Zhong, ZHANG Shan-Shan, XIE Er-Qing. *Chinese Physical Letters*, **2011,** *28*. 2.
37. Matsumura H , *Materials Research Society Symposium Proceedings***, 1999,** 557 67.
38. Z.Khalaj, S.Z.Taheri,S.N.Laheghi,P.A.Eslami, *Iranian Physical Journal*, **2009,** 3-1, 19.

OBSERVATION OF UV-VIS ABSORPTION PROPERTIES OF SOME PVA MEMBRANES WITH SILVER NANOPARTICLES

LUCIANA UDRESCU[a], BOGDAN MARTA[a], MIHAELA POP[a], CORNEL VIOREL POP[a], TRAIAN STEFAN[a], MIHAI TODICA[a]

ABSTRACT. The UV-vis absorption properties of polyvinyl alcohol (PVA) membranes containing 0.04 ml silver nanoparticles were investigated by UV-vis spectroscopy. The samples were investigated in initial state and after UV and gamma exposure. Some modification appears in the spectra of samples containing AgNPs after gamma irradiation. This behaviour indicates modifications induced in the local structure of the polymeric membranes.

Keywords: *Poly (vinyl alcohol), AgNPs, gamma irradiation, UV-vis spectroscopy*

INTRODUCTION

Poly (vinyl alcohol) (PVA) is a water-soluble polymer widely used in industry because of its high capability to form aqueous membranes and gels [1, 2]. Owing to hydroxyl groups present in each unit, PVA is characterized by strong hydrophilic and hydrogen bonding character; thus, it forms hydrogels applied in medicine and pharmacy [3, 4, 5]. The first polymeric matrices doped with nanoparticles were obtained by Koon and coworkers in 1984 [6, 7]. The metal nanoparticles doped in polymer have many applications, such as optical filters, magnetic and optical data storage [8].

The aim of our study is the investigation of the properties of PVA doped with AgNPs, after UV and gamma irradiation. To monitor the effect of doping on the optical properties, the UV-vis spectra were recorded for samples in initial state and after exposure.

RESULTS AND DISCUSSION

The main effect of UV irradiation of materials is the excitation of electronic orbital or modification of vibration state of molecular bonds. At high doses ionization, scission of molecules or conformational changes can appear, which can induce modification of the absorbance spectrum in the UV-vis domain. These effects can be observed in systems containing only a single component, but also for doped system containing many components, i.e.

---

[a] *Universitatea Babeş-Bolyai, Facultatea de Fizică, Str. Kogălniceanu, Nr. 1, RO-400084 Cluj-Napoca, Romania, lucianaudr@yahoo.com*

binary systems formed by polymers doped with different nanoparticles. For such systems the spectrum contains the absorption characteristics of both components. To observe this behaviour we compared the absorption spectrum of pure polymeric matrix with the spectrum of doped membrane before UV irradiation. The pure polymer is characterised by a single absorption band centred at 275 nm, (Figure 1, curve A). As reported in literature this band may be assigned to a $\pi \rightarrow \pi^*$ transition. This transition was related to the carbonyl groups (C=O) associated with ethylene unsaturated bond (C=C) of the type – (CH=CH$_2$) CO-. The existence of carbonyl functionalities is probably due to oxidation during manufacturing and processing [9, 10]. This band appears also in the spectrum of the doped membrane, but its amplitude is greater. A supplementary band, centred at 450 nm, appears in this spectrum. As reported in literature, this band is assigned to the plasmonic resonance frequency of silver nanoparticles [11].
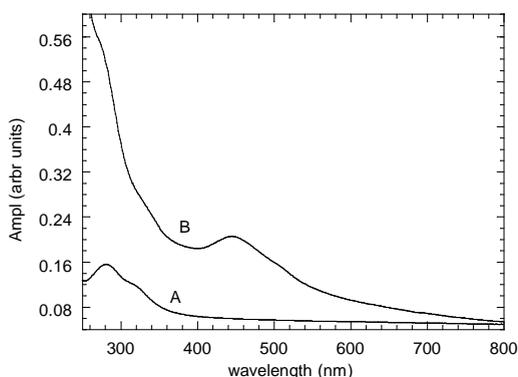
Figure 1. The UV-vis absorption spectra for the non doped and doped PVA membrane before irradiation. A). non doped sample; B). doped sample

The doped membranes were exposed to UV radiationat 254 nm for different time intervals and the absorption spectra were recorded. The main characteristics of the spectrum - the absorption bands at 275 and 450 nm - appear in all spectra but some differences can be observed depending on the dose of radiation. The absorption peaks at 450 nm were blue shifted as the time of UV irradiation increases, (Figure 2). After 4 hours of irradiation the absorption peak shifts to 432 nm. Blue shift means increasing of plasmonic resonance frequency, an effect which can be correlated with the existence of reduced size silver nanoparticles [11]. Some mechanisms can be suggested. UV irradiation facilitates the rearrangement of local chains and the migration of isolated Ag$^+$ ions existing in the system. By a self assembled mechanism such ions can give rise to new nanoparticles with different size compared to those existing initially in the system. Other

possible mechanism is the scission of conglomeration nanoparticles, effect induced also by the rearrangement of local polymeric chains under UV exposure. The intensities of the peaks increase with increasing the time of UV irradiation (1.1 a.u for 1 hour UV irradiation, 1.7 a.u for 2 hours UV irradiation, 2.1 a.u for 3 hours UV irradiation and 2.3 a.u for 4 hours UV irradiation) [12]. This behaviour indicates the increase of the proportion of the absorbents domains in the system by scission of conglomeration of nanoparticle or apparition of supplementary nanoparticle by self assembled mechanism.
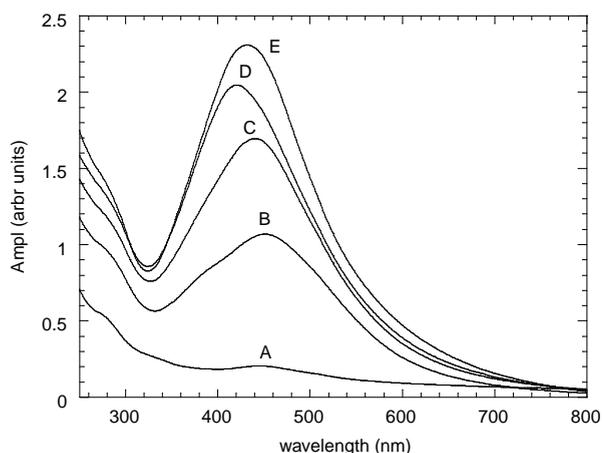

Figure 2 UV-vis absorption spectra for the doped sample before and after different time intervals of UV irradiation. A). before irradiation; B). after 1 hour irradiation; C). after 2 hours irradiation; D). after 3 hours irradiation; E). after 4 hours irradiation

Gamma irradiation produces the same effects as UV irradiation, except that processes requiring high energy, ionization or molecular breaking bonds, are more probable. Figure 3 shows the UV-vis spectrum of doped membrane before irradiation and the spectra for different gamma doses (729 Gy, 1478 Gy and 2217 Gy) [14]. For the unirradiated sample, the nearly zero absorption in the wavelength range 300-800 nm is followed by a continuous increase in the absorption in the wavelength range 200-300 nm. A very small absorption peak appears at 450 nm. When AgNPs is embedded in PVA membrane, the optical properties are the result of the electronic transition of the two materials. The absorbance in the domain 200-300 nm is characteristic to polymeric support, whereas the peak at 450 nm is assigned as plasmonic resonance band of the silver nanoparticles [13]. After gamma irradiation, the amplitude of absorption spectra increases. The amplitude of the 450 nm peaks is increasing from1.5 a.u at 739 Gy to 3.3 a.u at 1478 Gy and 4.6 a.u for the radiation dose at 2217 Gy).

The important enhancement in absorption is in agreement with the colour change of PVA samples, which varies from transparent for the unirradiated membrane to yellowish brown for the membrane irradiated with the highest irradiation dose (2217 Gy). This band is assigned as plasmonic resonance frequency of silver nanoparticles and it is associated to the striking colors of the samples [12]. As the radiation dose increased the plasmonic band is shifted from 450 to 432 nm. The plasmonic peak gets narrower and sharper and also increases in the intensity with increasing radiation dose from 0 Gy to 2217 Gy. As in the case of UV irradiation, we suggest as explanation the apparition of spontaneous silver nanoparticles or scission of conglomeration of such systems. The spontaneous formation of silver nanoparticles can be attributed to the direct redox between PVA and Ag^+ stimulated by the gamma irradiation. However, the amplitude of the absorption peak is greater in the case of gamma-irradiated samples, compared with the UV-irradiated samples, which suggests a greater probability of apparition of spontaneous silver nanoparticles or scission of agglomerations of nanoparticle under gamma irradiation.
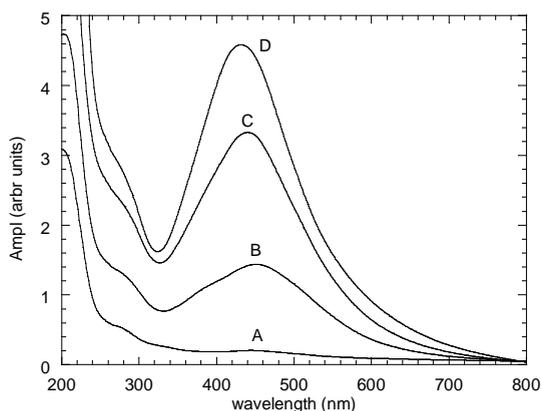
Figure 3 The UV-vis absorption spectra for doped samples irradiated at different gamma doses. A). before irradiation; B). after 739 Gy; C). after 1478 Gy; D). after 2217 Gy

CONCLUSIONS

The effect of UV radiation and gamma irradiation on the properties of PVA with AgNPs was observed by UV-vis spectroscopy. Compared with the spectrum of pure polymer, a supplementary absorption peak appears at 450 nm, attributed at AgNPs. The amplitude of the 450 nm absorption peak of doped membranes is increasing continuously with the time of UV exposure. A similar behaviour was observed after gamma irradiation, but the absorption effect is enhanced. This behaviour is associated with the

spontaneous formation of silver nanoparticles or scission of agglomeration of such systems.

EXPERIMENTAL SECTION

The aqueous PVA membrane had a polymer concentrations 20% in initial state, to which 0,04 ml AgNPs was added. The PVA was obtained by mixing the polymer with distilled water at 55^0 C for 3 hours, until a homogeneous dispersion was obtained. A 10-mL volume of 1.0 mM silver nitrate was added dropwise (about 1 drop/second) to 30 mL of 2.0 mM sodium borohydride solution that had been chilled in an ice bath. The mixture was stirred vigorously on a magnetic stirrer. The solution turned light yellow after the addition of 2 mL of silver nitrate and a brighter yellow when all of the silver nitrate had been added. The entire addition took about three minutes, after which the stirring was stopped and the stir bar removed. These samples were analyzed in their original state and after UV and gamma exposure. UV irradiation was achieved with a VL 215 G lamp at 254 nm and 76 mW/cm^2. The gamma exposure was performed using a ^{60}Co source for different time intervals corresponding to 739 Gy and 2217 Gy. The UV-vis spectra were measured with a Jasco V-670 system with scan speed 200 nm/min, UV-vis bandwidth 2 nm, and NIR bandwidth 8 nm.

ACKNOWLEDGMENT

REFERENCES

1. E. E. Shafee, H. F. Naguib, *Polymer*, **2003**, *44*, 1647

2. W. Li, F. Xue, R. Cheng, *Polymer*, **2005**, *46*, 12026

3. H. Trieu, S. Qutubuddin, *Polyme*r, **1995**, *36*, 2531

4. G. Paradossi, F. Cavalieri, E. Chiessi, C. Spagnoli, M. K. Cowman, *Journal of Materials Science: Materials in Medicine*, **2003**, *14*, 687

5. H. Kaczmarek, A. Podgorski, *Journal of Photochemistry and Photobiology A: Chemistry,* **2007**, *191*, 209

6. N. C. Koon, D. Weber, P. Penrsson, A. I. Shindler, *Materials Research Society Symposium Proceedings* **1984**, *27*, 445

7. P. E. Rehrsson, D. C. Weber, N. C. Koon, J. E. Campana, S. L. Rose, *Materials Research Society Symposium Proceedings*, **1984**, *27*, 429

8. P. P. Townsed, P. J. Chandler, L. Zhang, "Optical Effects of Ion Implantation", Cambridge University press, Cambridge, **1994**.

9. K. A. M Abd El-Kader, S. F. Abdel Hamied, *Journal of Applied Polymer Science*, **2002**, *86*, 1219

10. R. Jayasekara, I. Harding, I. Bowater, G. B. Y Christie, G. T. Lonergan, *Polymer Testing*, **2004**, *23*, 17

11. M. Potara, A. Gabudean, S. Astilean, *Journal of Materials Chemistry*, **2011**, *21*, 3625

12. Y. Badr, M. A. Mahmoud, *Journal of Materials Science*, **2006**, *41*, 3947

13. A. M. Whelan, M. E. Brenann, W. J. Blau, J. M. Kelly, *Journal of Nanoscience and Nanotechnology*, **2004**, *4*, 66

14. W. H. Eisa, Y. K. Abdel-Moneam, Y. Shaaban, A. A. Abdel-Fattah, A. M. Abou Zeid, *Materials Chemistry and Physics*, **2011**, *128*, 109

2-CONNECTIVITY INDEX AND ITS COMPUTATION
FOR TWO KINDS OF NANOSTARS

ALI MADANSHEKAF[a, *], MARJAN MORADI[a]

ABSTRACT. Dendrimers are highly branched organic macromo-lecules with successive layers or generations of branch units surrounding a central core [1]. These are key molecules in nanotechnology and can be used, e.g., in medicine as drug carrier molecules or contrast agents. In this article, we compute the 2-connectivity indices of three infinite classes of dendrimers.

Keywords: Connectivity index, Randić index, Second-order Connectivity, dendrimer nanostars.

INTRODUCTION

Molecular connectivity indices are associated to the molecular accessibility. The first and second-order connectivity indices model molecular accessibility areas and volumes, respectively, whereas the higher order indices represent magnitudes in higher dimensional spaces [2].

Let G be a simple graph and consider the m-connectivity index

$$^m\chi(G) = \sum_{i_1..to..i_{m+1}} \frac{1}{\sqrt{d_{i_1} d_{i_2} \ldots d_{i_{m+1}}}}$$

where $i_1, i_2, \ldots, i_{m+1}$ runs over all paths of length m in G and d_i denotes the degree of the vertex i. In particular, 2-connectivity index is defined as follows:

$$^2\chi(G) = \sum_{i_1..to..i_3} \frac{1}{\sqrt{d_{i_1} d_{i_2} d_{i_3}}}$$

Milan Randić introduced the branching index (now called Randić index) as,

$$^1\chi(G) = \chi(G) = \sum_{i,j} \frac{1}{\sqrt{d_i d_j}}$$

* amadanshekaf@semnan.ac.ir
a Department of Mathematics, Faculty of Mathematics, Statistics and Computer Science, Semnan University, Semnan, Islamic Republic of Iran

where i,j range over all pairs of adjacent vertices of *G*. This index has been successfully correlated with physico-chemical properties of organic molecules. Indeed, if *G* is the molecular graph of a saturated hydrocarbon then there is a strong correlation between $\chi(G)$ and the boiling point of the substance [3, 4, 5].

Dendrimer is a synthetic 3-dimentional macromolecule that is prepared in a step-wise fashion from simple branched monomer units. Dendrimers have gained a wide range of applications in supra-molecular chemistry, particularly in host-guest reactions and self-assembly processes. Their applications in chemistry, biology and nano-science are unlimited. We encourage the reader to consult papers by A. R. Ashrafi et al., M. B. Ahmadi et al., M. Ghorbani et al. and M. V. Diudea et al. [6-14]. In this article we compute the 2-connectivity index for two types of dendrimer nanostars.

RESULTS AND DISCUSSION

Consider a graph *G* on *n* vertices, where *n≥2*. The maximum possible vertex degree in such graph is *n-1*. Define d_{ijk} as the number of 2-edges paths with 3 vertices of degree *i, j* and *k* respectively. It is clear that $d_{ijk} = d_{jik} = d_{kij} = d_{jki} = d_{ikj}$, then

$$^2\chi(G) = \sum_{1 \le i \le j \le k \le n-1} \frac{d_{ijk}}{\sqrt{ijk}} \qquad (1)$$

We now consider two infinite classes $NS_1[n]$ and $NS_2[n]$ of dendrimer nanostars, of type Polyamidoamine (PAMAM) and Polypropylen-iminoctamine, respectively, Figures 1 and 2.
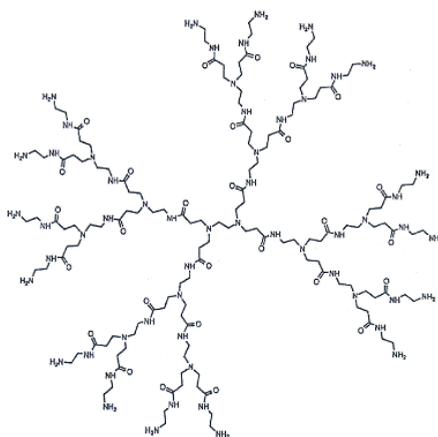
Figure 1. PAMAM Dendrimer
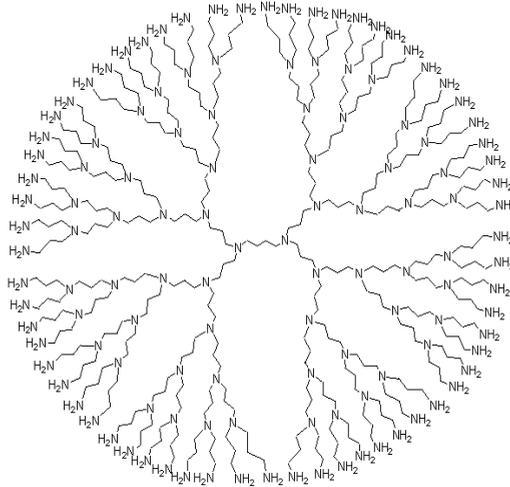
Figure 2. Polypropyleniminoctamine Dendrimer

The aim of this section is to compute the 2-connectivity index of these dendrimer nanostars.

For computing this index of the molecular graph of $G(n) = NS_1[n]$, where n represents the steps of growth in this type of dendrimer nanostar (Figure 1), define y_{123} to be the number of 2-edges paths with 3 vertices of degree 1, 2 and 3, y_{223} to be the number of 2-edges paths with two vertices of degree 2 and a vertex of degree 3, y_{222} to be the number of 2-edges paths with three vertices of degree 2, and y_{122} to be the number of 2-edges paths with a vertex of degree 1 and two vertices of degree 2. Since $NS_1[n]$ has four similar branches and three extra edges for *n=1 we have,*

$$y_{ijk} = \begin{cases} 4, & ijk = 122 \\ 8, & ijk = 123 \\ 8, & ijk = 222 \\ 24, & ijk = 223 \end{cases}$$

for n=2, we have

$$y_{ijk} = \begin{cases} 8, & ijk = 122 \\ 24, & ijk = 123 \\ 12, & ijk = 222 \\ 64, & ijk = 223 \end{cases}$$

187

and for n=3, we get

$$y_{ijk} = \begin{cases} 16, & ijk=122 \\ 56, & ijk=123 \\ 28, & ijk=222 \\ 144, & ijk=223 \end{cases}$$

In Figures 3 and 4 below, one branch of PAMAM dendrimer and the generation for n=1 is shown:

Figure 3. One branch of PAMAM dendrimer

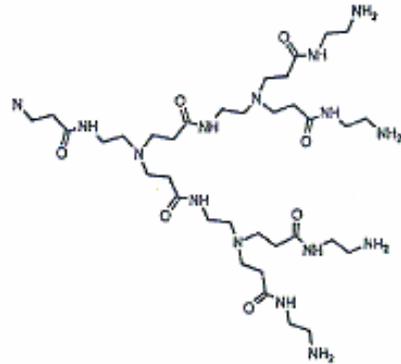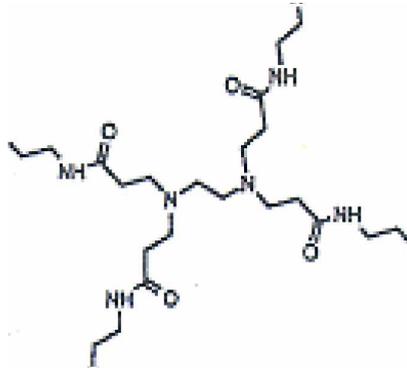**Figure 4.** PAMAM dendrimer $NS_1[n]$ at generation n=1

By induction argument and a simple calculation, one can prove that $y_{123} = 2 \cdot 2^n$, $y_{123} = 8 \cdot 2^n - 8$, $y_{222} = 4 \cdot 2^n - 4$ and $y_{223} = 20 \cdot 2^n - 16$. Now we have the following result:

Theorem 1. The 2-connectivity index of $G(n) = NS_1[n]$ is computed by formula:

$$^2\chi(G) = (\frac{4}{3}\sqrt{6} + \frac{10}{3}\sqrt{3} + \sqrt{2} + 1)2^n - (\frac{4}{3}\sqrt{3} + \frac{10}{3}\sqrt{6} + \sqrt{2})$$

Proof. According to (1) and the above calculations we have

$$^2\chi(G) = \sum_{1 \leq i \leq j \leq k \leq n-1} \frac{1}{\sqrt{ijk}}$$

$$= \frac{2.2^n}{\sqrt{1.2.2}} + \frac{4.2^n - 4}{\sqrt{2.2.2}} + \frac{8.2^n - 8}{\sqrt{1.2.3}} + \frac{20.2^n - 16}{\sqrt{2.2.3}}$$

$$= (\frac{4}{3}\sqrt{6} + \frac{10}{3}\sqrt{3} + \sqrt{2} + 1)2^n - (\frac{4}{3}\sqrt{3} + \frac{10}{3}\sqrt{6} + \sqrt{2})$$

And we get the result.

For computing 2-connectivity index of the second class of dendrimer nanostars, we consider $H(n) = NS_2[n]$ with four similar branches and five extra edges, *n* represents the steps of growth of this dendrimer nanostar (Figure 2).

In Figures 5 and 6 below, one branch is shown and the dendrimer at generation n=1:
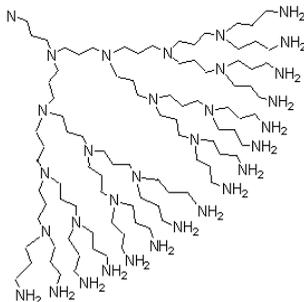
Figure 5. One branch of polypropyleniminoctamin dendrimer
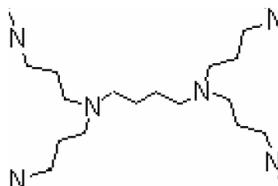
Figure 6. Polypropyleniminoctamin dendrimer $NS_2[n]$ at generation n=1

Again, define z_{223} to be the number of 2-edges paths with two vertices of degree 2 and a vertex of degree 3, z_{222} to be the number of 2-edges paths with three vertices of degree 2, and z_{122} to be the number of 2-edges paths with a vertex of degree 1 and two vertices of degree 2. For n=1 we have:

$$z_{ijk} = \begin{cases} 4, & ijk = 122 \\ 6, & ijk = 222 \\ 12, & ijk = 223 \end{cases}$$

for n=2 we have:

$$z_{ijk} = \begin{cases} 8, & ijk = 122 \\ 14, & ijk = 222 \\ 36, & ijk = 223 \end{cases}$$

and finally for n=3 we get:

$$z_{ijk} = \begin{cases} 16, & ijk = 122 \\ 30, & ijk = 222 \\ 84, & ijk = 223 \end{cases}$$

Using a similar argument as in theorem 1, one can see that $z_{122} = 2.2^n$, $z_{222} = 4.2^n - 2$, and $z_{223} = 12.2^n - 12$.

Now we can state the final result.

Theorem 2. The 2-connectivity index of $H(n) = NS_2[n]$ is computed as follows:

$$^2\chi(H[n]) = (2\sqrt{3} + \sqrt{2} + 1)2^n - (\frac{\sqrt{2}}{2} + 2\sqrt{3})$$

Proof. Using formula (1) above and some simple calculations we see that

$$^2\chi(H[n]) = \sum_{1 \le i \le j \le k \le n-1} \frac{z_{ijk}}{\sqrt{ijk}}$$

$$= \frac{2.2^n}{\sqrt{1.2.2}} + \frac{4.2^n - 2}{\sqrt{2.2.2}} + \frac{12.2^n - 12}{\sqrt{2.2.3}}$$

$$= (2\sqrt{3} + \sqrt{2} + 1)2^n - (\frac{\sqrt{2}}{2} + 2\sqrt{3})$$

and the result is obtained.

In Table 1, the 2-connectivity indices of $NS_1[n]$ and $NS_2[n]$ arecomputed for n=1,…, 10.

Table1. *Computing 2-connectivity index for dendrimers $NS_1[n]$ and $NS_2[n]$*

n	2-connectuvity index of $NS_1[n]$	2-connectuvity index of $NS_2[n]$
1	12.5618	7.5854
2	35.5592	19.3421
3	81.3740	42.8553
4	173.0037	89.8818
5	356.2629	183.9349
6	722.7814	372.0410
7	1455.8000	748.2531
8	2921.9000	1500.7000
9	5854.0000	3005.5000
10	11718.0000	6015.2000

ACKNOWLEDGMENTS

REFERENCES

1. K. Yamamoto, M. Higuchi, S. Shiki, M. Tsuruta and H. Chiba, *Nature,* **2002,** *415*, 509.
2. M. B. Aahmadi, M. Sadeghmehr, *Digest Journal of Nanomaterials and Biostructures,* **2009**, *4*, 639.
3. M. Randić , *Journal of The American Chemical Society,* **1975**, *97*, 6609.
4. A. R. Ashrafi, P. Nikzad, *Digest Journal of Nanomaterials and Biostructures,* **2009,** *4,* 269.
5. B. Bollobas, P. Erdos, *Ars Combinatorica*, **1998,** *50*, 225.
6. X. Li, I. Gutman, Mathematical Chemistry Monographs, **2006,** 1, 330.
7. A. R. Ashrafi, S. Yousefi, *MATCH - Communications in Mathematical and in Computer Chemistry,* **2007**, *57*, 403 .
8. A. R. Ashrafi, S. Yousefi, *Nanoscale Res. Lett.*, **2007,** *2*, 202.

9. M. V. Diudea, A. Graovac, *MATCH - Communications in Mathematical and in Computer Chemistry*, **2001,** *44*, 93.

10. M. V. Diudea, John P. E., *MATCH - Communications in Mathematical and in Computer Chemistry*, **2001**, *44*, 103.

11. M. V. Diudea, *Bulletin of the Chemical Society of Japan*, **2002**, *75*, 487.

12. M. V. Diudea, *MATCH - Communications in Mathematical and in Computer Chemistry*, **2002**, *45*, 109.

13. A. Madanshekaf, M. Ghaneei, *Optoelectronics and Advanced Materials – Rapid Communications*, **2010,** *4,* 1849.

14. A. Madanshekaf, M. Ghaneei, *Digest Journal of Nanomaterials and Biostructures* , **2011,** *6,* 477.

SYNTHESIS AND CHARACTERIZATION OF STRONTIUM CONTAINING PHOSPHOSILICATE BIOGLASSES

ROZALIA VERES[a, b], CONSTANTIN CIUCE[b], VIORICA SIMON[a]

ABSTRACT. The structural properties of strontium containing silicophosphate glasses synthesized by sol-gel process were studied and compared with those of the strontium-free material. The samples were characterized by differential thermal analysis (DTA), X-ray diffraction (XRD), Fourier transform infrared spectroscopy, and BET surface area analysis. Based on the DTA results, the 100 ºC dried gels were subjected to heat treatments at 300 ºC and 650 ºC. X-ray diffractograms show a predominant amorphous character for all samples, even after the thermal treatments. The FT-IR analysis indicates weak changes in the local structure of Sr-free samples induced by progressive addition of SrO addition, as well as by increasing treatment temperature. The BET data reveal that the glasses are mesoporous.

Keywords: silicophosphate bioglasses; sol-gel; strontium; mesoporosity.

INTRODUCTION

Bioceramics and bioglasses are extensively used in the treatment of bone defects and osteoporotic problems [1]. An important requirement for bioglasses to be used as bone implant is to have osteoinductive properties. If a bone is damaged, the osteoclasts remove the damaged fragments and the osteoblasts reconstruct the bone. However, the natural reconstruction is slow and usually bone ceramics and glasses are used in order to assist bone reparation. The properties of bioglasses for stimulation and acceleration of new bone formation can be improved by incorporating bone stimulating ions into their chemical composition [2]. Besides zinc and magnesium, strontium is another element that has a positive effect on osteoblastic cell proliferation, differentiation and bone mineralization [3-5].

It is demonstrated that strontium reduces bone resorption and stimulates the bone formation. In vitro and in vivo studies have indicated `that strontium increases bone formation and reduces osteoporosis, leading to a gain in bone mass and improved bone mechanical properties in animals and humans [6–7].

[a] *Babeş-Bolyai University, Faculty of Physics & Institute of Interdisciplinary Research in Bio-Nano-Sciences,RO-400084 Cluj-Napoca, Romania, rozsiveres@yahoo.com*
[b] *Iuliu Hatieganu University of Medicine and Pharmacy, Faculty of Medicine,RO-400012 Cluj-Napoca, Romania*

The aim of the present study was to produce sol-gel derived silicophophate glasses with different SrO contents and to compare their physico-chemical properties to those of strontium-free glass using proper analytical techniques.

RESULTS AND DISCUSSION

Samples of $(95-x)SiO_2 \cdot xSrO \cdot 5P_2O_5$ glass system, $0 \leq x \leq 10$ mol%, with four different SrO/SiO_2 molar ratios (Table 1) treated at 100, 300 and 650 ^{o}C were investigated.

Table 1. Compositions and codes of samples**.**

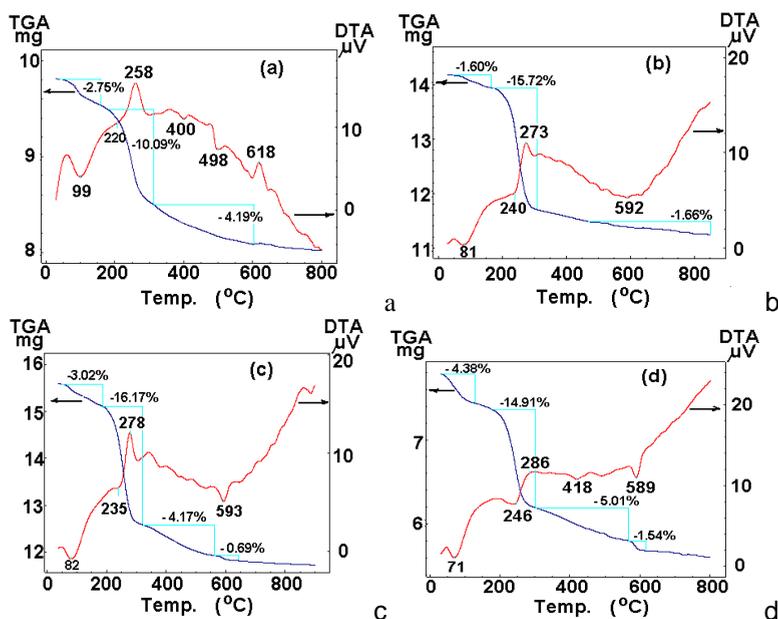| Sample code	SiO$_2$ (mol %)	SrO (mol %)	P$_2$O$_5$(mol %)
M	95	-	5
S1Sr	92	3	5
S2Sr	88	7	5
S3Sr	85	10	5

Figure 1. DTA and TGA runs of sol-gel derived samples: (a) M; (b) S1Sr; (c) S2Sr; (d) S3Sr.

The TGA curves for all the samples present several regions of weight loss (Figure 1). The first weight loss that occurs around 90 ^{o}C coincides with an endothermic peak in DTA signal and it can be associated with the removal of free water molecules. A second weight loss with two

corresponding peaks in the DTA curve can be observed until 300 ºC. This loss can be associated with the elimination of water caged in the pores and the decomposition of residual ammonium nitrate. Further weight losses are observed until 650ºC and correspond to the elimination of hydroxyl groups. Based on this result, a thermal treatment at 650 ºC was also considered.

The XRD patterns of the 100ºC dried samples (Figure 2) indicate a prevalent amorphous state in all samples. It can be observed that with the increase of the strontium amount, besides the large diffraction peak that dominates the XRD patterns, there are peaks indicating the presence of minor crystalline phases, that could be assigned to some strontium nitrate crystals (JCPDS 25-0746) from the precursor used as SrO source, or formed during the samples synthesis. After thermal treatment at 300 ºC the peaks corresponding to strontium nitrate crystals are still present. The XRD patterns of 650 ºC heat treated samples indicate an amorphous phase for all the samples, excepting S3Sr which evidences the tendency to develop a nanocrystalline phase.
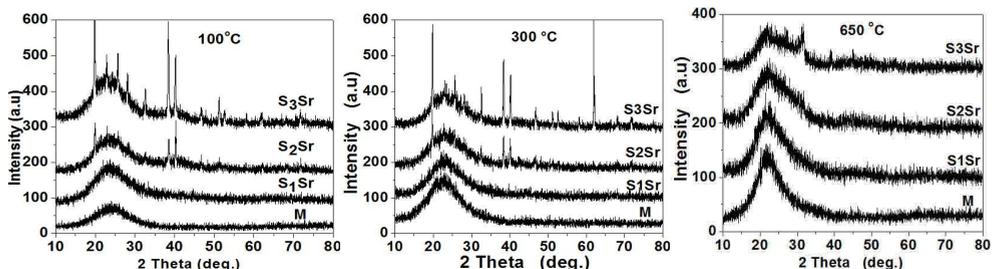
Figure 2. XRD patterns after treatments at different temperatures.

The FT-IR spectra (Figure 3) consist of broad absorption bands recorded in the spectral range 3750-2600 cm^{-1} which are assigned to vibrations of Si-OH bonds, molecular water and organic residues [8-12]. The peak at 3540 cm^{-1} is associated to silanol groups linked to molecular water through hydrogen bonds. The large absorption band at 3400 cm^{-1} is assigned to molecular water. The bands at 3300-2600 cm^{-1} correspond to the symmetric and asymmetric fundamental stretching vibration of CH_2 and CH_3 groups belonging to residues from the TEOS precursor used in the sol-gel process. After thermal treatment the broad band from 3750-2600 cm^{-1} decreased in intensity by eliminating of water and hydroxyl groups. The peak at 1620 cm^{-1} also corresponds to vibration of molecular water. The absorption band recorded around 1360 cm^{-1} is assigned to symmetric stretching vibration modes of C-H bonds, but also to the stretching vibration of NO_3^- ions [13]. A decrease in the intensity of this band is observed with increase of SrO content and after thermal treatments too. The bands at 1265-830 cm^{-1} are due to the Si-O-Si and P-O stretching mode [14, 15]. A

195

decrease in intensity is noticed with increasing of SrO content on the account of SiO_2 content. By addition of SrO, a shift of the absorption band assigned to Si–O–Si vibrations to lower wavenumbers was also observed, that suggests the shortening of Si–O–Si bonds in the vicinity of large Sr cations [16]. This peak may also indicate the presence of Si–O–Sr bond in silicate compounds [17]. The bands at 780 and 445 cm^{-1} are assigned to Si-O-Si bonds [18], and that at 610 cm^{-1} to Si-Si stretching vibrations [19].
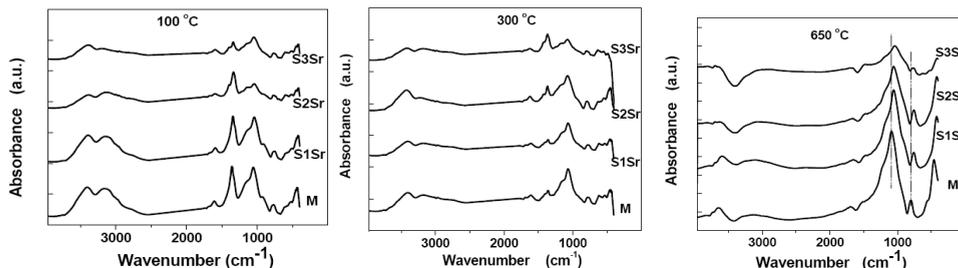
Figure 3. FT-IR spectra of the samples treated at different temperatures.

Figure 4 illustrates the mesopores distribution as a function of the amount of strontium. The strontium containing samples versus the strontium-free sample exhibit a more uniform and narrow size distribution of the mesopores with a pore diameter between 2 and 7 nm.
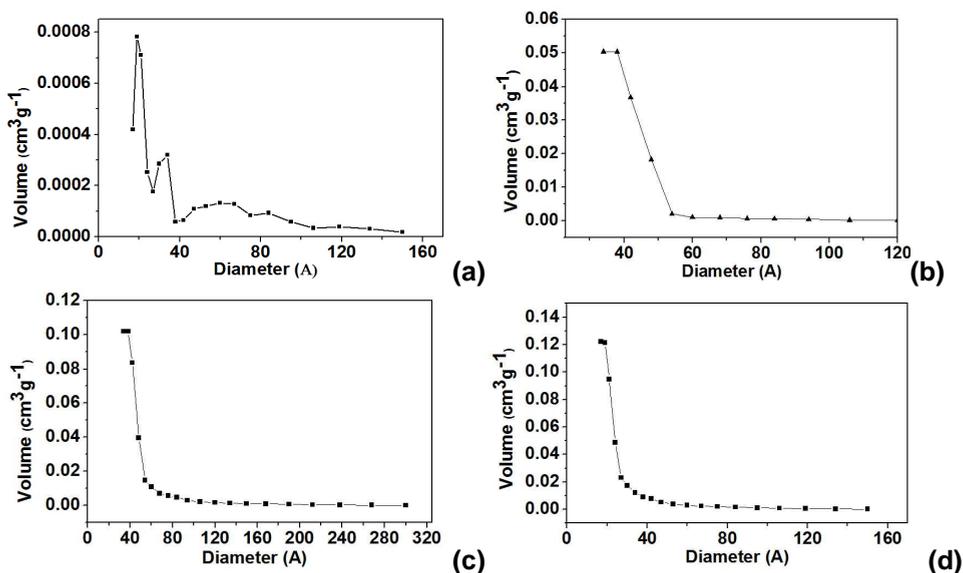
Figure 4. Textural pore size distribution of the prepared sample, obtained from BJH analysis of nitrogen desorption branch: (a) M, (b) S1Sr, (c) S2Sr and (d) S3Sr.

On the other hand, it was observed that the specific surface area of the investigated samples (Table 2) pronouncedly increases as only 3 mol % SrO is added into the phosphosilicate glass matrix, but with further increase of strontium concentration the specific surface area slightly diminishes.

Table 2. Specific surface area of the samples

Sample	M	S1Sr	S2Sr	S3Sr
Specific surface area (m^2/g)	27	191	187	172

In the calcosilicate sol-gel derived bioactive glasses no significant effect of strontium addition on specific surface area is observed [20], while in phosphosilicate glasses strontium induces pronounced textural changes.

CONCLUSIONS

Both sol-gel derived glasses based on SiO_2-P_2O_5-SrO system and strontium-free phophosilicate glass matrix have a prevalent amorphous character and remain amorphous after thermal treatments up to 650 ^{o}C. The FT-IR analysis shows weak changes in the local structure of strontium-free samples induced by SrO addition, as well as in function of SrO content. The BET data indicate that the glasses are mesoporous. The specific surface area pronouncedly increases from 27 m^2/g, for the phophosilicate glass matrix, to 191 m^2/g, by addition of only 3 mol % SrO, but it slightly decreases for higher SrO contents. The samples can be considered for further investigation with respect to their bioactivity required for biomaterials used as scaffolds in bone tissue regeneration.

EXPERIMENTAL SECTION

The (95-x)SiO_2·xSrO·5P_2O_5 glass samples, 0 ≤ x ≤ 10 mol%, were prepared following the sol-gel route. The indicated compositions (Table 1) are related to the amounts of the SiO_2, SrO and P_2O_5 precursors used in the synthesis of these samples. The precursors were TEOS ($Si(OC_2H_5)_4$), strontium nitrate ($Sr(NO_3)_2$) and dibasic ammonium phosphate ((NH_4)$_2HPO_4$). Nitric acid (HNO_3) was used as catalyst in TEOS solution. The precursors were separately stirred with distilled water, for 30 min. Then both strontium and phosphorous containing solutions were added to TEOS solution under continuous stirring. The obtained solution was left overnight for gelation at room temperature. After 7 days of aging at room temperature, the samples were heat treated for 24 h at 100º C.

Differential thermal analysis (DTA) and thermogravimetric analysis (TGA) were performed on a Shimadzu type derivatograph DTG-60H, with a heating

rate of 5ºC/min using alumina open crucibles, in order to investigate the thermal behavior of the dried samples, and to assess the heat treatment temperatures.

The structure of the samples was characterized by X-ray diffraction (XRD) analysis using X-ray Shimadzu XRD-6000 diffractometer with Ni-filter, and CuKα radiation (λ = 1.5418Å). The operation voltage and current were 40 kV and 30 mA, respectively. The measurements were performed at a scan speed of 2º/min in 2θ scan range from 10º to 80º.

After 100 ºC drying, the samples were ground in an agate ball mixer mill Retsch MM300, and then they were thermally treated at 300 ºC and 650ºC.

FT-IR spectra were recorded in the range of 4000-400 cm-1 in transmission mode on a FT/IR-6200 Spectrometer by Jasco using the KBr pellet technique. Samples were prepared by mixing 1 mg of powder with 250 mg of KBr and pressing into pellets.

The specific surface area, pore volume, and pore radius of the samples were obtained from N_2-adsorption measurements, using a Sorptomatic 1990 apparatus. The BET method was used for calculation of surface area, and the BJH method was used for determination of porosity parameters.

ACKNOWLEDGMENTS

REFERENCES

1. C.R. Anderegg, D.C. Alexander, M. Freidman, *Journal of Periodontology*, **1999**, *70*, 384.
2. E. Bonnelye, A. Chabadel, F. Saltel, P. Jurdic, *Bone*, **2008**, *42*, 129.
3. A. Oki, B. Parveen, S. Hossain, S. Adeniji, H. Donahue, *Journal of Biomedical Materials Research Part A,* **2004**, *69*, 216.
4. A. Saboori, M. Sheikhi, F. Moztarzadeh, M. Rabiee,S. Hesaraki,M. Tahriri et all, *Advances in Apllied Ceramics*, **2009**, *108*, 155.
5. Y.W. Chen, G.Q. Shi, Y.L. Ding, X.X. Yu, X.H. Zhang , C.S. Zhao et all, *Journal of Materials Science: Materials in Medicine*, **2008**, *19*, 2655.
6. E. Canalis, M. Hott, P. Deloffre, Y. Tsouderos, P.J. Marie, *Bone*, **1996**, *18*, 517.
7. J. Buehler, P. Chappuis, J.L. Saffar, Y. Tsouderos, A. Vignery, *Bone*, **2001**, *29*, 176.
8. G. Orcel, J. Phalippou, L.L. Hench, *Journal of Non-Crystallin Solids*, **1986**, *88*, 114.
9. R.F. Bartholomeu, B.L. Butler, H.L. Hoover, C.K. Wu, *Journal of the American Ceramic Society*, **1980**, *63*, 481.

10. R.M. Almeida, G.C. Pantano, *Journal of Applied Physics*, **1990**, *68*, 4225.
11. R.S. McDonald, *Journal of the American Ceramic Society*, 1958, *62*, 1168.
12. D.L. Wood, E.M. Rabinovich, D.W. Johnson, J.B. Mac-Chesney, E.M. Vogel, *Journal of the American Ceramic Society*, **1983**, *66*, 693.
13. J.H. Choy, S.Y. Kwak, J.S. Park, Y.j. Jeong, J. Portier, *Journal of the American Chemical Society,* **1999,** 121, 1399.
14. M. Sitarz, M. Handke, W. Mozgawa, *Spectrochimica Acta Part A*, **2000**, *56*, 1819.
15. V. Aina, G. Malavasi, A. Fiorio Pla, L. Munaron, C. Morterra, *Acta Biomaterialia*, **2009**, *5*, 1211.
16. C. Chen, D. Huang, W. Zhu, X. Yao, *Applied Surfaces Science*, **2006**, *252*, 7585.
17. E.A. Abou Neel, W. Chrzanowski , D.M. Pickup, L.A. O'Dell, N.J. Mordan, R.J. Newport et all, *Journal of the Royal Society Interface*, **2009**, *6*, 435.
18. T. Kokubo, H. Kushitani, S. Sakka, T. Kitsugi, T. Yamamuro, *Journal of Biomedical Materials Research*, **1990**, *24*, 721.
19. P. Gupta, V.L. Colvin, S.M. George, *Physical Review B,***1988**, *37*, 823.
20. J. Isaac, J. Nohra, J. Lao, E.Jallot, J.M. Nedelec, A. Berdal, J.M. Sautier,*European Cells and Materials*, **2011**, 21, 130.

EVALUATION OF FREE RADICAL CONCENTRATION IN SOME NEW DENTAL COMPOSITE MATERIALS BY ESR SPECTROSCOPY

DOINA PRODAN[a], LAURA SILAGHI-DUMITRESCU[a], PREJMEAN CRISTINA[a], RADU SILAGHI-DUMITRESCU[b], LAURA BOLOJAN[c], G. DAMIAN[c, *]

ABSTRACT. During polymerization of dimethacrylate monomers employed in dental materials, the gel effect leads to entrapment of radicals and unreacted monomers in the crosslinked network, affecting physico-mechanical properties and the biocompatibility. Reported here is a study of the effect of the resin composition, irradiation time and storage time of some new light-cured dental composites upon the free propagating radical concentration, using Electron Spin Resonance (ESR). Six new experimental dental light-cured composites based on the Bis-GMA monomer - 2,2-bis[4-(2-hydroxy-3-methacryloyloxy-propoxy)phenyl]-propane, on the corresponding Bis-GMA dimer, 2-hydroxyethyl methacrylate (HEMA) and on 1,6-Bis-[2-methacryloyloxyethoxycarbonyl-amino]-2,4,4-trmethylhexane (UDMA) have been employed, with three different photoinitiator systems. The hybrid filler consisted of quartz, strontium/zirconium glass and fluoro-hydroxyapatite. ESR signals developed under visible light irradiation during polymerization were measured, with intensities dependent on the time of irradiation. These signals decay very slowly in time – on the scale of days or longer.

Keywords: Resin composites; ESR ; Free radicals

INTRODUCTION

Light-cured resin composite materials are frequently used for direct restoration of anterior and posterior teeth [1,2,3], as sealants for the prophylaxis of caries with children [4], and in prosthetic dentistry for the preparation of composite veneers, inlays and onlays [5,6]. A crosslinked three-dimensional network is formed by the polymerization of the monomer mixtures existing in dental resin composites. During the polymerization of dimethacrylate monomers, the gel effect occurs, leading to the closing of radicals and unreacted

[a] *"Raluca Ripan" Chemistry Research Institute, Str. Fantanele 30, RO-400294 Cluj-Napoca, "Babes-Bolyai" University, Romania*

[b] *Faculty of Chemistry and Chemical Engineering, Str. Arany Janos no.11, RO-400028 Cluj-Napoca, Babes-Bolyai University, Romania, rsilaghi@chem.ubbcluj.ro*

[c] *Faculty of Physics, Str. M.Kogalniceanu no.1, RO-400084, "Babes-Bolyai" University, Cluj-Napoca, Romania, grigore.damian@phys.ubbcluj.ro*

monomers in the crosslinked network [7]. The incomplete conversion of methacrylate groups affects the physico-mechanical properties and the biocompatibility of the dental composite materials [8]. The aim of the present work was to study the kinetics of free radicals formed as a result of the effect of the resin composition, irradiation time and storage time of some new light-cured dental composites, by Electron Spin Resonance (ESR) spectroscopy
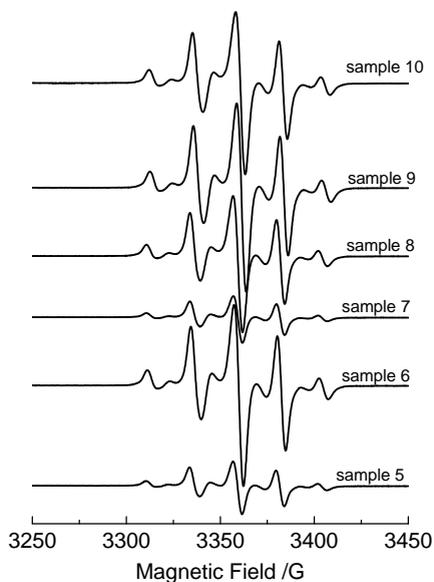
Figure 1. ESR spectra of free radicals after irradiation of the studied resin composite materials.

RESULTS AND DISCUSSION

Figure 1 shows ESR spectra measured immediately after polymerization by irradiation of the composite materials with visible light, cf. Materials and Methods. The nine line of ESR spectra are typicals, indicating the presence of polymer radicals of methacryl derivatives.

To characterize the kinetics of formation of radicals as function of the irradiation times, were determined relative concentrations of radicals for different periods of irradiation. The signal intensity, or the double integrated ESR spectrum, is proportional to the number of spins [9], and therefore can be used to estimate the relative concentration of the paramagnetic species.

Figure 2 shows the kinetic of radical formation, depending on the irradiation time. One may note that the intensity of the ESR signals is dependent on the time of irradiation and that this dependence shows saturation behavior at ~ 3 minutes.
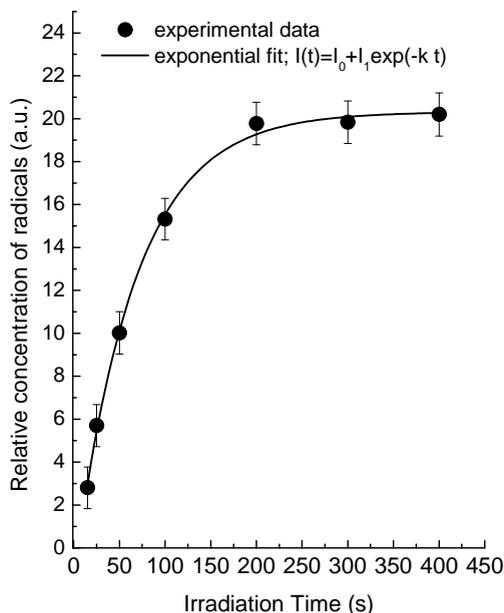
Figure 2. Dependence of relative signal intensity on the irradiation time.

In the case of samples 5 and 7 that contain the same CQ / DMAEM initiation system and different monomer mixtures, the initial relative free radicals concentrations were the lowest and presented closed values (6.5 for sample 7 and 6.2 for sample 5). For the other experimental samples (samples 5, 6, 7 and 8), the relative concentrations of free radicals were much higher, being situated in the range of 17 to 24 units of relative concentrations (17 arb. units for sample 8; 20 arb. units for sample 10; 22.5 arb. units for sample 6 and 24 arb. units for sample 9). Samples 6 and 8 contain the same initiation system -CQ / DMAEM / E-4-DMAB-, E-4-DMAB co-initiator being in addition to the samples 5 and 7. Samples 9 and 10 contain only CQ and E-4-DMAB as the initiator and co-initiator, respectively. Sample 8 and 10 contain UDMA in addition to monomer mixtures contained in sample 6 and 9.

The life-times of the radicals (time to reach half of the initial concentration) are consistent with different radical environments in the samples employed in the present study [8]. It is expected that the free radicals are closed in a highly cross-linked network having a long life-time. [2]. From the results obtained in the present study, it seems that CQ / DMAEM initiation system leads to the obtaining of the densest cross-linked network (the life-time of radicals are about 16 days). For the other samples, the life-time of radicals was in the range of 14 days (for sample 7) and 21 days (for sample 5).

From Figure 3 one can observe the general trend of decreasing the relative free radicals concentration in time, with different rates during samples aging, the concentration remaining constant after 60 days. The decay is bi-exponential.

CONCLUSIONS

Photopolymerization of dental resins at room temperature leads to the formation of long-life free radicals due to system vitrification. The kinetics of these free radicals was monitored by Electron Spin Resonance (ESR) spectroscopy. The ESR spectroscopy can provide new information which may lead to a better understanding of the phenomena existing in dental resins, like kinetics of generation and propagation of free radicals in the polymerization process and their stability.
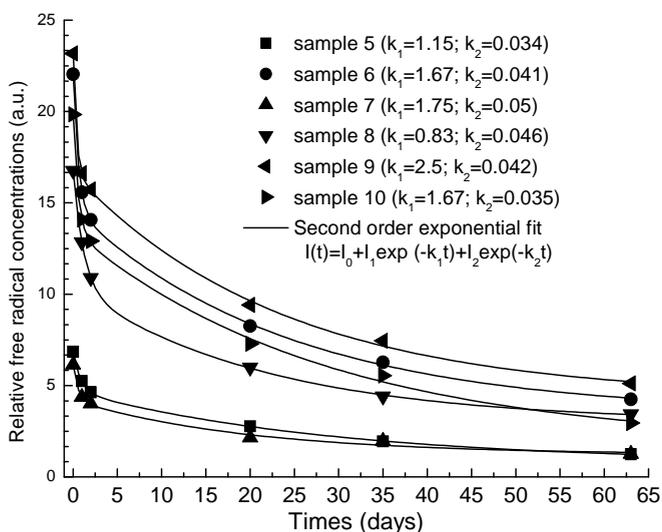
Figure 3. Dependence of relative signal intensity on the irradiation time.

Within the limits of the present experiments, the radical concentration depends primarily on the initiation system and secondly on the composition of the monomers used in experimental composites.

EXPERIMENTAL SECTION

Six new experimental dental light-cured composites were formulated using *two different monomer mixtures* based on Bis-GMA$_{336}$, 2-hydroxyethyl methacrylate (HEMA) and 1,6-Bis-[2-methacryloyloxyethoxycarbonyl-amino]-2,4,4-trmethylhexane (UDMA). Bis-GMA$_{336}$ was synthesized in our laboratory from the commercial epoxy resin D.E.R. 336 and contains the monomer 2,2-bis[4-(2-hydroxy-3-methacryloyloxy-propoxy)phenyl]-propane and the corresponding Bis-GMA dimmer [10]. *Three different photoinitiator systems* for free radical polymerization were used in the study based on the

204

photosensitizer -camphorquinone (CQ)- in an amount of 0.5wt%, and two co-initiator reducing agents, dimethylaminoethyl methacrylate (DMAEM) in an amount of wt1% and ethyl 4-dimethylaminobenzoate (E-4-DMAB) in an amount of 1wt% related to the monomer mixtures. Butylated hydroxy toluene (BHT) was added as an antioxidant in a quantity of 650 ppm. The formulas of the dimethacrylic oligomers used in the experiments are presented in Figure 4:

BIS-GMA$_{336}$ (n=0,1)

UDMA

HEMA
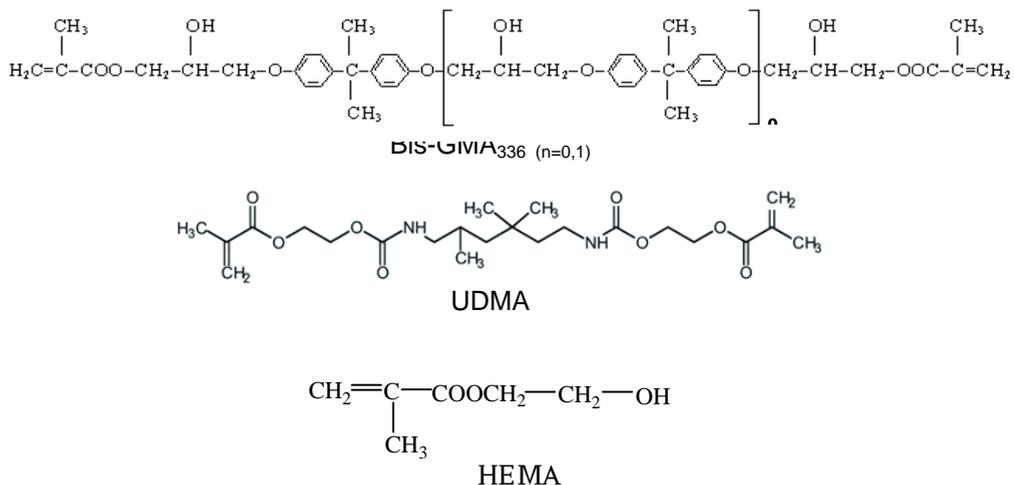
Figure 4. The chemical structures of methacrylate monomers used in the experiments

The hybrid filler (HF) was the same in all composite samples and consisted of quarts (40 wt %), strontium/zirconium glass (40 wt%), and fluoro-hydroxyapatite (20 wt%). The filler/monomer ratio was 4:1. The composition of the experimental dental light-cured composites are presented in Table 1.

The cured composite samples were obtained by exposing the paste composite samples to a visible radiation in the wavelength range of 400-500 nm. The radiation was generated by an Optilux dental lamp, produced by Demetron Research Corporation USA.

Table 1. Description of the samples examined in the present study

Monomer mixture + Hybrid filler / Initiation system	- Bis-GMA336 (12wt%) - HEMA (8wt%) + - Quartz (32wt%) - Sr/Zr glass (32wt%) - FHap (16wt%)	-Bis-GMA336 (7wt%) -UDMA (3wt%) -HEMA (10wt%) + - Quartz (32wt%) - Sr/Zr glass (32wt%) - FHap (16wt%)
-CQ - DMAEM	Sample 5	Sample 7

- CQ - - DMAEM - E-4-DMAB	Sample 6	Sample 8
- CQ - - E-4-DMAB	Sample 9	Sample 10

EPR spectra were recorded at room temperature with BRUKER-BIOSPIN EMX spectrometer operating at X-band (9-10 GHz). The EPR parameters were set at 100 KHz modulation frequency, microwave power 0.5 mW, modulation amplitude 3 G; time constant 2.56 ms; scan time 60 s; receiver gain 10^3. Each sample was weighed and the concentration of free radicals has been reported per 1mg of sample. The integral intensities of EPR spectra were obtained by evaluating their double integrals using the Origin 8 program.

ACKNOWLEDGMENTS

REFERENCES

1. C. J.A. von Fraunhofer, P. Curtis Jr., *Dental Materials,* **1989**, 5(6), 365-368

2. I. Sideridou, V.Tserki, G.Papanastasiou, *Biomaterials,* **2003**, 24(4), 655-665

3. F. C.Calheiros, R. R.Braga, Y.Kawano, R. Y.Ballester, *Dental Materials,* **2004,** 20(10), 939-946

4. E. Komurcuoglu, S. Olmez,N. Vural, *Journal of Oral Rehabilitation*, **2005,** 32(2), 116-121

5. J.W.V van Dijken, *Journal of Dentistry*, 2000, 28(5), 299-306

6. P. Magne, U.C. Belser, *International Journal of Periodontics and Restorative Dentistry* **2003** 23(6), 543-555

7. A. Peutzfeldt A., *European Journal of Oral Sciences,* **1997**, *105*, 97-116

8. S.G. Pereira, J.P. Telo, T.G. Nunes, *Journal of Materials Science: Materials in Medicine*, **2008,** *19,* 3135-44

9. G. Damian, *Talanta,* **2003**, *60*, 923-927

10. C. Prejmerean, M. Moldovan, L. Silaghi-Dumitrescu, D. Prodan, G. Furtos, M. Trif, V. Popescu, V. Pascalau, C.Petrea, R. Silaghi-Dumitrescu, *Materiale Plastice,* **2011,** *48(1),* 27-32

ECCENTRIC CONNECTIVITY INDEX OF TOROIDAL FULLERENES

A. R. ASHRAFI[a], MODJTABA GHORBANI[b]

ABSTRACT. The eccentricity $\varepsilon(u)$ is the largest distance between u and any other vertex x of G. The eccentric connectivity index $\xi(G)$ of G is defined as $\xi(G) = \sum_{u \in V(G)} deg(u)\varepsilon(u)$. In this paper a new method is presented by which it is possible to compute the eccentric connectivity index of molecular graphs. We apply our method to compute the eccentric connectivity index of toroidal fullerenes.

Keywords: Toroidal Fullerene, Eccentric Connectivity index, Topological indices.

INTRODUCTION

The discovery of C_{60} bucky-ball, which has a nanometer-scale hollow spherical structure in 1985 by Kroto and Smalley revealed a new form of existence of carbon element other than graphite, diamond and amorphous carbon [1,2]. Fullerenes are molecules in the form of cage-like polyhedra, consisting solely of carbon atoms. Suppose p, h, n and m are the number of pentagons, hexagons, carbon atoms and bonds between them, in a given fullerene F. Since each atom lies in exactly 3 faces and each edge lies in 2 faces, the number of atoms is n = (5p + 6h)/3, the number of edges is m = 3/2n = (5p + 6h)/2 and the number of faces is f = p + h. By the Euler's formula n – m + f = 2, one can deduce that (5p + 6h)/3 – (5p + 6h)/2 + p + h = 2, and therefore p = 12, v = 2h + 20 and e = 3h + 30. This implies that such molecules made up entirely of n carbon atoms and having 12 pentagonal and (n/2 – 10) hexagonal faces, where n ≠ 22 is a natural number equal or greater than 20 [3,4].

Let G = (V, E) be a connected bipartite graph with the vertex set V = V(G) and the edge set E = E(G), without loops and multiple edges. Suppose u and v are vertices of G. The distance d(u,v) is defined as the length of a shortest path connecting them. The eccentricity $\varepsilon(u)$ is the largest distance between u and any other vertex x of G. The maximum eccentricity over all vertices of G is called the diameter of G and denoted by

[a] *Institute of Nanoscience and Nanotechnology, University of Kashan, Kashan 87317-51167, I. R. Iran*
[b] *DepartmentofMathematics, Faculty of Science, Shahid Rajaee Teacher Training University, Tehran, 16785 – 136, I R. Iran; e- mail:ghorbani30@gmail.com*

D(G) and the minimum eccentricity among the vertices of G is called radius of G and denoted by R(G). The set of vertices whose eccentricity is equal to the radius of G is called the center of G. It is well known that each tree has either one or two vertices in its center. The eccentric connectivity index $\xi(G)$ of G is defined as $\xi(G) = \sum_{v \in V(G)} deg(v) \varepsilon(v)$ [5-9]. We encourage the reader to consult papers [10-13] for mathematical properties of this new proposed topological index.

RESULTS AND DISCUSSION

In this section, the eccentric connectivity index of a toroidal fullerene is computed [14,15]. To do this, we apply an algebraic approach. Let us recall some definitions and notations. An automorphism of a graph G is a permutation g of the vertex set V(G) with the property that, for any vertices u and v, g(u) and g(v) are adjacent if and only if u is adjacent to v. The set of all automorphisms of G, with the operation of the composition of permutations, is a permutation group on V(G), denoted by Aut(G). Suppose G is a group and X is a set. G is said to act on X when there is a map φ : G × X → X such that for all elements x∈ X (i) $\varphi(e,x) = x$, where e is the identity element of G, and,(ii) $\varphi(g,\varphi(h,x)) = \varphi(gh,x)$ for all g, h ∈ G. In this case, G is called a transformation group on X, X is called a G-set, and φ is called the group action. For simplicity we define $gx = \varphi(g,x)$. In a group action, a group permutes the elements of X .The identity does nothing, while a composition of actions corresponds to the action of the composition. For a given X ,the set {gx | g ∈ G}, where the group action moves x, is called the group orbit of x. If G has exactly one orbit, then G is said to be vertex transitive. It is easily seen that in a vertex transitive graph, degree of vertices are equal and it is denoted by r = r(G). In such a case G is called r-regular. The following simple lemma is crucial in this section. Here our notations are standard and mainly taken from [16-22].

Lemma 1 — Suppose G is a graph, A_1, A_2, …, A_t are the orbits of Aut(G) under its natural action on V(G) and $x_i \in A_i$, $1 \le i \le t$. Then $\xi(G) = \sum_{j=1}^{t} |A_j| deg(x_j) \varepsilon(x_j)$. In particular, if G is vertex transitive then $\xi(G) = r(G)|V(G)|\varepsilon(x)$, for every vertex x.

Proof — It is easy to see that if vertices u and v are in the same orbit, then there is an automorphism φ such that $\varphi(u) = v$. Choose a vertex x such that $\varepsilon(u) = d(u,x)$. Since φ is onto, for every vertex y there exists the vertex w such that $y = \varphi(w)$. Thus $d(v,y) = d(\varphi(u), \varphi(w)) = d(u,w)$ and so $\varepsilon(v) = \max\{d(v,y)\}_{y \in V(G)} = \max\{d(u,w)\}_{w \in V(G)} = \varepsilon(u)$. On the other hand, it is a well – known fact that the vertices of a given orbit have equal degrees.

208

Therefore, $\xi(G) = \sum_{j=1}^{t}\left|A_j\right|deg(x_j)\varepsilon(x_j)$ and if G is vertex transitive then $\xi(G) = r(G)|V(G)|\varepsilon(x)$, for every vertex x. This completes our proof.

▲

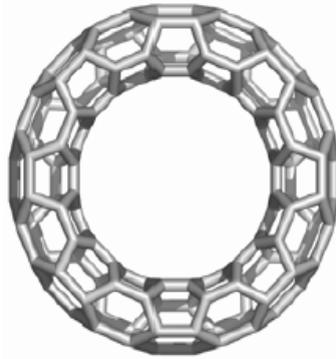**Figure 1.** The Zig-zag Polyhex Nanotube.

Apply our method on a toroidal fullerene R = R[p,q], in terms of its circumference (q) and its length (p), Figure 1. To compute the eccentric connectivity index of this fullerene, we first prove its molecular graph is vertex transitive.
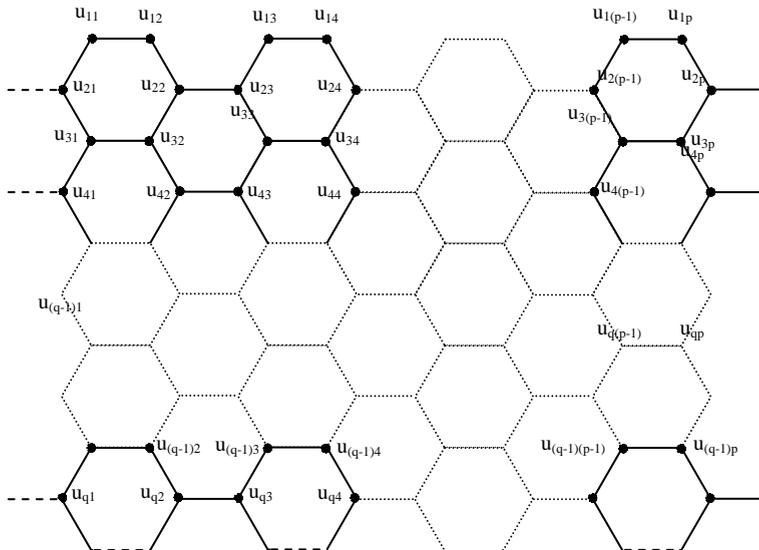

Figure 2. A 2-Dimensional Lattice for T[p,q].

Lemma 2 — The molecular graph of a polyhex nanotorus is vertex transitive.

Proof — To prove this lemma, we first notice that p and q must be even. Consider the vertices u_{ij} and u_{rs} of the molecular graph of a polyhex nanotori T = T[p,q], Figure 2. Suppose both of i and r are odd or even and σ is a horizontal symmetry plane which maps u_{it} to u_{rt}, $1 \leq t \leq p$ and π is a vertical symmetry which maps u_{tj} to u_{ts}, $1 \leq t \leq q$. Then σ and π are automorphisms of T and we have $\pi\sigma(u_{ij}) = \pi(u_{rj}) = u_{rs}$. Thus u_{ij} and u_{rs} are in the same orbit under the action of Aut(G) on V(G). On the other hand, the map θ defined by $\theta(u_{ij}) = \theta(u(p+1-i)j)$ is a graph automorphism of T and so if "i is odd and r is even" or "i is even and r is odd" then again u_{ij} and u_{rs} will be in the same orbit of Aut(G), proving the lemma. ▲

Theorem 3 — $\xi(T[p,q]) = 3pq^2$.

Proof — From Figure 2, it can easily seen that $|V(T[p,q])| = pq$. By Lemma 2, T[p,q] is vertex transitive and by Lemma 1, $\xi(T[p,q]) = 3pq\varepsilon(x)$, for a vertex x. Now the proof is follows from this fact that $\varepsilon(x) = q$, proving the result. ▲

REFERENCES

1. H. W. Kroto, J. R. Heath, S. C. O'Brien, R. F. Curl and R. E. Smalley, *Nature*, **1985***, 318*, 162.

2. H. W. Kroto, J. E. Fichier, D. E Cox, The Fulerene, Pergamon Press, *New York*, **1993**.

3. P. W. Fowler and D. E. Manolopoulos, An Atlas of Fullerenes, Oxford Univ. Press, *Oxford*, **1995**.

4. B. Kostant, Notices of the AMS, **1995**, *9,* 959.

5. V. Sharma, R. Goswami and A. K. Madan, *Journal of Chemical Information and Computational Science*, **1997**, *37*, 273.

6. H. Dureja and A. K. Madan, *Medicinal Chemistry Research*, **2007**, *16*, 331.

7. V. Kumar, S. Sardana and A. K. Madan, *Journal of Molecular Modeling*, **2004**, *10*, 399.

8. S. Sardana and A. K. Madan, *MATCH - Communications in Mathematical and in Computer Chemistry*, **2001**, *43*, 85.

9. S. Gupta, M. Singh and A. K. Madan, *J. Math. Anal. Appl.*, **2002**, *266*, 259.

10. B. Zhou and Z. Du, *MATCH - Communications in Mathematical and in Computer Chemistry*, **2010**, *63*, 181.

11. A. Ilic and I. Gutman, *MATCH - Communications in Mathematical and in Computer Chemistry*, to appear.

12. T. Doslic, M. Saheli and D. Vukicevic, submitted.

13. T. Doslic and M. Saheli, submitted.

14. M. Saheli and A. R. Ashrafi, *Journal of Chemistry and Chemical Engineering*, (in press).

15. M. Saheli and A. R. Ashrafi, *Journal of Computational and Theoretical Nanoscience*, (in press).

16. The Hyper Chem package, Release 7.5 for Windows, Hypercube Inc., *Florida, USA*, **2002**.

17. M. V. Diudea, O. Ursu and Cs. L. Nagy, TOPOCLUJ, *Babes-Bolyai University, Cluj*, **2002**.

18. The GAP Team, GAP, Groups, Algorithms and Programming, Lehrstuhl De fur Mathematik, RWTH, Aachen, **1992**.

19. M. Ghorbani, A. R. Ashrafi and M. Hemmasi, *Optoelectronics and Advanced Materials – Rapid Communications*, **2009**, *3*, 1306.

20. A. R. Ashrafi, M. Ghorbani and M. Jalali, *Optoelectronics and Advanced Materials – Rapid Communications*, **2009**, *3,* 823.

21. A. R. Ashrafi and M. Ghorbani, *Optoelectronics and Advanced Materials – Rapid Communications*, **2009**, *3*, 595.

22. A. R. Ashrafi, M. Ghorbani and M. Hemmasi, *Digest Journal of Nanomaterials and Biostructures*, **2009**, *4*, 483.

STRUCTURE, MORPHOLOGY AND OPTICAL PROPERTIES OF Al - DOPED ZnO THIN FILMS

DORINA GIRBOVAN[a], MARIUS AUREL BODEA[b], DANIEL MARCONI[a], JOHANNES DAVID PEDARNIG[b], AUREL POP[a, *]

ABSTRACT. Undoped and Al-doped ZnO thin films (AZO) were prepared on Si substrates by using the RF magnetron sputtering technique. In order to improve the film crystallinity of ZnO films, different target-substrate distances were used. Atomic force microscopy (AFM) and scanning electron microscopy (SEM) show that the surface morphology changes function of synthesis parameters and it is influenced by Al doping. From X-ray diffraction (XRD), it is found that all films have c-axis preferred orientation and that the grain size is influenced by both target-substrate distance and doping with Al. The influence of Al doping on electrical properties was studied by electrical resistivity measurement as a function of temperature. Optical reflectance spectra were performed for undoped and Al doped ZnO thin films, both grown under the same conditions.

Keywords: ZnO, AZO thin films, morphology, structure, electrical resistance, reflectance

INTRODUCTION

Zinc oxide (ZnO) is a material intensely researched in the last years due to its variety of applications in solar cells, transparent conductors, thin film transistors, laser diodes and ultraviolet diodes. All these electronic and optoelectronic applications can be accredited to its wide band gap of 3.37 eV and its large exciton binding energy of 60meV [1-4]. For ranges between VIS and IR, it displays transparency and it is resistant to reductive ambient, reasons for which it is used in transparent electrode window layer for solar cells [5].

Transparent conducting oxide (TCO) thin films are used in semiconductors industry, due to their high transparency and electrical conductivity and due to their cheap value and no toxicity [6]. There are a couple of techniques used to deposit these thin films. Among these techniques are spray pyrolysis

---

[a] *Babes-Bolyai University, Physics Faculty, M. Kogalniceanu No. 1, 400084, Cluj-Napoca, Romania*

[b] *Institute of Applied Physics, Johannes Kepler University Linz, A-4040 Linz, Austria*

corresponding author: aurel.pop@phys.ubbcluj.ro

[7], metal-organic chemical vapor deposition [4,8], sol-gel synthesis [9,10], magnetron sputtering [11-14], pulse laser deposition [15], etc. The magnetron sputtering technique is considered one of the best techniques in deposition of thin films, because it allows a growth of uniform and transparent ZnO thin films at low temperature and it has a high reproducibility with strong adhesion to substrates [16]. ZnO exhibits an excellent thermal and chemical stability, an exact electrical and optoelectronic properties specific for II-VI semiconductors [17]. It was observed that, when doped with Al, ZnO thin films exhibit comparable high optical transmittance and low electrical resistivity, more stable in hydrogen plasma with respect to other environments [12,18]. These TCO thin films are already used in industry, example Tin –doped or Indium doped oxides (ITO), but the costs are high and they will become higher due to the fact that these materials are non-renewable. Compare with these oxides, Al doped ZnO will have low cost and high availability since only a little amount of Al can give the same properties as ITO [10,14,19]. Also, ZnO thin films have unstable electrical properties at high temperatures, but doped with Al, the thin films generates a better electrical conductivity.

RESULTS AND DISCUSSIONS

The analysis of EDX data (figure 1) shows that the degree of substitution of Zn by Al is around 2% in AZO film and that the chemical formula of thin film is ZnO for the undoped sample.

The crystallinity of ZnO and AZO films was investigated with respect to the distance d between target and substrate. Figure 2 shows the diffraction patterns of ZnO thin films for different distances d and of AZO thin film for d=8 cm. In both cases, the strong (002) reflection is detected at about 51.5°, reflecting the wurtzite structure of the growing films with the c-axis oriented normal to the substrate.

Furthermore, for ZnO thin films, a small shift of the (002) peak toward larger angles is observed with increasing d to 8 cm. This shift is associated with the increment of the lattice constant c with increasing distance. The lattice constant c of the samples calculated by Bragg formula, evidenced a small increase from c=0.549nm for d=2cm to 0.554 nm for d=8 cm. The main effect of increasing distance d, target-substrate in synthesis ZnO thin films is the change of linewidth of (002) diffraction peak, suggesting changes in mean value of the grains size [20]. The crystallite sizes of the films were calculated using the Scherrer equation:

$$D = \frac{0,9\lambda}{B\cos\theta}$$

where λ, θ, and B are the X-ray wavelength $\lambda_{CrK\alpha1}$, diffraction angle and FWHM (full width at half maximum) of the diffraction (002) peak.

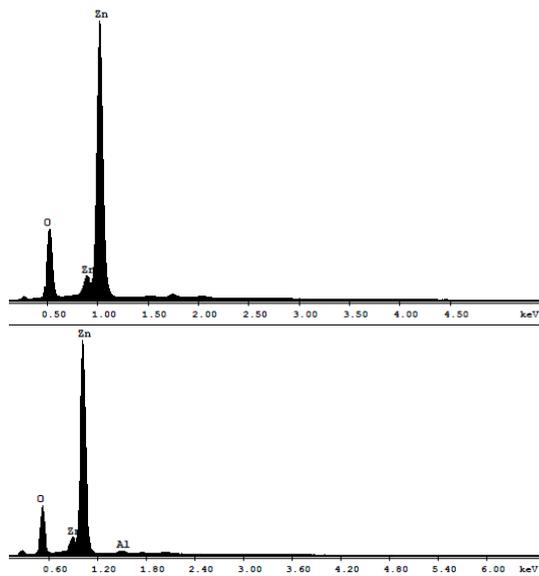**Figure 1.** EDAX analysis of ZnO and AZO thin films (d=8cm for both samples)
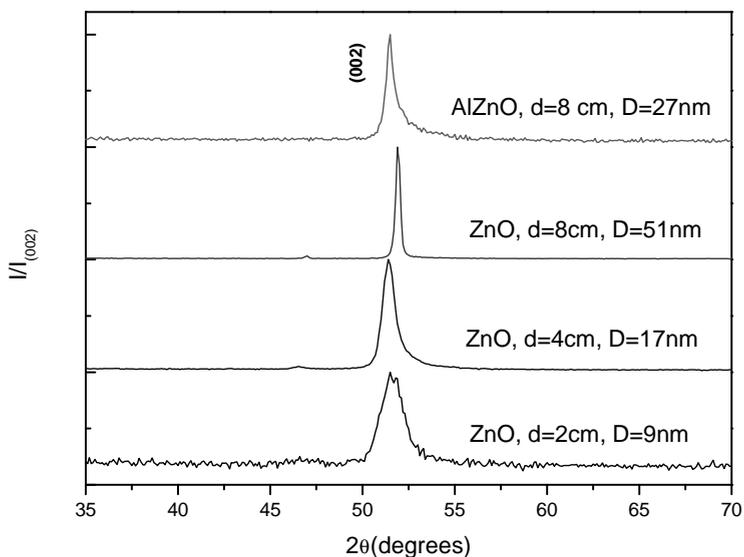

Figure 2. The XRD spectra of ZnO and AZO films grown at the same substrate temperature and varying distance d between target and substrate.

215

In order to determine more precisely the position and FWHM of the linewidth, the Lorentz fit of (002) peak was performed. The increase of d up to 8 cm leads to the increase of crystallite size from 9 nm (d=2cm) to 51nm (d=8cm). These results are in accordance with other reports on pure ZnO [21,22]. Above d=8 cm a small decrease of crystallite size was observed. The optimal process parameters (including d=8cm) used to obtain the best crystallinity of ZnO thin film were used to obtain AZO films. The partial substitution of Zn with 2%Al leads to the decrease of crystallite size to around 27 nm. The decrease of crystallite size reinforced the decrease of film crystallinity. This behavior may be considered to be due to the moderate quantity of Al atoms that can exist at interstitial sites and to the fact that Al together with Zn atoms share oxygen atoms.

The typical surface morphology of ZnO and AZO thin films grown in optimal conditions and measured by SEM and AFM is shown in figure 3.
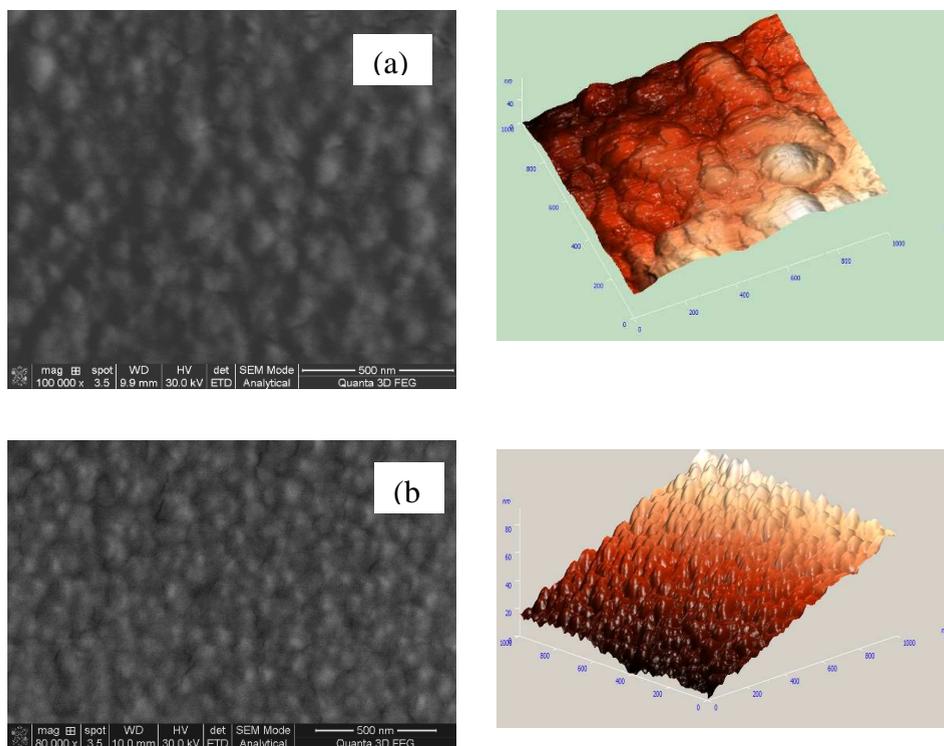

Figure 3. Typical SEM (left) and AFM (right) images of ZnO (figure 2a) and AZO films (figure 2b) surface.

Left side images of figure 3 show the surface morphology from SEM, whereas the right side images of figure 3 show the films microstructure from AFM measurements. SEM and AFM characterization of the film surfaces revealed that grain size decreases after the partial substitution of Zn with Al. The characteristic of these films is the presence of grains of different dimensions with a strong tendency to form agglomerations as it is shown in figure 3. It also shows the presence of columnar morphologies with increased roughness for 2% Al thin films and a small increase in the height of the grains.

A decrease in resistance with increasing temperature following semiconducting behaviour of ZnO and AZO films is observed. The activation energy was determined by using the equation

$$R = R_0 \, exp(E_a/kT)$$

where R is the resistance at temperature T, R_0 is a constant, E_a is the activation energy and k is the Boltzmann constant.

The value of activation energy from resistivity measurements is around 0.31 eV for both undoped ZnO and AZO thin films. An activation barrier value of 0.3 eV for ZnO film was reported earlier [23]. A small change in the activation barrier by 2% Al doping is undetectable from resistivity measurements. Electrical resistivity for AZO film at room temperature is 8.6 mΩcm in agreement with results reported in reference [24]. However, for AZO film, the decrease of resistance by approximately 25% in the entire temperature range studied (300K-450K) shows that Aluminum atoms are incorporated into the ZnO lattice and they contribute with conduction electrons which improve the electrical conduction.

Figure 4 shows the reflectance of undoped ZnO film and 2% Al doped film, grown under the same conditions.

The increase in reflectance for wavelength longer than 1000 nm for AZO thin films indicates an increase in free carriers absorption and consequently a higher carrier concentration for the Al-doped film. These results are confirmed by electrical resistivity measurements.

CONCLUSIONS

Epitaxial ZnO and Al doped ZnO thin films deposited on Si substrates were obtained by radio-frequency (RF) reactive magnetron sputtering method. The effect of distance target-substrate and the Al doping on the morphological, structural, electrical and optical properties of the ZnO film was analyzed.

(1) EDX data show that the degree of substitution of Zn by Al is around 2% in AZO films and XRD data evidence the growing films with the c-axis oriented normal to the substrate.

(2) SEM and AFM characterization of the film surfaces revealed that grain size decreases after the partial substitution of Zn with Al

(3) XRD facts that the main effect of increasing the distance target-substrate d in the synthesis of ZnO thin films is the change in the mean value of the grain size. The best crystallinity is obtained for d=8cm

(4) The value of activation energy obtained from electrical resistance function of temperature is 0.31 eV for both undoped ZnO and AZO films. The increase in reflectance for wavelength longer than 1000 nm indicates a higher carrier concentration for the Al-doped film.
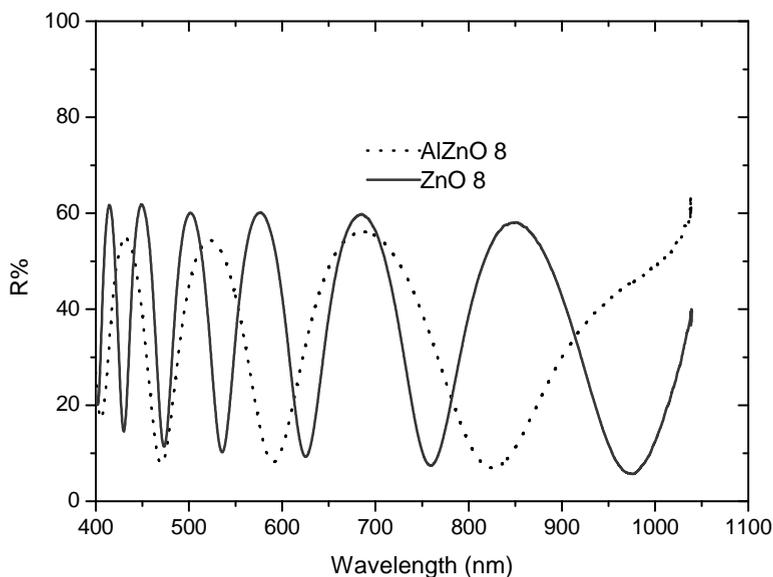
Figure 4. Optical reflectance spectra of undoped and Al doped ZnO thin film, both grown under the same conditions (d=8cm).

EXPERIMENTAL

The ZnO and Al doped ZnO thin films were deposited by RF magnetron sputtering technique. Ceramic targets with chemical formula ZnO and $Al_{0.02}Zn_{0.98}O$ (sample AZO) were obtained by solid state reaction method, using mechanical mixed powders of 99.99% pure ZnO and 99.97% pure A_2O_3. These circular ceramic targets were used to prepare the ZnO and AZO thin films. The films were deposited in an oxygen–argon atmosphere (with the ratio $Ar:O_2$=10:6 sccm) on Si substrates. The substrate temperature was 150^0C. The deposition pressure in the chamber was 2×10^{-2} mbar and the target-to-substrate distance was varied from 2 to

12 cm. The films' thicknesses of ZnO increased from 100 nm to 300 nm by increasing distance from 2 cm to 12 cm. The best cristallinity in ZnO film with thickness 200 nm was obtained for d=8cm. This is the reason for choosing the same process parameters for AZO film.

The surface morphology was characterized by atomic force microscopy (AFM) in tapping mode using NT-MDT Ntegra Solaris atomic force microscope. SEM imagines were recorded using FEI Quanta 3D FEG 200/600 and Scanning Electron Microscope. The samples were covered with metals in order to amplify the secondary electrons signal. This covering was performed with Pt. X-ray diffraction (XRD) using a Bruker D8 diffractometer with Cr K_α X-rays was done in order to determine the crystal structure of the deposited films.

The optical reflectance spectra were measured at normal incidence with a miniature spectrometer (Ocean Optics USB4000 UV-vis). The spectrometer was equipped with a QR200-7-VIS/BX reflection optical fiber probe consisting of a tight bundle of 7 optical fibers of 200 mm diameter (6 illumination fibers around 1 read fiber).

The electrical characterization of the films was carried out in a tube furnace by monitoring the variation of electrical resistance (R) as a function of temperature (T) using conventional DC two-probe technique. The range of temperature investigated was 300-450 K with a control accuracy of (±)1 K. Approximately 30 mm long silver (Ag) contacts, separated by 7 mm, were made on ZnO films for electrical measurements.

ACKNOWLEDGMENTS

REFERENCES

1. L.-Y. Lin, M.-C. Jeong, D.-E. Kim, J.-M. Myoung, *Surface and Coatings Technology*, **2006**, *201,* 2547
2. M. Berginski, J. Hupkes, M. Schulte, G. Schope, H. Stiebig, B. Rech, and M. Wuttig, *Journal of Applied Physics* 2007, *101*, 074903
3. S. Fernández, F.B. Naranjo, *Solar Energy Materials and Solar Cells* **2010**, *94 (2),* 157-163

4. I. Volintiru, M. Creatore, and M. C. M. van de Sanden, *Journal of Applied Physics* **2008**, *103,* 033704

5. Wei Li, Yun Sun, Yaxin Wang, Hongkun Cai, Fangfang Liu, Qing He, *Solar Energy Materials and Solar Cells*, **2007**, *91(8)*, 659

6. J. Garnier, A. Bouteville, J. Hamilton, M.E. Pemble, I.M. Povey, *Thin Solid Films*, **2009**, *518,* 1129

7. M. Gaba, N.T.Barrett, J.R.Ramos-Barrado, S.Gota, T.C.Rojas , M.C.Lopez-Escalante, *Solar Energy Materials & Solar Cells* **2009**, *93,* 1356

8. T. Soderstrom, F.J. Haug, X. Niquille, C. Ballif, *Progress in Photovoltaics: Research and Applications*, **2009**, *17*, 165

9. K.E. Lee, M. Wang, E.J. Kim, S.H. Hahn, *Current Applied Physics*, **2009**, *9,* 683

10. Y.S. Kim, W.P. Tai, Electrical and optical properties of Al-doped ZnO thin films by sol–gel process, *Applied Surface Science* **2007**, *253*, 4911

11. Dorina Ciomos, D. Marconi, Radu Redac, A. V. Pop, *Studia Universitatis Babes-Bolyai Seria Physica*, **2011**, *LVI, 1*, 3

12. Fang-Hsing Wang, Hung-Peng Chang, Chih-Chung Tseng, Chia-Cheng Huang, Han-Wen Liu, *Current Applied Physics*, **2011**, *11 (1) (1),* S12

13. Zhiyun Zhang**,** Chonggao Bao**,** Wenjing Yao**,** Shengqiang Ma**,** Lili Zhang and Shuzeng Hou**,** *Superlattices and Microstructures*, **2011**, *49 (6)*, 644

14. Y.H. Kim, K.S. Lee, T.S. Lee, B. Cheong, T.Y. Seong, W.M. Kim, *Applied Surface Science* **2009**, *255*, 7251

15. R.S. Ajimsha, R. Manoj, P.M. Aneesh, M.K. Jayaraj, *Current Applied Physics* **2010**, *10,* 693

16. J. Lee, D. Lee, D. Lim, K. Yang, *Thin solid Films*, **2007**, *515*, 6094

17. V.S. Khomchenckoa, T. G. Kryshtabb, A. K. Savina, *Superlattices Microstructures*, **2007***, 42*, 94

18. J. Hupkes, J. Muller, B. Rech, R. Hull, R.M. Osgood, J. J. Parisi, H. Warlimont, *Transparent Conductive Zinc Oxide*, **2008**, *104*, 359

19. K.H. Kim, K.C. Park, D.Y. Ma, *Journal of Applied Physics*, **1997***, 81,* 7764

20. J.J.Ding, S.Y.Ma, H.X.Chen,X.F.Shi, T.T.Zhou, L.M.Mao, *Physica B* **2009**, *404,* 2439

21. A. Klini, A. Manousaki, D. Anglos, C. Fotakis, *Journal of Applied Physics* **2005**, *98*, 123301.

22. E.L. Papadopoulou, M. Varda , K. Kouroupis-Agalou, M. Androulidaki, E. Chikoidze, P. Galtier, G. Huyberechts, E. Aperathitis, *Thin Solid Films* **2008**, *516*, 8141

23. P. Mitra and J. Khan, *Materials Chemistry and Physics* **2006**, *98*, 279

24. Wei Lin, R. Ma, Wei Shao, Bin Liu, *Applied Surface Science*, **2007**, *253*, 5179

X-RAY CRYSTAL STRUCTURE AND DYNAMICS REVEAL HIV-1 PROTEASE DRUG INTERACTIONS

YONG WANG[a], TAMARIA G. DEWDNEY[a], ZHIGANG LIU[a], SAMUEL J. REITER[a], JOSEPH S. BRUNZELLE[b], IULIA A. KOVARI[a], LADISLAU C. KOVARI[a]

ABSTRACT. The dynamic movement of HIV-1 protease is an important feature for inhibitor design. The wide-open form of multi-drug resistant HIV-1 protease solved by our group exhibits an increase in flap distance. Stabilizing the protease flaps could be a strategy to overcome drug resistance. A peptidic inhibitor stabilizing the protease-inhibitor complex and a structural novel inhibitor targeting the wide-open form protease have been identified as a new scaffold for drug development.

Keywords: multi-drug resistance, HIV-1 protease, drug design,

INTRODUCTION

Drug resistance is a major obstacle in the long-term treatment of HIV/AIDS patients. The drug-resistance mutations accumulated on HIV-1 protease during antiretroviral therapy change the protease conformation and decrease the efficacy of protease inhibitors. While most HIV-1 protease inhibitors are designed to mimic the substrate cleavage intermediates, structurally diverse inhibitors are needed to maintain efficacy against the highly flexible protease [1]. The discovery of new inhibitor scaffolds is the first step to increase the diversity of HIV-1 protease inhibitors. The HIV-1 protease structures greatly facilitate the discovery of new inhibitors.

Few ligand-free 3-dimensional structures of HIV-1 protease have been deposited to the Protein Data Bank. We have previously reported one such structure of an uncomplexed multi-drug resistant (MDR) HIV-1 protease, MDR 769 [2]. As shown in Figure 1, the available ligand-free HIV-1 protease can be classified into two classes, wide-open form and curled

[a] *Department of Biochemistry and Molecular Biology, School of Medicine, Wayne State University, Detroit, MI, U.S.A., kovari@med.wayne.edu*
[b] *Department of Molecular Pharmacology and Biological Chemistry, Feinberg School of Medicine, Northwestern University, Evanston, IL, U.S.A.*

form [3]. Considering the flexibility and dynamic movement of the protease, the structure of unbound HIV-1 protease is as important as the ligand-bound structure in successful drug design.
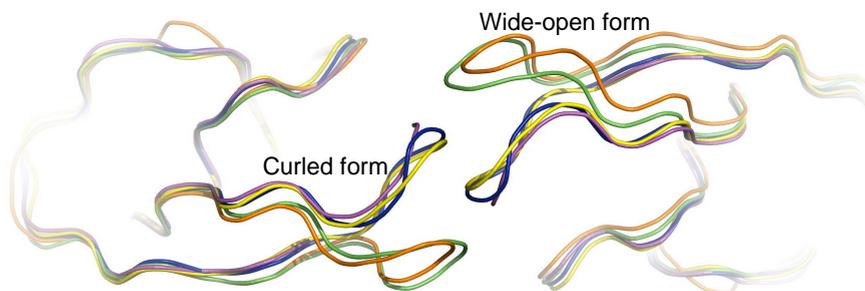

Figure 1. Apo HIV-1 protease structures. The structures include the wild-type (WT) HIV-1 protease NL4-3 (PDB ID: 2HB4, blue), the HIV-1 protease with mutations L24I, M46I, F53L, L63P, V77I, and V82A (PDB ID: 2HB2, magenta), the WT HIV-1 protease isolate BRU (PDB ID: 1HHP, yellow), another WT HIV-1 protease (PDB ID: 2PC0, green), and the HIV-1 protease MDR 769 with mutations L10I, M36V, M46L, I54V, I62V, L63P, A71V, V82A, I84V, and L90M (PDB ID: 1TW7, orange)

Understanding the structural diversity of the target protease is essential for inhibitor development. The plasticity of the HIV-1 protease flap region is critical in binding substrates and inhibitors [3]. The increased flap flexibility may enhance drug cross-resistance by altering the binding pocket of protease inhibitors. Flap movement distorts the binding cavity and therefore reduces the binding affinity to inhibitors. Direct measurement using pulsed double electron-electron resonance (DEER) has confirmed a larger distance between the flaps of (MDR) HIV-1 protease as compared to the wild-type structure [4]. Therefore, the wide-open form of HIV-1 protease can serve as a nontraditional model to develop inhibitors targeting the open form protease. A crystal structure (PDB ID: 3BC4) has shown that the HIV-1 protease with open-flap conformation binds two symmetric pyrrolidine diester inhibitors [5].The range of opening and conformational flexibility of protease flaps demonstrate the importance of protein flexibility in structure-based drug design. Using ensembles of protein conformations as receptors for docking is a powerful method to increase accuracy [6,7]. Designing inhibitors based on both the open and closed form of HIV-1 MDR protease partially represents the HIV-1 protease dynamics and improves drugs' adaptation to the flexible movement of the protease.

RESULTS AND DISCUSSION
Four multi-drug resistant HIV-1 protease isolates are resistant to inhibitors at various levels

Table 1. Sequences of HIV-1 protease variants

HIV-1 protease	Sequences*
NL4-3	PQITLWKRPL VTIKIGGQLK EALLDTGADD TVLEEMNLPG
	RWKPKMIGGI
	GGFIKVRQYD QILIEICGHK AIGTVLVGPT PVNIIGRNLL TQIGCTLNF
769	PQITLWKRPI VTIKIGGQLK EALLDTGADD TVLEEVNLPG
	RWKPKLIGGI GGFVKVRQYD QVPIEICGHK VIGTVLVGPT
	PANVIGRNLM TQIGCTLNF
807	PQITLWKRPI VTIKIGGQLK EALLDTGADD TVLEEMNLPG
	KWKPKIIVGI
	GGFTKVRQYD NVQIEICGHK VIGAVLIGPT PANIIGRNLL TQLGCTLNF
1385	PQITLWKRPF VTIKIGGQLK EALLDTGADD TVLEEIDLPG
	RWKPKIIGGI
	GGFIKVKQYD QIPIEICGHK VIGTVLVGPT PTNIIGRNMM TQLGCTLNF
3761	PQITLWKRPI VAIKVGGQII EALLDTGADD TVLEEMNLPG
	RWKPKIIGGI
	GGFIKVRQYD QIPVEICGHK IITTVLVGST PVNVIGRNLM TQLGCTLNF

*The polymorphic changes are underlined. The drug-resistance mutations are highlighted in red.
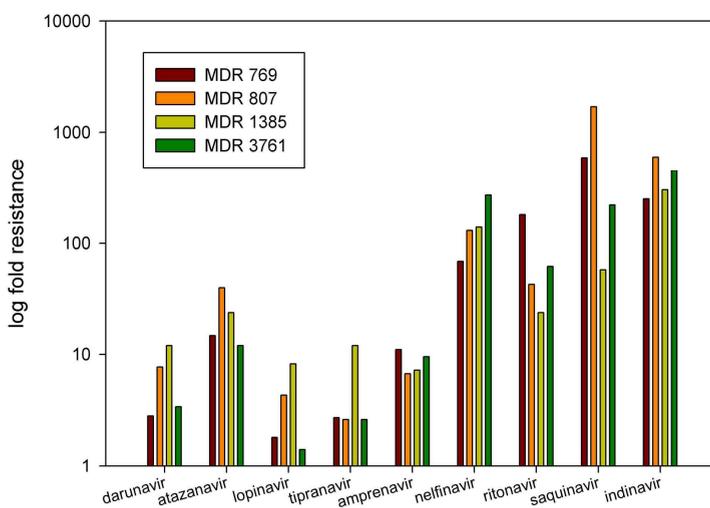

Figure 2. Fold resistance of four multi-drug resistant HIV-1 protease variants.

Four MDR HIV-1 protease variants were isolated by Palmer *et al.* from patients failing protease inhibitor-containing antiretroviral regimens (Table 1) [8]. The drug-resistance profiles of four clinical MDR HIV-1 protease isolates were identified using enzyme inhibition assays. Four MDR protease variants were resistant to all FDA-approved HIV-1 protease inhibitors at various levels (Figure 2). The second generation of HIV-1 protease inhibitors (darunavir, atazanavir, lopinavir, and tipranavir) encountered relatively lower fold resistance. Among the four MDR protease variants tested here, MDR 807 and MDR 1385 were more resistant to the second generation HIV-1 protease inhibitors. According to the guidelines for the use of antiretroviral agents in HIV-1-infected adults and adolescents, darunavir and atazanavir are preferred first-line antiretroviral drugs [9]. Our results showed that there was higher resistance to atazanavir comparing to darunavir. These results confirmed the *in vitro* resistance observed of the clinical isolates of HIV-1 protease.

Potent inhibitors induced flap closure of the multi-drug resistant HIV-1 protease
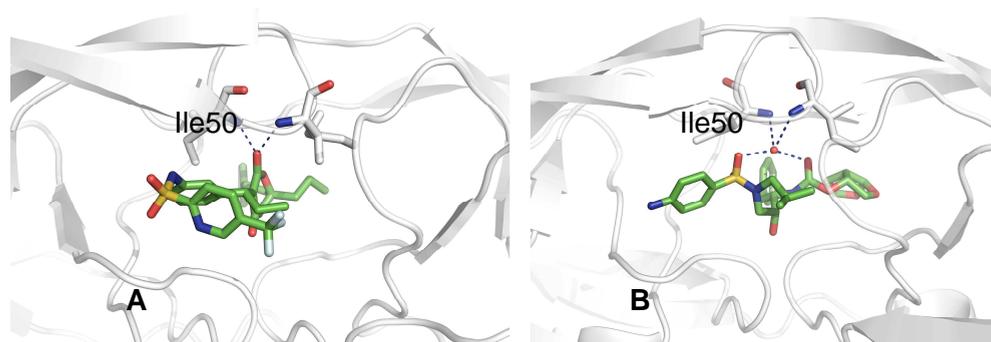
Figure 3. The hydrogen bonds between HIV-1 protease flaps and inhibitors. (A) tipranavir-MDR 769 complex structure. (B) darunavir-MDR 769 complex structure. The hydrogen bonds are represented as blue dash lines. The bridging water molecule is represented in a red dot.

Darunavir and tipranavir are among the protease inhibitors exhibiting the most potency and least fold resistance. The tipranavir-MDR 769 82T complex crystallized in the hexagonal space group $P6_1$ while the darunavir-MDR 769 82T complex crystallized in the orthorhombic space group $P2_12_12_1$. The crystal structure was determined at 1.24 Å resolution and 2.87 Å resolution, respectively. The other seven FDA-approved HIV-1 protease inhibitors crystallized with MDR 769 in an open form. The binding of tipranavir or darunavir effectively closes the open flaps of MDR 769. Tipranavir directly interacts with Ile50 while darunavir interacts with Ile50 through a bridging

water molecule (Figure 3). Therefore, incorporating a chemical group to contact the protease flaps is a useful strategy to increase inhibitor potency and decrease fold resistance. From the drug modification point of view, the tipranavir-like direct protease flap contact stabilizes protease-inhibitor complex, which is concluded based on a protease complex denaturation experiment [10].

A peptidic inhibitor reduced fold resistance by stabilizing the multi-drug resistant HIV-1 protease complexes

Table 2. The half maximal inhibitory concentration (IC_{50}) of mutated CA-p2 peptides

CA-p2 mutagenesis	Sequences	IC_{50} (nM)		Fold resistance
		Wild-type	MDR 769	
P1'F	Arg-Val-Leu-Phe-Glu-Ala-Met	2.6	4.4	1.7
P1'F, P1F	Arg-Val-Phe-Phe-Glu-Ala-Met	30.7	142	4.6
P1'F, P1A	Arg-Val-Ala-Phe-Glu-Ala-Met	4873	5020	1.0
P1'F, P2F	Arg-Phe-Leu-Phe-Glu-Ala-Met	1143	770	-
P1'F, P2A	Arg-Ala-Leu-Phe-Glu-Ala-Met	78.2	74.1	-
P1'F, P2'F	Arg-Val-Leu-Phe-Glu-Phe-Met	1010	1263	1.3
P1'F, P2'A	Arg-Val-Leu-Phe-Ala-Ala-Met	232.3	233.7	1

The cleavage of the CA-p2 site is a rate-limiting step of gag polyprotein maturation. Mutations were introduced to the CA-p2 heptapeptide with a reduced scissile peptide bond to test the inhibitory efficacy. One of the peptidic inhibitors, CA-p2 P1'F, displayed high inhibitory efficacy and low resistance. CA-p2 P1'F inhibited both wild-type (WT) HIV-1 protease and MDR 769 at low nanomolar concentration (Table 2). The combination of phenylalanine and leucine analogues at the P1 and P1' site could be employed to the peptidomimetic inhibitors.

Based on the crystal structure of MDR 769 in complex with CA-p2 P1'F, the homologous complex models were built for MDR 807, MDR 1385, MDR 3761, and NL4-3. After 10 ns molecular dynamics simulation, the movement of CA-p2 P1'F was analyzed for the last 40 ps of simulation. The root-mean-square deviation (RMSD) of each residue of CA-p2 P1'F was plotted in Figure 4. The RMSD values of CA-p2 binding to MDR proteases were significantly lower compared to that of CA-p2 binding to the WT HIV-1 protease. The lower RMSD value suggests a tighter substrate-protease complex. This result indicates that CA-p2 P1'F stabilizes MDR protease complexes and could serve as a template to be further developed as a resistance overcoming peptidomimetic inhibitor.
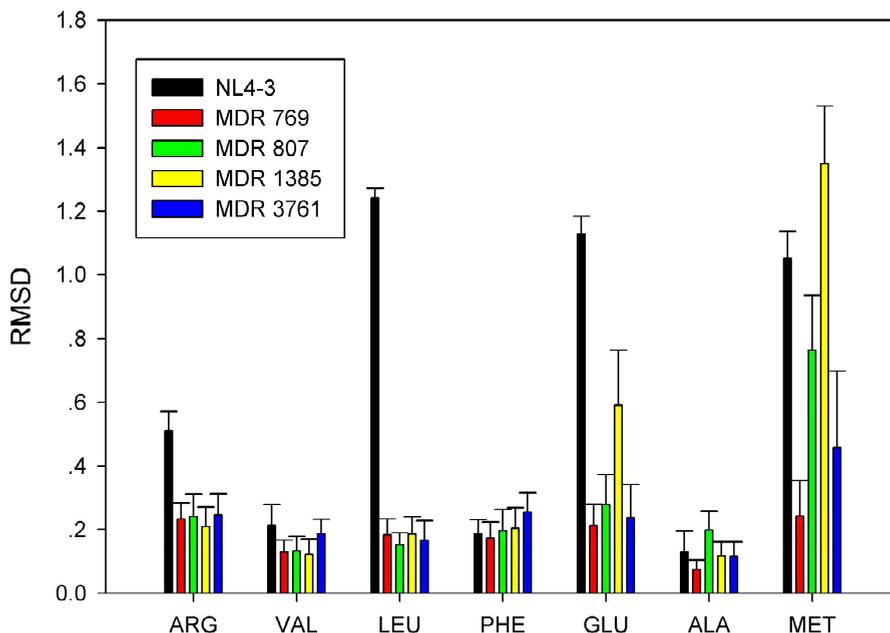
Figure 4. The root-mean-square deviation (RMSD) of CA-p2 P1'F binding to HIV-1 protease variants.

Based on the open and closed form HIV-1 protease structures, a resistance overcoming inhibitor candidate was identified using virtual screening.

The open form MDR 769 structure was used as a receptor to identify potential inhibitor scaffolds from commercially available compounds through virtual screening. One compound, GR346 (Figure 4), showed the best docking scores against the open form MDR 769. The binding of GR346 was then confirmed by docking it to the closed formed MDR 769. The docking conformation of GR346 is shown in Figure 5. GR346 was originally synthesized as a SIRT2 inhibitor (IC_{50}=56.7 μM) [11]. The HIV-1 protease inhibitory efficacy was tested using *in vitro* enzyme assays (Figure 6). GR346 inhibited a larger percentage of MDR 769 enzyme activity at various concentrations comparing to its inhibition against the WT HIV-1 protease. At the lower compound concentration (6.25 μM), GR346 did not inhibit the WT HIV-1 protease but inhibited MDR 769 activity by 10%. The wide-open conformation of MDR 769 flaps allowed the bulky compound, GR346, to easily enter into the protease active site. This result suggested a possibility of designing large flexible inhibitors could fit better to the expanded active site of MDR HIV-1 protease.
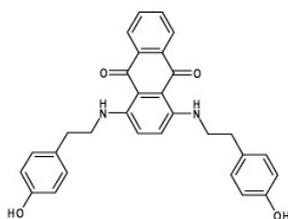
Figure 4. The structure of compound GR346

A   **B**
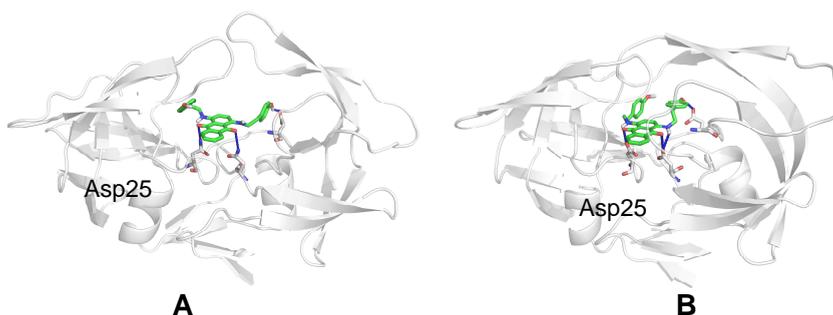
Figure 5. The docking conformation of GR346 in the active site of MDR 769. (A) GR346 was docked to the open form MDR 769. (B) GR346 was docked to the closed form MDR 769. The blue line represents possible hydrogen bonds.

CONCLUSIONS

Protein flexibility is an important feature to be considered in drug design. The movement of HIV-1 protease flaps may interrupt drug binding and cause resistance. Designing drugs that make contacts with the protease flaps to reduce protease flexibility, and targeting the open form protease could be options to overcome drug resistance caused by protease flap conformation and flexibility.

EXPERIMENTAL SECTION
Protein expression and purification

Table 1 lists the protein sequences of MDR proteases. Active and inactive MDR protease genes were codon optimized for *E. coli* expression, synthesized by GENEART, Inc. (Regensburg, Germany), and inserted into the pET21b plasmid. To prevent auto-proteolyses, Q7K mutation was introduced into the active MDR genes. The A82T mutation was introduced to facilitate crystallization. The protein expression, purification, and refolding procedures were described previously [12]. The final protein buffer was 20 mM sodium acetate, pH 5.0, 1 mM dithiothreitol (DTT), and 10% (v/v) glycerol. The proteases prepared for crystallization were concentrated to 1.5 mg/ml using Amicon concentrators with 5 kDa molecular mass cut-off (Millipore Corporate, Billerica, MA, USA).

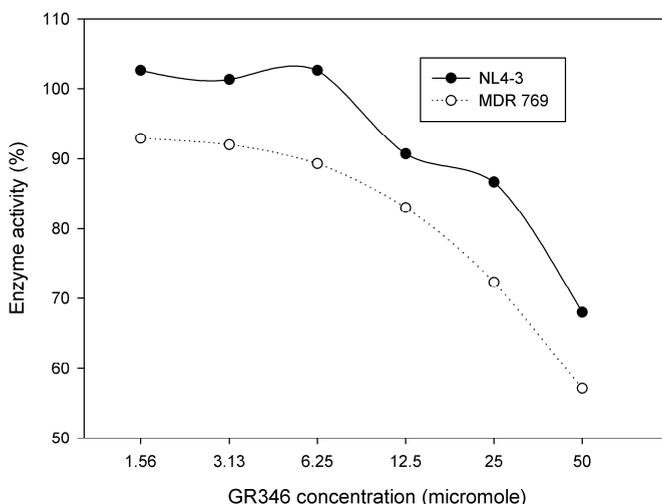**Figure 6.** The enzyme inhibition of GR346

Protease inhibition assays

HIV protease Forster Resonance Energy Transfer (FRET) substrate I, purchased from AnaSpec, Inc. (Fremont, CA, USA), was used in the IC_{50} determination experiments. The fluorescence emitted by substrate cleavages was monitored by a microplate reader (SpectraMax M5, Molecular Devices, Sunnyvale, CA, USA) at a 340 nm excitation wavelength with an emission wavelength of 490 nm. The HIV-1 protease reaction buffer was adjusted to pH 4.7 [0.1 M sodium acetate, 1.0 M sodium chloride, 1.0 mM ethylenediaminetetraacetic acid (EDTA), 1.0 mM DTT, 10% dimethylsulfoxide (DMSO), and 1mg/ml bovine serum albumin (BSA)]. In the reaction buffer containing 5 μM FRET substrates, the protease concentration was adjusted to a substrate cleavage velocity of 5 Relative Fluorescence Units (RFU)/min. The active proteases and inhibitors were pre-incubated at 37℃ for 20 min prior to signal monitoring. An inhibitor-free control was used to determine the background fluorescent signal. The progress of the reaction was monitored over 20 min sampling at 1 min intervals. The FRET data were plotted with the software SoftMax Pro V5.2 (Molecular Devices, Sunnyvale, CA, USA) to determine the IC_{50} values.

Crystallization and data collection

Inhibitors (tipranavir and darunavir) or substrates (CA-p2) were co-crystallized with the MDR769 inactive protease by the hanging drop vapor diffusion method. The protease and ligand were pre-mixed at a molar ratio of 1:20 before crystallization set-up. The protease-ligand mixture was then mixed at 2:1 v/v ratio with the precipitant solution. The optimal crystallization was screened from a set of precipitant solution (0.1 M citric acid/MES/HEPES

and 0.8~2.8 M ammonium sulfate at pH 4.0~6.0). The reservoir volume was 750 µl. The co-crystal grew within a week to a suitable size for diffraction. The crystals were placed in a 30% w/v glucose cryoprotectant before being frozen in liquid nitrogen. Diffraction data were collected at the Life Sciences Collaborative Access Team (LS-CAT) at the Advanced Photon Source (APS) Sector 21, Argonne National Laboratory (Argonne, IL, USA) and processed with HKL2000 program suite [13].

Virtual screening and protein-ligand docking

The large scale screening was conducted using a fast pre-screening tool, LASSO (Ligand Activity in Surface Similarity Order) 2009 [14]. The smaller library with thousands of compound was further validated using eHiTS (Electronic High Throughput Screening), a fast and automated docking program [15]. Compound libraries were downloaded from the ZINC database of commercially-available compounds (zinc.docking.org). To confirm the lead compound from virtual screening, the compound with the best eHiTS score was docked into the binding pocket of HIV-1 protease using AutoDock4 [16].

Molecular dynamics simulation

The MD simulation was performed using Scaling NAno Molecular Dynamics (NAMD) V 2.7b [17]. The protease complex model was solvated in an orthogonal TIP3P water box. The cut-off of non-bonded interactions was 10 Å. The systems were minimized and gradually heated from 70 K to 310 K in 200 ps. Simulations were conducted at 310K and 1.0 atm for 10 ns using the CHARMM force field23 and a timestep of 2 fs.

REFERENCES

1. N. Ozer, C. A. Schiffer, T. Haliloglu, Rationale for more diverse inhibitors in competition with substrates in HIV-1 protease, *Biophysical journal*, **2010**, *99*, 1650.
2. P. Martin, J. F. Vickrey, G. Proteasa, Y. L. Jimenez, Z. Wawrzak, M. A. Winters, T. C. Merigan, L. C. Kovari, "Wide-open" 1.3 A structure of a multidrug-resistant HIV-1 protease as a drug target, *Structure*, **2005**, *13*, 1887.

3. H. Heaslet, R. Rosenfeld, M. Giffin, Y. C. Lin, K. Tam, B. E. Torbett, J. H. Elder, D. E. McRee, C. D. Stout, Conformational flexibility in the flap domains of ligand-free HIV protease, *Acta crystallographica. Section D, Biological crystallography*, **2007**, *63*, 866.
4. L. Galiano, F. Ding, A. M. Veloro, M. E. Blackburn, C. Simmerling, G. E. Fanucci, Drug pressure selected mutations in HIV-1 protease alter flap conformations, *Journal of the American Chemical Society*, **2009**, *131*, 430.
5. J. Bottcher, A. Blum, S. Dorr, A. Heine, W. E. Diederich, G. Klebe, Targeting the open-flap conformation of HIV-1 protease with pyrrolidine-based inhibitors, *ChemMedChem*, **2008**, *3*, 1337.
6. E. S. Bolstad, A. C. Anderson, In pursuit of virtual lead optimization: pruning ensembles of receptor structures for increased efficiency and accuracy during docking, *Proteins*, **2009**, *75*, 62.
7. S. Y. Huang, X. Zou, Ensemble docking of multiple protein structures: considering protein structural variations in molecular docking, *Proteins*, **2007**, *66*, 399.
8. S. Palmer, R. W. Shafer, T. C. Merigan, Highly drug-resistant HIV-1 clinical isolates are cross-resistant to many antiretroviral compounds in current clinical development, *AIDS*, **1999**, *13*, 661.
9. Panel on Antiretroviral Guidelines for Adults and Adolescents, *Guidelines for the use of antiretroviral agents in HIV-1-infected adults and adolescents*, **2011**, 41.
10. Y. Wang, Z. Liu, J. S. Brunzelle, I. A. Kovari, T. G. Dewdney, S. J. Reiter, L. C. Kovari. The higher barrier of darunavir and tipranavir resistance for HIV-1 protease, *Biochemical and Biophysical Research Communications*, **2011**, *412*, 737
11. P. H. Kiviranta, J. Leppanen, S. Kyrylenko, H. S. Salo, M. Lahtela-Kakkonen, A. J. Tervo, C. Wittekindt, T. Suuronen, E. Kuusisto, T. Jarvinen, A. Salminen, A. Poso, E. A. Wallen, N,N'-Bisbenzylidenebenzene-1,4-diamines and N,N'-Bisbenzylidenenaphthalene-1,4- diamines as Sirtuin Type 2 (SIRT2) Inhibitors, *Journal of Medicinal Chemistry*, **2006**, *49*, 7907.
12. J. F. Vickrey, B. C. Logsdon, G. Proteasa, S. Palmer, M. A. Winters, T. C. Merigan, L. C. Kovari, HIV-1 protease variants from 100-fold drug resistant clinical isolates: expression, purification, and crystallization, *Protein Expression and Purification*, **2003**, *28*, 165.
13. C. W. Carter, R. M. Sweet, "Methods in Enzymology", Academic Press, Inc., New York, **1997**, chaper 20.
14. A. Simon, D. Reid, B. S. Sadjad, Z. Zsoldos, LASSO-ligand activity by surface similarity order: a new tool for ligand based virtual screening, *Journal of Computer-Aided Molecular Design*, **2008**, *22*, 479.
15. Z. Zsoldos, D. Reid, A. Simon, S. B. Sadjad, A. P. Johnson, eHiTS: a new fast, exhaustive flexible ligand docking system, *Journal of Molecular Graphics and Modelling*, **2007**, *26*, 198.
16. G. M. Morris, R. Huey, W. Lindstrom, M. F. Sanner, R. K. Belew, D. S. Goodsell, A. J. Olson, AutoDock4 and AutoDockTools4: Automated docking with selective receptor flexibility, *Journal of computational chemistry*, **2009**, *30*, 2785.
17. J. C. Phillips, R. Braun, W. Wang, J. Gumbart, E. Tajkhorshid, E. Villa, C. Chipot, R. D. Skeel, L. Kale, K. Schulten. Scalable molecular dynamics with NAMD. *Journal of Computational Chemistry*, **2005**, *26*, 1781.

CAN GEOMETRICAL DISTORTIONS MAKE A LACCASE CHANGE COLOR FROM BLUE TO YELLOW?

ALEXANDRU LUPAN[a], CSONGOR MATYAS[a], AUGUSTIN MOT[a], RADU SILAGHI-DUMITRESCU[a]

ABSTRACT. Laccases contain a blue mononuclear copper center known as 'type-1', and thought to be the primary electron acceptor from organic substrates during the catalytic cycle. A small group of laccases are also known that lack the 600 nm band and hence the blue color ("yellow laccases"). We report on the use of semiempirical (ZINDO/S-CI) calculations in order to simulate UV-vis spectral parameters for the laccase type 1 copper, attempting to assign geometrical and electronic structure elements that may control the color of this site. The ~600-nm band of the type 1 copper is confirmed to arise mainly from sulfur-to-copper charge transfer, and strong distortions allowing for its displacement by more than 200 nm and/or its dissolution are identified.

Keywords: laccase, type 1, copper, UV-vis, EPR, DFT, ZINDO/S

INTRODUCTION

Laccase enzymes contain a mononuclear copper centre known as 'type-1' (Figure 1) [1]. This site is thought to be the primary electron acceptor from organic substrates. This site is characterized by a 610 nm band in UV-vis spectra and a small hyperfine coupling constant in electron paramagnetic resonance (EPR) spectra [2]. A small group of laccases are also known that lack the 600 nm band and hence the blue colour ("yellow laccases") [3-5]. Several authors postulated that the yellow laccases are formed by modification of the blue form with low-molecular-weight lignin decomposition products [5, 6], even though there's no experimental proof yet. Numerous yellow laccases have been purified from a number of organisms such as the common mushroom *Agaricus biosporus* [7], phytopathogenic ascomycete *Gaeumannomyces graminis* [8], *Schizophyllum commune* [9], *Phlebia radiata* [5], *Phellinus ribis* [10], and *Pleurotus ostreatus* D1 [3], *Ph. tremellosa* [5].

We have recently characterized a "yellow" laccase, whose type 1 copper centre lacks the characteristic 610 nm band, but does still show an EPR spectrum typical of a blue laccase is shown in detail [11]. We now report

---

[a] *Universitatea Babeş-Bolyai, Facultatea de Chimie şi Inginerie Chimică, Str. Kogălniceanu, Nr. 1, RO-400084 Cluj-Napoca, Romania, alupan@chem.ubbcluj.ro*

on the use of density functional theory (DFT) and semiempirical (ZINDO/S-CI) calculations in order to simulate spectral parameters for the laccase type 1 copper as found in blue and in yellow laccases, attempting to assign geometrical and electronic structure elements that may control the trends observed experimentally in EPR coupling constants and in UV-vis spectra.
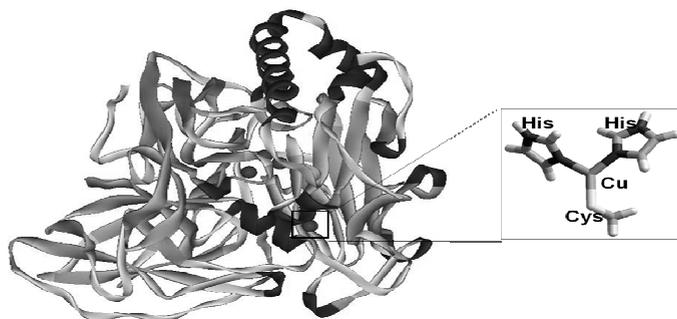
Figure 1. General structure of laccases (based on pdb ID 2Q9O), highlighting the four copper ions and the coordination environment around the type 1 copper center.

RESULTS AND DISCUSSION

Figure 2 shows the model employed in the present work for the type 1 copper. ZINDO/S- configuration interaction calculation calculations, with a 20 eV excitation window allowed prediction of a single band in the visible region of the UV-vis spectrum of this species, as also shown in Figure 2. This band had a wavelength of 624 nm and an oscillator strength of 0.16, both of which are in reasonable agreement with experimental data known for laccases (a band at ~600 nm with sulphur-to-copper charge-transfer character).
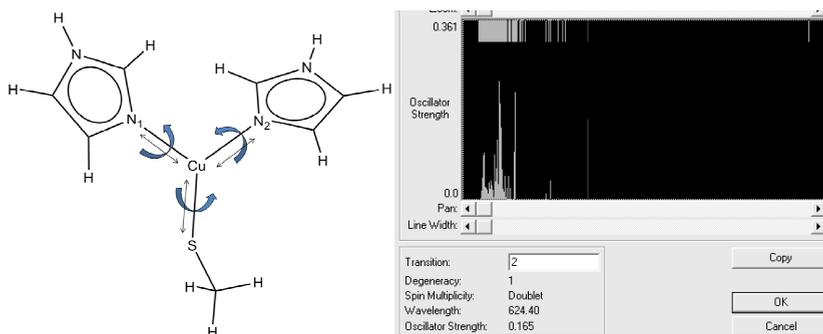
Figure 2. Model of the type 1 copper of laccases, employed in the present work. Arrows indicate bonds around/along which distortions were performed. Right panel: ZINDO/S-CI spectrum computed for this model prior to applying distortions

The 624 nm band shown in Figure 2 was found to arise dominantly from a single electronic transition. Namely, involved were the CI states 1 (with a contribution of 0.99689 from the ground state) and 3, with a contribution of -0.82884 from an excitation for which the two orbitals responsible for it are shown in Figure 3. These are the π and π* orbitals of the Cu-S bond.

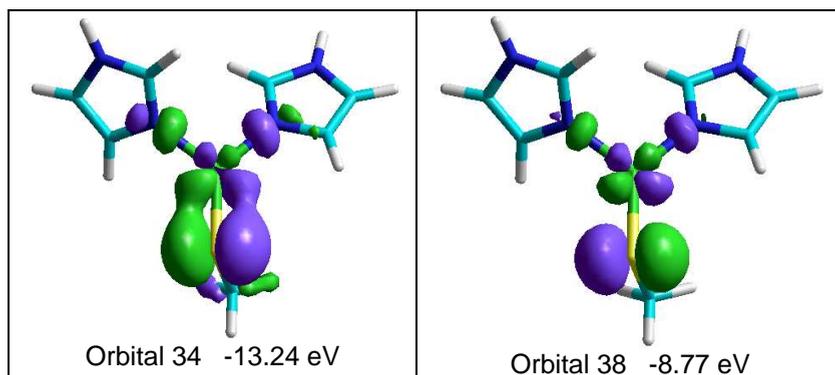Orbital 34   -13.24 eV

Orbital 38   -8.77 eV

Figure 3. The main orbitals responsible for the blue color of the laccase type 1 center, according to ZINDO/S-CI calculations.

The oscillator strength relates to the experimentally-measured extinction coefficient; values shown here between 0.01 and 0.1 equate to extinction coefficients in the range of thousands. Analyzing the effect of distortions on the 624-nm band of the type 1 copper site, we note that even 0.1-Å changes in the Cu-S bond length are predicted to lead to clearly detectable shifts in the maximum (up to 100 nm). In fact, elongation to 2.48 Å (a value not uncommon for other metal-sulphur bonds in proteins) would take the sulphur-to-copper charge transfer up by ~200 nm in energy, to a region already dominated by histidine-to-copper charge transfer bands from the other two ligands (not to mention overlapping absorbance of the same from the other three copper ions in the protein, all three of which have their own histidine ligands). Another distortion with a strong effect is rotation around the Cu-S bond; this was expected, since such rotation will affect the efficiency of the π interaction between the copper and the sulphur – an interaction which as shown above is essential for the 624-nm band computed in the initial structure. Thus, rotation to 51º (60º relative to the initial value) would take the charge-transfer band down in energy by ~ 200 nm, as would rotation to 231º - in both cases with a decrease in extinction coefficient. Rotation to 81º (only 30º relative to the initial structure) and to 351º are predicted to still allow for bands in the 600-nm region, only with extinction coefficients ~20 times lower than those of the initial structure.

Table 1. Computed absorption maxima (nm) for the type 1 laccase centre, as seen in a crystal structure of a "blue" site ("initial", pdb 1Q9O) and then subjected to compressions, elongations or rotations around bonds indicated in Figure 2. Numbers in the first column indicate the values taken by the parameters modified (bond lengths in Å, torsion angles in º). The initial values of these parameters were 2.18 Å Cu-S, 2.01 Å Cu-N1,1.94 Å Cu-N2, 111º CSCuN, 129º CN1CuS and 155º CN2CuS. Also shown are the energies (eV) of the two orbitals mainly responsible for the band computed to occur at 624 nm in the "initial "structure.; "n.a.": a single orbital displaying the given character was no longer identifiable.

	Absorption maxima	Oscillator strength	π	π*
intial	624	0.165	-13.243	-8.769
Cu-S 1.98	448	0.073	-13.787	-8.252
Cu-S 2.08	514	0.133	-13.528	-8.537
Cu-S 2.28	775	0.161	-12.977	-8.952
Cu-S 2.38	840	0.116	-12.788	-9.080
Cu-S 2.48	432	0.021	n.a.	-8.946
Cu-S 2.58	768	0.045	n.a.	-9.254
Cu-S 2.68	790	0.021	n.a.	-9.400
Cu-N11.91	621	0.163	-13.103	-8.618
Cu-N1 2.11	611	0.168	-13.368	-8.896
Cu-N1 2.21	617	0.152	-13.459	-9.018
Cu-N1 2.31	597	0.151	-13.552	-9.120
Cu-N1 2.41	594	0.142	-13.625	-9.227
Cu-N2 2.04	617	0.157	-13.371	-8.894
Cu-N2 2.14	591	0.156	-13.489	-8.998
Cu-N2 2.24	599	0.137	-13.566	-9.111
Cu-N2 2.34	572	0.135	-13.666	-9.200
Cu-N2 2.44	578	0.122	-13.724	-9.301
CSCuN 51	806	0.095	-13.017	-8.893
CSCuN 81	505, 507, 583	0.001, 0.005, 0.003	-12.802	-9.013
CSCuN 171	610	0.002	-12.598	-9.384
CSCuN 201	457, 519	0.013, 0.006	n.a.	-9.269
CSCuN 231	818	0.105	-12.949	-8.907
CSCuN 291	612	0.168	-13.267	-8.762
CSCuN 351	632	0.007	-12.809	-9.272
CN1CuS 9	627	0.158	-13.268	-8.780
CN1CuS 69	626	0.170	-13.248	-8.778
CN1CuS 189	640	0.143	-13.225	-8.767
CN1CuS 249	625	0.166	-13.246	-8.779
CN1CuS 309	616	0.169	-13.309	-8.788
CN2CuS 35	637	0.159	-13.205	-8.786
CN2CuS 95	627	0.173	-13.200	-8.764
CN2CuS 215	626	0.171	-13.235	-8.784
CN2CuS 275	622	0.180	-13.229	-8.781
CN2CuS 335	624	0.167	-13.256	-8.790

Perhaps expectedly, no distortion along the copper-imidazole bonds (be it rotation or elongation/compression) appears to cause dissolution of the 624-nm band – although shifts of up to ~50 nm in wavelength and ~10% in extinction coefficients are still seen, as illustrated in Table 1.

Table 2 shows DFT-derived relative energies entailed by some of the strongest distortions discussed in Table 1. It can be seen that all of these distortions are energetically feasible, costing at most 10 kcal/mol, and some less than 5 kcal/mol – all of which can easily be compensated by the protein environment. The initial structure seems to lie slightly higher in energy than two of the "distorted" ones; we interpret this as evidence for protein-induced sterical constraints on the active site geometry – unavoidable when one considers the need to fit the β carbon atoms of the aminoacid ligands, as well as the atoms connected to them.

Table 2 also shows DFT-derived partial atomic charges at the copper and at the three atoms coordinated to it do suffer well-defined changes in some of the distorted structures, both along the Cu-S and along the Cu-N distortions. In particular, the changes in spin density at the copper suggest that such distortions (some of them already shown to cause strong effects on the UV-vis spectra) would also be detectable in EPR, by way of hyperfine coupling constants. Conversely, changes in Cu-N bond lengths, which did not entail disappearance of the 624-nm band in UV-vis calculations, are shown to cause changes of up to 40% in spin density at the copper, again implying that such a distortion might be detectable with EP spectroscopy.

Table 2. DFT-derived relative energies and selected electronic structure parameters for the laccase type 1 site.

Structure	Rel E kcal/mole	Mulliken atomic charges//atomic spin densities			
		N1	N2	Cu	S
initial	+0.8	-0.09/0.04	-0.14/0.04	0.38/0.52	0.04/0.41
Cu-S 1.98	+7.7	-0.07/0.04	-0.13/0.04	0.34/0.47	0.04/0.45
Cu-S 2.38	+5.7	-0.12/0.03	-0.16/0.03	0.42/0.45	0.05/0.47
Cu-N1 1.91	+2.2	-0.08/0.05	-0.16/0.04	0.35/0.53	0.03/0.38
Cu-N1 2.41	+8.5	-0.19/0.02	-0.17/0.025	0.49/0.37	0.14/0.59
Cu-N2 2.44	+10.1	-0.12/0.03	-0.19/0.02	0.44/0.31	0.16/0.65
CSCuN 291	+0.5	-0.11/0.04	-0.11/0.04	0.37/0.50	0.05/0.42
CN1CuS 309	0.0	-0.11/0.03	-0.15/0.04	0.39/0.52	0.02/0.41
CN2CuS 335	+0.2	-0.07/-0.00	-0.14/0.04	0.34/0.52	-0.01/0.40

Table 3 shows geometrical parameters along the Cu-N and Cu-S bonds in known crystal structures of laccases. All of these structures represent "blue" laccases. It may be seen that none of these features a Cu-S bond at ~2.4-2.5 Å (a value which according to calculations would have turned it from blue to yellow), and that dihedral angles tend to be grouped at values of at most +/- 30⁰ relative to the average.

Table 3. Relevant geometrical parameters at intact type 1 copper centers in structures of laccases found in the Protein Data Bank.

pdb ID	Resolution (Å)	Cu-S	Cu-N 1	Cu-N 2	SCu-NC(1)	SCu-NC(1)
1A65	2.33	2.28	1.91	1.87	-19	-55
1GSK	1.70	2.20	2.05	2.06	-8	-51
1GW0	2.40	2.20	1.91	1.93	-2	-70
		2.22	1.93	1.92	-1	-73
1GYC	1.90	2.19	2.02	2.04	-5	-50
1HFU	1.68	2.19	2.07	2.03	-7	-45
1KYA	2.40	2.20	2.36	2.23	9	-36
		2.25	2.36	2.17	6	-38
		2.23	2.31	2.22	7	-36
		2.31	2.35	2.14	9	-37
1OF0	2.45	2.15	2.07	2.10	-7	-46
1UVW	2.45	2.11	2.11	2.23	-33	-12
1V10	1.70	2.17	2.14	2.15	-32	-56
1W6L	2.00	2.22	2.02	1.98	-16	-32
1W6W	2.20	2.16	2.02	2.07	-17	-44
1W8E	2.20	2.21	2.01	1.99	1	-47
2BHF	2.50	2.26	1.98	2.00	-5	-54
2FQD	2.40	2.22	2.17	2.31	-22	-40
2FQE	1.92	2.18	2.06	2.05	-13	-53
2FQF	2.00	2.22	2.03	2.13	-18	-28
2FQG	2.30	2.17	2.05	2.16	-6	-35
2H5U	1.90	2.31	2.00	1.99	13	-29
2HRG	1.58	2.15	2.06	2.03	3	-47
2HRH	2.60	2.14	2.09	2.09	-44	-52
2HZH	2.60	2.11	2.53	2.37	2	-49
2IH8	2.00	2.18	1.92	1.95	3	-59
		2.18	1.95	1.94	-2	-58
2IH9	2.00	2.16	1.94	1.91	-13	-46
		2.16	1.92	1.95	-8	-64
2Q9O	1.30	2.18	1.94	2.02	-12	-52
		2.15	2.00	2.00	-19	-46
2QT6	1.50	2.23	2.03	2.01	3	-47
		2.25	2.03	2.01	0	-47
2VDS	2.30	2.12	2.35	2.49	5	-45
2VDZ	1.70	2.22	2.10	2.11	7	-56
2WSD	1.60	2.27	2.03	2.01	-1	-51
2X87	2.00	2.27	2.01	2.01	2	-49

pdb ID	Resolution (Å)	Cu-S	Cu-N 1	Cu-N 2	SCu-NC(1)	SCu-NC(1)
2X88	1.80	2.21	2.08	2.07	-5	-54
2ZWN	1.70	2.24	2.08	1.99	-5	-62
		2.25	2.10	2.06	1	-67
		2.27	2.08	2.03	-2	-66
3CG8	2.68	2.20	2.01	1.89	-28	-48
		2.16	2.01	1.91	-28	-49
		2.19	1.97	1.97	-27	-52
3DIV	1.76	2.09	2.52	2.21	29	-46
3DKH	2.40	2.19	2.16	2.28	22	-60
		2.12	2.14	2.08	9	-54
3FPX	1.80	2.24	2.01	2.05	6	-38
3FU7	1.67	2.13	2.03	2.08	-16	-50
		2.19	2.00	2.05	-15	-54
3FU8	1.80	2.06	2.10	2.11	-26	-49
		2.13	2.04	1.99	-18	-51
3FU9	2.00	2.13	1.81	2.37	-10	-54
		2.01	2.06	2.28	-22	-85
3KW7	3.44	2.13	2.14	2.05	3	-71
		2.08	2.06	2.12	-8	-73
Average		2.20	2.07	2.08	-7	-50

CONCLUSIONS

Using computational methods, torsion and elongation-type deformations have been identified, which allow a "blue" tri-coordinated type 1 copper center to apparently lose its characteristic 600-nm band responsible for its blue color both by shifting it by more than 200 nm, and, in some cases, by decreasing the extinction coefficients. However, DFT calculations suggest that such distortions might also be detectable with EPR spectroscopy. Last but not least, we note that some of the distortions, while perfectly feasible in the small models employed in the present study, may well leave the site too exposed to a fourth ligand and thus may entail a lack of stability that would preclude facile experimental observation of such a distorted center.

EXPERIMENTAL SECTION

All data reported here are single-point energy calculations; attempts to optimize the geometry at the DFT level led to significant deviations from the initial conformations of the ligands. ZINDO/S-CI calculations were performed in the Hyperchem software package [12]. An excitation window of 20 eV was chosen; a ~ 600-nm band of reasonable intensity was found

to already be computed with windows as low as 14 eV, and its wavelength appeared to converge towards a stable value as the excitation window was gradually increased up to 20 eV. DFT calculations on selected structures were performed in the Gaussian09 software package [13], M062X/6-311+G** using the SCF=Tight option.

ACKNOWLEDGMENTS

REFERENCES

1. L. M. Mirica, X. Ottenwaelder, T. D. Stack, *Chemica. Reviews*, **2004**, *104*, 1013.
2. E. I. Solomon, U. M. Sundaram, T.E. Machonkin, *Chemical Reviews*, **1996**, *96,* 2563.
3. N. N. Pozdnyakova, J. Rodakiewicz-Nowak, O. V. Turkovskaya, *Journal of Molecular Catalalysis B*: **2004**, *30*,19.
4. G. Palmieri, P. Giardina, C. Bianco, A. Scaloni, A. Capassoi, G. Sannia. *Journal of Biological Chemistry*, **1997**, *272*, 31301.
5. A. A. Leontievsky, T. Vares, P. Lankinen, J. K. Shergill, N. M. Pozdnyakova, N. Kalkkinen, L. A. Golovleva, R. Cammack, C. F. Thurston, A. Hatakka. *FEMS Microbiological Letters*, **1997**, *156*, 9.
6. A. A. Leontievsky, N. M. Myasoedova, B. P. Baskunov, N. N. Pozdnyakova, T. Vares, N. Kalkkinen, A. I. Hatakka, L. A. Golovleva, *Biochemistry (Moscow),* **1999**; *64*, 1150.
7. D. A. Wood, *Journal of General Microbiology*, **1980**, *117*, 327–338.
8. W. A. Edens, T. Q. Goins, D. Dooley, J. M. Henson, *Applied and Environmental Microbiology,* **1999**, *65*, 3071.
9. O. M. H. Vries, W. H. C. F. Kooistra, G. H. Wessels, *Journal of General Microbiology*, **1986**, *132*, 2817.
10. K. Min, Y. H. Kim, Y. W. Kim, H. S. Jung, Y. C. Hah, *Archives of Biochemistry and Biophysics*, **2001**, *392*, 279.
11. A. C. Moț, M. Pârvu, G. Damian, R. Silaghi-Dumitrescu, *manuscript in preparation.*
12. Hyperchem(TM) Molecular Modelling System, Release 5.01 for Windows, Hypercube, Inc. 1998
13. M. J. Frisch et al, Gaussian 09; Gaussian, Inc., Wallingford CT, 2004

ADSORPTION AND RELEASE STUDIES OF TETRACYCLINE FROM A BIOACTIVE GLASS

EMILIA VANEA[a], SIMONA CAVALU[b], FLORIN BĂNICĂ[b], ZSOLT BENYEY[a], GÜLTEKIN GÖLLER[c],VIORICA SIMON[a,*]

ABSTRACT. This study aims to characterize a bioactive glass and to evaluate its ability to adsorb and release antimicrobial agents like tetracycline. Tetracycline adsorption and release were investigated using Fourier transform infrared spectroscopy, X-ray photoelectron spectroscopy and scanning electron microscopy. The amounts of withdrawn solution, after drug release, were analyzed by differential pulsed voltammetry and UV-Vis spectroscopy. The investigated glass system promotes an efficient response concerning the tetracycline loading and release in terms of drug delivery system for biomedical applications.

Keywords: tetracycline, XPS, SEM, FTIR, UV-vis, bioactive glass

INTRODUCTION

Bioactive glasses have achieved great application success in orthopaedic surgery and dentistry [1]. One major problem frequently associated with implants is the incidence of the osteomielitis that may lead to implant failure. Because of the poor blood circulation in osseous defect sites, antimicrobial drugs must be supplied directly to the affected regions [2], in this way the adverse effects of the systemic administration are avoided and a higher concentration of antimicrobial agent reaches the affected site [1]. In order to diminish the bacteriological risk associated with the implant materials, the addition of an antimicrobial drug such as tetracycline can be considered due to its broad antibiotic spectrum together with bone resorption inhibition and anti-inflammatory action [3-5]. This antibiotic can thus be used to improve bone growth and regeneration in the treatment of bone defects.

The objective of this study was to characterize a bioactive glass and to evaluate its ability as a controlled release system of tetracycline. For this

---

* Corresponding author: viosimon@phys.ubbcluj.ro
[a] *Babes-Bolyai University, Faculty of Physics & Institute of Interdisciplinary Research in Bio-Nano-Sciences, Kogalniceanu 1, 400084 Cluj-Napoca, Romania*
[b] *University of Oradea, Faculty of Medicine and Pharmacy, 1 Decembrie 10, 410073 Oradea, Romania*
[c] *Istanbul Technical University, Metallurgical and Materials Engineering Department, 34469 Istanbul, Turkey*

purpose we used different spectroscopic methods like Fourier transform infrared spectroscopy, X-ray photoelectron spectroscopy, UV-Vis spectroscopy, as well as scanning electron microscopy, and differential pulse voltammetry.

RESULTS AND DISCUSSION

SEM images of tetracycline free sample and after drug uptake (Figure 1) show that the surface gets a fuzzy appearance associated to tetracycline adsorption [2].
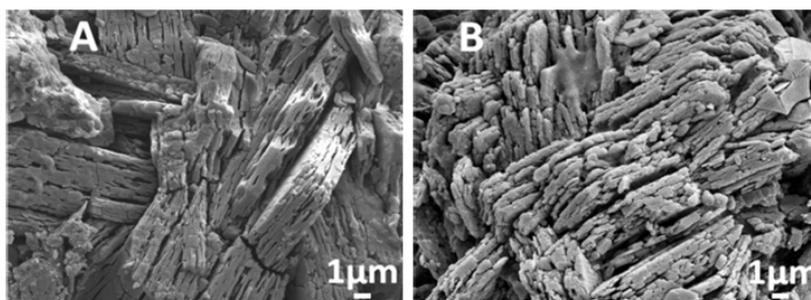

Figure 1. SEM images of bioactive glass before (A) and after (B) tetracycline loading.

XPS spectra (Figure 2) recorded for pure tetracycline, for free tetracycline and tetracycline loaded samples both before and after immersion in SBF aimed to determine the composition of the outermost layer of the investigated bioactive glass, based on the fact that XPS is a highly surface-specific *technique* with a typical analysis depth of 5—10 nm [8]*.* The results are presented in Table 1.

Both carbon and nitrogen can be used as markers of tetracycline adsorption [9] because the two elements are not present in glass, even though carbon contamination is unavoidable and unpredictable in practice. Table 1 shows that the level of nitrogen was almost zero for unloaded sample and increased significantly for the tetracycline incubated one. The elemental analysis also indicates a remarkable increase of carbon content after incubation, content close to the value obtained for tetracycline itself, which proves tetracycline adsorption. The level of the elements entering the glass composition, i.e. Si, Ca, P, Na and O, decreases after immersion of the bioactive glass in both SBF and tetracycline solution, but more drastically in tetracycline solution, which also denotes an advanced coverage of the glass surface with tetracycline.

The N 1s, C1s and O 1s high resolution XPS spectra of (Figure 3) strengthen these results. One observes the high intensity of the nitrogen and carbon spectra (Figs. 3Ad and 3Bd) recorded from the tetracycline loaded glass, according to the tetracycline corresponding ones (Figs. 3Ac and 3Bc). The O 1s high resolution spectra (Figure 3C) show that before immersion
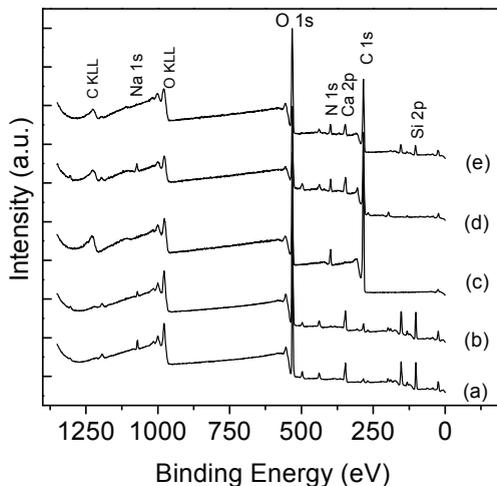
Figure 2. XPS survey spectra of glass (a), glass immersed in SBF (b), tetracycline (c), and glass with tetracycline (d) and of glass after 96 hr immersion in SBF for tetracycline release (e).

Table 1. Surface chemical composition before and after immersion of the bioactive glass (BG) in tetracycline (TCL) solution and after 96 hr immersion in SBF.

Sample	Elemental composition (at %)						
	C	N	O	Si	Ca	P	Na
BG	5.6	-	53.1	32.6	5	2.3	1.4
BG/SBF	8.8	0.5	52.3	30.8	4.7	2.1	0.8
TCL	72.9	5.4	21.7	-	-	-	-
BG/TCL	65.7	5.3	23.6	-	3.2	1	1.2
BG after TCL release	54.4	4.2	30.1	8.3	2.1	0.9	-

in tetracycline solution the O 1s photoelectron peak consists of a component at 532.4 eV, related to the bridging oxygen atoms implied in the structural units of the glass [10] but they could be assigned also to hydroxyl groups present on the glass surface due to the chemisorbed water molecules from environmental moisture [11]. After immersion in tetracycline solution, the O 1s peak decreases in intensity and shifts to lower binding energy and the amount recorded is comparable to the value recorded for pure tetracycline which is less rich in oxygen atoms.

After the release process the amounts of C, N slightly decrease while O increases together with silica which is revealed at the surface of the sample again. This means the tetracycline was released in great amount, but significant quantity is still detected at the surface of the glass, which can be considered irreversibly bound.
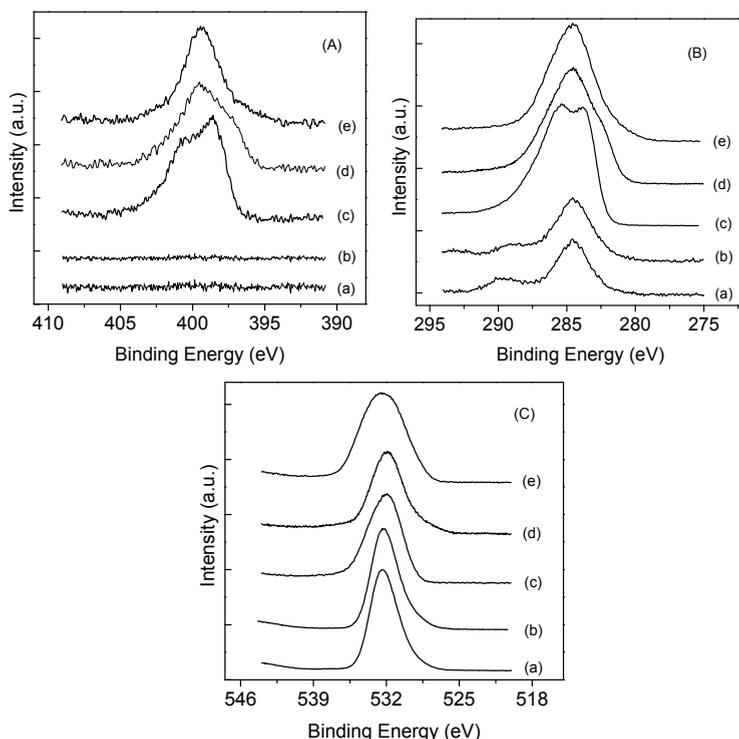
Figure 3. XPS high-resolution N 1s (A), C 1s (B), O 1s (C) spectra of glass (a), glass immersed in SBF (b), tetracycline (c), glass with tetracycline (d), and of glass after 96 hours immersion in SBF for tetracycline release (e).

The analysis of FTIR spectra (Figure 4) recorded from glass and tetracycline, as well as from glass immersed in SBF, tetracycline loaded glass and after 7 days glass immersion in SBF for tetracycline release brings additional information on the glass/tetracycline interaction. The absorption bands at 1418 and 1470 cm^{-1} can be attributed to carbonate impurities present in the samples and peaks at 1200, 1090, 800, 466 cm^{-1} are associated to the vibration of Si-O-Si bonds in the glass network [2]. The absorption band around 960 cm^{-1} is due to the Si-OH vibrations [12]. The doublet at 606 and 564 cm^{-1} is assigned to bending vibrations of PO_4^{3-} ions [13]. The FTIR spectra of tetracycline and tetracycline-loaded glass are very similar showing the same amide I band around 1600 cm^{-1} [14, 15], a proof of tetracycline adsorption in great amount. The release of tetracycline after 96 hours immersion in SBF solution under dynamic condition is evidenced by reappearance of absorption bands specific to glass network like the one present at 1090 cm^{-1}. The carbonate specific peak is also well evidenced. The great intensity of the peak at 1600 cm^{-1} is explained by the presence of water in great amount considering the sample cannot be dried at high temperature to not affect the tetracycline structure.
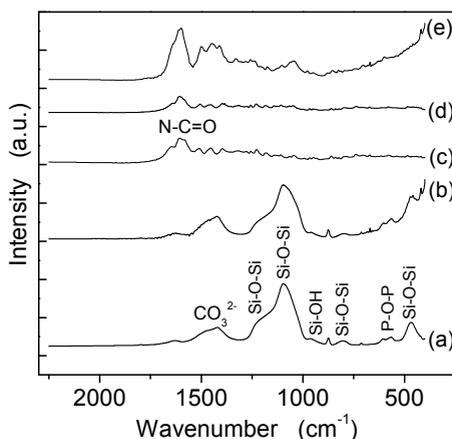
Figure 4. FT-IR spectra of glass (a), glass immersed in SBF (b), tetracycline (c),
glass with tetracycline (d) and of glass after 96 hours immersion
in SBF for tetracycline release (e).

Ultraviolet-visible absorption spectroscopy (UV-vis) was used to estimate the amount of tetracycline released following the evolution of the absorption peak at 269 nm [1]. The drug release is found to be fast for the initial 2 hours, gets slower for the next 5 and 24 and finally the release becomes constant for longer periods of time (Figure 5).

The tetracycline release profile in SBF was also obtained by determining the tetracycline concentrations (Table 2) using differential pulsed voltammetry (DVP) curves (Figure 6).

Figure 5. UV-vis spectra recorded after 2 (a), 5 (b), 24 (c), 48 (d)
and 96 (e) hours of tetracycline release from glass sample.

Figure 6. DPV curves obtained after 2 (a), 5 (b), 24 (c), 48 (d)
and 96 (e) hours of tetracycline release from glass sample.

Table 2. Tetracycline concentration obtained by pulsed voltammetry.

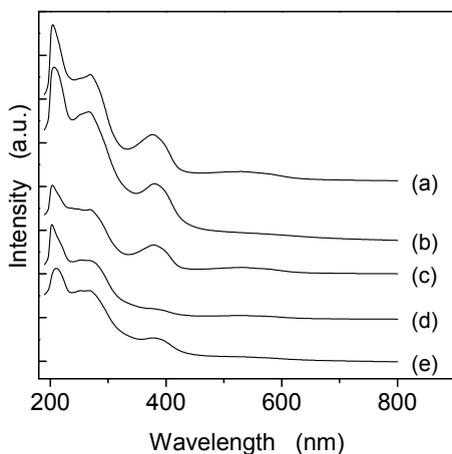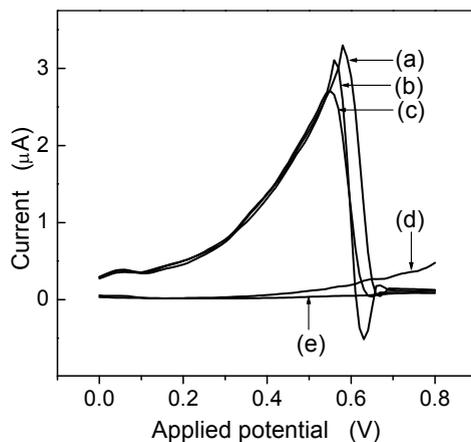| Time (hr)	2	5	24	48	96
Current intensity (µA)	3.28	3.11	2.73	0.25	0.15
Concentration (µM)	0.71	0.61	0.37	0.04	0.02

The data obtained by this technique show a constant decrease in the tetracycline concentration in the first 24 hours, followed by very low release values in the next periods. Because the concentrations of tetracycline released from a controlled delivery system [16] are reported to have reached steady-state levels within 2-3 days, the low values determined after 2 and 4 days (Table 2) are most likely steady-state concentrations.

CONCLUSIONS

The results obtained in the present study show that the investigated bioactive glass can be loaded with tetracycline that is released to the highest degree in the first 24 hours. Even though the drug concentration found in the solutions after 96 hours is highly diminished, a great amount of tetracycline is still detected on the sample surface, suggesting that a part of the drug is strongly attached to the bioactive glass and could act for longer time as antimicrobial agent.

MATERIALS AND METHODS

The bioactive glass with the composition $45SiO_2 \cdot 24.5CaO \cdot 24.5Na_2O \cdot 6P_2O_5$ (mol %) was synthesized by means of sol-gel method using as starting materials tetraetoxisilan (TEOS), $Ca(NO_3)_2 \cdot 4H_2O$, $(NH_4)_2 \cdot HPO_4$ and

Na_2CO_3 as SiO, CaO, P_2O_5 and Na_2O precursors, respectively. After maturation at room temperature for 30 days, the sample was heat treated at 310°C for 1 hour.

Tetracycline adsorption was carried out by incubating the sample in phosphate buffered saline (PBS) enriched with tetracycline (7 mg/ml). The sample was analysed after immersion at 37°C for about 6 hours in order to establish the amount of adsorbed tetracycline.

For delivery assays, 35 mg tetracycline loaded glass was individually immersed in 10 ml simulated body fluid (SBF) prepared according to Kokubo protocol [6], pH 7.4, and kept at 37°C for 2, 5, 24, 48 and 96 hours in Falcon tubes, with continuous agitation. After each period, the SBF solution was completely removed from the tube for analysis and replaced by another freshly prepared solution. The same amount of glass without tetracycline was immersed in SBF for a total time of 96 hr and the SBF was replaced according to the immersion periods of time previously mentioned. The amounts of withdrawn solution were analyzed by UV-vis Spectroscopy and Differential Pulsed Voltammetry (DPV). The concentration of the released tetracycline was monitored in a three electrode configuration TRACELAB 150, using a hanging mercury drop electrode [7].

Sample characterization was made using Scanning Electron Microscopy (SEM), Fourier Transform Infrared Spectroscopic (FTIR) and X-ray Photoelectron Spectroscopy (XPS).

SEM images before and after tetracycline loading were recorded using a JEOL JSM 7000F Scanning Electron Microscope. XPS measurements were performed using a SPECS PHOIBOS 150 MCD system equipped with monochromatic Al-K_α source (250 W, hv=1486.6 eV), hemispherical analyser and multichannel detector. The vacuum in the analysis chamber during the measurements was in the range of 10^{-9}-10^{-10} mbar. The binding energy scale was charge referenced to the C 1s at 284.6 eV. The FTIR spectra were recorded in reflection configuration by a Jasco IRT-5000 FT-IR spectrometer in the range 4000-650 cm^{-1} with a resolution of 4 cm^{-1}.

ACKNOWLEDGMENTS

REFERENCES

1. A.L. Andrade, D.M. Souza, W.A. Vasconcellos, R.V. Ferreira, R.Z. Domingues, *Journal of Non-Crystalline Solids*, **2009**, *355*, 811.

2. A.L Andrade, D. Manzi, R.Z. Domingues, *Journal of Non-Crystalline Solids*, **2006**, *352*, 3502.

3. Z.R. Domingues, M.E. Cortes, T.A. Gomesa, H.F. Diniz, C.S. Freitas, J.B. Gomes, A.M.C. Fariac, R.D Sinisterra, *Biomaterials,* **2004***, 25*, 327.

4. U.M.E. Wikesjo, P.J. Baker, L.A. Christersson, R.J. Genco, R.M. Lyall, S. Hic, R.M. Diflorio, V.P. Terranova, *Journal of Periodontal Research*, **1986**, *21*, 322.

5. B.N.A. Vandekerckhove, M. Quirynen, D. van Steenberghe, *Journal of Periodontology*, **1997**, *68*, 353.

6. T. Kokubo, H. Kushitani, S. Sakka, T. Kitsugi, T. Yamamuro, *Journal of Biomedical Materials Research*, **1990**, *24*, 721.

7. Y. Ni, S. Li, S. Kokot, *Food Chemistry*, **2011**, *124*, 1157.

8. M.I. Goller, C. Barthet, G.P. McCarthy, R. Corradi, B.P. Newby, S.A. Wilson, S.P. Armes, S.Y. Luk, *Colloid and Polymer Science*, **1998**, *276*, 1010.

9. E. Vanea, V. Simon, *Applied Surface Science*, **2011**, *257*, 2346.

10. S. Simon, R.V.F. Turcu, T. Radu, M. Moldovan, V. Simon, *Journal of Optoelectronics and Advanced Materials*, **2009**, *11*, 1660.

11. G. Polzonetti, M.V. Russo, A. Furlani, G. Iucci, *Chemical Physics Letters*, **1991**, *185*, 105.

12. H. Yoshino, K. Kamiya, H. Nasu, *Journal of Non-Crystalline Solids*, **1990**, *126*, 68.

13. I. Rehman, W. Bonfield, *Journal of Materials Science: Materials in Medicine*, **1997**, *8*, 1.

14. G. Reiter, N. Hassler, V. Weber, D. Falkenhagen, U.P. Fringeli, *Biochimica et Biophysica Acta*, **2004**, *1699*, 253.

15. G. Falini, E. Foresti, I.G. Lesci, B. Lunelli, P. Sabatino, N. Roveri, *Chemistry - A European Journal*, **2006**, *12*, 1968.

16. L. Olanoff, J.M. Anderson, *Journal of Pharmaceutical Science*, **1979**, *68*, 1151.

THE RHEOLOGICAL STUDY OF SOME SOLUTIONS BASED ON SURFACE-ACTIVE AGENTS (II)

ANDRA TĂMAŞ[a], MARTIN VINCZE[b]

ABSTRACT. The paper presents the rheological behavior study of some solutions based on surface-active agents used as auxiliaries in oil extraction technology. The influence of surfactants' structure and concentration was determined, as well as that of temperature, on the rheological behavior, by setting the dependence between the shear stress τ and the shear rate $\dot{\gamma}$. The analysis of dependence $\tau = f(\dot{\gamma})$ demonstrates that the solutions studied present non-Newtonian behavior (yield-pseudoplastic and simple pseudoplastic).

Keywords: *Yield-pseudoplastic behavior, shear rate, shear stress, surfactant*

INTRODUCTION

In the oil extraction process, after a certain period of operation, oil-wells depletion occurs, that means a drasting drop in productivity. The phenomenon is mostly significant in the case of the deposits whose structure is based on clays [1]. In order to increase the layer porosity and permeability, a porous material (usually sand of a certain granulation) is introduced in the deposit through the existing cracks. The sand spreading must be done by means of a fluid carrier. The first types of fluid carriers were hydrogels (hydroxyethyl-cellulose, carboxymethylcellulose). Subsequently, viscoelastic solutions (with cationic surfactants content) were used. Surfactant molecules in solution can self-assemble into aggregates (micelles). The shape and size of micelle depend on the molecular structure of the surfactant, nature of solvent and additives and their molar composition.

Wormlike micelles are large one-dimensional aggregates and behave like a semi-flexible polymeric chain. Their rheological properties in aqueous solutions have a remarkable resemblance to those of polymers in a good solvent [1]. The addition of inorganic salts decreases the electrostatic interactions between monomers in the micelle, which induces micellar growth and viscosity increment [1].

---

[a] *Universitatea "Politehnica" din Timişoara, Facultatea de Chimie Industrială şi Ingineria Mediului, P-ţa Victoriei 2, RO-300006 Timişoara, România, andra.tamas@chim.upt.ro*
[b] *vinczemartin@hotmail.com*

The main characteristics of the surface-active agents (A, B, VB, VAD) are found in Table 1, and the composition of the solutions with A and B content is presented in Table 2. The composition of the solutions with VAD and VB content can be expressed as PA_{i-j}, where i is the wt % of VAD and j is the wt % of VB (For example: PA$_{3-9}$ contains 3%VAD+9% VB + 88% water).

Table 1. The properties of the surface-active agents used

Symbol	Type	Active substance %	Molecular weight, $kg \cdot kmol^{-1}$	pH of 1% aq. solution
VB	amphiphilic	30	355	7÷7.5
VAD	weakly cationic	100	488	-
A	cationic (alkyl trimethyl NH$^+_4$ chloride)	30	263	-
B	aromatic carboxylic acid (Na salt)	40	180	-

Table 2. The composition of solutions with A and B content

Symbol	Composition, wt %
PC$_1$	1% B + 99% sol.1*
PC$_2$	2% B + 98% sol.1*
PC$_3$	3% B + 97% sol.1*
PC$_4$	4% B + 96% sol.1*
PC$_5$	5% B + 95% sol.1*

* The composition of sol. 1 is (wt %): 88.24% water + 9.8% A + 1.96% NaCl.

The preparation of solutions was done by dispersing water under intense stirring in surfactants mixture (VAD+VB and A+B, respectively) at room temperature (t~25°C).

The rheological characterization of the solutions prepared was carried out using rotational viscometer Rheotest-2, under thermostatic conditions. It was followed the establishment of rheological relations $\tau = f(\dot{\gamma})$ where τ and $\dot{\gamma}$ are the shear stress and the shear rate, respectively, as well as the calculation of the activation energy of viscous flow E_a.

The characterization of liquids flow in ring-shaped spaces is expressed using the Taylor-Reynolds number, Ta_{Re} which depends on the geometry of the ring-shaped space (radii of the two cylinders, r_o, r_i), shear rate $\dot{\gamma}$ or revolution n, liquid density ρ and apparent viscosity η_a [2]:

$$Ta_{Re} = \frac{2 \cdot \pi \cdot n \cdot \left(r_o^2 - r_i^2\right) \cdot \rho}{\eta_a} \qquad (1)$$

$$\dot{\gamma} = \frac{2 \cdot \pi \cdot n \cdot r_o^2}{r_o^2 - r_i^2} \qquad (2)$$

RESULTS AND DISCUSSION
1. The temperature influence

The influence of temperature on the rheological behavior was determined for samples PA_{2-8}, $PA_{2.5-8}$, and the series PC_1-PC_5. In Figure 1, dependence $\tau = f(\dot{\gamma})$ is shown, at different temperature values, for $PA_{2.5-8}$.
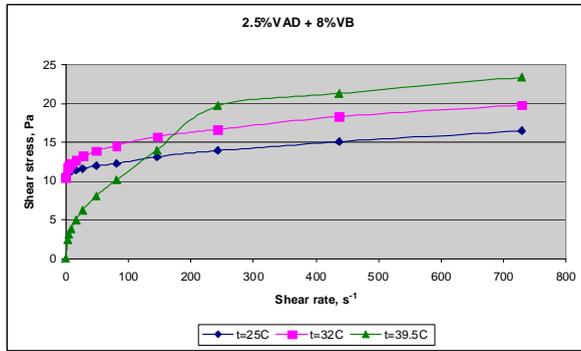
Figure 1. Dependence $\tau = f(\dot{\gamma})$ for $PA_{2.5-8}$ at different temperatures

The rheological equations for samples PA_{2-8} and $PA_{2.5-8}$ are presented in Tables 3 and 4.

Table 3. Rheological equations for PA_{2-8} sample at various temperatures

Temperature, ⁰C	Equation
32	$\tau = 13.9 + 0.78 \cdot \dot{\gamma}^{0.263}$
39.5	$\tau = 12.8 + 0.47 \cdot \dot{\gamma}^{0.553}$

Table 4. Rheological equations for $PA_{2.5-8}$ sample at various temperatures

Temperature, ⁰C	Equation
25	$\tau = 10.8 + 0.13 \cdot \dot{\gamma}^{0.575}$
32	$\tau = 10.4 + 0.86 \cdot \dot{\gamma}^{0.363}$
39.5	$\tau = 1.5 \cdot \dot{\gamma}^{0.435}$

From the analysis of rheological equations can be observed the non-Newtonian behavior with yield point τ_0, similar to the yield-pseudoplastic fluids, with flow exponent $n < 1$. Also, for the samples with $\tau_0 \neq 0$, it is observed that the temperature increasing leads to the increase of the shear stress values, with preservation of non-Newtonian behavior.

A particular situation presents $PA_{2.5-8}$ sample to t= 39.5°C, to which is noticed the shape curve change with the shear rate increasing. For the presumptive inflection point corresponding to $\dot{\gamma} = 215.7\,s^{-1}$ and $\tau = 19.5\,Pa$ the apparent viscosity is obtained $\eta_a = \tau/\dot{\gamma} = 0.09\,Pa \cdot s$ and, taking into account the geometrical dimensions of S/S_1 system, the calculated Ta_{Re} value is 0.75 (laminar domain being for $Ta_{Re} \leq 60$) [3].

In Figures 2 and 3 is shown the $\tau = f(\dot{\gamma})$ dependence for PC_1 and PC_5 solutions at different temperature values, and in Table 5 are the obtained rheological equations.
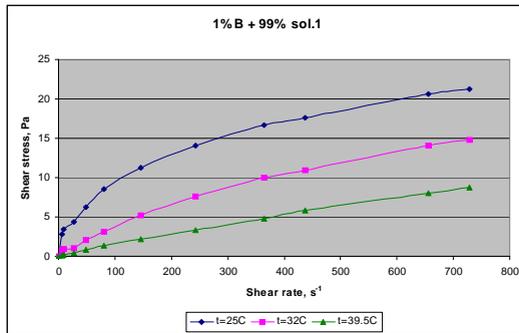

Figure 2. Dependence $\tau = f(\dot{\gamma})$ for sample PC_1
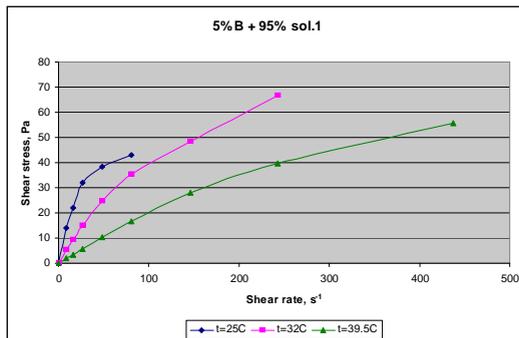
Figure 3. Dependence $\tau = f(\dot{\gamma})$ for sample PC_5

Table 5. Rheological equations for PC$_{1-5}$ solutions

Temperature, °C	Equation		
	PC$_1$	PC$_4$	PC$_5$
25	$\tau = 1.4 \cdot \dot{\gamma}^{0.414}$	$\tau = 19.7 \cdot \dot{\gamma}^{0.185}$	$\tau = 6.6 \cdot \dot{\gamma}^{0.439}$
32	$\tau = 0.25 \cdot \dot{\gamma}^{0.618}$	$\tau = 3.9 \cdot \dot{\gamma}^{0.500}$	$\tau = 2.1 \cdot \dot{\gamma}^{0.630}$
39.5	$\tau = 0.04 \cdot \dot{\gamma}^{0.802}$	$\tau = 0.55 \cdot \dot{\gamma}^{0.810}$	$\tau = 0.74 \cdot \dot{\gamma}^{0.715}$

Through the measurements achievement at different temperatures it was possible to establish the dependence $\ln \tau = f(1/T)$ and to calculate the E_a values. For PC$_{1-5}$ solutions, the E_a changes with the content of surfactant B is shown in Figure 4. It is observed that there is a range of concentrations at which E_a has minimum values minimum values of $(25 \div 65)\, kJ \cdot mol^{-1}$.
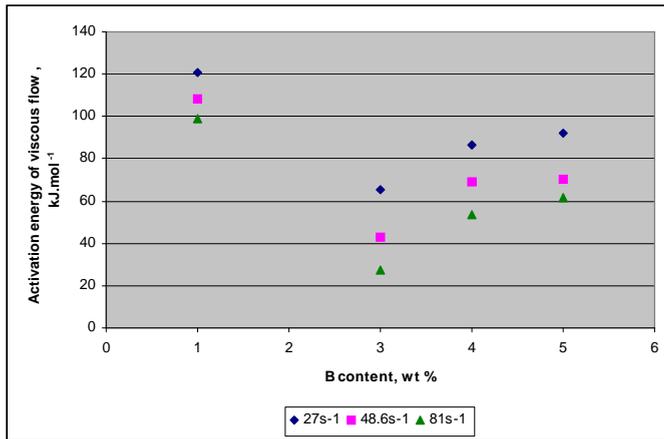
Figure 4. The activation energy evolution for PC$_{1-5}$ samples

2. The preservation time influence

That influence was studied for sample PC$_2$ at 32°C, and $\tau = f(\dot{\gamma})$ dependence is presented in Figure 5. It can be observed that preservation does not change the non-Newtonian behavior but increases the shear stress values.
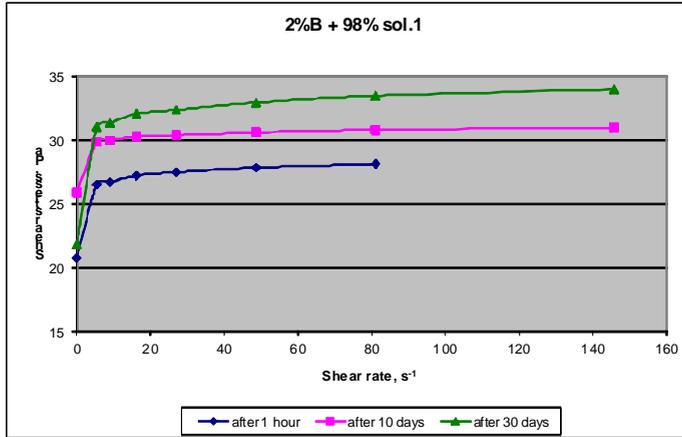
Figure 5. Dependence $\tau = f(\dot{\gamma})$ for sample PC$_2$ (t=32°C)

3. The influence of the amphiphilic surfactant VB

For samples PA$_{3\text{-}9}$, PA$_{3\text{-}10}$ and PA$_{3\text{-}12}$, in Figure 6, is shown the $\tau = f(\dot{\gamma})$ dependence, and the evolution of apparent viscosity with amphiphilic surfactant content is shown in Figure 7. From the obtained rheological equations (Table 6) is observed the non-Newtonian behavior specific to yield-pseudoplastic fluids, and the increase of apparent viscosity with increasing the concentration of amphiphilic component, respectively.
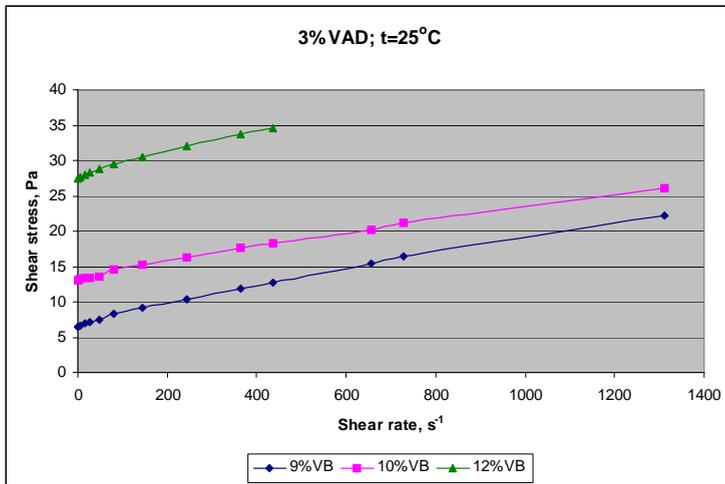
Figure 6. Dependence $\tau = f(\dot{\gamma})$ for PA$_{3\text{-}9}$, PA$_{3\text{-}10}$ and PA$_{3\text{-}12}$
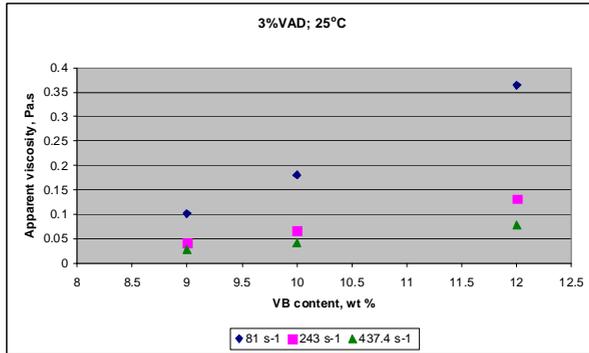
Figure 7. The apparent viscosity vs. the VB concentration

Table 6. Rheological equations for PA$_{3-9}$, PA$_{3-10}$ and PA$_{3-12}$ solutions (t =25°C)

VB content, wt%	Equation
9	$\tau = 6.5 + 0.040 \cdot \dot{\gamma}^{0.824}$
10	$\tau = 13.1 + 0.034 \cdot \dot{\gamma}^{0.830}$
12	$\tau = 27.4 + 0.081 \cdot \dot{\gamma}^{0.740}$

The evolution of apparent viscosity of the solutions with 2%VAD and different percentages of the VB (PA$_{2-7}$ and PA$_{2-10}$) is shown in Figure 8.
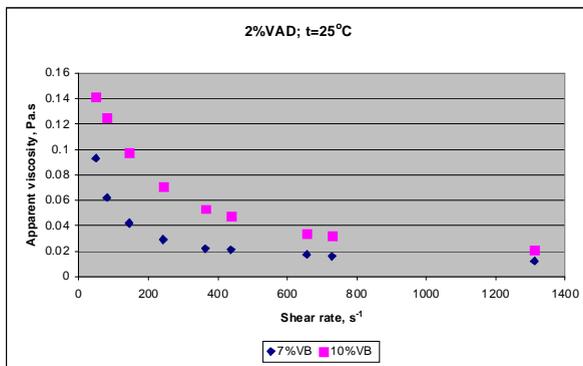
Figure 8. The apparent viscosity vs. shear rate

The obtained viscosity curves, with apparent viscosity decreasing with the increase of shear rate, show specific pseudoplastic behavior. It is also found in this case that increase of VB amphiphilic surfactant concentration

increases the apparent viscosity. Also, at the same temperature, the solutions with 3%VAD have apparent viscosities higher than 2% VAD samples.

4. The influence of weakly cationic (VAD) or anionic (VA) surfactant

The evolution of apparent viscosity of samples with 10%VB and different percentages of VAD (PA_{2-10}, $PA_{2.5-10}$, PA_{3-10}) is shown in Figure 9.
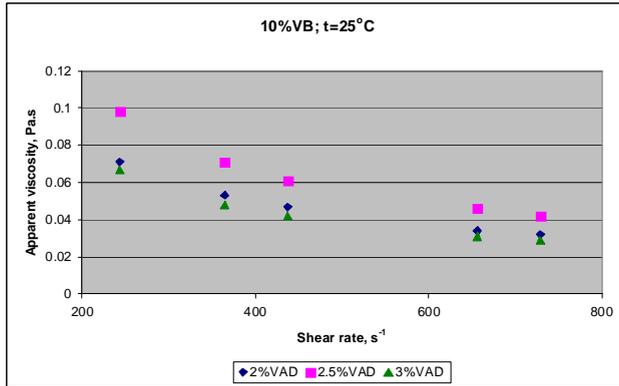
Figure 9. The apparent viscosity vs. shear rate

In Figure 10 is shown the shear stress dependence of shear rate for solutions containing 10%VB and 3%VA (P_{42}) [4] and 3%VAD (PA_{3-10}), respectively, at two temperatures. The obtained rheological equations are shown in Table 7. The non-Newtonian behavior is maintained, regardless of surfactant type (anionic or weakly cationic), but in the case of cationic one the shear stress increases with temperature increasing.
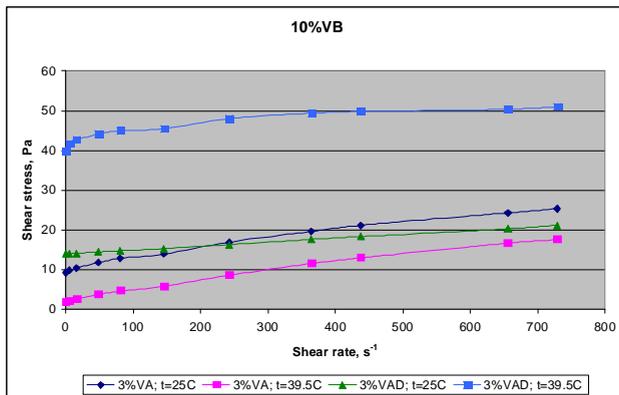
Figure 10. Dependence $\tau = f(\dot{\gamma})$ for samples P_{42} and PA_{3-10}

Table 7. Rheological equations for P_{42} and PA_{3-10}

Surfactant	Equation	
	25˚C	**39.5˚C**
3% VA	$\tau = 9.2 + 0.16 \cdot \dot{\gamma}^{0.707}$	$\tau = 1.7 + 0.09 \cdot \dot{\gamma}^{0.788}$
3% VAD	$\tau = 13.9 + 0.01 \cdot \dot{\gamma}$	$\tau = 39.7 + 1.1 \cdot \dot{\gamma}^{0.356}$

CONCLUSIONS

The rheological behavior of solutions based on active-surface agents was studied, monitoring the influence of the nature and concentration of surfactants, temperature and preservation time.

Specific rheological equations $\tau = \tau_0 + K \cdot \dot{\gamma}^n$ were established, showing non-Newtonian (pseudoplastic and yield-pseudoplastic) behavior of analyzed samples.

Increasing temperature and preservation time does not change the non-Newtonian nature of $\tau = f(\dot{\gamma})$ dependence.

EXPERIMENTAL SECTION

Determinations were made using the viscometer Rheotest-2 with the system vat-drum S/S_1, in temperature range 25÷40°C.

The samples were analyzed after one hour of preparation. Conservation of these solutions, at room temperature (~25°C), for 2-3 months has not led to significant changes in rheological properties.

REFERENCES

1. D-G Choi, W-J Kim, S-M Yang, *Korea-Australia Rheological Journal,* **2000,** *12,* 143.
2. N.Borş, "Contribuţii la studiul influenţei unor substanţe chimice asupra îmbunătăţirii curgerii lichidelor", Teză de doctorat, Univ."Politehnica" Timişoara, **2010.**
3. N.Borş, A. Tămaş, *Studia Univ. Babes-Bolyai Seria Chemia,* **2010**, *55(3),* 139. A.Tămaş, M. Vincze, *Studia Univ. Babes-Bolyai Seria Chemia*, **2011** *(submitted).*

EFFECT OF CATALYST LAYER THICKNESS
ON GROWTH OF CVD DIAMOND

FATEMEH SHAHSAVARI[a, b], MAHMOOD GHORANNEVISS[a, †],
ZAHRA KHALAJ[a], MIRCEA V. DIUDEA[c]

ABSTRACT. Tungsten Nanocrystalline Diamond (NCD) films were grown on silicon substrates by Hot Filament Chemical Vapor Deposition (HFCVD) method using three different catalyst layer thicknesses. At first, the silicon substrates are ultrasonically cleaned in acetone; ethanol and demonized water for 15 minutes in each step to remove organic contaminants, then gold layers were deposited on silicon substrate by DC magnetron sputtering. Nitrogen gas 80 Sccm was introduced into HFCVD chamber for 40 minutes and the growing process were done in a mixture of CH_4/H_2 for 75 minutes. Crystal structure investigations were carried out by X-ray diffraction (XRD) measurements for deposited films. The XRD spectra of the NCD films demonstrated different diffraction peaks for different catalyst layer thicknesses that confirmed the presence of crystalline diamond. Morphology of the diamond films were investigated by scanning electron microscopy. The thickness of the gold nanolayer of each substrate was measured by DEKTAK surface profile measuring system.

Keywords: Nanocrystalline diamond films, Catalyst, Hot filament CVD, Etching.

Introduction

Synthesis of diamond films by chemical vapor deposition (CVD) have been extensively studied during the last decades because of their unique properties and potential applications in mechanics, optics and electronics [1-7]. Diamond films could be produced by various chemical vapor deposition (CVD) methods, including microwave plasma [8-12], hot filament [13-17], arc plasma jet system [18-20] and magnetically enhanced radio frequency assisted plasma [21-22] methods. Among these methods, hot filament chemical vapor deposition (HFCVD) has been one of the most common methods for synthesis of diamond films.

[a] *Plasma Physics Research Center, Science and Research Branch, Islamic Azad University,Tehran,Iran.P.O.Box:14665/678*
[b] *Eghbal Techno-Center, Yazd Scientific and Technology Park,Yazd, Iran*
[c] *Faculty of Chemistry and Chemical Engineering, Babes-Bolyai University, Cluj, Romania*
[†] *E-mail address: Ghoranneviss @gmail.com*

During the HFCVD system, various gas species formed on and near the filament which their transport to substrate play an important role in growing of diamond film [17]. Therefore the parameters, such as the gas pressure [16-17, 23], the temperature of filament and substrate [24-28], the composition of the source gas [13, 16, 29-30] play an important role in CVD diamond growth. Another important part in growing of CVD diamond deposition is nucleation. Various nucleation processes were used such as bias enhanced nucleation (BEN) [24, 31-33], seeding the substrates by scratching with diamond powder, and ultrasonic agitation of substrate with diamond powder [16, 34-36]. It can also be done by etching gas [37]. In the present work, nitrogen used as etching gas to provide suitable nucleation sites for growing nano diamonds.

Using catalyst nano layer, is a useful method to reduce the time from over than four hours to about one hour in HFCVD systems [16], so we used catalyst nano layer to reduce time into around one hour. To study the effect of different catalyst layer and find the best catalyst thickness layer on the growth of NCD films, different catalyst nano layer's thickness were deposited on the substrates. The XRD spectra of the NCD films demonstrate different diffraction peaks for different catalyst thicknesses layer which confirm the presence of crystalline diamond. Scanning electron microscopy (SEM) shows the various morphologies of the films.

RESULTS AND DISCUSSION

1. Catalyst Layer Thickness Measurements

The thickness of the catalyst nano layer varied within the range of 21.6-62nm. The Fig. 1 shows the thickness measurement of the catalyst nano layer for the three samples by Dektak3 profilometer. Fig.1 (a) shows the 21.6 nm thickness for the first sample. Fig. 1(b) and Fig. 1(c) corresponded to second and third sample with thickness of 49 and 62.4 nm for catalyst layer, respectively. These three samples were named A, B and C, respectively.

2. Morphology study

Fig. 2 shows the SEM morphology of the NCD films deposited at different layer thicknesses of the catalyst. The morphology of the samples are similar, as shown in the Fig. 2, revealing diamond films with cauli-flower like structure.

A wide dispersion of NCD structures were observed in sample A with a lowest thickness layer (Fig.2a). By increasing the catalyst thickness layer to 49nm in sample B, the film morphology became denser and smoother and the whole surface is covered by diamond film (see Fig. 2b). In the sample C with the highest catalyst thickness layer, the crystal size increased around 200nm (see Fig. 2c). In Fig. 2c there is also changes in nucleation density and the films became less dense. For comparing the

grain size of samples B and C was shown in the inset of Fig. 2. The smallest grain size with around a couple of tens nanometers corresponded to sample B. The second nucleation made bigger particles in sample C.
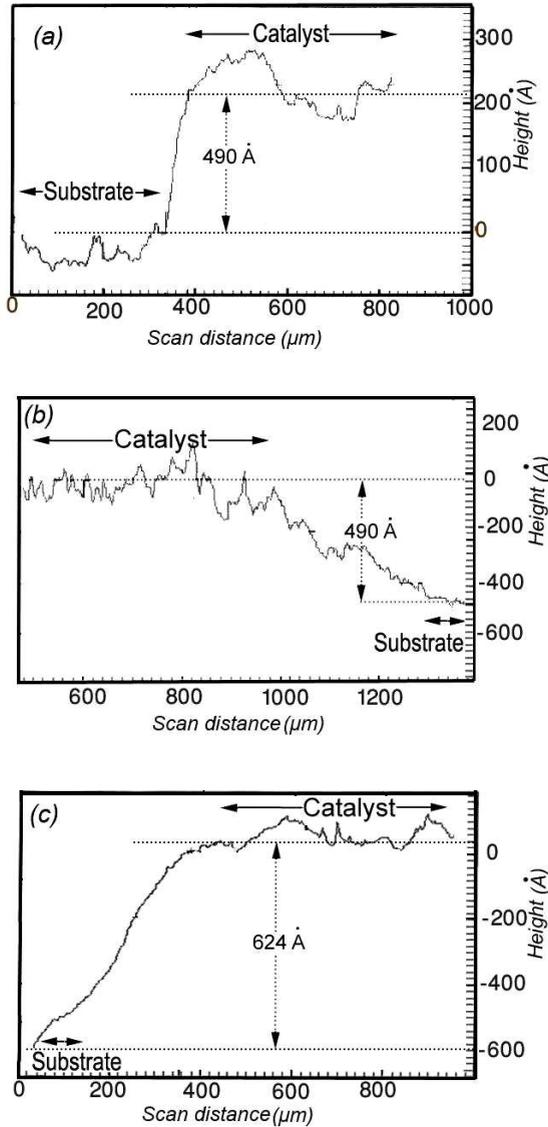

Fig. 1. DEKTAK profilometer results show: a) sample A with 21.6nm, b) Sample B with 49nm, and c) sample C with 62.4 nm, for thickness layer.

259

3. *X-ray diffraction*

XRD patterns of the diamond films deposited for different catalyst layer thicknesses were shown in Fig. 3. For diamond films in sample A, XRD patterns exhibit four peaks from (1 1 1), (104), (110), and (311) crystal planes of diamond. By increasing the layer thickness in sample B, five different crystalline structure of(101), (1 0 2), (104), (108) and (311) was observed, in which the best quality of the diamond peaks refer to the structure with (101) crystallinity. For sample C, the diamond peaks with (111) and (106) crystal planes were only observed. To investigate more, the XRD results were summarized in Table 1. Crystalline structures of (104) and (311) existed in both sample A and B, which they had a higher relative intensity and FWHM in sample B. Regarding to Sherrer's formula, sample B had a better quality and smaller grain size. There was the same crystalline structure of (111) for sample A and C which had the same amount of FWHM and different relative intensities. In XRD spectra of sample C, a sharper peak at 16.3˚ and 33.13˚ corresponded to non-diamond structures. The results show that, by increasing the thickness of the catalyst layer, from 49nm to 62nm, we can see some extra structures. It can be concluded that catalyst thickness layer directly changed the quality, grain size and even crystalline structure of deposited diamond films. XRD studies confirmed previous observation in SEM images that the smallest grain size was corresponding to sample B, which has also the best quality of diamond films. In all samples, the peak at 2theta≈69.2˚ corresponded to Si, the substrate.
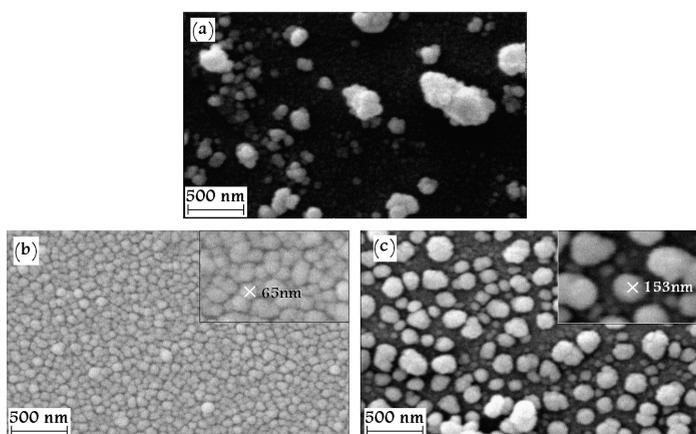
Fig, 2. SEM morphologies of the nanocrystalline diamond deposited in various thicknesses of catalyst layers: (a) sample A, (b) sample B, and (c) sample C. The inset shows the Increasing of the grain size in 200nm scale by increasing the thickness of the nano catalyst layer from sample B to C.
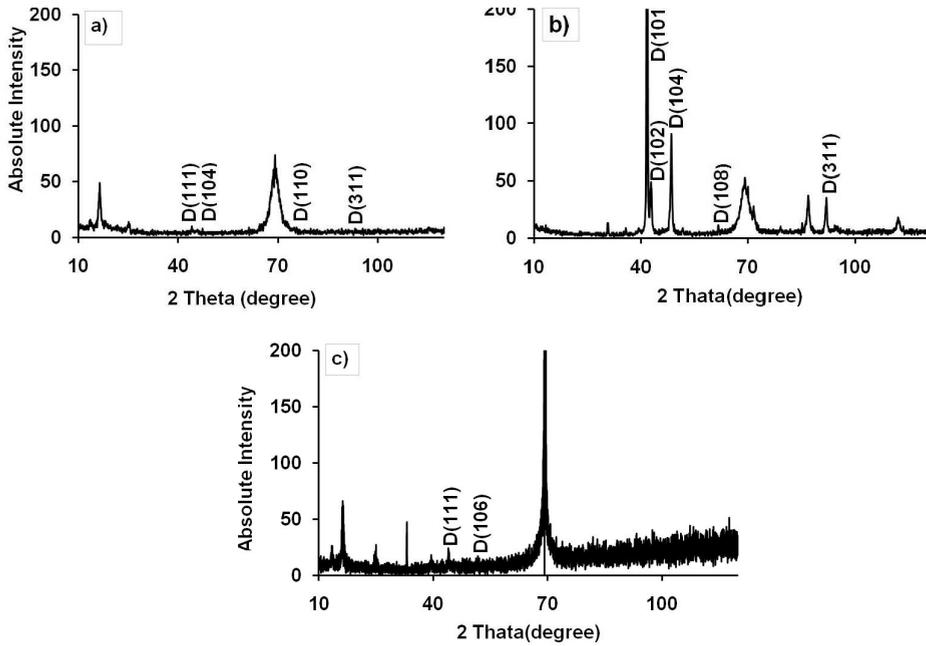
Fig. 3. X-ray diffraction spectra of the diamond films for (a) sample A, (b) sample B, (c) sample C.

Table 1. Results of the XRD studies of the diamond films grown at different catalyst layer thicknesses

Sample	Catalyst layer thickness	Orientation of plane	Pos. [°2Th.]	Height [cts]	FWHM [°2Th.]	Rel. Int. [%]
A	21.6 (nm)	[111]	44.02	2.89	0.315	6.98
		[104]	47.28	2.72	0.236	6.58
		[110]	75.55	2.15	0.315	5.19
		[311]	92.48	1.15	0.197	2.78
B	49 (nm)	[101]	41.68	279.04	0.275	100
		[102]	42.88	38.67	0.315	13.86
		[104]	48.55	84.73	0.275	30.36
		[108]	61.69	6.66	0.197	2.39
		[311]	92.02	28.74	0.275	10.3
C	62.4 (nm)	[111]	44.07	10.76	0.315	0.06
		[106]	53.40	2.28	0.236	0.01

CONCLUSIONS

In this study, the effect of different thicknesses layer of the Au catalyst was investigated in HFCVD system. Different thicknesses of nano catalyst layers within the range of 21-62nm, has different effects on CVD diamond growth. XRD characterizations presented changes in diffraction peaks of crystalline diamond within changing the catalyst thickness layer. Optimized catalyst layer thickness found in sample B with the sharpest peak and small FWHM which indicates the higher quality of CVD diamonds. In sample C with the highest catalyst layer thickness, the quality of diamond films decreased and other non diamond structures appeared.

EXPRIMENTAL SECTION

A hot filament CVD system was used for deposition of nanocrystalline diamond in which the tungsten filament was 1.1mm in diameter and about 1.5 cm in length. P-type silicon wafers with [100] orientation were used as the substrates. The substrates were ultrasonically cleaned in acetone, ethanol and deionized water for 15 minutes in each step to remove organic contaminants.

After pretreatment of Si substrates, to deposit different catalyst layers of gold [38], they were loaded in a DC magnetron sputtering system at 1.3 Pa $(10^{-2}$ Torr) in Ar with Au target. The thickness of the gold nano layer of each substrate was measured by DEKTAK3 surface profile measuring system. Then the substrates put into the stainless steel subholder below the hot filament wires. The distance between filament and substrates was 1.5 cm. The chamber was pumped down to the base pressure of 1.3 Pa with a rotary pump and after that reached to 2×10^{-2} Pa $(1.5\times10^{-4}$ Torr) with diffusion pump.

In the first step, argon gas with flow ratio of 208 sccm was introduced into the chamber for etching the substrates with total pressure of 4 KPa (30 Torr) for 45 minutes. In the second step, nitrogen was introduced into the chamber as an etching gas with flow rate of 80 sccm. At this time, the filament was reached to about 1600℃. The working p ressure was kept in 667 Pa (5 Torr) and duration of time was 40 minutes. In the last step, for growing the nanocrystalline diamond, a mixture of precursor gases of methane and hydrogen were introduced into the chamber. Methane and hydrogen were introduced to the reaction chamber with a total flow rate of 150 sccm to keep the CH4/H2 ratio at 10%. The working pressure in this step was 4 KPa and nanocrystalline diamond was grown after only 75 minutes. During each step, the substrate temperature was controlled by the thermocouple and was kept on 600°C.

The deposited films were characterized by scanning electron microcopy (SEM, XL30), X-ray diffraction spectroscopy (Cu Kα, λ=0.1541 nm), and DEKTAK3 version 2.13 at room temperature.

REFRENCES

1. R.F. Davis, "Diamond Films and Coatings", Noyes publication, New Jersey, **1992**.
2. K. E. Spear, J.P. Dismukes, "Synthetic Diamond: Emerging CVD Science and Technology", John Wiley, New York, **1993**.
3. R.L.C. Wu, A.K. Rai, A. Garscadden, P. Lee, H.D. Desai,K. Miyoshi, *Journal of Applied Physics,* **1992**, *72*, 110.
4. C. Zuikeer, A.R. Krauss, D.M. Guren, X. Pan, J.C. Li, R. Csencsits, A. Erdemir, C. Bindal, G. Fenske, *Thin Solid Films*, **1995**, *270*, 154.
5. J. Lee, B. Hong, R. Messier, R.W. Collins, *Applied Physical Letters*, **1996**, 69, 1716.
6. K. Kobashi, "Diamond Films: Chemical Vapor Deposition for Oriented and Heteroepitaxial Growth", first edn. Elsevier Science, Oxford, **2005**.
7. O.A. Shenderova, D.M. Gruen. "Ultrananocrystalline Diamond - Synthesis, Properties, and Applications", William Andrew Publishing, New York, **2006**.
8. N.Jiang, K.Sugimoto, K.Eguchi, T. Inaoka, Y.Shintani, H.Makita, A.Hatta, A.Hiraki, *Journal of Crystal Growth*, **2001**, *222*, 591.
9. L.C. Chen, T.Y. Wang, J.R. Yang, K.H. Chen, D.M. Bhusari, Y.K.Chang, H.H. Hsieh, W.F.Pong, *Diamond and Related Materials*, **2000**, *9*, 877.
10. H.Yoshikawa, C.Morel, Y.Koga, *Diamond and Related Materials*, **2001**, *10*, 1588.
11. A. Stacey, I. Aharonovich, S. Prawer, J. E. Butler, *Diamond and Related Materials*, **2009**, *18*, 51.
12. T. Tachibana, Y. Ando, A. Watanabe, Y. Nishibayashi, K. Kobashi, T. Hirao, K. Oura, *Diamond and Related Materials*, **2001**, *10*, 1569.
13. L. Chow, D. Zhou, A. Hussain, S. Kleckley, K. Zollinger, A. Schulte, H. Wang, *Thin Solid Films*, **2000**, *368*, 193.
14. A.Heiman, I.Gouzman, S.H.Christiansen, H.P. Strunk, A.Hoffman, *Diamond and Related Materials*, **2000**, *9*, 866.
15. S. Rakha, Z. Xintai, D. Zhu, Y. Guojun, *Current Applied Physics*, **2010**, *10*, 171.
16. M. Pandey, R. D'Cunha, A.K. Tyagi, *Journal of Alloys and Compounds*, **2002**, *333*, 260.
17. Sh. Yang, Zh. He, Q. Li, D. Zhu, J. Gong, *Diamond and Related Materials*, **2008**, *17*, 2075.
18. W.Tang, C.Zhu, W.Yao, Q.Wang, C.Li, F.Lu, *Thin Solid Films*, **2003**, *429*, 63.
19. T. B. Huang, W. Z. Tang, F. X. Lu, N. Ali, J. Gracio, *Thin Solid Films*, **2003**, *429*, 108.
20. J. A. Smith, K. N. Rosser, H. Yagi, M. I. Wallace, P. W. May, M. N. R. Ashfold, *Diamond and Related Materials*, **2001**, *10*, 370.
21. S.S. Proffitt, S.J. Probert, M.D. Whitfield, J.S. Foord, R.B. Jackman, *Diamond and Related Materials*, **1999**, *8*, 768.
22. M. P. Pai, D. V. Musale and S. T. Kshirsagar, *Diamond and Related Materials*, **1998**, *7*, 1526.

23. K. Fabisiak, A. Banaszak, M. Kaczmarski, M. Kozanecki, *Optical Materials*, **2006**, *28*, 106.

24. M.M. Larijani, A. Navinrooz, F. Le Normand, *Thin Solid Films*, **2006**, *501*, 206.

25. S.A. Rakha, Sh. Yang, Zh. He, I. Ahmed, D. Zhu, J. Gong, *Current Applied Physics*, **2009**, *9*, 698.

26. Q.P. Wei, Z.M. Yu, L. Ma, D.F. Yin, J.Ye, *Applied Surface Science*, **2009**, *5*, 1322.

27. N.A. Braga, C.A.A. Cairo, E.C. Almeida, M.R. Baldan, N.G. Ferreira, *Diamond and Related Materials*, **2009**, *18*, 1065.

28. D.C. Barbosa, F.A. Almeida , R.F. Silva, N.G. Ferreira, V.J. Trava-Airoldi, E.J. Corat, *Diamond and Related Materials*, **2009**, *18*, 1283.

29. L.C. Chen, T.Y. Wang, J.R. Yang, K.H. Chen, D.M. Bhusari, Y.K. Chang, H.H. Hsieh, W.F. Pong, *Diamond and Related Materials*, **2000**, *9*, 877.

30. V.Baranauskas, H.J. Ceragioli, A.C. Peterlevitz, S.F. Durrant, *Thin Solid Films*, **2001**, *398-399*, 250.

31. N. Jiang, K. Sugimoto, K. Eguchi, T. Inaoka, Y. Shintani, H. Makita,A. Hatta, A. Hiraki, *Journal of Crystal Growth*, **2001**, *222*, 591.

32. J. T. Huang, W. Y. Yeh, J. Hwang, H. Chang, *Thin Solid Films*, **1998**, *315*, 35.

33. G. H. Song, C. Sun, B. Wang, A. Y. Wang, R. F. Huang, L. S. Wen, *Materials Letters*, **2001**, *48*, 8.

34. J.G. Buijnsters, L. Vázquez, J.J. ter Meulen, *Diamond and Related Materials*, **2009**, *18*, 1239.

35. K. Fabisiak, W. Masierak, E. Staryga, M. Kozanecki, *Optical Materials*, **2008**, *30*, 763.

36. Tien-Syh Yang, Jir-Yon Lai, Chia-Liang Cheng, Ming-Show Wong, *Diamond and Related Materials*, **2001**, *10*, 2161.

37. Z. Khalaj, M. Ghoranneviss, S. Nasirilaheghi, Z. Ghorannevis, R. Hatakeyama, *Chinese Journal of Chemical Physics*, **2010**, *23*, 689.

38. Chih-Kuang Kao, Jhih-Kun Yan, Li Chang, Shih-Yin Cho, Hou-Gaung Chen, *Diamond and Related Materials*, **2004**, *13*, 585

SPECTRAL INVESTIGATIONS AND DFT STUDY OF MIXED THEOPHYILLINE-N,N-CHELATING LIGAND COPPER(II) COMPLEXES

CSILLA NAGY[a], CRISTINA SOMEŞAN[a], ATTILA-ZSOLT KUN[b], BÉLA MIHÁLY[b], EDIT FORIZS[b, *], LEONTIN DAVID[a]

ABSTRACT. Three new mixed-ligand theophylline (th) complexes, $[Cu(th)_2(dmen)(H_2O)] \cdot H_2O \cdot (1)$, $[Cu(th)_2(tmeda)(H_2O)] \cdot 0.5H_2O$ (2) and $[Cu(th)_2(dpen)(H_2O)] \cdot 5H_2O$ (3), were synthesized and investigated by means of infrared and ESR spectroscopic methods. As co-ligands the following ethylenediamine derivatives were used: N,N-dimethyl-ethylenediamine (dmen), N,N,N',N'-tetramethyl-ethylenediamine (tmeda) and *meso*-1,2-diphenyl-ethylenediamine (dpen). Structural parameters of the complexes were investigated by using the unrestricted Becke three-parameter hybrid exchange functional, combined with the Lee–Yang–Parr correlation functional (B3LYP) and LANL2DZ basis set for geometry optimizations. Complexes 1-3 adopt square pyramidal geometries.

Keywords: *copper(II) complexes, electron paramagnetic resonance, meso-1,2-diphenyl-ethylenediamine, N, N-dimethyl-ethylenediamine, N, N, N', N'-tetramethyl-ethylenediamine, theophylline, DFT*

INTRODUCTION

Derivatives of xanthine group nucleobases, like theophylline, have been known for a long time, and commonly used for their biologic effects. Their coordination compounds may serve as model compounds for the interaction of metal ions with molecules of biologic interest.

Theophylline (Scheme 1), *i.e.,* 1,3-dimethyl-2,6-dioxo-purine, in neutral or basic media acts as monodentate ligand and coordinates through the N7 atom which is the preferred binding site in 6-oxopurines [1–3]. The deprotonated theophylline may act as bidentate ligand forming N7/O6 chelates [4].

In our previous works, we reported some new mixed-ligand complexes containing theophyllinato anions and bidentate N,O-donor and N,N-donor ligands [5-7].

* *E-mail: eforizs@chem.ubbcluj.ro*
[a] *Babeş-Bolyai University, Faculty of Physics, RO-400084, Cluj-Napoca, Romania*
[b] *Babeş-Bolyai University, Faculty of Chemistry and Chemical Engineering, RO-400028 Cluj-Napoca, Romania*

Here we report the synthesis and spectroscopic investigations of three new mixed-ligand copper(II)-theophylline complexes containing N,N-donor chelating co-ligands. The geometry of complexes was optimized at B3LYP/LANL2DZ level of theory.
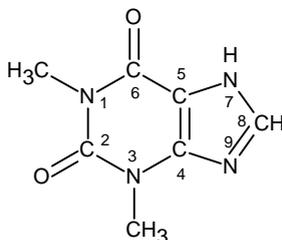
Scheme 1

RESULTS AND DISCUSSION

The complexes $[Cu(th)_2(dmen)(H_2O)]\cdot H_2O$ (**1**), $[Cu(th)_2(tmeda)(H_2O)]\cdot 0.5H_2O$ (**2**) and $[Cu(th)_2(dpen)(H_2O)]\cdot 5H_2O$ (**3**) were synthesised from theophylline and appropriate N,N-chelating diamine copper(II) complexes in basic media according to published methods [5, 7]. Compounds **1**–**3** were isolated in good yield as microcrystalline solids and were characterized by elemental analyses, IR and ESR spectroscopy.

The infrared spectra of all copper(II) complexes show the two strong bands of theophylline assigned to the stretching vibration of carbonyl groups shifted towards lower wavenumbers, due to the deprotonation of theophylline and participation of C(6)=O and C(2)=O groups in intra- or intermolecular hydrogen bond formation. The C=N vibrations of the theophylline are shifted to lower wave numbers in complexes suggesting that the ligand coordinates through one of the imidazole nitrogen atoms, acting as monodentate ligand.

In all spectra of complexes the symmetric and antisymmetric stretching vibrations of coordinated NH_2 groups can be assigned in the 3285–3154 cm^{-1} region. There are significant changes in the bands assigned to N–H vibrations due to deprotonation of theophylline at N(7) site and coordination of the diamine type ligands The diamines are coordinated as bidentate ligands through the nitrogen atoms.

The ν_{CH} vibrations of ligands appear at 2851–2954 cm^{-1} and 3027–3066 cm^{-1} for aliphatic CH_2 and aromatic CH, respectively.

The presence of strong broad bands in FTIR spectra of the complexes at 3500–3200 cm^{-1} may be assigned to various types of hydrogen bonds [5].

Complexes **1** - **3** are monomeric. The room temperature ESR powder spectrum of [Cu(th)$_2$(tmeda)(H$_2$O)]·0.5H$_2$O (**2**) (Fig. 1a) exhibits four hyperfine lines in the $g_\parallel$ region and a strong absorption signal in the $g_\perp$ region. The shape of the spectrum and the values of ESR parameters ($g_\parallel$ = 2.244 and $g_\perp$ = 2.038, $A_\parallel$ = 186 G) correspond to a square pyramidal symmetry suggesting a CuN$_4$O environment for copper ion. The powder ESR spectrum of [Cu(th)$_2$(dpen)(H$_2$O)]·5H$_2$O (**3**) at room temperature indicates a square-pyramidal symmetry. The axial components of the g tensor ($g_\parallel$=2.177, $g_\perp$ = 2.067) are typically for a CuN$_4$O chromophore around the metal ion. For complexes **1-3** no hyperfine splitting was observed because of the interaction of paramagnetic electron with the nitrogen nuclei.

a

b
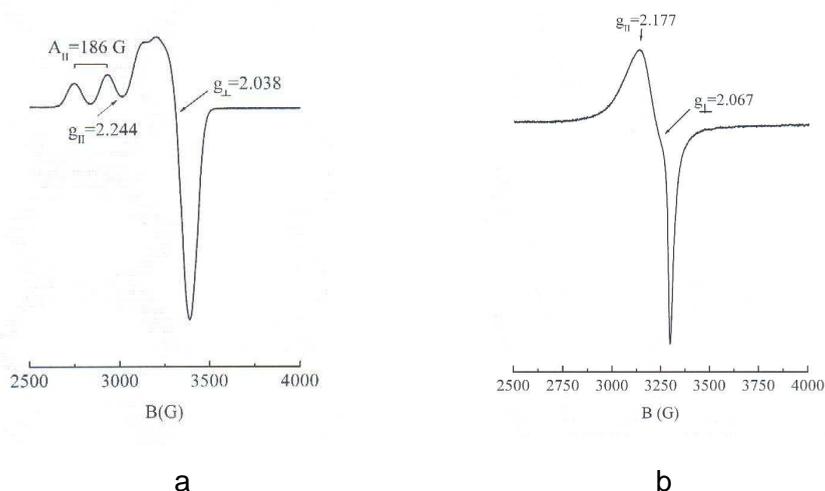
Figure 1. Powder ESR spectra of **2** (a) and **3** (b).

Computational details

Geometry optimizations were performed by using the density functional theory (DFT), and the unrestricted Becke three-parameter hybrid exchange functional, combined with the Lee–Yang–Parr correlation functional (B3LYP) and LANL2DZ basis sets. The *Gaussian09* electronic structure program package was used for calculations [8].

Optimized geometries

The molecular structures of the complexes **1**–**3** were optimized in the gaseous phase. The optimized structures are displayed in Figure 2.

Three possible binding modes were modelled: without bonding of the water molecule, with one coordinated water molecule and with two

coordinated water molecules. The results showed that the pyramidal structure presents higher stabilization energy than the octahedral and (strongly distorted) tetrahedral by 10–20 kcal/mol. The optimized structure of complexes **1-3** presents square pyramidal geometry around the pentacoordinated Cu(II), the base of distorted pyramid consisting of four N atoms of the diamine ligand and the N7 atom of each of the two theophyllinate moieties. One of the water molecules is positioned on the coordination axis, in axial position. The second water molecule in complexes **1-2** and the remaining 5 molecules in the case of complex **3** are relatively far from the central Cu(II) atom; consequently, it can be considered as being located outside the coordination sphere of Cu(II).

The main geometric parameters of complexes **1-3**, optimized at B3LYP/LANL2DZ level of theory, are listed in Table 1. Theoretical calculations revealed that the majority of optimized bond lengths are slightly longer than the experimental values of pentacoordinated copper(II) ion with same donor atoms. This can be a consequence of having performed the theoretical calculations for isolated molecules in gaseous phase, while the experimental results obtained for complexes were recorded for the compounds in solid state. Thus for complex **1** the Cu-N distances for coordinated diamine are slight longer than Cu-N distances (2.121, and 1.192 Å) found in ([Cu^{II}(dmen)(1,2-dtsq)]$_n$ (1,2-dtsq = 1,2-dithiosquarate), where the copper(II) ions bind to 1,2-dtsq oxygen atoms with relatively strong axial bonds [9].

In complex **2** the calculated Cu–N distances for the diamine are longer than in [$Cu(NCS)_2(C_6H_{16}N_2)(H_2O)$] (2.042 and 2.026 Å), and the Cu–O_w distance is shorter than Cu–O_w distance (2.342 Å) found in [$Cu(NCS)_2(C_6H_{16}N_2)(H_2O)$], where the copper(II) has also a square pyramidal coordination [10].

In complex **3** the calculated Cu–N distances for the chelating diamine are longer than in diaqua(1R,2R)-N,N'-bis(4-methylbenzyl)-1,2-diphenyl-ethane-1,2-diamine)-copper(II)diperchlorate dihydrate (1.987 and 2.033 Å), where the copper(II) displays square planar coordination [11].

The theophyllinato moieties coordinating by N7 present Cu–N calculated distance in the range 2.061–2.181 Å, longer than those found in diaqua-bis(theophyllinato)–bis(benzylamine)copper(II) (2.029 Å) centrosymmetrical complex whose structure has previously been determined [12].

According to the calculated values, only one of the water molecules considered for optimization is located inside the coordination sphere. Therefore, the Cu(II) atom is pentacoordinated, all Cu(II) complexes exhibit a distorted pyramidal geometry.

The Cu–O distances with all co-ligands and water follow the same behaviour. They do never differ by more than 0.031 Å. The differences between Cu–N bond lengths for N7 bonded theophylline are nearly 0.063 Å (see Table 1).
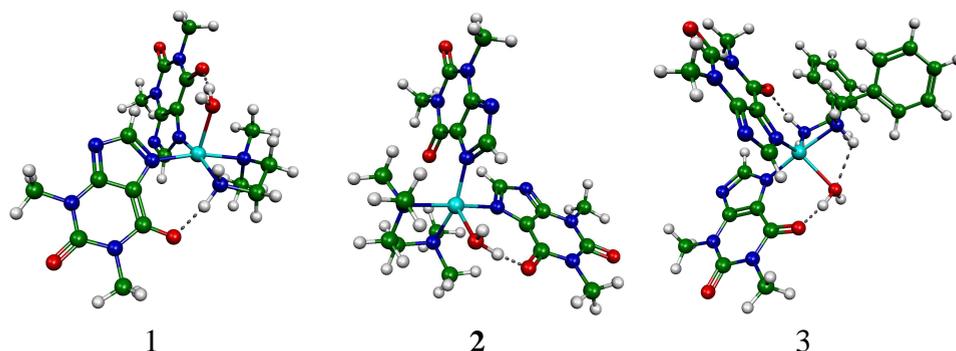
Figure 2. B3LYP/LANL2DZ optimized structures of the copper(II) complexes **1**-**3**.
(Color code: C – grey, N – blue, O – red, H – white, Cu – cyan)

The results show that in the most stable structures the C=O, OH and NH groups form intramolecular H-bonds of the type: C=O···H–N–H and C=O···H-O-H in **1**, C=O···H–O–H in **2**, and C=O···H–O–H, H–O–H···H–N–H, and C=O···H–N–H in **3** (Figure 2). These H-bonds have important role in the stabilization of molecules.

Table 1. Calculated structural parameters.

	1	**2**	**3**
Distances (Å)			
Cu–N$_7$	2.033	2.009	1.992
Cu–N$_7$'	2.023	2.055	2.015
Cu–N	2.161	2.157	2.056
Cu–N$^{'}$	2.061	2.186	2.108
Cu–O$_w$	2.239	2.248	2.270
Angles (°)			
N–Cu–N'	82.93	83.92	81.63
N$_7$–Cu–N$^{'}$	90.33	91.38	96.50
N$_7$–Cu–N$_7$$^{'}$	91.41	91.85	94.07
N$_7$$^{'}$–Cu–N	92.66	91.47	90.90
N$_7$–Cu–O$_w$	98.36	68.86	94.96

N$_7$ and N$_7$$^{'}$ represent the N7 donor atom of the theophylline ligands, N and N$^{'}$ the N donor atoms of the diamine ligand.

Vibrational analysis

The vibrational modes are analyzed by means of the atom movements, calculated in Cartesian coordinates and by visual inspection of the animated vibrations with Gabedit program [13]. Several selected calculated harmonic

frequencies are listed in Table 2, in comparison with the experimental data. The calculated values of the predicted harmonic vibrational frequencies are relatively close to the frequencies found in the experimental FTIR spectrum of the complex.

Table 2. Comparison of the observed and calculated vibrational spectra.

Assignment	Exp. IR 1 (KBr)	Calcd. 1	Exp. IR 2 (KBr)	Calcd. 2	Exp. IR 3 (KBr)	Calcd. 3
O–H str.	3435	3787	3567 3517	3785	3462	3778
N–H str.	3285 3154	3557 3097	–	–	3245 3161	3567 3328
C–H str.	2948 2924 2882 2851	3162 3079 3069 3025	2963 2929	3144 3079 3040 3023	2948 2918 2851	3220 3160 3076
C=O str.	1686 1642	1666 1625	1690 1636	1667 1631	1690 1641	1666 1623

CONCLUSIONS

In summary, we have synthesized and characterized three new mixed-ligand theophyllinato-N,N-donor coordination compounds. A combination of spectroscopic methods and density functional calculations has been used to describe the structure of complexes. For the Cu(II)theophylline complexes with diamine ligands the local symmetry around the Cu(II) ion is strongly influenced by the nature of amines. IR investigations suggest monodentate coordination of the theophylline, respectively the bidentate coordination of the diamine ligands to central copper ion with N atoms. According to the ESR data, all complexes contain the {CuN$_4$O} chromophore, with square pyramidal coordination geometries around the central copper(II) ion. The theophylline coordinates *via* the N7 nitrogen.

Theoretical investigations at B3LYP/LANL2DZ level of the theory revealed that the utilized technique is efficient in optimizing structural geometries of systems based on organic molecules and copper(II) ions.

EXPERIMENTAL SECTION

All reagents and solvents were commercially available and were used without further purification.

Synthesis of (N,N-dimethyl-ethylenediamine)(aqua)-bis(theophylli nato)-copper(II) monohydrate, [Cu(th)$_2$(dmen)(H$_2$O)]·H$_2$O (**1**): To a suspension of

theophylline (0.4 g, 2.02 mmol) in water (15 cm^3), N,N-dimethyl-ethylenediamine (0.5 cm^3) was added. The resulted clear solution was mixed with a second solution of Cu(NO$_3$)$_2$·2H$_2$O (0.2195 g, 1 mmol) in an N,N-dimethyl-ethylenediamine–water mixture (1:5). The reaction mixture was heated at 50°C for 60 min. under stirring and stored at room temperature over night. The resulted blue polycrystalline powder was collected by filtration, washed with aqueous N,N-dimethyl-ethylenediamine (5%) and dried. M.W.: 545.78. Yield: 81%. Elemental analysis: found (calc.) for C$_{18}$H$_{30}$N$_{10}$O$_6$Cu: C 39.58 (39.56), H 5.54 (5.45), N 25,66 (25.41).

(N,N,N',N'-tetramethyl-ethylenediamine)(aqua)-bis(theophyllinato) - copper(II) monohydrate, [Cu(th)$_2$(tmeda)(H$_2$O)]·0.5H$_2$O (**2**) was obtained similarly from N,N,N,N-tetramethyl-ethylenediamine. M.W.: 556.08. Yield: 62%.

Aqua-(meso-1,2-diphenyl-ethylenediamine)-bis(theophyllinato)-copper(II) pentahydrate (**3**), [Cu(th)$_2$(dpen)(H$_2$O)]·5H$_2$O was obtained with the same procedure, by heating at reflux for 3 hours, from (meso-1,2-diphenyl-ethylenediamine). Violet crystals were collected. M.W.: 742.25. Yield: 41%. Elemental analysis: found (calc.) for C$_{28}$H$_{42}$N$_{10}$O$_{10}$Cu: C 45.33 (45.31), H 5.18 (5.70), N 18.63 (18.87).

ACKNOWLEDGMENT

REFERENCES

1. W. J. Birdsall, M. S. Zitzman, *Journal of Inorganic and Nuclear Chemi*stry, **1979**, *41*, 116.

2. W. J. Birdsall, *Inorg. Chim. Acta*, **1985**, *99*, 59.

3. D. J. Szalda, T. J. Kistenmacher, L. *G.* Marzilli, *Journal of The American Chemical Society*, **1976**, *98 (26)*, 8371.

4. A. Romerosa, J. Suarez-Varela, M. A. Hidalgo, J. C. Avila-Roson, E. Colacio, *Inorganic Chemistry*, **1997**, *36*, 3784.

5 S. Gál, J. Madarász, E. Forizs, I. Labádi, V. Izvekov, G. Pokol, *Journal of Thermal Analysis and Cal*orimetry, **1998**, *53*, 343.

6. E. Forizs, A. Debreczeni, A.-Z. Kun, A. Patrut, L. David, O. Cozar, *Revue Roumaine de Chimie,* **2010**, *55*, 697.

7. B. Mihály, E. Forizs, A.-Z. Kun, I. Silaghi-Dumitrescu, *Acta Cryst*allographica, **2009**, *E65*, m579.

8. M. J. Frisch, G. W. Trucks, H. B. Schlegel, G. E. Scuseria, M. A. Robb, J. R. Cheeseman, G. Scalmani, V. Barone, B. Mennucci, G. A. Petersson, H. Nakatsuji, M. Caricato, X. Li, H. P. Hratchian, A. F. Izmaylov, J. Bloino, G. Zheng, J. L. Sonnenberg, M. Hada, M. Ehara, K. Toyota, R. Fukuda, J. Hasegawa, M. Ishida, T. Nakajima, Y. Honda, O. Kitao, H. Nakai, T. Vreven, J. A. Montgomery, Jr., J. E. Peralta, F. Ogliaro, M. Bearpark, J. J. Heyd, E. Brothers, K. N. Kudin, V. N. Staroverov, R. Kobayashi, J. Normand, K. Raghavachari, A. Rendell, J. C. Burant, S. S. Iyengar, J. Tomasi, M. Cossi, N. Rega, J. M. Millam, M. Klene, J. E. Knox, J. B. Cross, V. Bakken, C. Adamo, J. Jaramillo, R. Gomperts, R. E. Stratmann, O. Yazyev, A. J. Austin, R. Cammi, C. Pomelli, J. W. Ochterski, R. L. Martin, K. Morokuma, V. G. Zakrzewski, G. A. Voth, P. Salvador, J. J. Dannenberg, S. Dapprich, A. D. Daniels, O. Farkas, J. B. Foresman, J. V. Ortiz, J. Cioslowski and D. J. Fox, Gaussian 09, Revision A.02, Gaussian, Inc., Wallingford CT, 2009.

9. M. L. Calatayud, I. C.M. Julve, J. Sletten, *Journal of Molecular Structure*, **2008**, *876*, 328.

10. V. Vrábel, J. Garaj, J. Sivý, D. Oktavec, *Acta Crystallographica*, **1999**, *C55*, 551.

11. S. Kobayashi, R. Matsubara, Y. Nakamura, H. Kitagawa, M. Sugiura, *Journal of The American Chemical Society*, **2003**, *125*, 2507.

12. P. Bombicz, J. Madarász, E. Forizs, M. Czugler, G. Pokol, S. Gál, A. Kálmán, *Zeitschrift fur Kristallogrophie*, **2000**, *215 (5)*, 317.

13. A. R. Allouche, Gabedit 2.3.9, http://gabedit.sourceforge.net

TOPOLOGICAL SYMMETRY
OF TWO FAMILIES OF DENDRIMERS

M. MIRZARGAR[a, *], M.J. NADJAFI-ARANIA, A.R. ASHRAFIA

ABSTRACT. A dendrimer is an artificially manufactured or synthesized molecule built up from branched units called monomers. In this paper, the mathematical tools of group theory have been used extensively for the analysis of the symmetry properties of these macromolecules. We prove that it is possible to write the symmetry of a dendrimer, as wreath product of some finite groups. To prove, we consider two infinite classes of dendrimers and compute their topological symmetry groups.

Keywords: Symmetry group, dendrimer, wreath product.

INTRODUCTION

Dendrimers are one of the main objects of nanobiotechnology. They possess a well defined molecular topology. Their step-wise growth follows a mathematical progression. In an exact phrase, dendrimers are hyperbranched macromolecules, showing a rigorous, aesthetically appealing architecture [1-3].

Group theory is one of the most important branches of mathematics for studying molecular structures of compounds. By using tools taken from the group theory, it is possible to evaluate chemical structures according to their symmetry. Here, by symmetry of a molecule, we mean the automorphism group symmetry of its molecular graph. This type of symmetry also called a topological symmetry, accounts only for the bond relations between atoms, and does not fully determine the molecular geometry. The symmetry of a molecular graph does not need to be the same as (i.e. isomorphic to) the molecular point group symmetry. However, it does represent the maximal symmetry which the geometrical realization of a given topological structure may posses [4].

We first recall some algebraic definitions that will be used in the paper. The symmetry of a physical object can be formalized by the notion of a group action: every element of the group "acts" like a bijective map on some set. To clarify this notion, we assume that G is a group and X is a set.

* E-mail: mirzargar@grad.kashanu.ac.ir
[a] Institute of Nanoscience and Nanotechnology, University of Kashan, Kashan 87317-51167, Iran

G is said to act on X when there is a map $\phi : G \times X \longrightarrow X$ such that for all elements $x \in X$, (i) $\phi(e,x) = x$ where e is the identity element of G, and, (ii) $\phi(g, \phi(h,x)) = \phi(gh,x)$ for all $g,h \in G$. In this case, G is called a transformation group; X is called a G-set, and ϕ is called the group action. For simplicity we define $gx = \phi(g,x)$. In a group action, a group permutes the elements of X. The identity does nothing, while a composition of actions corresponds to the action of the composition. For a given X, the set $\{gx \mid g \in G\}$, where the group action moves *x*, is called the group orbit of *x*. The subgroup which fixes is the isotropy group of *x*.
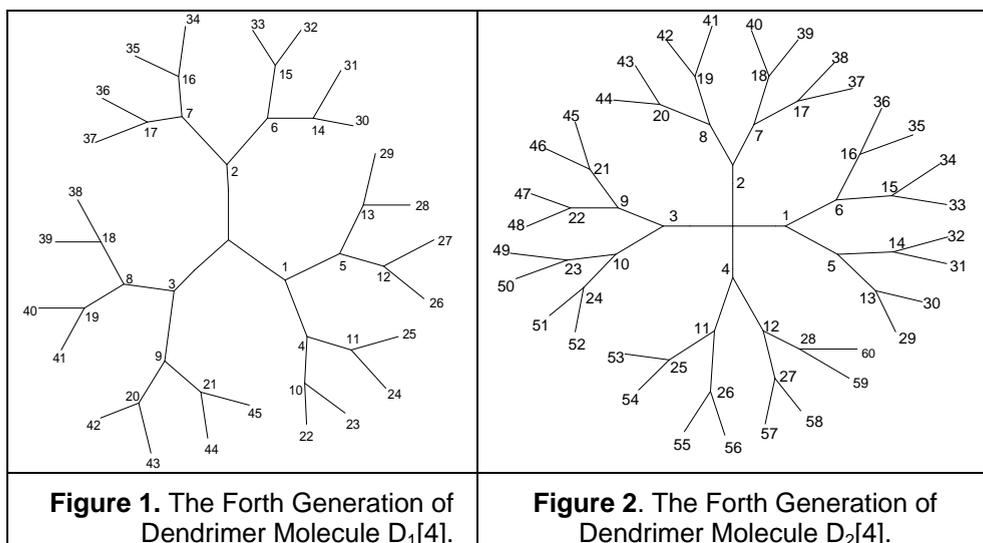
Let G be a group and N be a subgroup of G. N is called a *normal subgroup* of G, if for any $g \in G$ and $x \in N$, $g^{-1}xg \in N$. Moreover, if H is another subgroup of G such that $H \cap N = \{e\}$ and $G = HN = \{xy \mid x \in H, y \in N\}$, then we say that G is a semidirect product of H by N denoted by $H \wedge N$. Suppose X is a set. The set of all permutations on X, denoted by S_X, is a group which is called the symmetric group on X. In the case that $X = \{1, 2, \ldots, n\}$, we denote S_X by S_n or Sym(n).

Let H be a permutation group on X, a subgroup of S_X, and let G be a group. The set of all mappings $X \longrightarrow G$ is denoted by G^X, i.e. $G^X = \{f \mid f: X \longrightarrow G\}$. It is clear that $|G^X| = |G|^{|X|}$. We put $G \wedge H = G^X \times H = \{(f; \pi) \mid f \in G^X, \pi \in H\}$. For $f \in G^X$ and $\pi \in H$, we define $f_\pi \in G^X$ by $f_\pi = f o \pi^{-1}$, where "o" denotes the composition of functions. It is easy to check that the composition law $(f ; \pi)(f' ; \pi') = (ff'_\pi ; \pi \pi')$, makes $G \wedge H$ into a group. This group is called the wreath product of G by H [5]. In some leading papers, Balasubramanian [6–13] introduced the wreath product formalism for computing symmetry of molecules. The present authors continued the mentioned works [14-27] to present a computational approach which is valuable in practical problems. Our calculation within the paper was done by the computer algebra system GAP [28], which is freely accessible from internet.

RESULTS AND DISCUSSION

In this section, we describe our computational approach by GAP in computing symmetry of dendrimer, Figure 1. This method is appropriate for molecules which consist of a number of XY_2 or XY_3 groups (as CH_3 or NO_2) attached to a rigid framework. An Example of such molecule is a dendrimer, which is considered here in some detail, see Figures 1 and 2. With a geometric consideration of dynamic symmetries of the molecules we will show that the symmetry group of the molecule can be specified by wreath product of some known groups. Then based on the structure of the group we apply GAP as a useful package for computing the generating set and also the group structure of this molecule.

Figure 1. The Forth Generation of Dendrimer Molecule $D_1[4]$.

Figure 2. The Forth Generation of Dendrimer Molecule $D_2[4]$.

At first, we consider the dendrimer molecule $D_1[n]$, Figure 1. In order to characterize the symmetry of this molecule we note that each dynamic symmetry operation of $D_1[1]$, considering the rotations of XY_2 groups in different generations of the whole molecule $D_1[n]$, is composed of n sequential physical operations. We first have a physical symmetry of the framework (as we have to map the XY_2 groups on XY_2 groups which are on vertices of the framework). Such operations form the group G of order 6, which as is well known to be isomorphic to S_3 or Sym(3). After accomplishing the first framework symmetry operation we have to map each of the three XY_2 group on itself in the first generation and so on. This is a group isomorphic to $H = ((\ldots(Z_2 \wr Z_2) \wr Z_2) \wr \ldots)\wr Z_2) \wr Z_2$ with n − 1 components. Therefore, the whole symmetry group is isomorphic to $H \wr G$. This is a group of order $6 \times (2^{3(2^{n-1}-1)})$.

We now compute a generator set for this group. To do this, we apply computer algebra system GAP to find a generating set for $D_1[2]$, $D_1[3]$ and $D_1[4]$, see Table 1.

Table 1. Generating Sets for $D_1[2]$, $D_1[3]$ and $D_1[4]$.

$a_1 = (1,2)$	$a_2 = (1,2,3)$	$b_1 = (4,5)$	$b_2 = (6,7)$	$b_3 = (8,9)$	$b_4 = (10,11)$
$b_5 = (12,13)$	$b_6 = (14,15)$	$b_7 = (16,17)$	$b_8 = (18,19)$	$b_9 = (20,21)$	$b_{10} = (22,23)$
$b_{11} = (24,25)$	$b_{12} = (26,27)$	$b_{13} = (28,29)$	$b_{14} = (30,31)$	$b_{15} = (32,33)$	$b_{16} = (34,35)$
$b_{17} = (36,37)$	$b_{18} = (38,39)$	$b_{19} = (40,41)$	$b_{20} = (42,43)$	$b_{21} = (44,45)$	

Suppose $B_1 = \{a_1 , a_2\}$, $B_2 = \{b_1 , b_2 , b_3\}$, $B_3 = \{b_4 , b_5 , b_6 , b_7 , b_8 , b_9\}$ and $B_4 = \{b_{10} , b_{11} , b_{12} , b_{13} , b_{14} , b_{15} , b_{16} , b_{17} , b_{18} , b_{19} , b_{20} , b_{21}\}$. Then $B_1 \cup B_2$, $B_1 \cup B_2 \cup B_3$ and $B_1 \cup B_2 \cup B_3 \cup B_4$ are generating sets of the topological symmetry of $D_1[2]$, $D_1[3]$ and $D_1[4]$. From these calculations, we define permutations $b_{3(2^{i-2}-1)+1}$ and $b_{3(2^{i-2}-1)}$, $2 \le i \le n$, as follows:

$$b_{3(2^{i-2}-1)+1} = \left(3(2^{i-1} - 1) + 1 , 3(2^{i-1} - 1) + 2\right) b_{3(2^{i-2}-1)} = \left(3(2^i - 1) - 1 , 3(2^i - 1)\right)$$

.

Then $B_1 \cup B_2 \cup B_3 \cup \ldots \cup B_n$ is a generating set for $D_1[n]$, where $B_i = \{b_{3(2^{i-2}-1)+1}, \ldots, b_{3(2^{i-2}-1)}\}$.

We now consider the dendrimer molecule $D_2[n]$, Figure 2. The topological symmetry group of the core of this dendrimer is isomorphic to S_4. This group can be generated by $a_1 = (1,2)$, $a_2 = (1,3)$ and $a_3 = (1,4)$. In order to characterize the symmetry of this molecule we note that each dynamic symmetry operation of $D_2[n]$, considering the rotations of XY_2 groups in different generations of the whole molecule $D_2[n]$, is composed of n sequential physical operations. We first have a physical symmetry of the framework (as we have to map the XY_2 groups on XY_2 groups which are on vertices of the framework). Such operations form the group G of order 24, which as is well known to be isomorphic to S_4 or Sym(4). After accomplishing the first framework symmetry operation we have to map each of the four XY_2 group on itself in the first generation and so on. This is a group isomorphic to $H = ((\ldots(Z_2 \wr Z_2) \wr Z_2) \wr \ldots) \wr Z_2) \wr Z_2$ with $n - 1$ components. Therefore, the whole symmetry group is isomorphic to $H \wr G$. This is a group of order $24 \times 2^{(2^{n+1}-4)}$.

Suppose $B_1 = \{a_1 , a_2 , a_3\}$, $B_2 = \{b_1 , b_2 , b_3 , b_4\}$, $B_3 = \{b_5 , b_6 , b_7 , b_8 , b_9 b_{10} , b_{11} , b_{12} \}$ and $B_4 = \{b_{13} , b_{14} , b_{15} , b_{16} , b_{17} , b_{18} , b_{19} , b_{20} , b_{21}, b_{22} , b_{23} , b_{24} , b_{25} , b_{26} , b_{27} , b_{28} \}$, where b_i's are defined as follows:

Table 2. Generating Sets for $D_2[2]$, $D_2[3]$ and $D_2[4]$.

$b_1 = (5,6)$	$b_2 = (7,8)$	$b_3 = (9,10)$	$b_4 = (11,12)$	$b_5 = (13,14)$	$b_6 = (15,16)$
$b_7 = (17,18)$	$b_8 = (19,20)$	$b_9 = (21,22)$	$b_{10} = (23,24)$	$b_{11} = (25,26)$	$b_{12} = (27,28)$
$b_{13} = (29,30)$	$b_{14} = (31,32)$	$b_{15} = (33,34)$	$b_{16} = (35,36)$	$b_{17} = (37,38)$	$b_{18} = (39,40)$
$b_{19} = (41,42)$	$b_{20} = (43,44)$	$b_{21} = (45,46)$	$b_{22} = (47,48)$	$b_{23} = (49,50)$	$b_{24} = (51,52)$
$b_{25} = (53,54)$	$b_{26} = (55,56)$	$b_{27} = (57,58)$	$b_{28} = (59,60)$		

Then $B_1 \cup B_2$, $B_1 \cup B_2 \cup B_3$ and $B_1 \cup B_2 \cup B_3 \cup B_4$ are generating sets of the topological symmetry of $D_2[2]$, $D_2[3]$ and $D_2[4]$. From these calculations, we define two permutations $b_{4(2^{i-2}-1)+1}$ and $b_{4(2^{i-2}-1)}$, $2 \leq i \leq n$, as follows:

$$b_{4(2^{i-2}-1)+1} = \left(4(2^{i-1}-1)+1 \ , \ 4(2^{i-1}-1)+2\right),$$
$$b_{4(2^{i-2}-1)} = \left(4(2^i-1)-1 \ , \ 4(2^i-1)\right).$$

Then $B_1 \cup B_2 \cup B_3 \cup \ldots \cup B_n$ is a generating set for $D_2[n]$, where $B_i = \{b_{4(2^{i-2}-1)+1}, \ldots, b_{4(2^{i-2}-1)}\}$.

CONCLUSIONS

In this paper a general method for computing symmetry of a molecule is presented, which is useful for hyperbranched compounds. We apply our method for two different types of dendrimers and proved that the symmetry groups of these molecules can be reformulated as wreath product of a sequence of well-known finite groups. Using computer algebra system GAP the generating sets for these classes of dendrimers were computed. Our method is general and can be applied to other dendrimers and nanostars.

REFERENCES

1. F. Isaure, P. A. G. Cormack, D. C. Sherrington, *Reactive & Functional Polymers*, **2006,** *66*, 65.
2. H. Meier, M. Lehmann, *Angew. Chem. Int. Ed.*, **1998**, 37, 643.
3. N. C. Beck Tan, L. Balogh, S. F. Trevino, D. A. Tomali, J. S. Lin, *Polymer*, **1999,** *40***,** 2537.
4. G. S. Ezra, *Symmetry Properties of Molecules*, Lecture Notes in Chemistry 28, Springer, **1982**.
5. D. J. S. Robinson, *A course in the theory of groups*, Second edition. Springer-Verlag, New York, **1996**.
6. K. Balasubramanian, *Journal of Chemical Physics*, **1980**, 72, 665.
7. K. Balasubramanian, *Journal of Chemical Physics*, **1981**, *75*, 4572.
8. K. Balasubramanian, *Studies in Physical Theoretical Chemistry*, **1983**, *23*, 149.
9. X. Y. Liu, K. Balasubramanian, *Journal of Computational Chemistry*, **1990**, *11*, 589.
10. K. Balasubramanian, *Theoretica Chimica Acta*, **1990**, *78*, 31.

11. K. Balasubramanian, *Journal of Physical Chemistry*, **2004**, *108*, 5527.
12. K. Balasubramanian, *Chemical Physics Letters*, **2004**, *391*, 64.
13. K. Balasubramanian, *Chemical Physics Letters*, **2004**, *398*, 15.
14. A.R. Ashrafi, M. Hamadanian, *Croatica Chemica Acta*, **2003**, *76*, 299.
15. M. Hamadanian, A.R. Ashrafi, *Croatica Chemica Acta*, **2003**, *76*, 305.
16. A. R. Ashrafi, *MATCH - Communications in Mathematical and in Computer Chemistry*, **2005**, *53*, 161.
17. A. R. Ashrafi, *Chemical Physics Letters*, **2005**, *403*, 75.
18. M.R. Darafsheh, Y. Farjami, A.R. Ashrafi, *MATCH - Communications in Mathematical and in Computer Chemistry*, **2005**, *54*, 53.
19. M. R. Darafsheh, Y. Farjami, A. R. Ashrafi, *Bulletin of the Chemical Society of Japan*, **2005**, *78*, 996.
20. M. R. Darafsheh, A. R. Ashrafi, A. Darafsheh, *International Journal of Quantum Chemistry,* **2005**, *105*, 485.
21. M. R. Darafsheh, A. R. Ashrafi, A. Darafsheh, *Acta Chimica Slovenica,* **2005**, *52*, 282.
22. M.R. Darafsheh, A.R. Ashrafi, A. Darafsheh, *Chemical Physics Letters*, **2006**, *421*, 566.
23. M. R. Darafsheh, A.R. Ashrafi, A. Darafsheh, *International Journal of Quantum Chemistry*, **2007**, *107*, 340.
24. M.R. Darafsheh, Y. Farjami, A.R. Ashrafi, M. Hamadanian, *J. Math. Chem.,* **2007**, *41*, 315.
25. M.R. Darafsheh, Y. Farjami, A.R. Ashrafi, *MATCH - Communications in Mathematical and in Computer Chemistry,***2005**, *54*, 331.
26. M. R. Darafsheh, A. R. Ashrafi, A. Darafsheh, *MATCH Commun Math Comput Chem.*, **2007**, *58*, 47.
27. M. R. Darafsheh, A. R. Ashrafi, A. Darafsheh, *International Journal of Quantum Chemistry*, **2008**, *108*, 440.
The GAP Team, GAP, Groups, Algorithms and Programming, Lehrstuhl De für Mathematik, RWTH, Aachen, **1995**.

NEW 1-AZABICYCLO[3.2.2]NONANE DERIVATIVES OBTAINED BY NUCLEOPHILIC DISPLACEMENT AT CARBON C9 OF CINCHONA ALKALOIDS

SANDA BOTA[a], ION NEDA[b], LUMINIŢA SILAGHI-DUMITRESCU[c]

ABSTRACT. Nucleophilic substitution of mesylates prepared from cinchona alkaloids, generated new 1-azabicyclo[3.2.2]nonan derivatives by cage extension rearrangement reactions which accompanied the displacement of the leaving group. Moderate yields of substituted [3.2.2]azabicyclo derivatives were obtained when water, potassium cyanide or phthalimide nucleophiles were employed. The new substituted [3.2.2]azabicyclo derivatives were further functionalized by oxidation, reduction or condensation reactions.

Keywords: cinchona alkaloids, SN-displacement, 1-azabicyclo[3.2.2]nonane

INTRODUCTION

Cinchona alkaloids, isolated from the bark of several species of *cinchona* trees, are the organic molecules with the most colourful biography [1]. Their history dates back to the early seventeenth century when they were first introduced into the European market after the discovery of the antimalarial property of cinchona bark and the subsequent isolation of its active compound, quinine by P.J. Pelletier and J.B. Caverntou in 1820. Since then, cinchona alkaloids, especially quinine, have played a pivotal medicinal role in human society.

The role of cinchona alkaloids in organic chemistry was firmly established with the discovery of their potential as resolving agents by Pasteur in 1853, which ushered an era of racemate resolutions by the crystallization of diastereomeric salts [2]. Cinchona alkaloids are readily

---

[a] *Universitatea din Oradea, Facultatea de Stiinte, Str. Universităţii nr 1, RO-410087 Oradea,Romania, bsanda@rdslink.ro*
[b] *Technische Universitat Braunschweig, Institut für Organische Chemie, Hagenring 30, 38106 Braunschwei,Germany*
[c] *Universitatea Babeş-Bolyai, Facultatea de Chimie şi Inginerie Chimică, Str. Kogălniceanu, Nr. 1, RO-400084 Cluj-Napoca,Romania*

available as pairs of stereoisomers, such as quinine **1** and quinidine **2**, cinchonine **3** and cinchonidine **4** (figure 1).

Since 2000, explosively expanding interest in chiral organocatalysis as a new stream of catalysis has sparked a second renaissance in the use of cinchona alkaloids as organocatalysts. Thus, cinchona alkaloids and their derivatives are classified as the most "privileged organic chirality inducers", efficiently catalyzing nearly all classes of organic reactions in a highly stereoselective fashion [3].
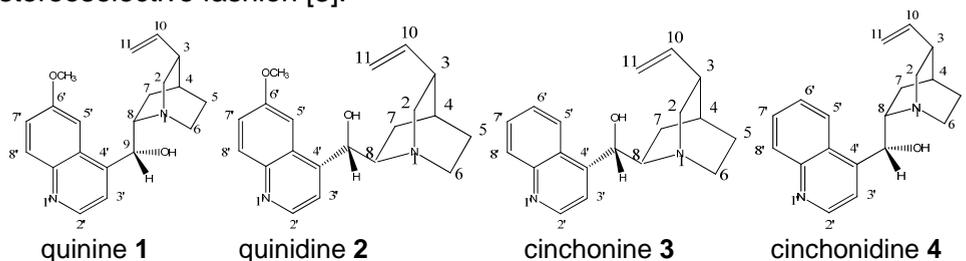

quinine **1**   quinidine **2**   cinchonine **3**   cinchonidine **4**

Figure 1. Structural formulae of cinchona alkaloids

The key feature responsible for cinchona alkaloids successful use is that they possess diverse chiral skeletons and are easily tuneable for different types of reactions. The presence of 1,2-aminoalcohol subunit containing the highly basic and bulky quinuclidine unit which complements the proximal acidic hydroxyl function, is primarily responsible for their use as additives in catalytic asymmetric reactions and for more other remarkable transformations and skeletal shifts [4].

Solvolytic displacements at the saturated carbon are among the best known and the most useful reactions in organic chemistry. Solvolytic displacements at the stereogenic saturated carbon atom linking the two heterocyclic units (C9), of cinchona natural alkaloids, were found to be accompanied by expansion of the 1-azabicyclo[2.2.2]octane structural unit to 1-azabicyclo[3.2.2]nonane, a structural motif which has been scarcely found in nature. A short and simple access to this particular bicyclic system is thus of high interest for exploring its biological and chemical properties. The cage expansion of 1-azabicyclo[2.2.2]octane may occur either *via* a configurationally stable bridgehead iminium ion, or a non classical nitrogen-bridged cation. Ground state conformation, stereoelectronic factors and solvent are crucial features in selecting the reaction conditions [4].

The aim of this work was the study of the nucleophilic displacements at C9 of cinchonine (CD) and cinchonidine (CN) substrates and the formation of 1-azabicyclo[3.2.2]nonane derivatives by cage extension.

RESULTS AND DISCUSSION

In the past, tosylate leaving groups have usually been investigated in solvolysis reactions. Substrates with a neighbouring basic amino function such as cinchona alkaloids gave rise to novel reactivity. Methanolysis of O-tosylated quinine, may appear to be hopelessly complex [1] and after the controversy in the 1960's, C9-functionalized cinchona alkaloids were completely ignored. Hoffmann and co-workers found that a change of the leaving group from tosylate (O-Ts) to methanesulfonate (O-Ms), appears advantageous for many nucleophilic substitutions at C9 and more conveniently, mesylates could be handled more easily [4].

By the reaction of cinchonine (CD) **3** and cinchonidine (CN) **4** substrates with methanesulfonyl chloride under standard conditions [5] we obtained the mesylates CDMs **5** and CNMs **6** respectively (scheme 1), in good yields (76% and 80% respectively).

Reagent and conditions: MsCl, NEt$_3$, THF, rt, 3-16 h
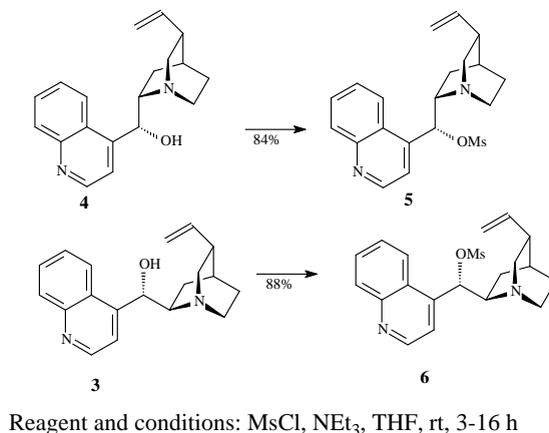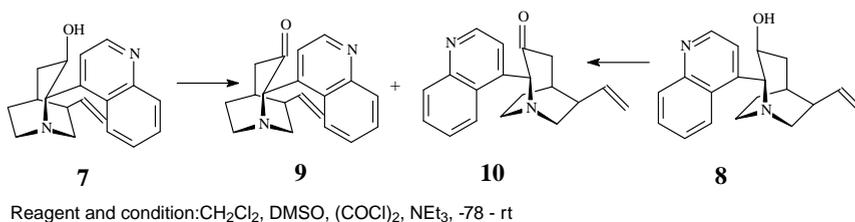
Scheme 1.

Hoffmann and co workers studied the hydrolysis of activated CDMs **5** and CNMs **6** [4]. They observed that CNMs **6** first melt, then dissolve and hydrolyze upon heating in water. After refluxing in pure water the [2.2.2]azabicyclic unit of the substrate is expanded to the [3.2.2]azabicycle product **7** (scheme 2). The hydrolysis of the mesylates can be considered as a green chemistry procedure, since reagents are inexpensive, biodegradable and toxicologically harmless [4,6].

The 1-azabicyclo[3.2.2]nonan derivative **8** was obtained in 52% yields starting with the prepared CNMs **6** (scheme 2).

5   **7**

6   **8**

Reagent and condition:H₂O, reflux, 4-5 h
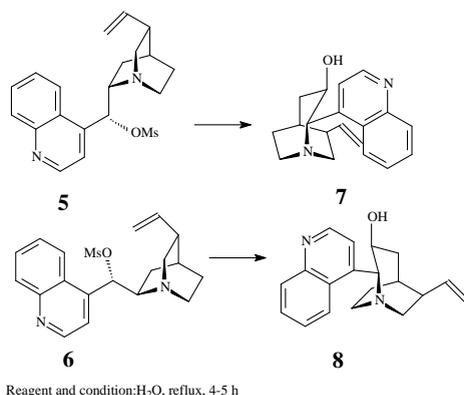
Scheme 2.

The reaction of dimethylsulfoxide (DMSO) with electrophilic activators has been proven as highly useful in the mild oxidation of alcohols to carbonyls [7]. Swern oxidation of β-aminoalcohol **7** gave not only the expected azabicyclic α-aminoketone **9** but also its epimer **10,** in 2:1 ratio (scheme 3).

7   **9**   **10**   **8**

Reagent and condition:CH₂Cl₂, DMSO, (COCl)₂, NEt₃, -78 - rt

Scheme 3.

Nitrogen containing compounds such as amine, hydroxylamine, hydrazine gave condensation reactions with ketone **9** (scheme 4).

**9**   **11**

R = H, OH, NH₂ alkyl,
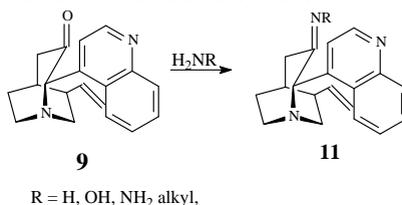
Scheme 4.

Numerous functional group transformations made the oximes very important intermediates in synthetic chemistry. The classical preparation method implies the reaction of carbonyl compounds with hydroxylamine hydrochloride,

in the presence of sodium hydroxide. This method afforded 38% yields of the oxime derived from carbonyl derivative **10**. The IR spectroscopic analysis of oxime **11** has confirmed the presence of characteristic bands due to stretching vibrations of functional groups such as N=C, N-O and O-H.

The synthesis of some other new compounds is based on the nucleophilic substitution previously described as "second cage expansion" rearrangement reaction, which proceed *via* a nitrogen-bridged cation intermediary. The second cage expansion is open to many synthetic variations and has been carried out in the presence of different nucleophiles under SN1-like conditions and thus, compounds with practical use in the preparation of drugs and additives for asymmetric synthesis were conveniently prepared [8]. In scheme 5 is presented the preparation of nitrile **12** starting with CDMs **5** and KCN.
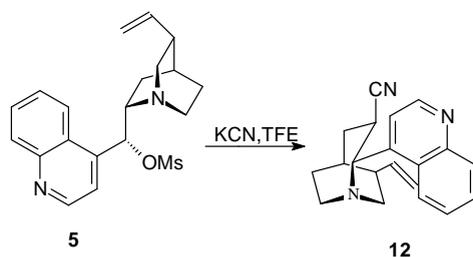
Scheme 5.

In 1972, Mitsunobu described the formation of amino-derivatives, by nucleophilic substitution of an alcohol substrate with phtalimide, followed by reduction of the intermediate with hydrazine [9]. The new 3-amino-1-azabicyclo[3.2.2]nonane **14** was obtained in 53% yields by a similar procedure, starting with CNMs **6**. Nucleophilic substitution of -OMs group generated the rearrangement product **13** which was successfully reduced with hydrazine (scheme 6).
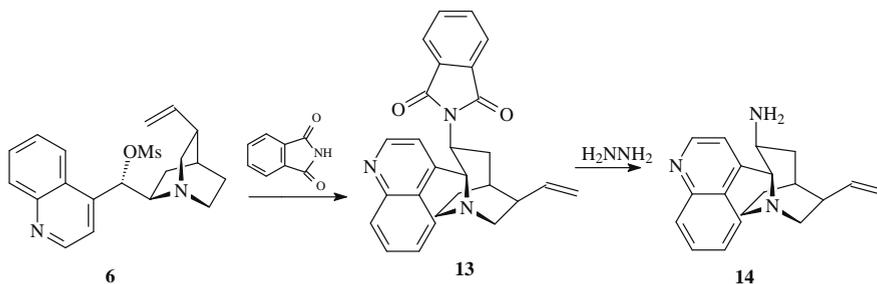
Scheme 6.

Further biological investigations are required in order to establish the potential of the new [3.2.2]azabicyclo derivatives **8, 9, 11, 12, 14** as building blocks in the development of new and effective medicinal products.

CONCLUSIONS

Solvolytic displacement of cinchonine mesylate, accompanied by rearrangement reaction generated the new 3-hydroxi-1-azabicyclo[3.2.2]nonan derivative. Other nuclephiles such as cyanide and phtalimide also produced 3-substituted [3.2.2]azabicyclo derivatives by similar cage extension reactions. Optimal experimental procedures for oxidation, condensation or reduction of the new 1-azabicyclo[3.2.2]nonan derivatives were selected.

EXPERIMENTAL SECTION

General. Preparative column chromatography was performed on J.T. Baker silica gel (particle size 30-60 mm), analytical TLC was carried out on aluminium-backed 0,2 mm silica gel 60 F_{254} plates(E. Merck). H-NMR spectra were recorded on a Bruker AM 400 spectrometer in deuterated chloroform unless otherwise stated, with TMS as internal standard.

9-O-Mesyl-cinchonine (6).

Cinchonine **3** (40 g, 0,136 mmol) was allowed to react according to the general procedure [4] to afford the corresponding mesily derivatives (38.8 g; η = 76%);H-NMR (400 Hz, CDCl₃): δ 8,95(d, J=4,5 Hz, H-2'); 8,21-8,11(m, H-8', H-5'); 7,79-7,72(m, H-7'); 7,67-7,60(m, H-6'); 7,54-7,47 (bl, H-3'); 6,37 – 6,15 (bl, H-9); 6,03 (dd, J=7,4 ,10,5 Hz, H-10); 5,18-5,08 (m, H-11); 3,45-3,29(m, H-8); 2,91-2,83(m,H-2,H-6); 2,72-2,60 (m, H-2, H-6, H-12,)Ms); 2,31-2,20(m, H-3); 2,01-1,91 (m,H-7); 1,90-1,84 (m, H-4); 1,83-1,68(m, H-7); 1,60-1,55(m, H-5) $C_{20}H_{24}N_2O_3S$(376,15): calc. C 64,92%, H 6,38%, N 7,44%; found C 65,14%, H 6,41%, N7,32%.

2-Quinolin-4-yl-6-vinyl-1-aza-biciclo[3.2.2]nonan-3-ol (8).

O-mesilyl cinchonine **6** (10 g, 0,0268 mmol) and 100 ml water was refluxed for 4 hours.To the reaction mixture was added 10 ml NaHCO₃ and pH was adjusted to 12 with NaOH solution. The reaction mixture was diluted with DCM and the organic layer was washed with sat. aq. NaHCO₃ and dried (Na₂SO₄). After removal of the solvent the crude product was purified by chromatography (MTBE:MeOH, 9:1), thus obtaining 4,1 g product (η=52%), H-NMR: (400 MHz, CDCl₃) δ8,84(d, J=4,5 Hz, H-2'); 8,10-8,05(m, H-8',H-5'); 7,69-7,63 (m,H-7'); 7,60-7,54(m,H-6'); 7,42(d, J=4,5 Hz, H-3'); 6,03(ddd, J=7,1 9,5,17,3 H-10); 5,18-5,09(m, H-11); 4,75-4,65 (m, H-3); 4,33(d, J=10,1 Hz, H-2); 3,59(dd, J=9,5, 15,1 Hz, H-7); 3,3-3,18(m,H-8); 2,61-2,51(m,H-7); 2,44-2,35(m,H-6); 2,29-2,21(m,H-4); 2,19-2,13(m, H-5); 2,07-2,0(m, H-4); 1,92-1,83(m, H-9). $C_{19}H_{22}N_2O$(294,45): calc. C 77,55%, H 7,48%, N 9,52%; found C 77.65%, H 7,58%, N 9,42%.

2-Quinolin-4-yl-6-vinyl-1-azabicyclo [3.2.2] nonan-3-one (9)

1g(3,4 mmol) compound **7** was oxidized under Swern procedure [7], with oxalyl chloride (0,88 g) and DMSO (0,53g). After the oxidation, saturated $NaHCO_3$ was added, followed by extraction with DCM; the organic layer was washed with sat. aq. $NaHCO_3$ and dried over anh. Na_2SO_4. After removal of the solvent the crude product was purified by column chromatography (PE:MTBE, 1:1) and resulted 0,57 g product (η=57%).H-NMR: (400 MHz, $CDCl_3$): δ 8,68(d, J=4,5, H-2'); 8,09-8,02(m,H-8'); 7,82-7,76(m,H-5'); 7,62-7,56(m, H-7'); 7,44-7,32(m,H-6'); 7,05(d, J=4,5, H-3'); 5,74(ddd, J=6,8, 9,8, 17,1, H-10); 4,97-5,03(m, H-11,H-11); 4,02-3,8(m, H-5,OH); 2,37-2,22(m,H-7); 2,29-2,19(m, H-8); 2,17(m, H-6); 1,74-1,89(m,H-9); 1,59-1,34(m,H-2).$C_{19}H_{20}N_2O$(292,36): calc. C 78,05%, H 6,89%, N 9,58%; found C 77,87%, H 7,03%, N 9,42%.

2-Quinolin-4-yl-6-vinyl-1-azabicyclo[3.2.2]nonan-3-oxime (11).

The reaction was conducted with 0,2 g(o,6 mmol) ketone(**9**), hydroxylamine hydrochloride 0,65g(0,03 mmol) in ethanol and solid NaOH. The reaction mixture was refluxed for 1 hour and then cooled to rt. The reaction mixture was diluted with HCl solution. The crystaline product formed was filtered and dried. The product was disolved in DCM purified by column chromatography (MTBE:MeOH, 3:1) and resulted 0,07 g product (η=38%).H-NMR: (400 MHz, $CDCl_3$): δ 8,92(d, J=4,6, H-2'); 8,65(d, J=8,2, H-5'); 8,05(d, J=8,2, H-8');7,66-7,58(m, H-7');7, 44(m, H-6'); 7,31(d, J=4,5 H-3'); 5,92(ddd, J=6,8, 10,5, 17,2, H-10); 5,26-5,17(m,H-11); 4,42(d, J=9,4, 14,3, H=7); 3,9(m,H-2); 3,37-3,27(m, H-7); 2,96-2,81(m,H-8); 2,53-2,43(m, H-8, H-4); 2,31-2,23(m, H-6); 2,11-2,04(m, H4,H5); 2,02-1,92(m, H-9).$C_{19}H_{21}N_3O$(307,38): calc. C 74,23%, H 6,88%, N 13,67%; found C 73,97%, H 6,96%, N 13,48%.

2-Quinolin-4-yl-6-vinyl-1-aza-biciclo[3.2.2]nonan-3-carbonitryl. (12)

O-mesilylcinchonine **6** (1 g, 0,0026 mmol) and 13 ml TFE and KCN(0,52g; 0,008 mmol) was refluxed for 3 days. The reaction mixture was washed with sat. aq. $NaHCO_3$ and dried (Na_2SO_4). After removal of the solvent the crude product was purified by chromatography (ether:MeOH, 9:1) and result 0,37 g product (η=47%). H-NMR: (400 MHz, $CDCl_3$): δ 8,93(d, J=4,5 Hz, H-8'); 8,15(d, J=8,4 Hz, H-8'); 8,01(d, J=8,4 Hz, H-5'); 7,76-7,71(m, H-7'); 7,65-7,59(m, H-6'); 7,39(d, J=4,6 Hz, H-3'); 5,97(m, H-10); 5,28-5,14(m, H-11); 4,80(d, J=11,7 Hz, H-2); 3,60-3,519M, H-3); 3,50-3,40(m, H-80; 3,23-3,13(m, H-8); 2,93-2,84(m, H-7,H-4); 2,56-2,44(m, H-6); 2,30-2,24(m, H-5); 2,11-1,85(m, H-4, H-9).$C_{20}H_{21}N_3$(303,38): calc. C 79,17%, H 6,97%, N 13,85%; found C 79,28%, H 7,09%, N 13,62%.

2-(2-Quinolin-4-yl)-6-vinyl-1-aza-biciclo[3.2.2]nonan-3-yl) izoindolin - 1,3-dione (13).

O-mesilylcinchonine **6** (1 g,0,00 26 mmol), TFE(3 ml), t-butylamonium hydrogensulphate(0,22g, 0,00085 mmol) and potasium

phtalimide (1,44 g, 0,0078 mmol) was refluxed for 3 days. The reaction mixture was washed with sat. aq. $NaHCO_3$ and dried (Na_2SO_4). After removal of the solvent the crude product was purified by chromatography (ether:MeOH, 9:1) and resulted 0,2 g product (η=18%).H-NMR: (400 MHz, $CDCl_3$): δ 8,68(d, J=4,6, H-2'); 8,43(d, J=7,9, H-5'); 8,27(dd, J= 4,6. 9,6, H2'', H5''); 8,13(d, J=8,2, H-8');7,78-7,72(m, H-7');7,69(m, H3'', H4''); 7,47(d, J=4,5 H-3'); 5,97(ddd, J=6,8, 10,5, 17,2, H-10); 5,63-5,55(m,H-3); 5,21-5,11(m,H-11); 4,52(d, J=9,4, 14,3, H=7); 3,23-3,17(m, H-7); 2,37-2,32(m,H-8); 2,68(s, H2); 2,26-2,21(m, H-8, H-4); 2,11-2,06(m, H-6); 2,05-2,0(m, H4,H5); 1,92-1,82(m, H-9).$C_{27}H_{25}N_3O_2$(438,48): calc. C 73,58%, H 5,83%, N 9,63%; found C 73,71%, H 5,96%, N 9,48%.

3-Amino-2-(Quinolin–4-yl)-6-vinyl-1-aza-bicyclo-[3.2.2]nonane   (14)

Compound **13** (0,13g, 0,0003 mol), hydrazine (0,2 ml, 0,004mol), ethanol (3ml) was heated at 60℃ for 5 hours. The reaction mixture was filtered, and then the solvent was removed. The residue was dissolved in DCM and then purified by column chromatography (eluent ether: ethanol 9:1) and resulted 0,052 g product ((η=52%).H-NMR: (400 MHz, $CDCl_3$): δ 8,78(d, J=4,6, H-2'); 8,38(d, J=8,1 H-5'); 8,05(d, J=7,8, H-8');7,58-7,51(m, H-7'); 7,44(d, J=6,1, G-6'); 7,34(d, J=4,6 H-3'); 5,89(ddd, J=6,8, 10,5, 17,2, H-10); 5,52-5,42(m, H-3); 5,33-5,23(m,H-11); 4,42(d, J=9,4, 14,3, H=7); 3,26-3,18(m, H-7); 2,86-2,77(m,H-8); 2,68(s, NH2); 2,66-2,53(m, H-8, H-4); 2,37-2,28(m, H-6); 1,83-1,74(m, H4,H5); 1,72-1,61(m, H-9).$C_{19}H_{23}N_3$(293,39): calc. C 77,77%, H 7,90%, N 14,32%; found C 77.86%, H 8,04%, N14,20%.

REFERENCES

1. C.E. Song, **"**Cinchona Alkaloids in synthesis and catalysis" ,Wiley-VCH,New-York **2009.**
2. W.M.Braje, R. Wartchow, H.M.R. Hoffmann, *Ang. Chem. Int. Ed*, **1999**, 2539.
3. C.Bolm, J.P.Hildebrand, K. Muniz, "Recent Advances in Ad and AA in Catalytic Asymmetric Synthesis", ed. I. Ojima, Wiley-VCH, New York, **2000.**
4. M. H. Franz, S, Roper, R. Wartchow, H.M.R. Hoffmann, *J.Org. Chem*, **2004**, *69*, 2983.
5. O. Schrake, H. M. Franz, R. Wartchow, H.M.R. Hoffmann, *Tetrahedron*, **2000**, *50*, 4453.
6. S. Roper, M.H. Franz, R. Wartchow, H.M.R. Hoffmann, *J. Or. Chem.*,**2003,** *68*,4944.
7. A.J.Mancuso, D. Swern, *Synthesis*, **1981,** 165.
8. H.M.R.Hoffmann, J. Frackenpohl, *Eur.J.Chem*,**2004,** 4293
9. O. Mitsunobu, M.Wada,T.Sano, *J.Am.Chem.Soc*,**1972,** *94*, 679